

Advancements in MR-ToF Technology and  
Implementation of Doppler and Sympathetic Cooling  
for the Study of Radioactive Ions

**I n a u g u r a l d i s s e r t a t i o n**

zur

Erlangung des akademischen Grades eines  
Doktors der Naturwissenschaften (Dr. rer. nat.)

der

Mathematisch-Naturwissenschaftlichen Fakultät

der

Universität Greifswald

vorgelegt von

Franziska Maria Maier

geboren am 28.07.1994

in Rohrbach-Berg, Österreich

Greifswald, 21.7.2023

Dekan: Prof. Dr. Gerald Kerth

1. Gutachter: Prof. Dr. Lutz Schweikhard

2. Gutachter: Prof. Dr. Maxime Brodeur

Tag der Disputation: 21.7.2023

# Contents

<b>Nomenclature</b>	<b>IV</b>
<b>1 Introduction</b>	<b>1</b>
1.1 Radioactive Ion Beam Facilities . . . . .	1
1.2 Nuclear-Structure Studies . . . . .	2
1.3 Charge Radii and Hyperfine Structure Measurements via Fluorescence-Based Collinear Laser Spectroscopy . . . . .	3
1.4 Ion Traps . . . . .	4
1.4.1 Paul Traps . . . . .	5
1.4.2 MR-ToF Devices . . . . .	6
<b>2 Fluorescence-Based Collinear Laser Spectroscopy in an MR-ToF device</b>	<b>7</b>
2.1 Scientific Motivation . . . . .	7
2.2 Introduction of the MIRACLS Technique . . . . .	10
2.3 The MIRACLS Proof-of-Principle Experiment . . . . .	12
2.4 MIRACLS' High Resolution Apparatus . . . . .	13
2.5 Outlook to Planned Measurement Campaigns . . . . .	14
<b>3 Photodetachment Studies in an MR-ToF Device</b>	<b>15</b>
3.1 Scientific Motivation . . . . .	15
3.2 Introduction of the MIRACLS Technique for Photodetachment Studies . . . . .	18
3.3 Experimental Results . . . . .	19
3.3.1 Boost in Signal Sensitivity . . . . .	19
3.3.2 Measurement of the Electron Affinity in $^{35}\text{Cl}$ . . . . .	20
3.4 Outlook to Future Applications for Rare Isotope Sciences . . . . .	21
3.4.1 High-Precision Isotope Shift Measurements Between $^{35,36,37}\text{Cl}$ . . . . .	21
3.4.2 Highly Sensitive $E_A$ Measurements of Various Radioactive Elements . . . . .	22
<b>4 Doppler and Sympathetic Cooling for the Investigation of Short-Lived Radionuclides</b>	<b>23</b>
4.1 Motivation and Introduction of the Technique . . . . .	23
4.2 Experimental Results . . . . .	24
4.3 Outlook to Future Experiments at RIB Facilities . . . . .	26
<b>5 Highly Selective and High-Flux Mass Separation for Short-Lived Radionuclides</b>	<b>27</b>
5.1 Motivation and Current Challenges . . . . .	27
5.2 MR-ToF Mass Resolving Power and Space Charge Simulations and their Experimental Benchmarking . . . . .	28
5.3 Conceptual Design and Simulation Results of the Envisioned Mass Separator .	30
5.4 Outlook . . . . .	31
<b>6 Conclusion</b>	<b>33</b>
<b>7 Bibliography</b>	<b>34</b>
<b>8 Cumulative Thesis Articles</b>	<b>54</b>
8.1 Doppler and Sympathetic Cooling for the Investigation of Short-Lived Radioactive Ions . . . . .	56

*Contents*

8.2	Simulation Studies of a 30-keV MR-ToF Device for Highly Sensitive Collinear Laser Spectroscopy . . . . .	76
8.3	Increased Beam Energy as a Pathway Towards a Highly Selective and High-Flux MR-ToF Mass Separator . . . . .	91
<b>9</b>	<b>Curriculum vitae</b>	<b>116</b>
<b>10</b>	<b>Acknowledgments</b>	<b>121</b>

# Nomenclature

## Acronyms

$\chi$ -EFT	.....	chiral effective field theory
BNG	.....	Bradbury-Nielsen Gate
CLS	.....	collinear laser spectroscopy
CRIS	.....	Collinear Resonance Ionization Spectroscopy
DC	.....	direct current
ISCOOL	.....	ISOLDE's general purpose linear Paul trap
ISOLDE	.....	radioactive ion beam facility at CERN
MIRACLS	.....	Multi Ion Reflection Apparatus for Collinear Laser Spectroscopy
MR-ToF	.....	Multi-Reflection Time-of-Flight
PUMA	.....	antiProton Unstable Matter Annihilation Project
QCD	.....	quantum chromodynamics
RF	.....	radio frequency
RIB	.....	radioactive ion beam
rms	.....	root mean square
ToF	.....	time-of-flight
VS-IMSRG	....	in-medium similarity renormalization group

## Symbols

$\delta\langle r^2 \rangle^{A,A'}$	.....	difference in rms charge radius
$\delta\nu^{A,A'}$	.....	optical isotope shift
$\delta\nu_{\text{FS}}^{A,A'}$	.....	field shift
$\delta\nu_{\text{MS}}^{A,A'}$	.....	mass shift
$\Delta E_A$	.....	error in the electron affinity
$\Delta m$	.....	mass difference
$\Gamma$	.....	signal sensitivity for photodetachment measurements
$\hbar$	.....	reduced Planck's constant

<b>L</b>	total orbital momentum
<b>S</b>	spin angular momentum
$\nu_0^A$	centroid of hyperfine spectrum
$\Phi_{\max}$	maximal ion flux
$\Phi_{\text{ph}}$	laser photon flux
$\sigma_{\text{ph}}$	photodetachment cross section
$\sigma_E$	energy spread
$\sigma_f$	Doppler broadening
$\Theta$	Heaviside step function
$A$	mass number
$A_w$	scaling factor in the Wigner law
$E$	ion's kinetic energy
$E_{\text{ph}}$	photon energy
$E_A$	electron affinity
$F_{\text{FS}}$	field-shift factor
$k_B$	Boltzman constant
$K_{\text{MS}}$	mass-shift factor
$l$	orbital angular momentum quantum number
$m$	ion's mass
$N$	neutron number
$n$	atomic shell number
$N_{\text{ev}}$	photodetachment events
$N_{\text{ion}}$	number of ions
$N_{\max}$	maximal number of simultaneously stored ions in MR-ToF device
$N_{\text{MS}}$	normal mass-shift factor
$q$	ion's charge
$r$	distance between additional electron and the nucleus of a negatively-charged ion
$R_{\text{inf}}$	finally attainable mass resolving power
$S_{\text{MS}}$	specific mass-shift factor
$T$	temperature
$t_{\text{proc}}$	processing time for MR-ToF mass separation
$w$	line width of atomic transition

# 1 Introduction

## 1.1 Radioactive Ion Beam Facilities

Radioactive ion beam (RIB) facilities around the world [13–21]<sup>1</sup> produce beams of short-lived radioactive ions and are, hence, major drivers in the expansion of our knowledge in nuclear structure, in nuclear astrophysics, i.e. in understanding the formation of chemical elements, and allow searches for new physics beyond the standard model of particle physics [22, 23]. Additionally, RIB facilities provide unique opportunities for applications in medical physics, material science, chemistry and biophysics.

For these reasons, an enormous effort is invested into the capabilities of RIB facilities in terms of enhanced production of radionuclides, RIB purification and ion optical quality to meet the constantly growing requirements imposed by present and future experimental programs. Simultaneously, the measurement apparatus themselves are further advanced in order to experimentally access the most exotic radionuclides far away from stability which can only be produced in very low quantities and often with a large isobaric contamination, i.e. unwanted ions of similar mass.

Ion traps such as Paul traps and Multi-Reflection Time-of-Flight (MR-ToF) devices have over the years significantly gained in importance at RIB facilities [24–41]. For instance, they are widely used for the preparation of high-quality radioactive ion beams for subsequent experiments. In particular, buffer-gas-filled linear Paul traps are employed for ion beam accumulation, cooling and bunching while MR-ToF devices are utilized as highly selective mass separators. In this PhD work, Doppler- and sympathetic cooling is implemented in a typical linear Paul-trap cooler-buncher enabling a reduction of the longitudinal emittance of radioactive ion beams resulting in a significant improvement of the ion beam quality (chapter 4). Moreover, a next-generation MR-ToF device is conceptualized in order to achieve isobaric pure beams with a higher ion intensity than state-of-the-art MR-ToF devices can provide (chapter 5). Both of these advances are expected to become important for a wide range of experimental programs pursued at low-energy branches of RIB facilities ranging from fundamental symmetry studies, nuclear structure, rare isotope studies with antimatter, searches of physics beyond the standard model to material science and the production of medical isotopes.

Furthermore, MR-ToF devices have enabled precise measurements of many previously unknown nuclear masses (see e.g. references [42–45] for exemplary results published in 2022) as well as mass measurements of isomeric nuclear states [46, 47]. Very recently, the Multi Ion Reflection Apparatus for Collinear Laser Spectroscopy (MIRACLS) has been envisioned to access electromagnetic properties of scarcely produced radionuclides [1–6]. By trapping ions between the two electrostatic mirrors of an MR-ToF device, the same ion bunch is probed by a laser for thousands of times in the MIRACLS approach compared to a single passage in traditional collinear laser spectroscopy (CLS). The resulting increase in experimental sensitivity is beneficial for the measurement of nuclear properties via fluorescence-based CLS of very rare, positively-charged radionuclides (see chapter 2) as well as for electron-affinity measurements of negatively-charged ions via laser-photodetachment-threshold spectroscopy (see chapter 3).

These MIRACLS measurements will serve as important benchmarks for modern atomic and

---

<sup>1</sup>Citation numbers 1-12 are reserved for those references where the author of this thesis is one of the authors.

nuclear theory especially in its description of nuclear charge radii. Section 1.2 hence provides a short overview over modern nuclear theory and section 1.3 discusses charge radii measured via CLS. In section 1.4 the general operational principles of Paul traps and MR-ToF devices are explained, as needed for chapters 2-5 which discuss Doppler and sympathetic cooling, highly selective and high-flux MR-ToF mass separation and the MIRACLS approach for highly sensitive measurements of nuclear properties and electron affinities.

## 1.2 Nuclear-Structure Studies

The atomic nucleus contains protons and neutrons, that are bound together via the strong force. Certain atomic nuclei made out of a specific number of protons or neutrons, so-called magic numbers, show an extraordinary stability behaviour. For example, the nuclear charge radius along an isotopic chain decreases towards a magic number [48] or the binding energy of nuclei consisting of specific proton or neutron numbers is significantly larger than expected by the Bethe-Weizsäcker semiempirical mass formula [49] which is based on the liquid drop model of the nucleus. Maria Goeppert Mayer and J. Hans D. Jensen received a part of the Nobel prize for physics in 1963 “for their discoveries concerning nuclear shell structure” with which they explained the occurrence of the magic numbers: Similarly to the electrons in an atom, protons and neutrons in an atomic nuclei occupy quantum levels that are separated by energy gaps, so called “shells” [50]. While in 1960 this was a purely phenomenological description, modern nuclear theory traces the magic numbers down to nucleon-nucleon forces inspired by low-energy quantum chromodynamics (QCD).

Unexpectedly, far away from the valley of stability shell closures at established magic numbers are disappearing and new ones are emerging at other nucleon numbers [51, 52]. To pin down the microscopic origin of this so-called shell evolution remains a central theme of contemporary research. Modern nuclear theory aims to explain these discontinuities with the ultimate goal to predict all nuclear-structure phenomena across the entire nuclear chart in one consistent and first-principle-based framework.

In the last 20 years a remarkable progress was made in microscopic descriptions of atomic nuclei, in particular in nuclear ab-initio theory [53, 54]. In this framework, the atomic nucleus is described based on two- and three-body nucleon interactions inspired by QCD, the underlying theory describing the strong interaction between quarks and gluons. Since QCD is non-perturbative for low energies [53] most nuclear-structure calculations based on the underlying theory of QCD are not tractable<sup>2</sup>. Hence, low-energy effective theories of QCD are formulated, such as the chiral effective field theory  $\chi$ -EFT [56], which treats the nuclear many-body problem at an adequate resolution scale instead of working explicitly with the more elementary quarks and gluons. In particular, the effective degrees of freedom of  $\chi$ -EFT are pions and nucleons instead of quarks and gluons. Free parameters of  $\chi$ -EFT are fixed to experimental data such as phase shifts in nucleon scattering and observables in light nuclei with  $A \leq 4$ . This microscopic description of the atomic nucleus based on  $\chi$ -EFT-based nuclear forces is commonly referred to as ab-initio.

After the construction of the nucleon interaction potentials from  $\chi$ -EFT, the Schrödinger equation needs to be solved to calculate nuclear properties. The nuclear Hamiltonian is given as a sum of the single-particle kinetic energies of the individual nucleons, the 2-body interaction potentials between two nucleons up to the multi-body interaction potential between multiple nucleons [57]. A truncation after the 3-body interaction potential is normally performed. A solution of the nuclear many-body problem from first principles is possible via e.g. the Coupled

---

<sup>2</sup>Note, that lattice QCD allows to approach nuclear problems directly based on the underlying QCD. Due to its large computational demands, it is so far however limited to very light nuclei [55].

Cluster theory [58] or the Valence Space In-Medium Renormalization group method [59] and nuclear properties such as nuclear charge radii or binding energies can be calculated along large regions of the nuclear chart.

While modern nuclear theory continues to advance its description of atomic nuclei, new experimental data are in high demand to gauge validity and accuracy of these theoretical calculations. Especially, nuclear properties of exotic radionuclides with “extreme” neutron-to-proton ratios as available at RIB facilities constitute valuable benchmarks for nuclear-structure theory. The ultimate goal of modern nuclear theory is to obtain an universal description of nuclear properties across the entire nuclear chart, which is rooted in QCD.

### 1.3 Charge Radii and Hyperfine Structure Measurements via Fluorescence-Based Collinear Laser Spectroscopy<sup>3</sup>

For more than four decades fluorescence-based CLS has been employed to determine properties of short-lived radionuclides and to hence provide insight into the nuclear structure far away from stability [60–64]. In this technique, a fast beam of ionic or neutral atoms is superimposed with a continuous-wave, narrow-band laser beam. Fluorescence photons from laser-excited ionic or neutral atoms are detected by photomultiplier tubes. By scanning the laser around the resonance frequency, the hyperfine structure of the optical transition is obtained. A fine structure splitting of the atomic energy levels occurs due to the spin-orbit coupling of the total orbital momentum  $\mathbf{L}$  with the spin angular momentum  $\mathbf{S}$  of all electrons, that are moving in the Coulomb field of a point-like nucleus. An additional splitting (hyperfine splitting) of the fine structure levels arises when taking the internal structure of the nucleus into account. Hence, due to the interaction of the nucleus with the surrounding electron cloud, many properties of the nucleus are encoded in the atomic or ionic energy spectra.

To increase the signal-to-noise ratio, current state-of-the-art CLS experiments employ bunched ion beams formed in a Paul-trap cooler-buncher [61, 65], see section 1.4.1. Photon signals are only accepted when the ion bunch is within the optical detection region such that a time-gated spectrum is obtained. The influence of background originating from laser-stray light or detector dark counts is hence reduced by around 4 orders of magnitude [61, 65]. Moreover, fast ion beams with a kinetic energy  $E$  of tens of kiloelectronvolts are typically employed. This minimizes the Doppler broadening  $\sigma_f$  of the measured transition according to  $\sigma_f \propto \sigma_E/\sqrt{E}$  [66], where  $\sigma_E$  is the energy spread of the ions, and a spectral resolution approaching the natural line width of the transition is obtained. Due to its high precision, accuracy and resolution, CLS is a powerful experimental technique for accessing nuclear spins, magnetic dipole and electric quadrupole moments of short-lived radionuclides from the observed hyperfine spectra, fully independent from nuclear models.

Moreover, changes in the root-mean-square (rms) charge radii between different isotopes of the same element are accessible by laser spectroscopy. To this end, the hyperfine structure is probed and shifts in the atomic or ionic energy levels between different isotopes of the same element are evaluated. The measurable optical isotope shift  $\delta\nu^{A,A'}$  is defined as difference in the transition energies between two fine structure states of two different isotopes with mass numbers  $A$  and  $A'$  [63, 67],

$$\delta\nu^{A,A'} = \nu_0^A - \nu_0^{A'} = \delta\nu_{\text{FS}}^{A,A'} + \delta\nu_{\text{MS}}^{A,A'}, \quad (1.1)$$

where  $\nu_0^A$  is the centroid frequency of the hyperfine spectrum for the isotope with mass number  $A$ ,  $\delta\nu_{\text{FS}}^{A,A'}$  is the field shift and  $\delta\nu_{\text{MS}}^{A,A'}$  is the mass shift between the two isotopes  $A$  and  $A'$ .

---

<sup>3</sup>The first two paragraphs of this section are largely reproduced from thesis article II [6].

The mass shift describes the change in the energy of the fine structure states due to a different motion in the centre-of-mass system of the nucleus  $A$  compared to  $A'$  [63, 67],

$$\delta\nu_{\text{MS}}^{A,A'} = \frac{m^{A'} - m^A}{m^A m^{A'}} (N_{\text{MS}} + S_{\text{MS}}). \quad (1.2)$$

The masses of the two isotopes are  $m^{A'}$  and  $m^A$ . The normal mass shift factor  $N_{\text{MS}}$  only describes single-valence-electron systems accurately and is exactly calculable. Due to electron correlations in multi-electron systems the specific mass shift factor  $S_{\text{MS}}$  arises additionally. Its theoretical prediction is often a challenge for atomic theory.

A change in neutron number does not only lead to a different motion of the nucleus in the centre-of-mass system but also to a different nuclear charge-density distribution. This causes another shift in the energy of the fine structure state, the so-called field or volume shift [63, 67],

$$\delta\nu_{\text{FS}}^{A,A'} = F_{\text{FS}} \delta\langle r^2 \rangle^{A,A'}, \quad (1.3)$$

with  $F_{\text{FS}}$  being the field-shift factor and  $\delta\langle r^2 \rangle^{A,A'}$  being the difference in the rms charge radii between the two isotopes  $A$  and  $A'$ .

For light nuclei the field shift is several orders of magnitude smaller than the mass shift, hence it is especially important to have a good estimate on the specific mass shift factor  $S_{\text{MS}}$ . If  $S_{\text{MS}}$  and  $F_{\text{FS}}$  are known it is possible to extract changes in the rms charge radii between two different isotopes from the measurable optical isotope shift  $\delta\nu^{A,A'}$  (combine equations 1.1-1.3). For the determination of the mass-shift factor  $K_{\text{MS}} = N_{\text{MS}} + S_{\text{MS}}$  and field-shift factor  $F_{\text{FS}}$  a King plot analysis [68] is normally applied. To this end, absolute rms charge radii from at least 3 stable elements are required, which can often be measured by electron scattering and/or muonic and X-ray spectroscopy [69]. There are however many elements where no experimental data for absolute rms charge radii is available. In this case a theoretical calculation of  $S_{\text{MS}}$  and  $F_{\text{FS}}$  is required.

If the absolute rms charge radii of at least one isotope along the isotopic chain is available from other experimental approaches and if  $K_{\text{MS}}$  and  $F_{\text{FS}}$  can be either extracted via the King plot analysis or calculated, all other absolute charge radii along the entire isotopic chain follow from the measurable optical isotope shifts  $\delta\nu^{A,A'}$ . Even though in some cases atomic theory is required for the extraction of  $\delta\langle r^2 \rangle^{A,A'}$ , the determination of  $\delta\langle r^2 \rangle^{A,A'}$  from optical isotope shifts is independent of the nuclear model and hence provides an excellent benchmark for nuclear theory.

## 1.4 Ion Traps

Since the invention of the first ion traps around 60 years ago, ion-trap technology and application fields of ion traps have rapidly evolved over time. Nowadays, ion traps are exploited at virtually all radioactive ion beam facilities worldwide and play a vital role in the study or preparation of radioactive ion beams. For confining charged particles at very low energy in a small volume, one either combines static and time-dependent radio-frequency electric fields as in Paul traps (see figure 1.1) or magnetic and electrostatic fields as in Penning traps (see figure 1.2). The confinement of charged particles with energies at the kiloelectronvolts range is possible by only employing electrostatic fields in electrostatic storage rings or in Multi-Reflection Time-of-Flight (MR-ToF) devices, which are also called electrostatic ion beam traps.<sup>4</sup> Since Paul traps and MR-ToF devices are most relevant for the topics discussed in this thesis, their operation principles will be explained in more detail in the next two sections.

<sup>4</sup>Since in the rest frame of the ions the electric field is changing, storage rings and MR-ToF devices do not violate the Earnshaw theorem, which states that it is not possible to keep ions in a stable equilibrium by only applying electro- or magnetostatic fields.

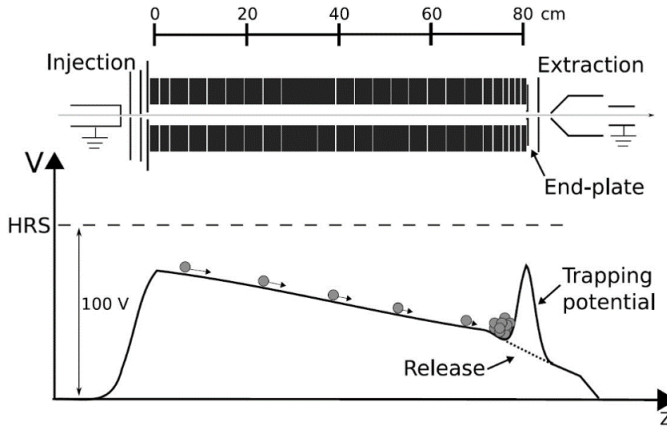


**Figure 1.1:** The upper half of the figure shows a schematic side view of ISCOOL, ISOLDE’s general-purpose linear Paul trap [35]. ISOLDE itself is the RIB facility at CERN. The Paul-trap cooler-buncher consists of four rods that provide the radio-frequency fields for radial ion confinement. The rods are surrounded by 25 segmented direct-current (DC) electrodes to create a potential gradient that guides the ions towards the potential minimum, where the ions are accumulated and cooled. Figure taken from reference [35].

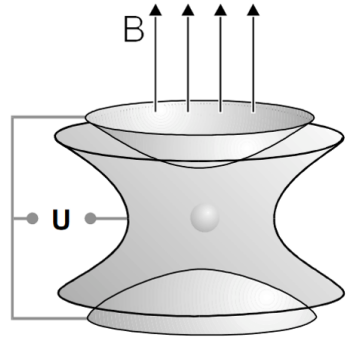


**Figure 1.2:** Schematic overview of a Penning trap. The ions are trapped by the superposition of an homogeneous magnetic field and an electric quadrupole field. Figure taken from reference [70].

#### 1.4.1 Paul Traps

Paul-trap cooler-bunchers at RIB facilities are often installed between the radioactive ion source and the experimental stations [34–41]. A continuous beam of radioactive ions is injected, accumulated and transformed into a bunched beam which consists of low-emittance ion pulses/packages, required for instance for reducing the signal-to-noise ratio for CLS (see section 1.3) or high-precision mass measurements in downstream Penning traps or MR-ToF devices.

The first radio-frequency ion trap was described by Wolfgang Paul [71], who was together with Hans Georg Dehmelt in 1989 awarded part of the Nobel prize in physics “for the development of the ion-trap technique”. In a linear radio-frequency Paul trap, static electric fields confine the ions in axial direction and radio-frequency fields limit the ion motion in transversal direction.

At RIB facilities Paul traps are typically filled with room-temperature buffer gas such as helium to damp the ions’ motion by collisions of the ions with the buffer gas atoms [34]. A continuous beam of externally produced ions with an initial kinetic energy of a few electronvolts at the trap’s entrance is within a storage time of typically a few milliseconds cooled down to 300-K beam temperature. After accumulation and cooling of the ion beam in the Paul trap, the ions are extracted as well defined ion bunches by switching an extraction endcap electrode to a lower potential. Depending on the extraction field strength, one can either reach small energy spreads or small time spreads of the extracted ion bunches since the longitudinal emittance is conserved. The longitudinal emittance is directly proportional to the beam temperature [36, 72]. For low extraction field strengths (around 2 V/mm) the energy spread is typically around 1 eV while the ion bunch is at the time-focus plane a few 100 ns wide. For large extraction field strengths ( $>10$  V/mm), time spreads of less than 10 ns are feasible at the time-focus point, but the energy spread is a few tens of electronvolts, see e.g. reference [73]. The time-focus point corresponds to the moment when the slower ions, which left the Paul trap first, are overtaken by the faster ions, which are initially at the end of the ion bunch. The larger the extraction field strength, the more the time-focus point shifts closer towards the Paul trap [73]. After the

time-focus point the ion-bunch disperses in longitudinal direction.

### 1.4.2 MR-ToF Devices

Multi-Reflection Time-of-Flight (MR-ToF) devices are important tools at RIB facilities for high-precision mass spectrometry and highly selective mass separation of short-lived radionuclides [24–33]. They are also the heart of the MIRACLS technique dedicated to highly sensitive laser spectroscopy.

MR-ToF devices consist of two opposing electrostatic mirrors surrounding a central drift tube, see figure 1.3. Each mirror is typically made of four to six concentric ring electrodes. The outermost electrodes provide the axial confinement of the ions while the one or two innermost mirror electrode(s) ensure(s) radial ion refocusing during each passage of the ions. For ion in- and ejection two possibilities exist: Either the potentials of the outermost mirror electrodes are switched to lower values (mirror switching [30]) or the kinetic energy of the ions is changed by switching the central drift tube between ground potential for ion storage and some other potential during ion in- and ejection (in-trap lift switching [74]). This then enables the ions to pass the mirror electrodes during in- and ejection.

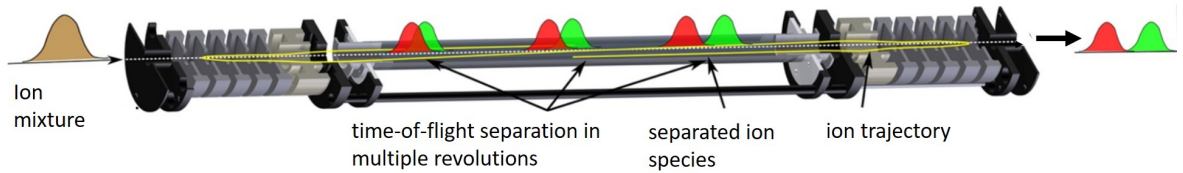


**Figure 1.3:** Schematic overview of an MR-ToF mass separator. The mass-over-charge separation of two ion species during the ions' storage time in the MR-ToF device is illustrated. Figure slightly modified from [29].

During the ions' storage time in the MR-ToF device the ions are separated in time-of-flight according to their mass-over-charge ratio. For well-tuned geometries and potentials, a mass resolving power  $m/\Delta m$  exceeding  $1e5$  is achieved in a few (tens of) milliseconds while the ions are bouncing back and forth within the table-top device. After ejection of the ions, either time-of-flight measurements are performed on an ion detector for measuring the ions' masses or the time-of-flight mass-separated contaminants are removed, e.g. by a Bradbury-Nielsen Gate (BNG) [28].

For optimal MR-ToF operation, Paul-trap cooler-bunchers are installed in front of an MR-ToF device and the time-focus point of the Paul trap is normally positioned slightly behind the MR-ToF device at the detector or beam-gate plane. To achieve best MR-ToF performance, the entire path of the ions from cooling in the Paul trap up to the storage of the ions in the MR-ToF device needs to be optimized.

## 2 Fluorescence-Based Collinear Laser Spectroscopy in an MR-ToF device

### 2.1 Scientific Motivation

Modern nuclear theory has made remarkable progress over the last decade to predict properties of exotic radionuclides, see also section 1.2. Leading ab-initio theories [53] and nuclear density functional theory<sup>1</sup> [75–79] are currently in the process of calculating nuclear charge radii along large regions of the nuclear chart, also accessing mid-shell regions [80–82]. To test their predictive power, new experimental data of exotic nuclei far away from the valley of stability is in high demand.

For instance, charge-radii measurements of neutron-rich and neutron-deficient Mg isotopes are of high interest for nuclear-structure benchmarks. Existing charge-radii measurements of  $^{21-32}\text{Mg}$  isotopes [83] show changes in the nuclear structure due to the filling of the respective neutron shells very clearly, see the three linear regions between  $A = 21 - 26$ ,  $A = 26 - 30$  and  $A = 31 - 32$  in figures 2.1 and 2.2 in addition to the odd-even staggering<sup>2</sup>. Between  $^{21-26}\text{Mg}$  the neutron  $d_{5/2}$  orbital is filled, in  $^{27}\text{Mg}$  one neutron populates the  $s_{1/2}$  subshell and between  $^{28-30}\text{Mg}$  the additional neutrons occupy either the  $s_{1/2}$  or the  $d_{3/2}$  state. In  $^{31,32}\text{Mg}$  a cross-shell excitation of two neutrons takes place which is associated with the island of inversion around  $N = 20$ . At the island of inversion the ordering of single-particle orbitals is changed and the neutron shell gap is reduced [85]. Due to the onset of deformation at the island of inversion, the slope of the linear trend for  $A = 26 - 30$  is suddenly increasing for  $A = 31 - 32$  ( $N = 19 - 20$ ). The disappearance of the expected  $N = 20$  neutron shell closure represents the ‘collapse of the conventional shell-model ordering in very neutron-rich isotopes of Na and Mg’ [86].

Reproducing these sudden changes in rms charge radius is an excellent benchmark for modern nuclear theory. Different ab-initio methods, such as the Krenciglowa-Kuo in-medium renormalization [84], the in-medium similarity renormalization group (VS-IMSRG) [80] as well as the coupled-cluster approach [81] are since recently able to calculate nuclear charge radii along the Mg isotopic chain (see figures 2.3 and 2.4). All three models predict a continuation of the increase of the rms charge radii for  $A > 31$ . Experimental data for  $^{33,34}\text{Mg}$  could hence provide a new benchmark of these nuclear theories right in the island of inversion.

For neutron-deficient  $^{20}\text{Mg}$  at the neutron shell closure  $N = 8$  the predictions in references [80, 81] deviate from each other (compare figures 2.3 and 2.4). The former predicts an increase in charge radii of  $^{20}\text{Mg}$  compared to  $^{22}\text{Mg}$ , but the latter a decrease. In this case, new experimental data could discriminate between the two different methods and provide a valuable benchmark for modern nuclear theory. To sum up, new measurement data for  $^{20,33,34}\text{Mg}$  is in high demand.

---

<sup>1</sup>In this theory, effective inter-nucleon interactions are modelled by an energy density functional, which is tuned to experimental data. This method is successful in the description of heavy and medium-mass nuclei.

<sup>2</sup>Isotopes with an even neutron number yield larger rms charge radii than their neighbours with an odd neutron number along almost all isotopic chains. Up to today, it is a challenge to model this effect, even though density functional theory and nuclear ab-initio methods start becoming capable of doing so.

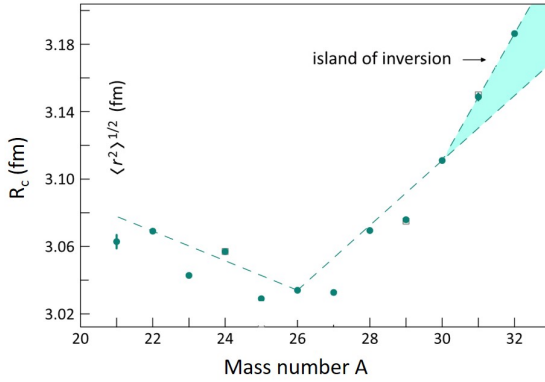


**Figure 2.1:** Experimental rms nuclear charge radii of Mg isotopes measured via traditional single-passage collinear laser spectroscopy. Only statistical errors are shown. The dashed lines indicate the three linear regions associated with the filling of the respective neutron orbital. Figure slightly modified from [83].

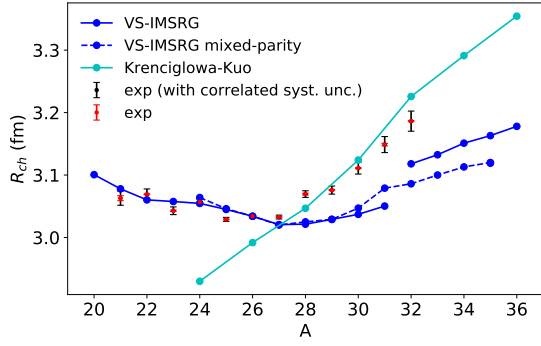


**Figure 2.3:** Experimental rms charge radii of Mg isotopes [83] are compared to preliminary results of the VS-IMSRG method [80] and the Krenciglowa-Kuo method [84]. The VS-IMSRG results are shifted by 0.155 fm to achieve a better agreement with the experimental data. The statistical errors of the experimental measurement are shown in red, the correlated systematic uncertainties are shown in black. Figure in analogy to [7].

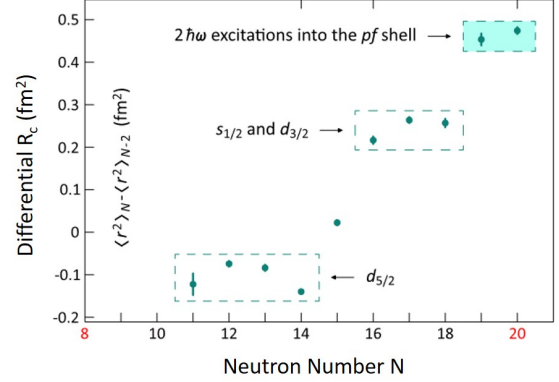


**Figure 2.2:** Experimental differential rms charge radii of Mg isotopes measured via traditional single-passage collinear laser spectroscopy. Only statistical errors are shown. Figure taken from [83].

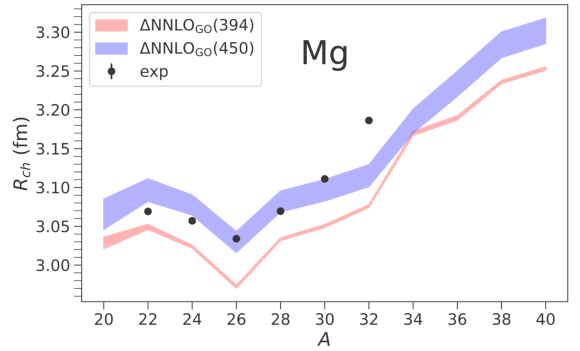


**Figure 2.4:** Experimental rms charge radii of even-mass Mg isotopes are compared to the coupled cluster method with momentum cutoffs of either 394 or 450 MeVc<sup>-1</sup>. Only statistical errors are shown. Figure taken from [81].

Similarly as for magnesium, also for cadmium new experimental data far away from the valley of stability would provide a viable benchmark of different nuclear theories. The excellent reproduction of charge radii measurements of  $^{100-130}\text{Cd}$  isotopes with the Fayans density functional theory is very intriguing (see figure 2.5) [78], especially when taking into account that the Fayans density functional is tuned for the Ca and not the Cd isotopic chain. The odd-even staggering is generally well reproduced, only slightly exaggerated. Moreover, the parabolic trend between  $A = 108 - 132$  is described although with a somewhat stronger curvature. For neutron-deficient Cd isotopes there is hence a slight deviation from experimental data.

The relativistic mean field (RMF) density functional model with pairing correlations (BCS) and short-range correlations RMF(BSC)\* [81] replicates the experimental data (see figure 2.6),

too, but shows a slightly different behaviour around the  $N = 82$  neutron shell closure compared to the Fayans density functional theory, which predicts a kink at  $N = 82$ . Additionally to density functional theory, ab-initio theory is able to access nuclear properties in close proximity to cadmium isotopes [87, 88] and is soon expected to calculate rms charge radii of cadmium, too.

As of today, experimental data is only available between  $^{100-130}\text{Cd}$ . For an improved benchmark of the different nuclear theories experimental data especially at and beyond the  $N = 50$  and  $N = 82$  neutron shell closures would be in high demand. Moreover,  $^{98}\text{Cd}$  resembles  $^{100}\text{Sn}$  without 2 protons and can hence provide more insights into the structure of the presently inaccessible doubly-magic<sup>3</sup>  $^{100}\text{Sn}$  nucleus.

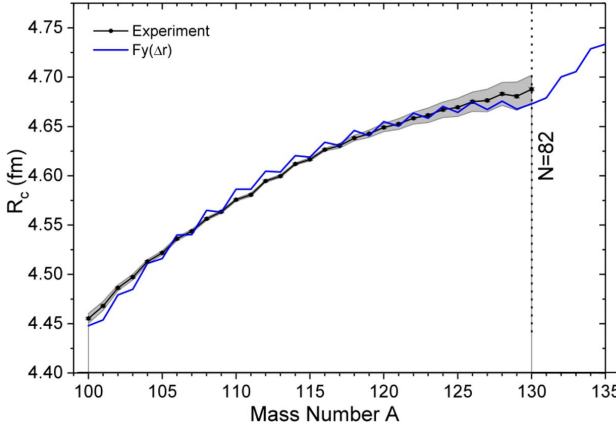


**Figure 2.5:** Experimental rms nuclear charge radii of Cd isotopes are compared to the Fayans density functional theory [78]. The gray band depicts the systematic uncertainty of the measurement, which in the meantime could however be significantly reduced by a more accurate determination of the field-shift factor  $F_{\text{FS}}$  and mass-shift factor  $K_{\text{MS}}$  via laser-induced fluorescence spectroscopy from sympathetically cooled and stable Cd isotopes in a linear Paul trap [89] (see chapter 4 for more details). Figure slightly modified from [78].

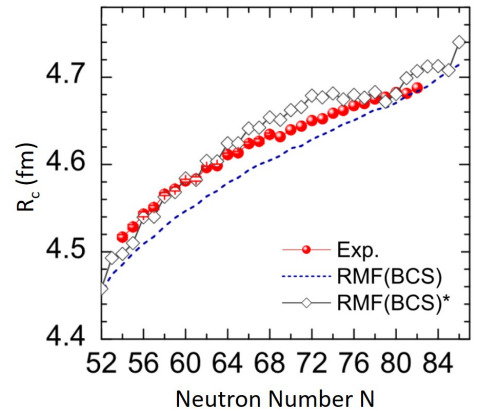


**Figure 2.6:** Experimental rms charge radii of Cd isotopes are compared against the RMF(BCS) method and the RMF(BCS)\* method which takes short-range correlations into account. Figure slightly modified from [81].

Since radionuclides far away from the valley of stability, such as the discussed  $^{20,33,34}\text{Mg}$  isotopes and  $^{98,99,131-134}\text{Cd}$  isotopes, can only be produced in very low quantities, the sensitivity of the experimental apparatus needs to be improved in order to access the most exotic radionuclides. To this end, various different methods such as Collinear Resonance Ionization Spectroscopy (CRIS) [90-92], high-resolution in-source laser spectroscopy [93], in-gas jet spectroscopy [94, 95] or more specialised techniques [96] have been or are being developed. The Multi Ion Reflection Apparatus for CLS (MIRACLS), an alternative approach, currently in development at ISOLDE/CERN will be discussed in the next section.

<sup>3</sup>Nuclides which have both their proton and neutron shells fully occupied are called doubly-magic.

## 2.2 Introduction of the MIRACLS Technique

The Multi Ion Reflection Apparatus for CLS (MIRACLS) is a novel tool for highly sensitive and high-resolution fluorescence-based collinear laser spectroscopy of short-lived radionuclides that are beyond the reach of conventional techniques due to their low production yields [1–6]. By storing ions between the two electrostatic mirrors of an MR-ToF device, the same ion bunch is probed by a laser for thousands of times compared to a single passage in traditional CLS (see figure 2.7). Thus, the observation time is extended and the experimental sensitivity will be increased by more than one to two orders of magnitude (see figure 2.8). The experimental sensitivity is limited by the signal-over-noise ratio of the detected fluorescence photons.

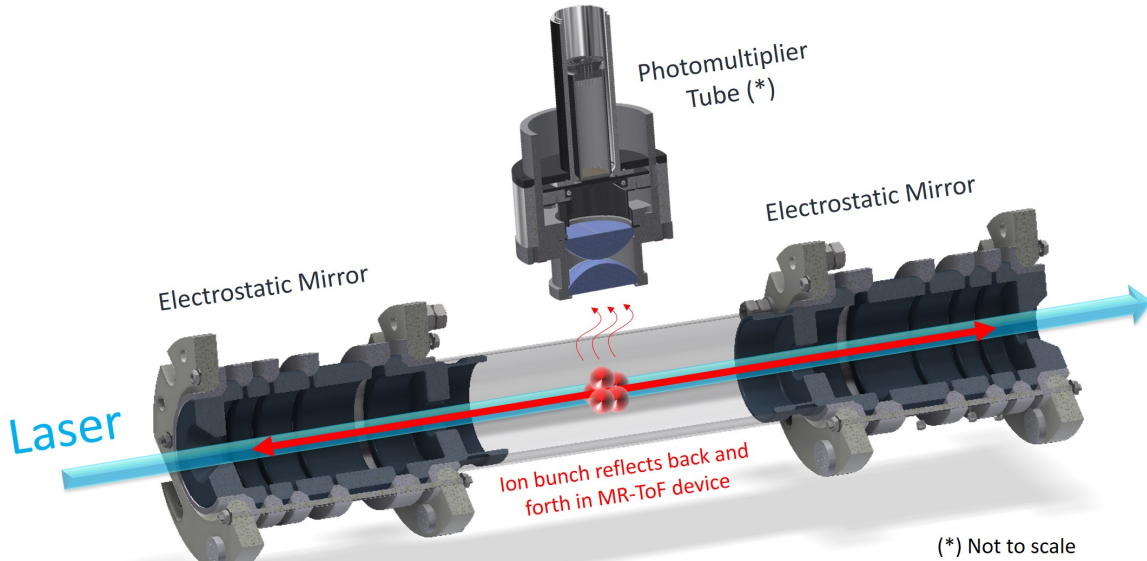


**Figure 2.7:** Schematic overview of the MIRACLS concept: Ion bunches are stored between the two electrostatic mirrors of an MR-ToF device such that the laser beam is probing the ions during each revolution. An optical detection system consisting of photomultiplier tubes is located between the two electrostatic mirrors.

The improvement in sensitivity of the MIRACLS approach in comparison to traditional single-passage CLS depends on the chosen ionic transition, the half-life and mass of the nuclide and the storage time in the MR-ToF device. The latter is limited by ion losses through collisions with residual gas particles and by the loss of the bunched-beam structure, which then leads to an increase of laser-induced background, see section 1.3. Moreover, for an optimal sensitivity boost, the laser-excited ions should decay back into the ground state without populating other hyperfine-structure states such that they can be probed indefinitely by a laser beam. Hence, MIRACLS is specifically well suited for isotopes with a closed two-level system in their ionic structure as it is the case for even-even Mg and Cd isotopes.

Figure 2.8 shows the improvement factor in sensitivity in comparison to traditional single-passage CLS for selected even-even Mg and Cd isotopes, taking radioactive decay into account (for the calculations see reference [8]). Note that the shown improvement factor assumes idealized MR-ToF performance which leaves the ion-bunch structure unaffected during the entire storage time. If the actual loss of the bunched beam structure after a storage time of around 1.2 s in the MR-ToF device is considered, too, (see thesis article II [6]), we expect for  $^{98}\text{Cd}$  an improvement factor of around 200.

Figure 2.8 compares MIRACLS' improvement with single-passage measurements in the same apparatus. Additionally, there are other advances implemented which may increase MIRACLS' performance over traditional single-passage fluorescence-based CLS beamlines. At MIRACLS, a reduction of laser-induced background will be facilitated by dedicated stray-light reduction mechanisms [97] as well as by the possibility to set narrower time gates in which photon counts are accepted. Whereas for traditional single-passage CLS the ion-bunch width is a few  $\mu\text{s}$  [65], the optimized interplay of a new, compact Paul trap [98, 99] and the MR-ToF configuration will enable ion-bunch widths which range from a few 100 ns to a few  $\mu\text{s}$ , depending on the storage time in the MR-ToF device (see thesis article II [6]). The reduced temporal peak width at MIRACLS for small to middle-range storage times will enable to set narrower time-gates during the first part of the ions' storage time in the MR-ToF device. This will result in an improved suppression of laser-induced background and dark counts.

Summing up, the experimental sensitivity of MIRACLS will be one to two orders of magnitude larger compared to traditional single-passage CLS enabling to access radionuclides that can only be produced in low quantities at contemporary RIB facilities.

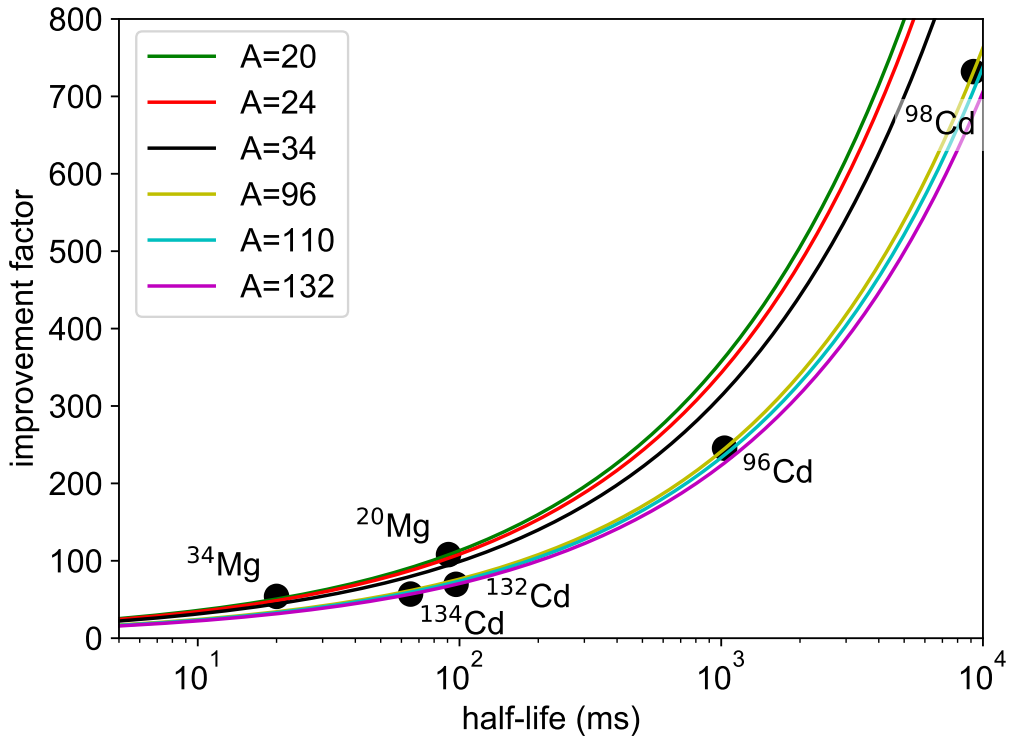


**Figure 2.8:** Improvement factor in experimental sensitivity at MIRACLS compared to traditional single-passage CLS as a function of the nuclide's half-life and mass number  $A$ . In analogy to reference [8], but with updated revolution periods based on the simulation studies in thesis article II [6]. The first science cases of MIRACLS are indicated.

## 2.3 The MIRACLS Proof-of-Principle Experiment

In order to demonstrate the feasibility of the MIRACLS approach, a proof-of-principle experiment was performed within an MR-ToF apparatus operating at around 1.5-keV beam energy [100, 101] which has been modified for CLS, see figure 2.9. Details of this work are discussed in references [1–5, 8]. In short, an offline electron-impact ion source produces a continuous beam of the three stable magnesium isotopes  $^{24–26}\text{Mg}$ . A linear Paul trap cooler-buncher transforms the continuous beam into a bunched beam, which is injected into the MR-ToF device and in-trap-lift captured [74]. The ions are stored at 1.5-keV beam energy. A quadrupole bender between Paul trap and MR-ToF device facilitates laser access and the continuous-wave narrow-band laser beam is superimposed with the stored ions. A photomultiplier tube (PMT) located above the central drift tube of the MR-ToF device detects the fluorescence photons emitted by the excited ions. Ion detectors installed up- and downstream of the MR-ToF device are used for ion beam diagnostics and optimization.

Systematic effects of the new technique are studied by comparing isotope-shift measurements between  $^{24,26}\text{Mg}$  in the MIRACLS approach with the well-known literature value, by monitoring the CLS characteristics as a function of the revolution number or by comparing MIRACLS measurements with ion optical simulations and traditional single-passage CLS measurements [3, 8]. In summary, the results of MIRACLS proof-of-principle experiment demonstrate the feasibility of the new technique, highlight its potential and establish the validity of an ion-optical simulation code for CLS in an MR-ToF device [1, 8].

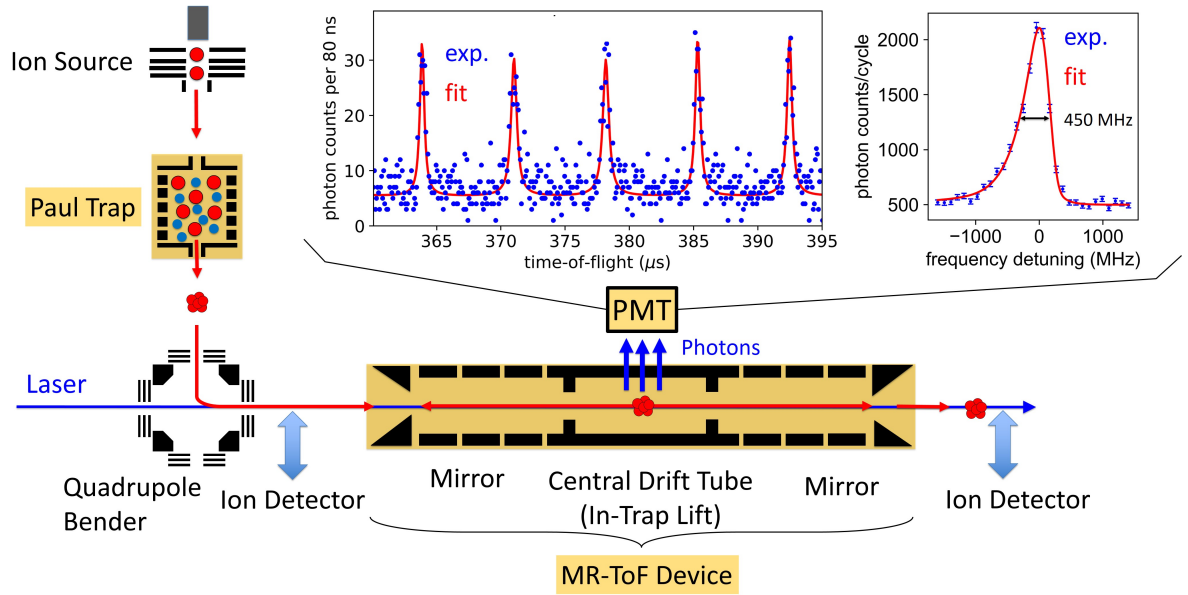


**Figure 2.9:** Simplified schematic overview of the MIRACLS low-energy setup. For an explanation of the ions' path see text. The left inset shows the detected photon count rate for  $^{24}\text{Mg}^+$  ions as a function of the time-of-flight since ion extraction from the Paul trap for revolutions 50–54 in the MR-ToF device. The laser frequency is set to the resonance frequency of the D2 transition in  $^{24}\text{Mg}^+$  ions. The right inset shows the resonance spectrum of  $^{24}\text{Mg}^+$  ions in the D2 line, taking 1000 revolutions in the MR-ToF device into account. The line width of the fine structure spectra is 450 MHz FWHM. Data from reference [8].

## 2.4 MIRACLS' High Resolution Apparatus

Based on the lessons learned from MIRACLS' proof-of-principle experiment, an entirely new apparatus consisting of a Paul trap [98, 99], a suitable injection optics and a 30-keV MR-ToF device is conceptualized (see thesis article II [6]). A kinetic energy of around 30 keV of the stored ions is advantageous to approach the natural line width of the isotope of interest, which is typically around a few tens of MHz in the transition of interest. Hence, when increasing the beam energy from 1.5-keV to 30-keV the high-resolution of conventional CLS can be maintained, see section 1.3. Since all MR-ToF devices built so far utilize ion beam kinetic energies of around a few kiloelectronvolts [24–33, 102–105], an entirely new MR-ToF device is developed (see thesis article II [6] and figure 2.10). Each electrostatic mirror is made of electrodes 1-6. The two innermost mirror electrodes 1-2 ensure radial ion refocusing and the four outermost electrodes 3-6 the axial ion confinement. Between the mirror electrodes and the central drift tube (electrode 7) two more electrodes are located (electrodes 8 and 9), which can serve as deflector electrodes [106] or be used for in-situ ion monitoring by pickup of image-charge signals [107]. Grounded electrodes 0 and fringe field suppression fins added to the individual mirror electrodes prevent any fringe fields from outside reaching into the MR-ToF device.

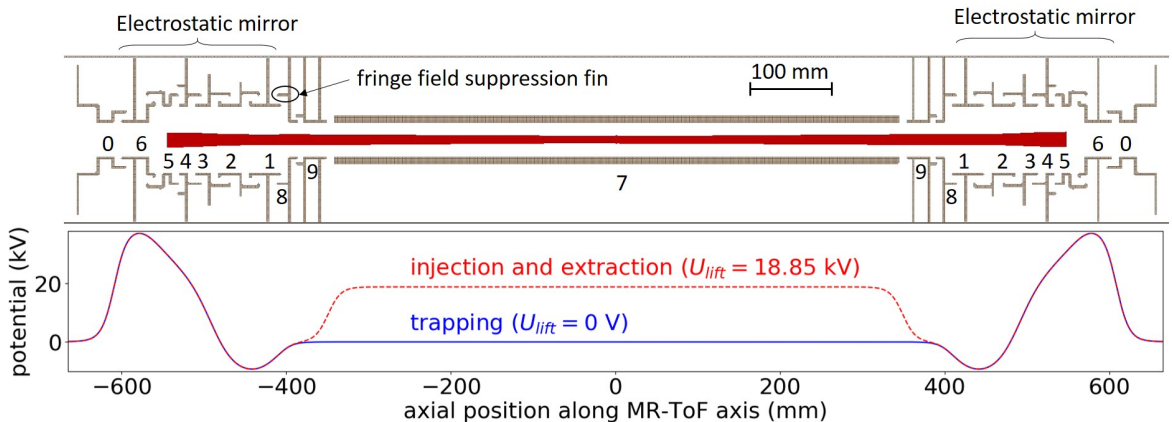


**Figure 2.10:** MIRACLS 30-keV MR-ToF device for highly sensitive and high-resolution CLS spectroscopy. (Top) Cut view of its electrode structure together with the simulated ions' trajectories in red. (Bottom) Electric potential along the central axis of the MR-ToF device for trapping (blue) and for in- and ejection (red) with an in-trap lift potential of  $U_{\text{lift}} = 18.85$  kV. Figure taken from thesis article II [6].

Building on the successful benchmarking of the simulation code against the experimental proof-of-principle data [8], extensive simulation studies of this new device and its injection optics are performed to guide physical design and initial operation of the setup (see thesis article II [6]). Taking the space constraints in the ISOLDE experimental hall into account, suitable geometries and potential combinations allowing for > 90% injection and storage efficiency, > 75% ion-laser overlap and a line width approaching the natural line width of the ion of interest could be found in the simulations. The shape of the simulated spectral line is hardly distorted by the combination of CLS and MR-ToF operation. Moreover, the simulation results suggest that systematic effects such as high-voltage instabilities or non-ideal high-voltage switches do not lead to any significant reduction in the performance of the MIRACLS technique.

It is however of utmost importance to determine the beam energy of the stored ions with 5-eV accuracy in order to keep systematic errors in the isotope shifts of the  $^{20-34}\text{Mg}$  isotopes below 20 MHz in MIRACLS' 30-keV MR-ToF device. However, by performing simultaneous co- and anticollinear CLS measurements in the MR-ToF device the systematic error due to the incomplete knowledge of the beam energy can be eliminated [108].

The simulation studies indicate that MIRACLS' accuracy and resolution will be close to traditional single-passage CLS, while its sensitivity will be enhanced for cases with closed-two level systems by more than one to two orders of magnitude enabling access to the most exotic radionuclides such as neutron-deficient and neutron-rich Mg and Cd isotopes.

## 2.5 Outlook to Planned Measurement Campaigns

The construction of the setup as discussed in thesis article II [6] is currently ongoing. After the commissioning of the setup, CLS measurements of  $^{33,34}\text{Mg}$  are planned as first science cases of MIRACLS [7]. This will allow one to experimentally access charge radii of neutron-rich Mg isotopes, right in the island of inversion. Even though  $^{33}\text{Mg}$  is not forming a closed two-level system, an improvement in sensitivity of around a factor 5 is expected compared to traditional single-passage CLS. This estimation is based on studies of the improvement factor in  $^{25}\text{Mg}^+$  ions within MIRACLS' low-energy setup [9]. Hence, a charge radii measurement of  $^{33}\text{Mg}$  is expected to become feasible, too.

### 3 Photodetachment Studies in an MR-ToF Device

#### 3.1 Scientific Motivation

After the successful demonstration of highly sensitive fluorescence-based CLS measurements in an MR-ToF device, the MIRACLS low-energy apparatus has been reconfigured for electron-affinity measurements of negatively-charged ions via laser-photodetachment-threshold spectroscopy in the MIRACLS approach. These measurements will support the understanding of electron-correlation effects. Several atomic spectroscopy studies aiming to answer questions in quantum chemistry, nuclear structure and fundamental symmetry, rely on atomic theories describing complex many-body systems, see e.g. references [109–114]. For instance, as discussed in section 1.3 an accurate theoretical calculation of the specific mass shift factor  $S_{\text{MS}}$  is often required to extract nuclear charge radii from measurable total isotope shifts. The specific mass shift is caused by a correlated motion of the electrons and is a purely atomic effect, see section 1.3. Since in negatively-charged ions electron correlations are dominant, negatively-charged ions are ideal systems to study many-body dynamics and to validate the atomic theory beyond the single particle model<sup>1</sup> [115, 117, 118].

In a neutral atom the Coulomb potential of the nucleus is almost fully screened. Hence, the binding of the additional electron, which is added to a neutral atom to form a negatively-charged ion, is mainly due to correlations between the electrons. An induced dipole polarization potential causes the attraction of the additional electron to the previously neutral atom [115, 117]. While the Coulomb potential scales with  $1/r$ , the induced dipole polarization potential scales with  $1/r^4$ , with  $r$  being the distance between the additional electron and the nucleus [117]. As a consequence, negatively-charged ions typically have very few or no bound excited electronic states and optically allowed transitions are only observed in very few negatively-charged ions [115]. As a result, there is often only one observable in negatively-charged ions, i.e. the electron affinity  $E_A$ . This is the energy released when an electron is attached to a neutral atom. It is typically in the order of 1 eV.

Atoms that tend to attract shared electrons in chemical bonds possess a large  $E_A$ . Hence, the  $E_A$  also plays an important role in chemistry. For example, the recent experimental determination of the  $E_A$  of astatine is important for the design of novel tumor-targeting biomolecules for the radionuclide therapy of cancer [118]. As such, measurements of the  $E_A$  are not only relevant to further constrain atomic models for a precise determination of the specific mass shift factor  $S_{\text{MS}}$ , but also play an important role in chemistry and medical applications.

Figure 3.1 shows the electron affinities across the periodic table of elements [118]. The heights of the blue columns depict the value of the measured  $E_A$  for each element. Generally, the  $E_A$  increases with the filling of an atomic shell. Once the respective atomic orbital is closed, the  $E_A$  is very low or the respective elements do not form stably bound negatively-charged ions

---

<sup>1</sup>In the single particle model each electron is described by moving in the mean field given by the nucleus and the charge distribution of the other electrons. The interaction between the electrons is hence neglected. While the single-particle model has been very powerful in understanding the electronic structure and behaviour of atomic systems, many effects cannot be explained [115] also including the bound formation of many negatively-charged ions [116].

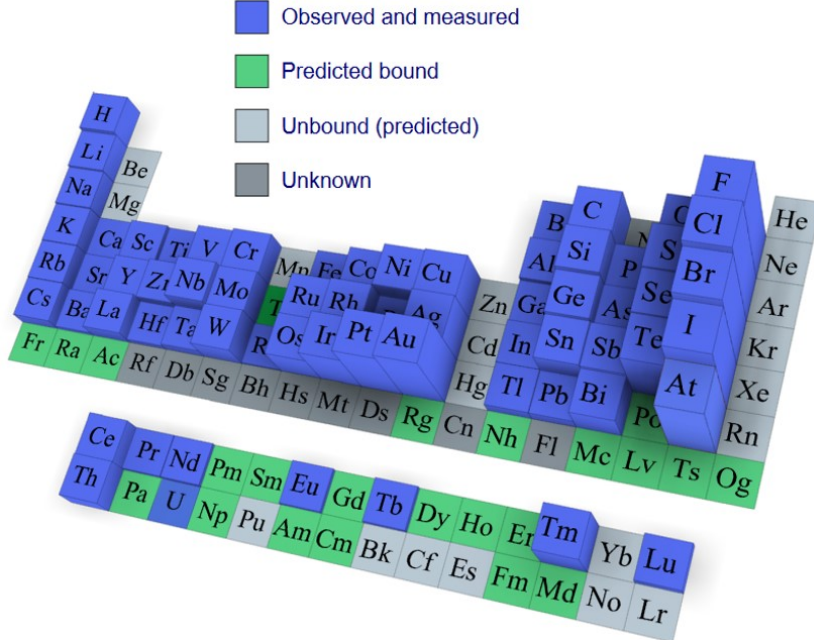


**Figure 3.1:** Electron affinities across the periodic table of elements. The heights of the blue columns depict the value of the measured  $E_A$  for each element. Chlorine is the most bound negatively-charged ion, which has hence the highest  $E_A$  of around 3.6 eV. The elements that do not form stably bound negatively-charged ions are depicted in light gray. Their electron affinities are hence negative, meaning that energy needs to be added to form a negatively-charged ion. In green those elements are shown that are predicted to be bound in theory but which  $E_A$  has not been measured yet. Dark-gray shows elements that are unknown to both experiment and theory. Figure slightly modified from [118].

at all. Hence, the halogens have the highest  $E_A$ , whereas negatively-charged noble gases do not exist. (Note that Og is due to pronounced relativistic effects however expected to form a bound negatively-charged ion.) The alkaline earth metals have a very small  $E_A$  or do not form stable negatively-charged ions since the  $s$  valence shell is filled and the additional electron would need to occupy a  $p$  orbital that is significantly higher in energy [119]. Similarly, Mn, Zn, Cd and Hg do not form stable negatively-charged ions since the additional electron would need to occupy a new subshell and they additionally have a very low atomic dipole polarizability [120].

Due to an increase of the atomic radius, the  $E_A$  normally drops from top to bottom within a group. The second element of the group is sometimes an exception due to an increased electron repulsion in the  $n = 2$  shell. For noble metals, the  $E_A$  increases within the group due to pronounced relativistic effects. Lanthanides and actinides are expected to have very low electron affinities, which often have not been measured up to now. Due to their complex electronic structure and pronounced relativistic effects, they are of high interest to benchmark theoretical calculations [121]. The multiconfigurational self-consistent-field approach or the fock-space coupled cluster method provide high-accuracy calculations of atomic properties including electron affinities, also of superheavy elements [122]. In superheavy elements the electron motion is highly correlated and relativistic effects are very pronounced, making them ideal test systems for fundamental atomic physics theories [122]. To further increase our understanding of the chemical and atomic properties of superheavy elements,  $E_A$  measurements in this mass region would be highly beneficial.

Additionally, by measuring small differences in the  $E_A$  between different isotopes of the same chemical element, the isotope shifts of the  $E_A$ , atomic models can be further constrained as needed for accurate theoretical calculations of the specific mass shift. The specific mass shift

is directly related to the isotope shift in  $E_A$  via equations 1.1 and 1.2. Accurate calculations of the specific mass shift are important in atomic physics as well as in nuclear physics to extract nuclear charge radii from measurable total isotope shifts (see section 1.3). Indeed, the theoretical uncertainty on the specific mass shift is often a leading contribution to the error estimate in nuclear charge radii [114]. However, isotope shifts in the  $E_A$  have been experimentally determined only for very few stable nuclides so far, and only with modest precision. As an example, the isotope shift between the two stable chlorine (Cl) isotopes is more precisely predicted in theory [123] than experimentally measured [124].

Hence, more precise  $E_A$  measurements as well as  $E_A$  measurements of scarcely produced (radioactive) elements are in high demand. Recently, successful  $E_A$  measurements have been performed at ISOLDE/CERN for radioactive  $^{128}\text{I}$  produced with around 35,000 ions/s [125] and radioactive  $^{211}\text{At}$  produced with around 3,750,000 ions/s [118]. For these experiments, the  $E_A$  was determined via laser-photodetachment threshold spectroscopy with a precision  $E_A/\Delta E_A$  in the order of 1e-5. To this end, a pulsed high-power laser beam is co- or anticollinearly overlapped with the beam of negatively-charged ions, see figure 3.2. If the energy of the laser exceeds a certain threshold, the additional electron can get detached and the neutral atom is detected by a dedicated neutral particle detector [126]. By counting the number of detected neutral atoms as a function of the photon energy  $E_{\text{ph}}$ , a cross-section curve  $\sigma_{\text{ph}}(E_{\text{ph}})$  is obtained, which follows a Wigner threshold law [127],

$$\sigma_{\text{ph}}(E_{\text{ph}}) = A_w (E_{\text{ph}} - E_A)^{l+1/2} \Theta(E_{\text{ph}} - E_A) \quad , \quad (3.1)$$

where the threshold energy  $E_A$  is the electron affinity,  $A_w$  a scaling factor,  $\Theta(E_{\text{ph}} - E_A)$  the Heavyside step function and  $l$  the orbital angular momentum quantum number of the outgoing electron. Thus, when fitting the Doppler-corrected signal curve to this equation the electron affinity  $E_A$  is obtained.

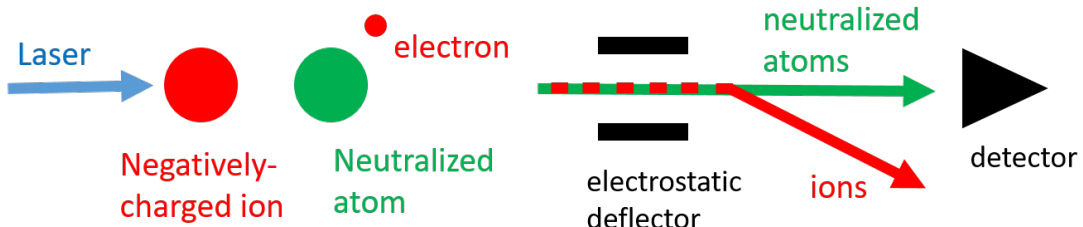


**Figure 3.2:** Illustration of the principle of collinear, single-passage laser-photodetachment threshold spectroscopy. See text for details.

Around the threshold the photodetachment probability is very low, hence a high photon and ion density is required for the measurement of the  $E_A$ . Thus, pulsed high-power lasers are typically employed. However, their large laser bandwidth limits the precision of the measurement. If the number of available radioactive ions drops below a few 10,000 ions/s as it is expected to be the case for many radioactive negatively-charged ions producible at RIB facilities, a measurement of the  $E_A$  will be even more challenging.

Moreover, for the determination of the specific mass shift,  $E_A$  measurements with a precision better than 1e-5 are needed to resolve the isotope shifts in the  $E_A$ . A very recent  $E_A$  measurement for  $^{16}\text{O}$  showed that a determination of the  $E_A$  is possible with a precision better than 1e-7 when employing narrow-bandwidth continuous-wave laser beams [128]. This high-precision measurement was performed in the electrostatic storage ring DESIREE. In a storage ring, the same ion bunch is repeatedly probed by the laser which increases the exposure

time and hence the photodetachment efficiency. This compensates the reduced photon density of continuous-wave laser beams and enables a much greater measurement precision.

### 3.2 Introduction of the MIRACLS Technique for Photodetachment Studies

As far as the repeated laser probing is concerned, storage rings and MIRACLS follow the same principle and offer a pathway towards highly sensitive and/or high-resolution photodetachment measurements with continuous-wave lasers. For the study of radioactive negatively-charged ions, the MIRACLS technique benefits from the compact nature of MR-ToF devices. Due to the small floor space of MR-ToF devices of around 2m x 1m, they can be readily coupled to existing RIB facilities.

In this work, the MIRACLS technique is extended to photodetachment studies and resulted in a successful measurement of the  $E_A$  in  $^{35}\text{Cl}^-$ , which is competitive to the literature value although an around 280,000-times lower ion sample has been required compared to the previous measurement [124] (see section 3.3.2). This breakthrough illustrates the potential of the technique also for rare samples.

For this purpose, MIRACLS' low-energy apparatus (see section 2.3) is modified to perform photodetachment measurements in an MR-ToF device. Similarly as in a storage ring, by trapping bunches of negatively-charged ions between the two electrostatic mirrors of MIRACLS' 1.5-keV MR-ToF device the same ion bunch is probed for a few 10,000 of times. The resulting increase in signal sensitivity will enable highly sensitive  $E_A$  measurements of scarcely produced (radioactive) ions and if combined with continuous-wave lasers an increase in measurement precision.

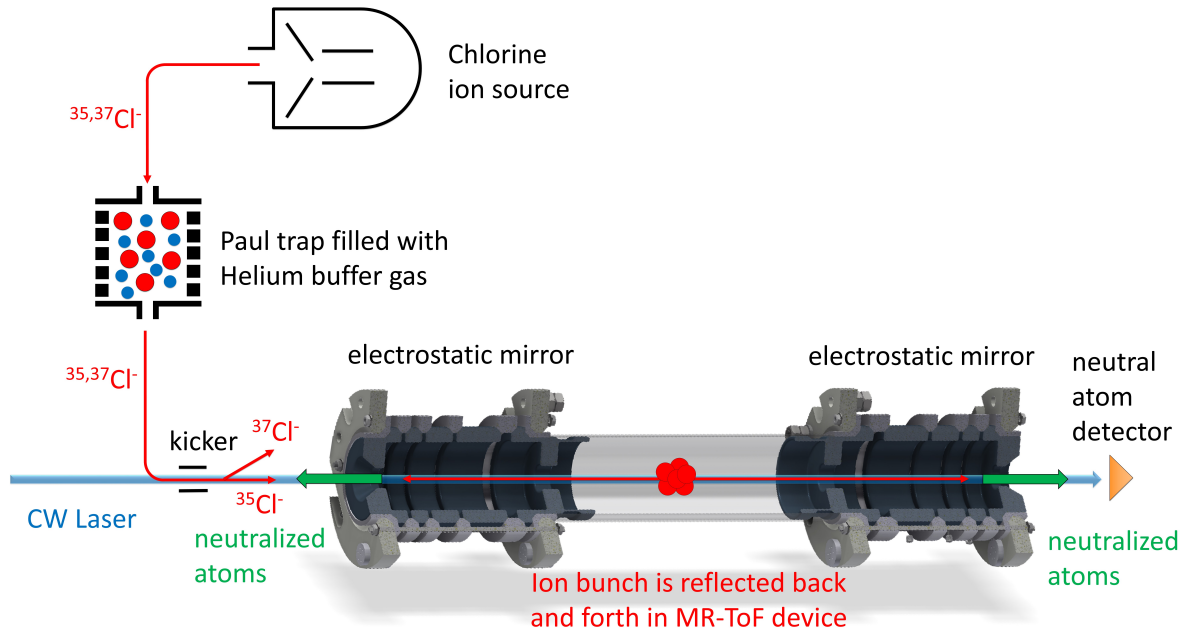


**Figure 3.3:** Schematic overview of the MIRACLS low-energy setup as modified for photodetachment spectroscopy of negatively-charged Chlorine ions. See text for details.

Figure 3.3 shows a schematic overview of MIRACLS' low-energy setup as modified for photodetachment measurements. A surface ion source [129] produces a continuous beam of stable  $^{35,37}\text{Cl}^-$  ions that are injected into the Paul trap filled with room-temperature Helium

buffer gas. After a specified cooling time, the ions are released in an ion bunch and guided onto the MR-ToF axis. A pair of steerers upstream of the MR-ToF device is used to deflect the  $^{37}\text{Cl}^-$  ions, such that only  $^{35}\text{Cl}^-$  ions are injected into the MR-ToF device and in-trap lift captured at around 1.5-keV beam energy. The stored ions are collinearly overlapped with a continuous-wave laser beam with around 2-mW laser power and a wavelength of around 343 nm. If a neutralization due to a collision with a residual gas atom or due to photodetachment occurs, the neutralized atom is no longer stored in the electrostatic fields of the MR-ToF device. Downstream of the MR-ToF device a detector is placed, which detects neutral atoms exiting the MR-ToF device along the direction of laser-beam propagation. A detailed description of the ion optical setup, the laser system and the measurement procedure will be published in an upcoming manuscript, currently in preparation [10].

### 3.3 Experimental Results

#### 3.3.1 Boost in Signal Sensitivity

Figure 3.4 shows the number of detected neutral atoms as a function of the storage time in the MR-ToF device. Even when no laser beam is overlapped with the ion beam, neutral atoms are impinging on the MagnetoF detector which are formed by collisional-induced neutralization. When the laser beam with, in this case, around 4.5 mW of laser power and an energy of around 0.05 eV above the photodetachment threshold is collinearly overlapped with the ion beam, an additional neutralization occurs due to laser-induced photodetachment. The number of detected photodetachment events  $N_{\text{ev}}$  shown in figure 3.5 is given by subtracting the number of detected neutral atoms with laser off from the number of detected neutral atoms with laser on. This very first photodetachment measurement in an MR-ToF device clearly shows the improvement in signal sensitivity when increasing the storage time of the ions in the MR-ToF device and hence the interaction time with the laser beam. After a storage time of around 400 ms the initially stored ions are reduced by half. For future measurements this could however be increased by improvements on the vacuum quality in the MR-ToF device.

To quantify the improvement in signal sensitivity of MIRACLS compared to conventional single-passage photodetachment measurements, the signal sensitivity  $\Gamma^2$  is here defined as

$$\Gamma = \frac{N_{\text{ev}}}{N_{\text{ion}} \cdot \Phi_{\text{ph}} \cdot \sigma_{\text{ph}}} \quad , \quad (3.2)$$

in which  $N_{\text{ev}}$  is the number of detected photodetachment events,  $N_{\text{ion}}$  is the number of ions employed in the procedure,  $\Phi_{\text{ph}}$  is the laser photon flux, so the number of photons per second, and  $\sigma_{\text{ph}}$  is the photodetachment cross section at the employed laser wavelength. The signal sensitivity  $\Gamma$  describes how efficient it is to convert an ion and a photon into a photodetachment event given the known photodetachment cross section from reference [130]. A preliminary analysis indicates that MIRACLS' signal sensitivity is three orders of magnitude larger compared to previous single-passage measurements [124, 125]<sup>3</sup>. Due to the outstanding boost in signal sensitivity a continuous-wave laser beam with a laser power of around 2 mW is sufficient for MIRACLS to observe the process of photodetachment around the threshold energy (see section 3.3.2).

<sup>2</sup>Note that there is a difference to the experimental sensitivity for fluorescence-based CLS introduced in chapter 2 which is limited by the signal-to-noise ratio.

<sup>3</sup>When improving the neutral particle detection efficiency for MIRACLS (e.g. by employing state-of-the-art neutral-particle detectors [126]) it is expected, that the signal sensitivity can be further increased.

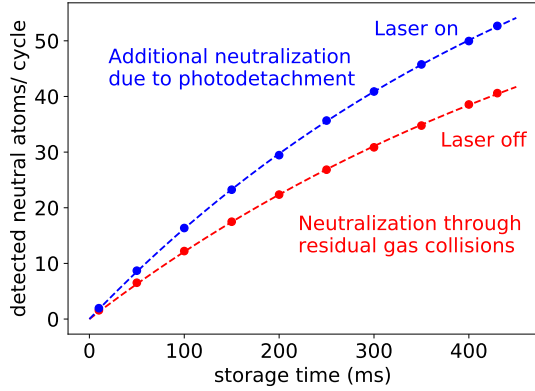


**Figure 3.4:** Number of detected neutral  $^{35}\text{Cl}$  atoms as a function of the storage time in the MR-ToF device for laser on (blue curve) and laser off (red curve). The dashed lines are an exponential fit of the measurement data. Error bars are too small to be visible on this scale. A laser beam with around 4.5 mW of laser power and an energy of around 0.05 eV above the photodetachment threshold is collinearly overlapped with the  $^{35}\text{Cl}^-$  ion beam.

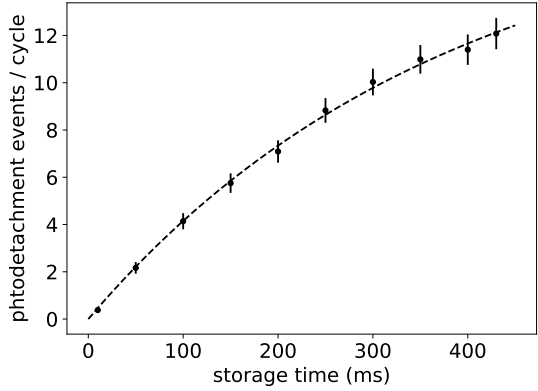


**Figure 3.5:** The number of detected photodetachment events  $N_{\text{ev}}$  is given by subtracting the number of detected neutral atoms with laser off from the number of detected neutral atoms with laser on. The dashed line represents an exponential fit of the measurement data. Note that only one measurement with 430 ms as storage time is performed. All the other storage times are obtained by setting cuts in the storage time during the post-analysis.

### 3.3.2 Measurement of the Electron Affinity in $^{35}\text{Cl}$

For determination of the  $E_A$  of  $^{35}\text{Cl}$ , an ion bunch containing approximately 6000 ions is confined in the MR-ToF device for 520 ms for each measurement cycle lasting 1.84 s. The photodetachment measurement is hence performed on around 3000 ions/s, which is around 280,000-times lower compared to the previous  $^{35}\text{Cl}$  measurement [124], around 1100-times lower compared to the  $^{211}\text{At}$  measurement [118] and around 10-times lower compared to the  $^{128}\text{I}$  measurement [125]. The measurement of the  $E_A$  of  $^{35}\text{Cl}$  is performed within 3 days, mimicking the conditions of a measurement run at a RIB facility. As discussed, a continuous-wave laser of around 2-mW of laser power is used and the laser frequency is scanned around the photodetachment threshold energy of Chlorine. Neutral atoms impinging on the MagneToF detector located downstream of the MR-ToF device are recorded as a function of the photon energy (see figure 3.6).

A fit with the Wigner threshold law (see equation 3.1) results in an  $E_A$  of 3.612751(14) eV for  $^{35}\text{Cl}$  which is in perfect agreement with the literature value of 3.612725(28) eV [124]<sup>4</sup>. This idealized analysis assumes a kinetic beam energy of 1435.8(61) eV. The uncertainty on the beam energy is mainly due to the transient behaviour of the high-voltages switches employed. This systematic error on the beam energy leads to an almost negligible systematic uncertainty on the electron affinity of around 2.3  $\mu\text{eV}$ . In reality, however, the energy of the stored ions in the MR-ToF device ranges from 0 to 5 keV, given that the ions are temporarily accelerated up to 5 keV in the radial refocusing section of the electrostatic mirrors before they are slowed down and reflected. This non-monochromatic velocity distribution of the ions requires to take a continuous Doppler shift into account for a complete evaluation of the photodetachment-threshold energy. Moreover, ions that move away from the detector also undergo photodetachment causing a blueshift depletion of the overall ion population. At photon energies slightly below the threshold a negative photodetachment signal is hence expected. A preliminary analysis of these effects

<sup>4</sup>The uncertainty of the literature value is a combination of statistical and systematic effects whereas for the MIRACLS result only the statistical error is given.

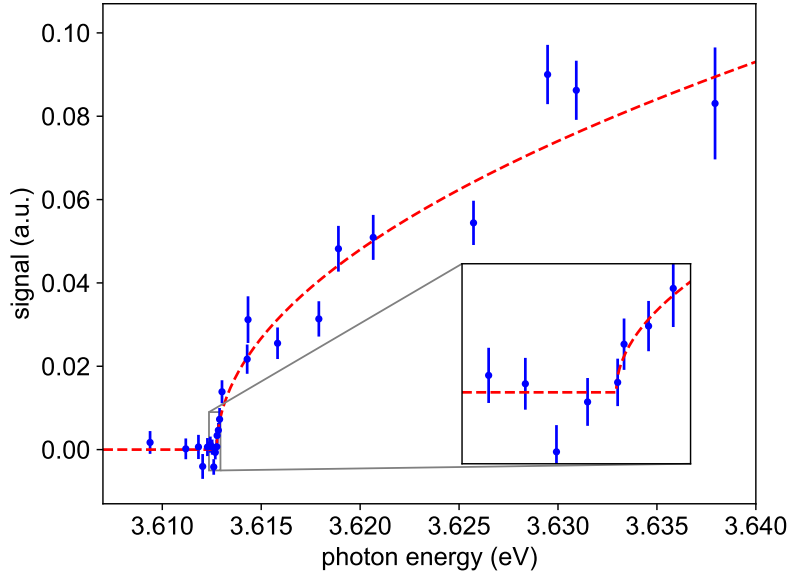


**Figure 3.6:** Cross section spectrum for  $^{35}\text{Cl}$  obtained with the MIRACLS technique employing a continuous-wave laser beam with around 2 mW of laser power around the photodetachment threshold. The blue data points represent the measurement data, the red dashed line the corresponding Wigner fit. The photon energy is given in the ions' rest frame, assuming a constant beam energy of 1435.8 eV. See text for details.

shows no significant degradation of the measurement precision of MIRACLS. More details about the determination of the electron affinity in the MIRACLS approach will be published in an upcoming manuscript, currently in preparation [10].

The first photodetachment-threshold measurement in an MR-ToF device provides confidence in the future application of the MIRACLS technique for high-precision isotope shift measurements as well as highly-sensitive  $E_A$  measurements of various (radioactive) species. Upgrades beneficial to increase MIRACLS' current precision are discussed in the next section.

## 3.4 Outlook to Future Applications for Rare Isotope Sciences

### 3.4.1 High-Precision Isotope Shift Measurements Between $^{35,36,37}\text{Cl}$

Since the isotope shift between the two stable chlorine (Cl) isotopes is more precisely predicted in theory [123] than experimentally measured [124], a more precise isotope shift measurement would provide a valuable benchmark of many-body particle calculations. For high-precision isotope shift measurements between  $^{35,37}\text{Cl}$  and the long-lived  $^{36}\text{Cl}$  with the MIRACLS technique major upgrades on the laser, vacuum and neutral particle detection system are required though.

Due to the lack of a dedicated differential pumping section between Paul trap and MR-ToF device in MIRACLS' low-energy device, the Helium buffer gas leaked into the Paul trap degrades the vacuum quality in the MR-ToF device. This causes increased collisional-induced neutralization and, thus, limits the half-life of ion storage in the trap. In a new MR-ToF setup, possibly operating at cryogenic temperatures, the vacuum quality is expected to be significantly improved and collisional-induced neutralization is hence minimized. MR-ToF devices operating at cryogenic temperatures have already been built in the past for other purposes, see e.g. references [102, 131].

Another increase in sensitivity could be possible by improving the laser power. The measure-

ments discussed above have been performed with the MIRACLS' laser system as previously used for fluorescence-based CLS [4]. A significant loss in laser power is due to a 25-m optical fibre which transports the laser light from the temperature-stabilized laser laboratory to MIRACLS' low-energy setup. While for fluorescence-based CLS a laser power of around 1 mW is sufficient, photodetachment measurements would strongly benefit from an increased laser power. When improving the laser setup and installing it directly next to the ion-optical setup, a boost in laser power by at least a factor 20 is feasible with the same laser equipment.

In combination with improvements of the neutral particle detection system (e.g. by modifying state-of-the-art neutral-particle detectors [126] to be almost background-free also for continuous-wave laser beams) the sensitivity of the MIRACLS technique is hence expected to be further increased. Since those neutral particle detectors are transparent to the laser light, co- and anticollinear measurements can be performed with a single laser beam. This way, the systematic uncertainty of the ion beam energy can be further reduced.

The improvements in sensitivity and accuracy attainable by these upgrades on the laser, vacuum and neutral particle detection system are expected to permit high-precision measurement of the isotope shift in the  $E_A$  between stable Cl isotopes as well as the long-lived  $^{36}\text{Cl}$  isotope. The MIRACLS technique is expected to become highly relevant for isotope shift measurements of various (radioactive) species after its first science case with Chlorine.

### 3.4.2 Highly Sensitive $E_A$ Measurements of Various Radioactive Elements

The demonstrated increase of signal sensitivity by 3 orders of magnitude of the MIRACLS technique will enable  $E_A$  measurements of various radioactive ion species for the first time. These measurements of scarcely produced (radioactive) elements will constitute powerful benchmarks of atomic theories reliant on many-body quantum mechanics. Especially, measurements of the  $E_A$  in superheavy elements provide an excellent test of the validity of fundamental atomic physics theories taking relativistic effects into account.

In summary, the first measurement campaign of  $^{35}\text{Cl}$  confirms MIRACLS' outstanding boost in signal sensitivity and additionally enables the measurement of the  $E_A$  of  $^{35}\text{Cl}$ , which is in perfect agreement with the literature value [124] even though continuous-wave lasers with a much reduced power density and a significantly smaller ion sample are employed. This experiment provides confidence in the application of the new technique for high-precision isotope shift measurements between  $^{35,36,37}\text{Cl}$  as well as highly sensitive and/or high-precision  $E_A$  measurements of various other (radioactive) species.

# 4 Doppler and Sympathetic Cooling for the Investigation of Short-Lived Radionuclides<sup>1</sup>

## 4.1 Motivation and Introduction of the Technique

The combination of ion traps and lasers at MIRACLS provides unique opportunities for the development of experimental techniques for next-generation RIB experiments. One of these is laser cooling to obtain ion bunches with unprecedented beam quality. Ever since its introduction in the mid 1970s [132, 133], laser cooling has become a fundamental technique to prepare and control ions and atoms for a wide range of precision experiments. In the realm of rare isotope science, for instance, specific atom species of short-lived radionuclides have been laser-cooled for fundamental-symmetries studies [134–139] or for measurements of hyperfine-structure constants [140] and nuclear charge radii [141, 142]. Nevertheless, because of its simplicity and element-universality, room-temperature buffer-gas cooling in a linear Paul trap cooler-buncher is more commonly used at contemporary RIB facilities. Recent advances in experimental RIB techniques, especially in laser spectroscopy and mass spectrometry, would however strongly benefit from ion beams at lower temperature.

The longitudinal emittance, which is at the time-focus point given by the product of the energy and time spread, is an important parameter to describe the beam quality of an extracted ion bunch from the Paul trap. Since the longitudinal emittance scales linearly with the beam temperature [36, 72], laser cooling can be beneficial to decrease the longitudinal emittance by several orders of magnitude. Doppler cooling allows one to achieve temperatures down to the Doppler cooling limit which is given by  $T = \hbar w / 2k_B$  with  $\hbar$  being the reduced Planck's constant,  $w$  the line width of the atomic transition and  $k_B$  the Boltzmann constant [143]. For singly-charged magnesium isotopes in the D1 or D2 line the Doppler cooling limit is for instance 1 mK. This is significantly smaller than 300 K as achievable with standard room-temperature buffer-gas cooling.

Sympathetic ion cooling by co-trapping with a laser-cooled ion species could open a path for a wide range of atomic and molecular sub-Kelvin RIBs. As such, the reduction in ion-beam temperature is no longer limited to laser-coolable ion species.

Laser and sympathetic cooling at RIB facilities is expected to become a powerful tool to push the current precision frontier in nuclear structure and searches for new physics with radionuclides. One recent measurement showed that by performing laser-induced fluorescence spectroscopy on sympathetically cooled, stable  $^{106,108,110,112,114,116}\text{Cd}$  ions stored in a Paul trap, a nearly five-fold precision increase of the rms charge radii measurements of  $^{100-130}\text{Cd}$  could be achieved [89]. To this end, stable Ca and Cd isotopes were simultaneously stored in the Paul trap, one laser beam was overlapped with the stored ions for Doppler cooling of Ca and another laser beam was used to probe the hyperfine structure of the atomic transition of the sympathetically cooled Cd isotopes. The emitted photons were detected by a photomultiplier tube located above the Paul trap. Hence, high-precision isotope shifts between the stable Cd isotopes were possible which allowed to extract the specific mass shift factor  $S_{MS}$  and the field shift factor  $F_{FS}$  more precisely. These improved factors were then used for the recalculation of

---

<sup>1</sup>Some of the text of this chapter is based on F.M.Maier and S.Sels, Isolde Newsletter 2022. Link: [https://isolde.web.cern.ch/sites/default/files/ISOLDE%20Newsletter%202022\\_0.pdf](https://isolde.web.cern.ch/sites/default/files/ISOLDE%20Newsletter%202022_0.pdf)

the nuclear charge radii for  $^{100-130}\text{Cd}$  resulting in a nearly fivefold precision increase. Note that Cd has also been identified as a good candidate in searches for new physics via King-plot nonlinearities [144]. Exploiting radioactive Cd ions for this purpose may constitute an intriguing opportunity to increase the sensitivity of these searches provided that the remarkable precision obtained with stable isotopes [89, 145, 146] can be translated to short-lived radionuclides, too. An important prerequisite for this is the Doppler or sympathetic cooling of radioactive ions. In order to prevent significant losses due to the radioactive decay of the ions, the cooling time needs however to be significantly reduced to cool externally produced radioactive ions.

## 4.2 Experimental Results

We demonstrate that laser cooling is compatible with the timescale imposed by short-lived radionuclides as well as with existing instrumentation at RIB facilities, see thesis article I [11]. A beam of externally produced  $^{24}\text{Mg}^+$  ions is injected into the linear Paul trap of the MIRACLS low-energy setup (see section 2.3) in which the ions are cooled by a combination of a low-pressure buffer gas and a 10-mW, continuous-wave laser beam with a wavelength of  $\approx 280$  nm. An overview of the Paul trap cooler-buncher is shown in figure 4.1.

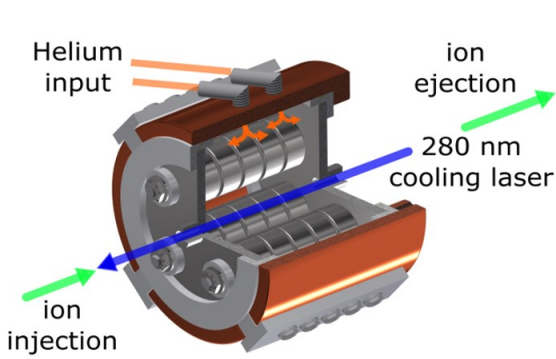


**Figure 4.1:** Schematic overview of the Paul trap cooler-buncher in MIRACLS' low-energy setup: The ions are either cooled through collisions with room-temperature Helium buffer gas or via Doppler cooling. For the latter a 280-nm continuous-wave laser beam is overlapped with the ions. Figure taken from thesis article I [11].

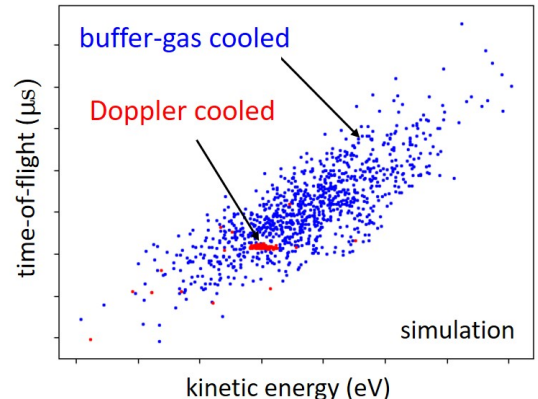


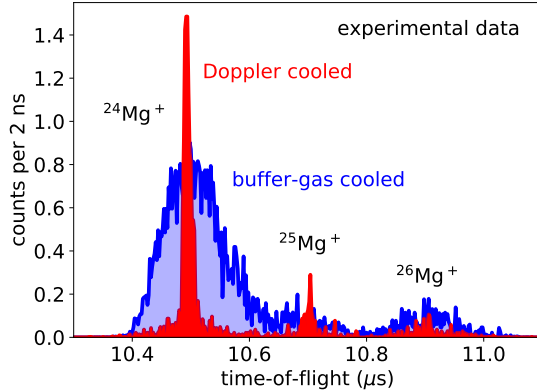
**Figure 4.2:** Simulated action diagram in longitudinal direction for Doppler and 300-K buffer-gas cooling. Each point corresponds to one simulated ion extracted from the Paul trap and transported to a near ToF detector. The simulations for Doppler cooling are performed with -150 MHz detuning in respect to the D2 transition frequency in  $^{24}\text{Mg}^+$  ions and 1e-6 mbar buffer-gas pressure.

The Paul trap operation with standard 300-K buffer gas is explained in section 1.4.1. Due to the combination of Doppler and low-pressure buffer-gas cooling temporal widths of the extracted ion bunch as low as a few nanoseconds have been achieved. This corresponds to an ion-beam temperature of around 6 K<sup>2</sup> and is obtained within a cooling time of  $\leq 200$  ms despite an initial kinetic energy of the incoming ions of a few electronvolts at the trap's entrance. The longitudinal emittance was hence improved by around a factor 50. Figure 4.2 depicts the action

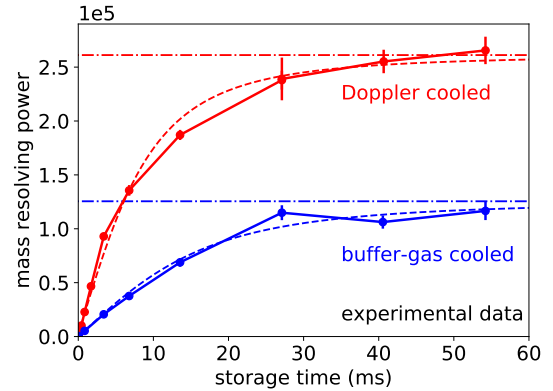
<sup>2</sup>Note that ion optical simulations indicate that the time-focus point for cooling at varying buffer-gas temperatures and laser-cooled ions occur at different spatial positions. Thus, the comparison of the ToF widths for different cooling schemes at a fixed detector position may provide an incomplete picture. In fact, the energy distribution of the simulated laser-cooled ions suggests that the (longitudinal) ion-cloud temperature is actually  $<1$  K, see thesis article I [11].

diagram in longitudinal direction for Doppler and 300-K buffer-gas cooling. Time-of-flight spectra of the stable Mg isotopes as measured on an ion detector after extraction from the Paul trap are shown in figure 4.3, for standard buffer-gas cooling (blue) and for Doppler cooling (red).

Moreover, sympathetic cooling of co-trapped  $K^+$  and  $O_2^+$  ions is demonstrated. The peak width could be reduced for  $^{16}O_2^+$  ions from 113(5) to 58(4) ns and for  $^{39}K^+$  ions from 180(13) to 145(5) ns. With future improvements such as a better tunability of the intensity ratios of the injected species, it is expected that the peak widths of the sympathetically cooled ion species can be reduced further. More details can be found in thesis article I [11].



**Figure 4.3:** Time-of-flight spectrum of  $^{24,25,26}Mg^+$  ions after extraction from the Paul trap cooler-buncher in MIRACLS low-energy setup for Doppler and 300-K buffer-gas cooling. The laser frequency is detuned by -150 MHz with respect to the D2 transition frequency in  $^{24}Mg^+$ .



**Figure 4.4:** Mass resolving power for  $^{24}Mg^+$  ions as a function of storage time in the MR-ToF device for Doppler and 300-K buffer-gas cooling. Note that the buffer-gas cooling measurement is performed with only the residual gas present in the Paul trap. If more helium buffer gas is leaked into the Paul trap, the MR-ToF vacuum quality is reduced and the mass resolving power degraded. For more details see thesis articles I and III [11, 12].

As a first application, a laser-cooled ion bunch of  $^{24}Mg^+$  ions is transferred into MIRACLS' low-energy MR-ToF device. This improved the mass resolving power and reduced the necessary MR-ToF storage time compared to conventional buffer-gas cooling (see figure 4.4 and thesis articles I and III [11, 12]). For buffer-gas cooling it takes around 22 ms to achieve a mass resolving power of  $1e5$ , while for laser cooling it only takes 4 ms. This is a consequence of the much smaller time spread of the ions. Also the finally reachable mass resolving power in the limit of infinite revolutions is for laser cooling significantly larger, which is related to the reduced energy spread for laser cooling.

In another show-case application, the time-of-flight of the extracted ions impinging on an ion detector located downstream of the Paul trap is measured as a function of the cooling laser frequency, see figure 4.5. The abrupt change in peak-width around the laser cooling-heating transition for  $^{24}Mg^+$  and  $^{26}Mg^+$  ions is used to extract the isotope shift in the D2 line between the two stable Mg isotopes,  $\delta\nu^{26,24} = 3090(4)_{\text{stat}}(26)_{\text{sys}}$ . The value is in good agreement with the literature value [147] and comparable in precision to collinear laser spectroscopy with fast ion beams at RIB facilities. This technique is applicable for all directly laser-coolable ions with sufficiently long half-lives to reach the cooling equilibrium in the Paul trap, such as for instance Be, Mg, Ca, Sr, Ba, Ra, Hg, Yb and Cd (some of them would require a second repumping laser though). Physics interests include the study of the nuclear shell structure [78, 86, 148–150] and nuclear shapes [108]. More details can be found in thesis article I [11].

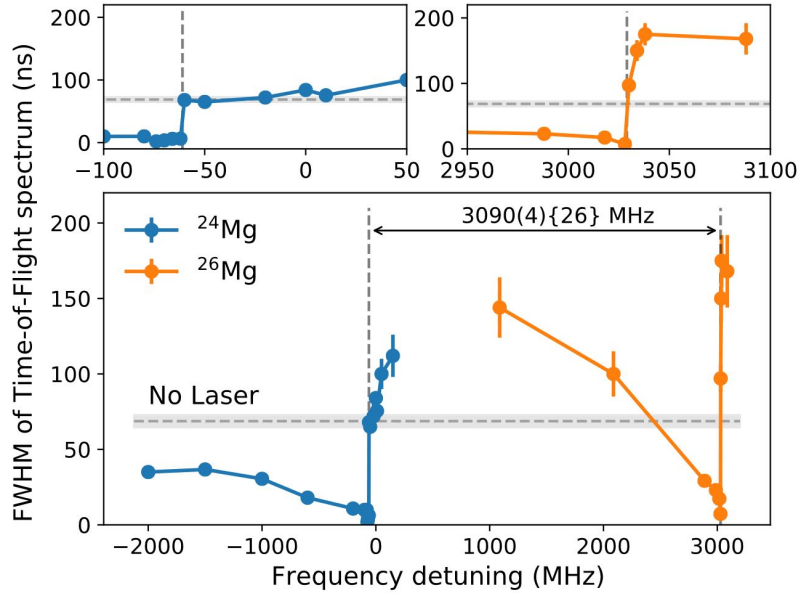


**Figure 4.5:** Peak-width of the experimental ToF signal as a function of the laser frequency, spanning laser cooling and heating of  $^{24}\text{Mg}^+$  and  $^{26}\text{Mg}^+$  ions. The x-axis offset is taken as the literature value for the absolute frequency of the D2 transition in  $^{24}\text{Mg}^+$  ions [147]. The two inserts on the top show a zoom of the data. Figure taken from thesis article I [11].

### 4.3 Outlook to Future Experiments at RIB Facilities

The presented results open a path towards a significant improvement in ion-beam emittance and thus unprecedented ion-beam qualities at RIB facilities, achievable with standard readily available equipment. In a next step, online laser-cooling experiments can be envisioned, for instance in the new MIRACLS Paul trap [98, 99]. In addition to the experimentally demonstrated improvement in performance for MR-ToF mass spectrometry, the simulation studies suggest a significant improvement in precision for Penning-trap-based mass measurements when combining laser-cooled ion bunches with the phase-imaging ion-cyclotron resonance method [151]. Moreover, collinear laser spectroscopy also benefits from an improved emittance achievable with laser cooling. Due to the simultaneously reduced time and energy spread of the Doppler or sympathetically cooled atoms or molecules, narrower time gates can be set for a reduction of the laser-induced background.

Even though many of the envisioned applications could be pursued in existing equipment at RIB facilities, a dedicated Paul trap for laser cooling could offer new possibilities. In such an improved setup, buffer-gas cooling would happen in a first stage and laser cooling in a second stage. This multi-stage approach would improve the efficiency and reduce the beam temperature further, see thesis article I [11]. A dedicated Paul trap for laser cooling would also house photodetectors for in situ monitoring of the cooling mechanism and for high-precision laser spectroscopy measurements within the Paul trap itself.

Summing up, laser cooling promises new opportunities for future high-precision studies with radioactive cold trapped ions and a significantly improved beam emittance at RIB facilities. Via sympathetic cooling this approach is universally applicable in providing cold ion beams to subsequent experimental stations. As such, it also offers a cooling option for radioactive molecules for fundamental physics research [96].

# 5 Highly Selective and High-Flux Mass Separation for Short-Lived Radionuclides

## 5.1 Motivation and Current Challenges

Many experiments at RIB facilities suffer from isobaric contamination, i.e. unwanted ions of similar mass. Over the last 20 years, MR-ToF devices have gained remarkable attention for mass separation of short-lived radionuclides at RIB facilities throughout the world [24–33, 152]. They exceed mass resolving powers of  $10^5$  within (some tens of) milliseconds, see section 1.4.2. MR-ToF mass separation is however only possible up to a limited number of ions. At large ion densities, Coulomb interactions between the stored ions become prominent and so-called space charge effects pose a challenge for mass separation. This limits the wider application of MR-ToF mass separators at RIB facilities since the ion species do not separate in mass-over-charge  $m/q$  any longer when too many ions are simultaneously confined [100, 101, 153, 154].

The maximal ion flux of an MR-ToF device is given by

$$\phi_{\max} = N_{\max}/t_{\text{proc}}, \quad (5.1)$$

where  $N_{\max}$  is the maximal number of simultaneously stored ions and  $t_{\text{proc}}$  is the experimental cycle duration which it takes to achieve the required mass resolving power in the MR-ToF system. It is here also called processing time.

Figure 5.1 shows the ion maximal ion flux of existing state-of-the-art MR-ToF devices versus the  $m/\Delta m$  ratio [30, 31, 100, 101, 155–157], where  $m$  is the mass of the isotope of interest and  $\Delta m$  is the mass difference between the isotope of interest and the contaminating species. For higher  $m/\Delta m$  ratios of around  $10^5$  ions/s the maximal ion flux drops to less than a few 100 ions/s.

However, many fields at RIB facilities would strongly benefit from isobaric pure beams with a larger ion intensity. An advanced MR-ToF mass separator apparatus could offer new opportunities for fundamental symmetry studies, nuclear structure, nuclear astrophysics or material science. For instance, pure radioactive ion beams with a higher ion intensity are important for the antiProton Unstable Matter Annihilation (PUMA) project [159] for the study of the interaction of antiprotons with radioactive nuclei. Another example where a high-flux beam purification would be highly beneficial are high-precision branching ratio measurements in  $^{10}\text{C}$  for weak interaction studies [160]. For this purpose,  $^{10}\text{C}^{16}\text{O}$  needs to be mass separated from the overwhelming contamination of  $^{13}\text{N}_2$  ( $m/\Delta m = 90,000$ ). Also for the production of innovative medical isotopes [161, 162] an MR-ToF system with a large ion throughput would be highly beneficial to reduce the need of chemical separation, radioactive activity during transport and handling and radioactive waste. Especially  $^{149}\text{Tb}$  is a promising candidate for in-vivo studies for diagnostics and therapy of tumor cells. It is the only  $\alpha$ -emitter below lead that has a half-life that is compatible with therapeutical applications. Since it also has a significant  $\beta^+$ -emission it can also be used for positron emission tomography to monitor the tumor cells during the therapy process [163]. At ISOLDE  $^{149}\text{Tb}$  is produced via  $\beta$ -decay of  $^{149}\text{Dy}$ . Unfortunately, Dy can only be produced with a large beam contamination of Eu, Gd and oxide sidebands [164]. To remove the unwanted contaminants directly after production a highly selective mass separation with  $m/\Delta m > 20,000$  would be required. To collect 1 ng

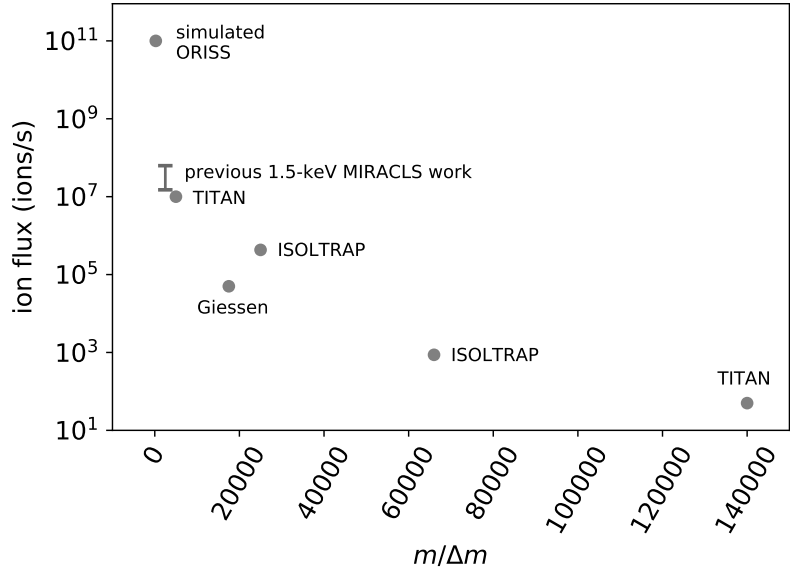


**Figure 5.1:** Measured maximal ion flux as a function of  $m/\Delta m$  for different existing state-of-the-art MR-ToF devices [30, 31, 100, 101, 155–157] and ion flux simulations in ORISS MR-ToF device [158]. Additional information: The reported maximal ion-flux values for TITAN are the limit for high-precision mass measurements, the ones for mass separation are expected to be slightly larger. For ISOLTRAP’s measurements of the maximal ion throughput more than 7% of the ions are overlapping, especially for  $m/\Delta m = 27,200$ , which is most likely explaining its offset from the maximal ion flux reported by Giessen.

over one  $^{149}\text{Tb}$  half life (4.1 hours) an ion flux of  $1\text{e}9$  ions/s is additionally needed. Current state-of-the-art MR-ToF systems however only provide an ion throughput of around  $1\text{e}5$  ions/s for this  $m/\Delta m$  ratio, see figure 5.1.

Ion-optical simulations including space charge effects show that the maximal ion flux in MR-ToF devices is significantly increased when changing the kinetic energy of the stored ions from 1.5 keV to 30 keV (see thesis article III [12]). Other approaches such as advanced ion beam preparation in the cooler-buncher are shown in the simulation to enhance the resolving power and/or processing speed while the maximal ion flux remains essentially the same. The validity of the simulation approach is benchmarked by comparing it with measurements in MIRACLS’ low-energy MR-ToF device (see section 5.2). Finally, the simulation code is used to configure and optimize a general-purpose MR-ToF mass separator for the ISOLDE community. Based on the simulation work, this instrument has the prospect of increasing the maximal ion flux by almost two orders of magnitude compared to existing state-of-the-art MR-ToF systems (see section 5.3).

## 5.2 MR-ToF Mass Resolving Power and Space Charge Simulations and their Experimental Benchmarking

For an in-depth benchmarking of the space-charge simulation code with experimental data, we take advantage of the fact that space charge effects in MR-ToF devices can not only prevent the mass separation of two simultaneously stored ion species but also affect the temporal ion bunch width of the stored ions [153, 154, 165–169].

An in-situ monitoring of the properties of the stored ion bunches is possible by observing

time-resolved photon emission following a collisional excitation [2]. After an inelastic collision between ions confined in the MR-ToF device and residual gas particles, emitted photons are detected by a photomultiplier tube installed above the central drift tube of MIRACLS' 1.5-keV MR-ToF device. Figure 5.2 shows the photon count rate versus time-of-flight since ion extraction from the Paul trap for  $^{24}\text{Mg}^+$  ions for around 4000 and 20,000 simultaneously stored ions for the 34th revolution in the MR-ToF device. When more ions are simultaneously confined, Coulomb interaction can for certain MR-ToF operation settings lead to a reduction of ToF peak width. This is referred to as selfbunching [153, 154, 165–169] and [2]. Simulation and experiment are in excellent agreement. More examples comparing simulation and experiment are shown in thesis article III [12].

Another benchmark of the space-charge simulation code is found by comparing the simulated ion-flux values of MIRACLS' 1.5-keV MR-ToF setup with experimental data from existing low-energy MR-ToF setups, see figure 5.3 and thesis article III [12]. All ion-flux values are within a factor of 4 the same even though the designs of the MR-ToF devices are fairly different, the mass numbers are ranging from  $A = 24$  to  $A = 238$  and the ratios between the number of ions of interest versus the number of contaminants are varying as well.

Moreover, the simulated and experimentally measured curves of mass resolving power versus storage time in MIRACLS' low-energy setup are in good agreement to each other for 300-K buffer-gas cooling and Doppler cooling (see figure 5.4), when correcting the finally attainable mass resolving power  $R_{\text{inf}}$  in the simulations by a factor 3. This factor 3 mismatch is most likely due to residual gas present in the experiment but not taken into account in the simulations, see thesis article III [12] for more details.

Given the excellent agreement between the ion-optical simulations and the experimental results, the simulations are in a next step used to explore different options to increase the mass resolving power and maximal ion flux (see section 5.3 and thesis article III [12]).

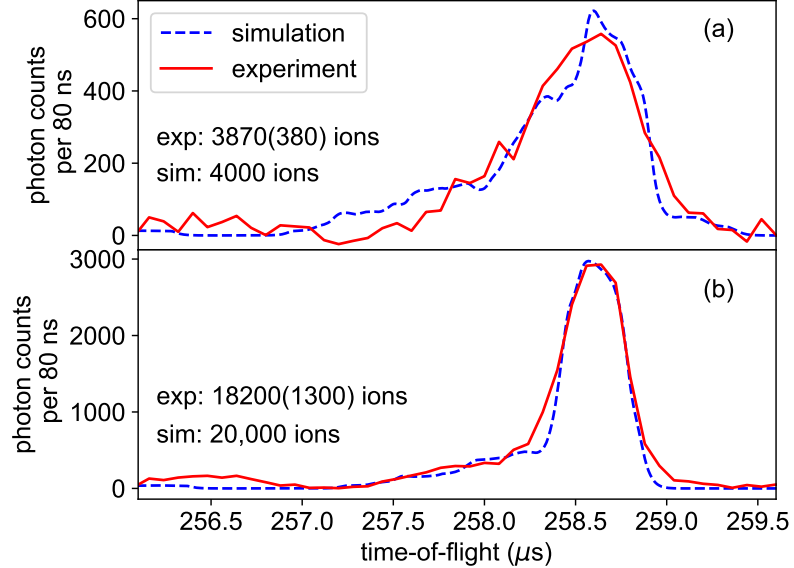


**Figure 5.2:** Photon counts versus time-of-flight since ion extraction from the Paul trap and after 34 revolutions in the MR-ToF device for  $^{24}\text{Mg}^+$  ions in MIRACLS' low-energy MR-ToF device. The experimental data (red) is compared to the simulated spectrum of the detected photons (blue). Figure taken from thesis article III [12].

### 5.3 Conceptual Design and Simulation Results of the Envisioned Mass Separator

The simulated maximal ion flux in MIRACLS' 1.5-keV MR-ToF system is around a factor 20 larger, when increasing the beam energy from 1.5 keV to 30 keV. Hence, MIRACLS' 30-keV MR-ToF setup as designed for high-resolution laser spectroscopy (see figure 2.10 and chapter 2) will also become beneficial for mass separation with high ion intensity. Indeed, after some slight design changes and reconfiguration MIRACLS' 30-keV MR-ToF device will allow highly selective mass separation with almost 2 orders of magnitude higher ion throughput compared to state-of-the-art low-energy MR-ToF devices as our simulation studies indicate (see thesis article III [12] and figure 5.3).

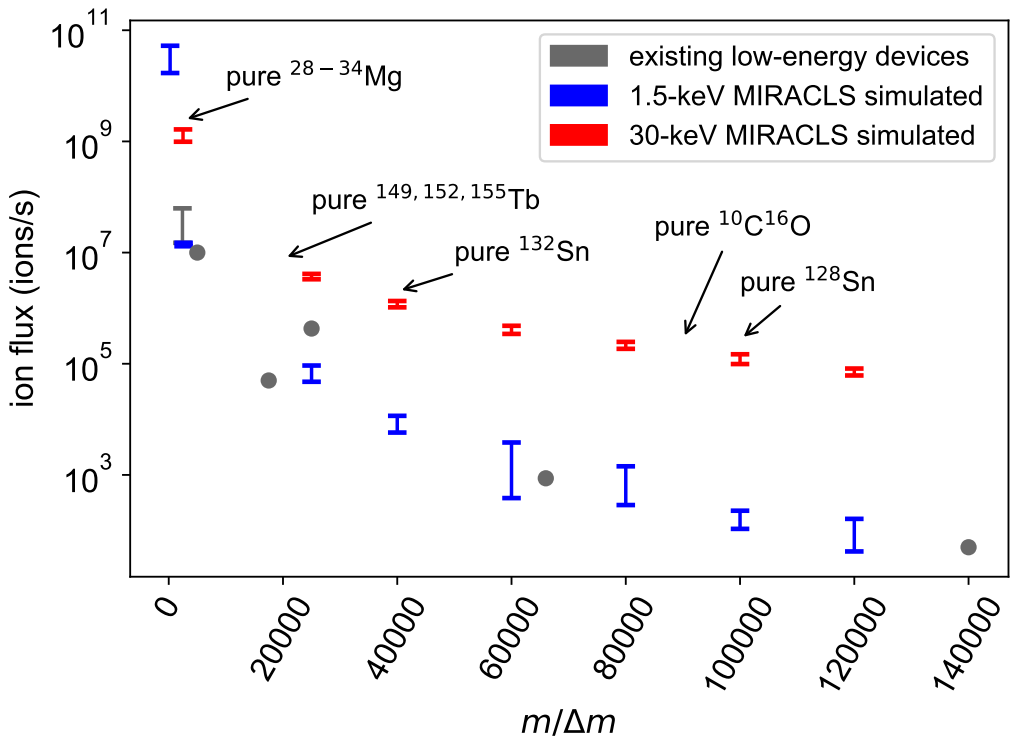


**Figure 5.3:** Experimental maximal ion flux versus  $m/\Delta m$  for different low-energy MR-ToF devices and simulated maximal ion flux for MIRACLS' 1.5-keV and 30-keV mass separator. The ion-flux values correspond to the total incoming ion beam consisting of ions of interest and contaminants. See thesis article III [12] for details. The maximal ion-throughput values for some first science cases of PUMA, medical isotope production and branching ratio measurements in  $^{10}\text{C}$  are indicated for MIRACLS' 30-keV MR-ToF device.

In order to obtain a high mass resolving power the length of the central drift tube of the MR-ToF device needs to be shortened from 690 to 425 mm. Only then an isochronous operation of the MR-ToF device becomes possible in which the revolution period is fairly independent from the energy of the ions. Moreover, to achieve a mass separation in less than a few milliseconds storage time a larger extraction field strength needs to be applied to MIRACLS' new room-temperature Paul trap [98, 99] compared to the laser spectroscopic application. This also requires a shortened distance between Paul trap and MR-ToF device for an ideal matching of the time-focus point onto the ToF detector or an ion selector (e.g. a Bradbury-Nielsen Gate), see section 1.4.1. After these modifications, a mass resolving power of 1e5 is reached

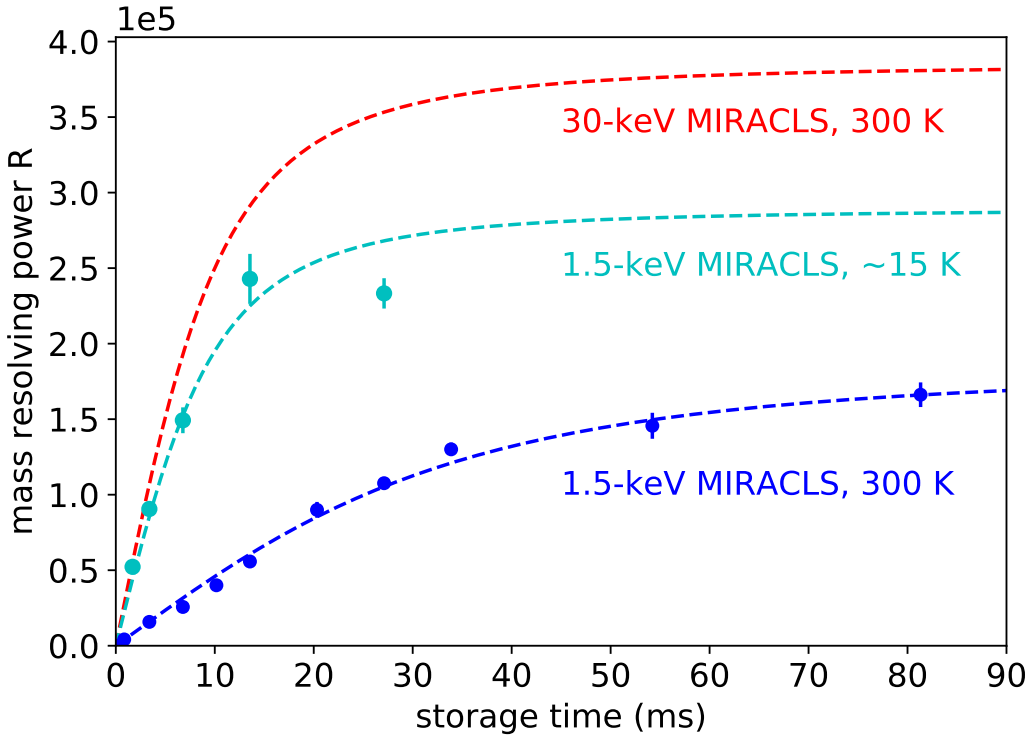


**Figure 5.4:** Simulated mass resolving power versus storage time for  $^{24}\text{Mg}^+$  ions in MIRACLS' 1.5-keV and 30-keV MR-ToF device (dashed lines). For MIRACLS' 1.5-keV device experimental measurements for 300-K buffer-gas cooling and around 15-K Doppler cooling are additionally shown (points). Note that the simulated finally attainable mass resolving power  $R_{\text{inf}}$  is in the simulations actually a factor 3 larger than in the experiment. This mismatch is attributed to residual gas present in the experimental setup but not in the simulations. The same correction factor for  $R_{\text{inf}}$  is also applied to the simulations of MIRACLS' 30-keV MR-ToF device although its exact value is difficult to anticipate. See thesis article III [12] for details.

in the simulations for a storage time in the MR-ToF device of 3 ms which corresponds to 750 revolutions for  $^{24}\text{Mg}^+$  ions (see figure 5.4). The maximal achievable mass resolving power  $R_{\text{inf}}$  in the simulations is  $1.15\text{e}6$  for  $^{24}\text{Mg}^+$  ions. For simulations with ion masses 132 u and 250 u a slightly better  $R_{\text{inf}}$  up to  $1.6\text{e}6$  is feasible. Due to the impact of residual gas present in the experimental setup we expect some reduction of  $R_{\text{inf}}$ . In MIRACLS' low-energy setup the reduction from simulated to experimental  $R_{\text{inf}}$  is a factor 3. The vacuum quality in the new setup will be improved by e.g. a dedicated differential pumping section to prevent Helium gas from the Paul trap to reach the MR-ToF device. The capabilities in mass resolving power of the envisioned new mass separator are hence expected to be better or comparable to existing state-of-the-art MR-ToF apparatus while the ion flux will be increased by almost 2 orders of magnitude, see figure 5.3.

## 5.4 Outlook

The newly envisioned 30-keV MR-ToF mass separator is expected to fulfil the requirements of PUMA. The ion flux for providing isobaric pure Mg or isobaric pure Sn isotopes, which are among the first science cases of PUMA that require an MR-ToF apparatus, is above  $1\text{e}5$  ions/s of total incoming beam. High-precision branching ratio measurements in  $^{10}\text{C}$  will also benefit

from a mass separation of  $^{10}\text{C}^{16}\text{O}$  from the contaminating  $^{13}\text{N}_2$  and  $^{12}\text{C}^{14}\text{O}$  molecules with an estimated ion throughput of around 1e5 ions/s in the new 30-keV MR-ToF mass separator. For mass separation of the  $^{149,152,155}\text{Dy}$  isotopes, which  $\beta$ -decay to  $^{149,152,155}\text{Tb}$  isotopes, that are of medical interest, the ion flux will be increased from the current 1e5 ions/s to 1e7 ions/s in the new apparatus. This is an important step towards the ultimate goal of 1e9 ions/s. If a breaking of the molecules forming the oxide sidebands could be realized either by collisions with buffer-gas atoms in the Paul trap [170, 171] or by laser-induced photo-dissociation, the ion flux could be further increased for the production of  $^{149,152,155}\text{Tb}$  isotopes.

Ultimately, the MR-ToF system should be embedded into a wider effort for RIB purification including target, ion source and magnetic mass separators to deliver a highly pure ion sample at high ion rates to RIB experiments. Virtually all fields of rare isotope science pursued at low-energy branches of RIB facilities would benefit from an improved mass separation. Once MIRACLS' 30-keV MR-ToF setup is fully constructed and commissioned and once the CLS measurements are completed, it will serve as a prototype towards a general-purpose mass separator for the ISOLDE community. At its initial stage it will deliver purified ion beams to PUMA and possibly travelling experiments.

## 6 Conclusion

Ion traps such as Paul traps and MR-ToF devices are indispensable tools at RIB facilities for the preparation of high-quality radioactive ion beams for subsequent experiments or for precise measurements of the properties of radioactive ions, such as nuclear binding energies or nuclear charge radii.

Within the work of this thesis, Doppler and sympathetic cooling at RIB facilities was implemented in a Paul-trap cooler-buncher enabling a reduction of the longitudinal emittance by a factor of around 50 (see thesis article I [11]). This attained ion beam quality achievable with standard readily available equipment improved the mass resolving power of MIRACLS' 1.5-keV MR-ToF device significantly. Other high-precision studies aiming to answer questions in nuclear structure and fundamental symmetry will also benefit from the improved ion beam emittance as dedicated simulation studies show.

Additionally, a new MR-ToF mass separator was conceptualized in order to provide isobarically pure beams with a high ion intensity to subsequent experiments (see thesis article III [12]). Once fully constructed and commissioned, it will operate at an unprecedented ion beam energy of 30 keV. Simulation studies indicate that the ion throughput of this new device will be almost 2 orders of magnitude higher while the mass resolving power of current state-of-the-art MR-ToF devices is maintained. The simulations studies were successfully benchmarked by experimental data taken in MIRACLS' 1.5-keV MR-ToF device. Isobarically pure beams with a high ion intensity will be beneficial for virtually all fields of rare isotope science, ranging from fundamental symmetry studies, nuclear structure, astrophysics, material science, production of medical isotopes to rare isotope studies with antimatter.

This 30-keV MR-ToF mass separator is based on MIRACLS' 30-keV MR-ToF device for highly sensitive and high-resolution collinear laser spectroscopy (see thesis article II [6]). By storing the ions in the Multi Ion Reflection Apparatus for CLS (MIRACLS), the same ion bunch is probed by a spectroscopic laser for thousands of times compared to a single passage in traditional CLS. Dedicated simulation studies show that the accuracy and resolution will be close to traditional single-passage CLS while the sensitivity is significantly enhanced. Hence, measurements of nuclear properties via fluorescence-based CLS of very rare radionuclides as well as highly sensitive and high-precision measurements of electron affinities via laser-photodetachment-threshold spectroscopy of negatively-charged (radioactive) ions will become possible.

First measurement campaigns employing MIRACLS' 1.5-keV MR-ToF device confirm the outstanding boost in signal sensitivity and provide confidence in the application of the MIRACLS technique for the measurement of scarcely produced radioactive ions that have been so far beyond the reach of conventional techniques (see references [1–5] and chapter 3). These measurements will serve as important benchmarks for modern atomic and nuclear theory, especially in its description of nuclear charge radii.

In summary, the implementation of Doppler and sympathetic cooling at RIB facilities, the conceptualization of a 30-keV MR-ToF apparatus for highly selective and high-flux mass separation as well as for highly sensitive and high-resolution fluorescence-based laser spectroscopy and the expansion of the MIRACLS technique for the study of negatively-charged ions will enable unprecedented new measurement opportunities at RIB facilities.

## 7 Bibliography

### Publications as (Co)author

- [1] F. M. Maier, P. Fischer, H. Heylen, V. Lagaki, S. Lechner, P. Plattner, S. Sels, F. Wienholtz, W. Nörtershäuser, L. Schweikhard, and S. Malbrunot-Ettenauer. Simulations of a proof-of-principle experiment for collinear laser spectroscopy within a multi-reflection time-of-flight device. *Hyperfine Interactions*, 240(1):54, 2019. [doi:10.1007/s10751-019-1575-x](https://doi.org/10.1007/s10751-019-1575-x).
- [2] S. Lechner, P. Fischer, H. Heylen, V. Lagaki, F. Maier, P. Plattner, M. Rosenbusch, S. Sels, F. Wienholtz, R. N. Wolf, W. Nörtershäuser, L. Schweikhard, and S. Malbrunot-Ettenauer. Fluorescence detection as a new diagnostics tool for electrostatic ion beam traps. *Hyperfine Interactions*, 240(1):95, 2019. [doi:10.1007/s10751-019-1628-1](https://doi.org/10.1007/s10751-019-1628-1).
- [3] V. Lagaki, P. Fischer, H. Heylen, F. Hummer, S. Lechner, S. Sels, F. Maier, P. Plattner, M. Rosenbusch, F. Wienholtz, R.N. Wolf, W. Nörtershäuser, L. Schweikhard, and S. Malbrunot-Ettenauer. Stray-light suppression for the MIRACLS proof-of-principle experiment. *Acta Physica Polonica B*, 51:571–576. URL: <https://www.actaphys.uj.edu.pl/fulltext?series=Reg&vol=51&page=571>.
- [4] S. Sels, P. Fischer, H. Heylen, V. Lagaki, S. Lechner, F.M. Maier, P. Plattner, M. Rosenbusch, F. Wienholtz, R.N. Wolf, W. Nörtershäuser, L. Schweikhard, and S. Malbrunot-Ettenauer. First steps in the development of the multi ion reflection apparatus for collinear laser spectroscopy. *Nuclear Instruments and Methods in Physics Research Section B: Beam Interactions with Materials and Atoms*, 463:310 – 314, 2020. URL: [http://www.sciencedirect.com/science/article/pii/S0168583X19302605](https://www.sciencedirect.com/science/article/pii/S0168583X19302605), [doi:https://doi.org/10.1016/j.nimb.2019.04.076](https://doi.org/10.1016/j.nimb.2019.04.076).
- [5] V. Lagaki, H. Heylen, I. Belosevic, P. Fischer, C. Kanitz, S. Lechner, F.M. Maier, W. Nörtershäuser, P. Plattner, M. Rosenbusch, S. Sels, L. Schweikhard, M. Vilen, F. Wienholtz, R.N. Wolf, and S. Malbrunot-Ettenauer. An accuracy benchmark of the MIRACLS apparatus: Conventional, single-passage collinear laser spectroscopy inside a MR-ToF device. *Nuclear Instruments and Methods in Physics Research Section A: Accelerators, Spectrometers, Detectors and Associated Equipment*, 1014:165663, 2021. URL: <https://www.sciencedirect.com/science/article/pii/S0168900221006483>, [doi:https://doi.org/10.1016/j.nima.2021.165663](https://doi.org/10.1016/j.nima.2021.165663).
- [6] F.M. Maier, M. Vilen, I. Belosevic, F. Buchinger, C. Kanitz, S. Lechner, E. Leistenschneider, W. Nörtershäuser, P. Plattner, L. Schweikhard, S. Sels, F. Wienholtz, and S. Malbrunot-Ettenauer. Simulation studies of a 30-keV MR-ToF device for highly sensitive collinear laser spectroscopy. *Nuclear Instruments and Methods in Physics Research Section A: Accelerators, Spectrometers, Detectors and Associated Equipment*, 1048:167927, 2023. URL: <https://www.sciencedirect.com/science/article/pii/S0168900222012190>, [doi:https://doi.org/10.1016/j.nima.2022.167927](https://doi.org/10.1016/j.nima.2022.167927).

- [7] M. Vilen, S. Malbrunot-Ettenauer, P. Fischer, H. Heylen, V. Lagaki, S. Lechner, F.M. Maier, W. Noertershaeuser, P. Plattner, S. Sels, L. Schweikhard, and F. Wienholtz. MIRACLS at ISOLDE: The Charge Radii of Exotic Magnesium Isotopes. Proposal to the ISOLDE and Neutron Time-of-Flight Committee, 2020. URL: <https://cds.cern.ch/record/2717986/files/INTC-P-565.pdf>.
- [8] F. M. Maier. Laser spectroscopy of short-lived- radionuclides in an ion trap: MIRACLS' proof-of-principle experiment and the simulation of the future 30-keV MR-ToF device. M.Sc. thesis, Johannes Kepler University Linz, 2019. URL: <https://epub.jku.at/obvulihs/download/pdf/3653073?originalFilename=true>.
- [9] S. Sels, S. Malbrunot-Ettenauer, M.L. Bissel, P. Fischer, C. Kanitz, V. Lagaki, S. Lechner, F.M. Maier, G. Neyens, W. Noertershaeuser, P. Plattner, L.V. Rodriguez, L. Schweikhard, M. Vilen, F. Wienholtz, and D.T. Yordanov. Laser spectroscopy of neutron-rich and neutron-deficient Cadmium isotopes using MIRACLS at ISOLDE. Proposal to the ISOLDE and Neutron Time-of-Flight Committee. URL: <https://cds.cern.ch/record/2731974/files/INTC-P-583.pdf>.
- [10] F.M. Maier, E. Leistenschneider, and et al. Highly-Sensitive Photodetachment Spectroscopy in an MR-ToF Device. *In preparation*, 2023.
- [11] S. Sels, F. M. Maier, M. Au, P. Fischer, C. Kanitz, V. Lagaki, S. Lechner, E. Leistenschneider, D. Leimbach, E. M. Lykiardopoulou, A. A. Kwiatkowski, T. Manovitz, Y. N. Vila Gracia, G. Neyens, P. Plattner, S. Rothe, L. Schweikhard, M. Vilen, R. N. Wolf, and S. Malbrunot-Ettenauer. Doppler and sympathetic cooling for the investigation of short-lived radioactive ions. *Phys. Rev. Research*, 4:033229, 2022. URL: <https://link.aps.org/doi/10.1103/PhysRevResearch.4.033229>, doi:10.1103/PhysRevResearch.4.033229.
- [12] F.M. Maier, F. Buchinger, L. Croquette, P. Fischer, H. Heylen, F. Hummer, C. Kanitz, A.A. Kwiatkowski, V. Lagaki, S. Lechner, E. Leistenschneider, G. Neyens, P. Plattner, A. Roitman, M. Rosenbusch, L. Schweikhard, S. Sels, M. Vilen, F. Wienholtz, and S. Malbrunot-Ettenauer. Increased Beam Energy as a Pathway Towards a Highly Selective and High-Flux MR-ToF Mass Separator. *Submitted*, 2023.

## Publications by Others

- [13] Maria J G Borge and Björn Jonson. ISOLDE past, present and future. *Journal of Physics G: Nuclear and Particle Physics*, 44(4):044011, 2017. URL: <https://dx.doi.org/10.1088/1361-6471/aa5f03>, doi:10.1088/1361-6471/aa5f03.
- [14] G C Ball, G Hackman, and R Krücken. The TRIUMF-ISAC facility: two decades of discovery with rare isotope beams. *Physica Scripta*, 91(9):093002, 2016. URL: <https://dx.doi.org/10.1088/0031-8949/91/9/093002>, doi:10.1088/0031-8949/91/9/093002.
- [15] J Gerl, M Gorska, and H J Wollersheim. Towards detailed knowledge of atomic nuclei—the past, present and future of nuclear structure investigations at GSI. *Physica Scripta*, 91(10):103001, 2016. URL: <https://dx.doi.org/10.1088/0031-8949/91/10/103001>, doi:10.1088/0031-8949/91/10/103001.

- [16] A Gade and B M Sherrill. NSCL and FRIB at Michigan State University: Nuclear science at the limits of stability. *Physica Scripta*, 91(5):053003, 2016. URL: <https://dx.doi.org/10.1088/0031-8949/91/5/053003>, doi:10.1088/0031-8949/91/5/053003.
- [17] H. Okuno, T. Dantsuka, M. Fujimaki, N. Fukunishi, H. Hasebe, Y. Higurashi, E. Ikezawa, N. Ikoma, H. Imao, O. Kamigaito, M. Kidera, M. Komiya, K. Kumagai, T. Maie, M. Nagase, T. Nagatomo, T. Nakagawa, M. Nakamura, J. Ohnishi, K. Ozeki, N. Sakamoto, K. Suda, U. Uchiyama, S. Watanabe, T. Watanabe, Y. Watanabe, K. Yamada, and H. Yamasawa. Present status of and recent developments at RIKEN RI beam factory. *Journal of Physics: Conference Series*, 1401(1):012005, 2020. URL: <https://dx.doi.org/10.1088/1742-6596/1401/1/012005>, doi:10.1088/1742-6596/1401/1/012005.
- [18] G. Savard, S. Baker, C. Davids, A.F. Levand, E.F. Moore, R.C. Pardo, R. Vondrasek, B.J. Zabransky, and G. Zinkann. Radioactive beams from gas catchers: The CARIBU facility. *Nuclear Instruments and Methods in Physics Research Section B: Beam Interactions with Materials and Atoms*, 266(19):4086–4091, 2008. Proceedings of the XVth International Conference on Electromagnetic Isotope Separators and Techniques Related to their Applications. URL: <https://www.sciencedirect.com/science/article/pii/S0168583X08006848>, doi:<https://doi.org/10.1016/j.nimb.2008.05.091>.
- [19] Y. Blumenfeld, T. Nilsson, and P. Van Duppen. Facilities and methods for radioactive ion beam production. *Physica Scripta*, 2013(T152):014023, 2013. URL: <https://dx.doi.org/10.1088/0031-8949/2013/T152/014023>, doi:10.1088/0031-8949/2013/T152/014023.
- [20] Juha Äystö, Tommi Erronen, Ari Jokinen, Anu Kankainen, Iain D. Moore, and Heikki Penttilä, editors. *Three decades of research using IGISOL technique at the University of Jyväskylä: A Portrait of the Ion Guide Isotope Separator On-Line Facility in Jyväskylä*. Springer, Berlin, Germany, 2014. doi:10.1007/978-94-007-5555-0.
- [21] G. Gaubert, C. Baru  , C. Canet, J. C. Cornell, M. Dubois, M. Dupuis, C. Eleon, J. L. Flambard, R. Frigot, P. Jardin, C. Leboucher, N. Lecesne, P. Leherissier, F. Lemagnen, R. Leroy, and J. Y. Pacquet. Status report of stable and radioactive ion beam production at GANIL. *Review of Scientific Instruments*, 79(2):02A309, 2008. URL: <https://aip.scitation.org/doi/abs/10.1063/1.2801677>, arXiv:<https://aip.scitation.org/doi/pdf/10.1063/1.2801677>, doi:10.1063/1.2801677.
- [22] R. F. Garcia Ruiz, R. Berger, J. Billowes, C. L. Binnersley, M. L. Bissell, A. A. Breier, A. J. Brinson, K. Chrysalidis, T. E. Cocolios, B. S. Cooper, K. T. Flanagan, T. F. Giesen, R. P. de Groote, S. Franchoo, F. P. Gustafsson, T. A. Isaev,   . Koszor  s, G. Neyens, H. A. Perrett, C. M. Ricketts, S. Rothe, L. Schweikhard, A. R. Vernon, K. D. A. Wendt, F. Wienholtz, S. G. Wilkins, and X. F. Yang. Spectroscopy of short-lived radioactive molecules. *Nature*, 581(7809):396–400, 2020. doi:10.1038/s41586-020-2299-4.
- [23] L. P. Gaffney, P. A. Butler, M. Scheck, A. B. Hayes, F. Wenander, M. Albers, B. Bastin, C. Bauer, A. Blazhev, S. B  nig, N. Bree, J. Cederk  ll, T. Chupp, D. Cline, T. E. Cocolios, T. Davinson, H. De Witte, J. Diriken, T. Grahn, A. Herzan, M. Huyse, D. G. Jenkins, D. T. Joss, N. Kesteloot, J. Konki, M. Kowalczyk, Th. Kr  ll, E. Kwan, R. Lutter, K. Moschner, P. Napiorkowski, J. Pakarinen, M. Pfeiffer, D. Radeck, P. Reiter, K. Reynders, S. V. Rigby, L. M. Robledo, M. Rudigier, S. Sambi, M. Seidlitz, B. Siebeck, T. Stora, P. Thoele, P. Van Duppen, M. J. Vermeulen, M. von Schmid, D. Voulot, N. Warr, K. Wimmer, K. Wrzosek-Lipska, C. Y. Wu, and M. Zielinska. Studies of

pear-shaped nuclei using accelerated radioactive beams. *Nature*, 497(7448):199–204, 2013. [doi:10.1038/nature12073](https://doi.org/10.1038/nature12073).

[24] A. Piechaczek, V. Shchepunov, H. K. Carter, J. C. Batchelder, E. F. Zganjar, S. N. Liddick, H. Wollnik, Y. Hu, and B. O. Griffith. Development of a high resolution isobar separator for study of exotic decays. *Nuclear Instruments and Methods in Physics Research Section B: Beam Interactions with Materials and Atoms*, 266(19):4510–4514, 2008. URL: <http://www.sciencedirect.com/science/article/pii/S0168583X08007660>, doi:<https://doi.org/10.1016/j.nimb.2008.05.149>.

[25] Wolfgang R. Plaß, Timo Dickel, Ulrich Czok, Hans Geissel, Martin Petrick, Katrin Reinheimer, Christoph Scheidenberger, and Mikhail I. Yavor. Isobar separation by time-of-flight mass spectrometry for low-energy radioactive ion beam facilities. *Nuclear Instruments and Methods in Physics Research Section B: Beam Interactions with Materials and Atoms*, 266(19-20):4560 – 4564, 2008. URL: <http://www.sciencedirect.com/science/article/pii/S0168583X08007763>, doi:[10.1016/j.nimb.2008.05.079](https://doi.org/10.1016/j.nimb.2008.05.079).

[26] P. Schury, K. Okada, S. Shchepunov, T. Sonoda, A. Takamine, M. Wada, H. Wollnik, and Y. Yamazaki. Multi-reflection time-of-flight mass spectrograph for short-lived radioactive ions. *The European Physical Journal A*, 42(3):343, 2009. doi:[10.1140/epja/i2009-10882-6](https://doi.org/10.1140/epja/i2009-10882-6).

[27] F. Wienholtz, D. Beck, K. Blaum, Ch. Borgmann, M. Breitenfeldt, R. B. Cakirli, S. George, F. Herfurth, J. D. Holt, M. Kowalska, S. Kreim, D. Lunney, V. Manea, J. Menéndez, D. Neidherr, M. Rosenbusch, L. Schweikhard, A. Schwenk, J. Simonis, J. Stanja, R. N. Wolf, and K. Zuber. Masses of exotic calcium isotopes pin down nuclear forces. *Nature*, 498(7454):346–349, 2013. doi:[10.1038/nature12226](https://doi.org/10.1038/nature12226).

[28] R. N. Wolf, Dietrich Beck, Klaus Blaum, Ch. Böhm, Ch. Borgmann, Martin Breitenfeldt, Frank Herfurth, A. Herlert, Magdalena Kowalska, Susanne Kreim, D. Lunney, S. Naimi, Dennis Neidherr, M. Rosenbusch, Lutz Schweikhard, J. Stanja, F. Wienholtz, and Kai Zuber. On-line separation of short-lived nuclei by a multi-reflection time-of-flight device. *Nuclear Instruments and Methods in Physics Research Section A*, 686, 2012. URL: <https://www.sciencedirect.com/science/article/pii/S016890021200575X>.

[29] R.N. Wolf, F. Wienholtz, D. Atanasov, D. Beck, K. Blaum, Ch. Borgmann, F. Herfurth, M. Kowalska, S. Kreim, Yu. A. Litvinov, D. Lunney, V. Manea, D. Neidherr, M. Rosenbusch, L. Schweikhard, J. Stanja, and K. Zuber. ISOLTRAP’s multi-reflection time-of-flight mass separator/spectrometer. *International Journal of Mass Spectrometry*, 349-350:123 – 133, 2013. 100 years of Mass Spectrometry. URL: <http://www.sciencedirect.com/science/article/pii/S1387380613001115>, doi:<https://doi.org/10.1016/j.ijms.2013.03.020>.

[30] T. Dickel, W.R. Plaß, A. Becker, U. Czok, H. Geissel, E. Haettner, C. Jesch, W. Kinsel, M. Petrick, C. Scheidenberger, A. Simon, and M.I. Yavor. A high-performance multiple-reflection time-of-flight mass spectrometer and isobar separator for the research with exotic nuclei. *Nuclear Instruments and Methods in Physics Research Section A: Accelerators, Spectrometers, Detectors and Associated Equipment*, 777:172 – 188, 2015. URL: <http://www.sciencedirect.com/science/article/pii/S0168900214015629>, doi:<https://doi.org/10.1016/j.nima.2014.12.094>.

[31] M.P. Reiter, S. Ayet San Andrés, J. Bergmann, T. Dickel, J. Dilling, A. Jacobs, A.A. Kwiatkowski, W.R. Plaß, C. Scheidenberger, D. Short, C. Will, C. Babcock,

E. Dunling, A. Finlay, C. Hornung, C. Jesch, R. Klawitter, B. Kootte, D. Lascar, E. Leistenschneider, T. Murböck, S.F. Paul, and M. Yavor. Commissioning and performance of TITAN's Multiple-Reflection Time-of-Flight Mass-Spectrometer and isobar separator. *Nuclear Instruments and Methods in Physics Research Section A: Accelerators, Spectrometers, Detectors and Associated Equipment*, 1018:165823, 2021. URL: <https://www.sciencedirect.com/science/article/pii/S0168900221008081>, doi:<https://doi.org/10.1016/j.nima.2021.165823>.

[32] P. Chauveau, P. Delahaye, G. De France, S. El Abir, J. Lory, Y. Merrer, M. Rosenbusch, L. Schweikhard, and R.N. Wolf. PILGRIM, a Multi-Reflection Time-of-Flight Mass Spectrometer for Spiral2-S3 at GANIL. *Nuclear Instruments and Methods in Physics Research Section B: Beam Interactions with Materials and Atoms*, 376:211 – 215, 2016. Proceedings of the XVIIth International Conference on Electromagnetic Isotope Separators and Related Topics (EMIS2015), Grand Rapids, MI, U.S.A., 11-15 May 2015. URL: <http://www.sciencedirect.com/science/article/pii/S0168583X16000732>, doi:<https://doi.org/10.1016/j.nimb.2016.01.025>.

[33] B. Liu, M. Brodeur, D.P. Burdette, J.M. Kelly, T. Kim, J. Long, and P.D. O'Malley. The performance of the commissioned Notre Dame multi-reflection time-of-flight mass spectrometer. *Nuclear Instruments and Methods in Physics Research Section A: Accelerators, Spectrometers, Detectors and Associated Equipment*, 985:164679, 2021. URL: <http://www.sciencedirect.com/science/article/pii/S0168900220310767>, doi:<https://doi.org/10.1016/j.nima.2020.164679>.

[34] F Herfurth, J Dilling, A Kellerbauer, G Bollen, S Henry, H.-J Kluge, E Lamour, D Lunney, R.B Moore, C Scheidenberger, S Schwarz, G Sikler, and J Szerypo. A linear radiofrequency ion trap for accumulation, bunching, and emittance improvement of radioactive ion beams. *Nuclear Instruments and Methods in Physics Research Section A: Accelerators, Spectrometers, Detectors and Associated Equipment*, 469(2):254–275, 2001. URL: <https://www.sciencedirect.com/science/article/pii/S0168900201001681>, doi:[https://doi.org/10.1016/S0168-9002\(01\)00168-1](https://doi.org/10.1016/S0168-9002(01)00168-1).

[35] E. Mané, J. Billowes, K. Blaum, P. Campbell, B. Cheal, P. Delahaye, K. T. Flanagan, D. H. Forest, H. Franberg, C. Geppert, T. Giles, A. Jokinen, M. Kowalska, R. Neugart, G. Neyens, W. Nörtershäuser, I. Podadera, G. Tungate, P. Vingerhoets, and D. T. Yordanov. An ion cooler-buncher for high-sensitivity collinear laser spectroscopy at isolde. *The European Physical Journal A*, 42(3):503–507, 2009. doi:[10.1140/epja/i2009-10828-0](https://doi.org/10.1140/epja/i2009-10828-0).

[36] S. Schwarz, G. Bollen, R. Ringle, J. Savory, and P. Schury. The LEBIT ion cooler and buncher. *Nuclear Instruments and Methods in Physics Research Section A: Accelerators, Spectrometers, Detectors and Associated Equipment*, 816:131–141, 2016. URL: <https://www.sciencedirect.com/science/article/pii/S0168900216001194>, doi:<https://doi.org/10.1016/j.nima.2016.01.078>.

[37] B.R. Barquest, G. Bollen, P.F. Mantica, K. Minamisono, R. Ringle, S. Schwarz, and C.S. Sumithrarachchi. RFQ beam cooler and buncher for collinear laser spectroscopy of rare isotopes. *Nuclear Instruments and Methods in Physics Research Section A: Accelerators, Spectrometers, Detectors and Associated Equipment*, 866:18 – 28, 2017. URL: <http://www.sciencedirect.com/science/article/pii/S0168900217305892>, doi:<https://doi.org/10.1016/j.nima.2017.05.036>.

[38] P. Campbell, A. Nieminen, J. Billowes, P. Dendooven, K. T. Flanagan, D. H. Forest, Yu.P. Gangrsky, J. A. R. Griffith, J. Huikari, A. Jokinen, I. D. Moore, R. Moore, H. L. Thayer, G. Tungate, S. G. Zemlyanoi, and J. Äystö. First results from laser spectroscopy on bunched radioactive beams from the jyfl ion-beam cooler. *The European Physical Journal A*, 15(1):45–48, 2002. [doi:10.1140/epja/i2001-10223-y](https://doi.org/10.1140/epja/i2001-10223-y).

[39] T. Brunner, M.J. Smith, M. Brodeur, S. Ettenauer, A.T. Gallant, V.V. Simon, A. Chaudhuri, A. Lapierre, E. Mané, R. Ringle, M.C. Simon, J.A. Vaz, P. Delheij, M. Good, M.R. Pearson, and J. Dilling. TITAN’s digital RFQ ion beam cooler and buncher, operation and performance. *Nuclear Instruments and Methods in Physics Research Section A: Accelerators, Spectrometers, Detectors and Associated Equipment*, 676:32–43, 2012. URL: <https://www.sciencedirect.com/science/article/pii/S0168900212001398>, doi:<https://doi.org/10.1016/j.nima.2012.02.004>.

[40] Emma Haettner, Wolfgang R. Plaß, Ulrich Czok, Timo Dickel, Hans Geissel, Wadim Kinsel, Martin Petrick, Thorsten Schäfer, and Christoph Scheidenberger. A versatile triple radiofrequency quadrupole system for cooling, mass separation and bunching of exotic nuclei. *Nuclear Instruments and Methods in Physics Research Section A: Accelerators, Spectrometers, Detectors and Associated Equipment*, 880:138–151, 2018. URL: <https://www.sciencedirect.com/science/article/pii/S0168900217310409>, doi:<https://doi.org/10.1016/j.nima.2017.10.003>.

[41] A.A. Valverde, M. Brodeur, J.A. Clark, D. Lascar, and G. Savard. A cooler-buncher for the  $N=126$  factory at Argonne National Laboratory. *Nuclear Instruments and Methods in Physics Research Section B: Beam Interactions with Materials and Atoms*, 463:330–333, 2020. URL: <https://www.sciencedirect.com/science/article/pii/S0168583X19302447>, doi:<https://doi.org/10.1016/j.nimb.2019.04.070>.

[42] W. S. Porter, E. Dunling, E. Leistenschneider, J. Bergmann, G. Bollen, T. Dickel, K. A. Dietrich, A. Hamaker, Z. Hockenberry, C. Izzo, A. Jacobs, A. Javaji, B. Kootte, Y. Lan, I. Miskun, I. Mukul, T. Murböck, S. F. Paul, W. R. Plaß, D. Puentes, M. Redshaw, M. P. Reiter, R. Ringle, J. Ringuette, R. Sandler, C. Scheidenberger, R. Silwal, R. Simpson, C. S. Sumithrarachchi, A. Teigelhöfer, A. A. Valverde, R. Weil, I. T. Yandow, J. Dilling, and A. A. Kwiatkowski. Investigating nuclear structure near  $N = 32$  and  $N = 34$ : Precision mass measurements of neutron-rich Ca, Ti, and V isotopes. *Phys. Rev. C*, 106:024312, 2022. URL: <https://link.aps.org/doi/10.1103/PhysRevC.106.024312>, doi:[10.1103/PhysRevC.106.024312](https://doi.org/10.1103/PhysRevC.106.024312).

[43] W. S. Porter, B. Ashrafkhani, J. Bergmann, C. Brown, T. Brunner, J. D. Cardona, D. Curien, I. Dedes, T. Dickel, J. Dudek, E. Dunling, G. Gwinner, Z. Hockenberry, J. D. Holt, C. Hornung, C. Izzo, A. Jacobs, A. Javaji, B. Kootte, G. Kripkó-Koncz, E. M. Lykiardopoulou, T. Miyagi, I. Mukul, T. Murböck, W. R. Plaß, M. P. Reiter, J. Ringuette, C. Scheidenberger, R. Silwal, C. Walls, H. L. Wang, Y. Wang, J. Yang, J. Dilling, and A. A. Kwiatkowski. Mapping the  $N = 40$  island of inversion: Precision mass measurements of neutron-rich Fe isotopes. *Phys. Rev. C*, 105:L041301, 2022. URL: <https://link.aps.org/doi/10.1103/PhysRevC.105.L041301>, doi:[10.1103/PhysRevC.105.L041301](https://doi.org/10.1103/PhysRevC.105.L041301).

[44] R. Silwal, C. Andreoiu, B. Ashrafkhani, J. Bergmann, T. Brunner, J. Cardona, K. Dietrich, E. Dunling, G. Gwinner, Z. Hockenberry, J.D. Holt, C. Izzo, A. Jacobs, A. Javaji, B. Kootte, Y. Lan, D. Lunney, E.M. Lykiardopoulou, T. Miyagi, M. Mougeot, I. Mukul, T. Murböck, W.S. Porter, M. Reiter, J. Ringuette, J. Dilling, and A.A. Kwiatkowski. Summit of the  $N=40$  island of inversion: Precision mass measurements and ab initio

calculations of neutron-rich chromium isotopes. *Physics Letters B*, 833:137288, 2022. URL: <https://www.sciencedirect.com/science/article/pii/S0370269322004221>, doi:<https://doi.org/10.1016/j.physletb.2022.137288>.

[45] Ali Mollaebrahimi, Christine Hornung, Timo Dickel, Daler Amanbayev, Gabriella Kripko-Koncz, Wolfgang R. Plaß, Samuel Ayet San Andrés, Sönke Beck, Andrey Blazhev, Julian Bergmann, Hans Geissel, Magdalena Górska, Hubert Grawe, Florian Greiner, Emma Haettner, Nasser Kalantar-Nayestanaki, Ivan Miskun, Frédéric Nowacki, Christoph Scheidenberger, Soumya Bagchi, Dimiter L. Balabanski, Ziga Brencic, Olga Charviakova, Paul Constantin, Masoumeh Dehghan, Jens Ebert, Lizzy Gröf, Oscar Hall, Muhsin N. Harakeh, Satbir Kaur, Anu Kankainen, Ronja Knöbel, Daria A. Kostyleva, Natalia Kurkova, Natalia Kuzminchuk, Israel Mardor, Dragos Nichita, Jan-Hendrik Otto, Zygmunt Patyk, Stephane Pietri, Sivaji Purushothaman, Moritz Pascal Reiter, Ann-Kathrin Rink, Heidi Roesch, Anamaria Spătaru, Goran Stanic, Alexandru State, Yoshiki K. Tanaka, Matjaz Vencelj, Helmut Weick, John S. Winfield, Michael I. Yavor, and Jianwei Zhao. Studying Gamow-Teller transitions and the assignment of isomeric and ground states at  $N = 50$ , 2022. URL: <https://arxiv.org/abs/2209.13713>, doi:[10.48550/ARXIV.2209.13713](https://doi.org/10.48550/ARXIV.2209.13713).

[46] Samuel Ayet San Andrés, Christine Hornung, Jens Ebert, Wolfgang R. Plaß, Timo Dickel, Hans Geissel, Christoph Scheidenberger, Julian Bergmann, Florian Greiner, Emma Haettner, Christian Jesch, Wayne Lippert, Israel Mardor, Ivan Miskun, Zygmunt Patyk, Stephane Pietri, Alexander Pihktelev, Sivaji Purushothaman, Moritz P. Reiter, Ann-Kathrin Rink, Helmut Weick, Mikhail I. Yavor, Soumya Bagchi, Volha Charviakova, Paul Constantin, Marcel Diwisch, Andrew Finlay, Satbir Kaur, Ronja Knöbel, Johannes Lang, Bo Mei, Iain D. Moore, Jan-Hendrik Otto, Ilkka Pohjalainen, Andrej Prochazka, Christophe Rappold, Maya Takechi, Yoshiki K. Tanaka, John S. Winfield, and Xiaodong Xu. High-resolution, accurate multiple-reflection time-of-flight mass spectrometry for short-lived, exotic nuclei of a few events in their ground and low-lying isomeric states. *Phys. Rev. C*, 99:064313, 2019. URL: <https://link.aps.org/doi/10.1103/PhysRevC.99.064313>, doi:[10.1103/PhysRevC.99.064313](https://doi.org/10.1103/PhysRevC.99.064313).

[47] T. Dickel, W.R. Plaß, S. Ayet San Andres, J. Ebert, H. Geissel, E. Haettner, C. Hornung, I. Miskun, S. Pietri, S. Purushothaman, M.P. Reiter, A.-K. Rink, C. Scheidenberger, H. Weick, P. Dendooven, M. Diwisch, F. Greiner, F. Heiße, R. Knöbel, W. Lippert, I.D. Moore, I. Pohjalainen, A. Prochazka, M. Ranjan, M. Takechi, J.S. Winfield, and X. Xu. First spatial separation of a heavy ion isomeric beam with a multiple-reflection time-of-flight mass spectrometer. *Physics Letters B*, 744:137–141, 2015. URL: <https://www.sciencedirect.com/science/article/pii/S0370269315002105>, doi:<https://doi.org/10.1016/j.physletb.2015.03.047>.

[48] I. Angeli and K.P. Marinova. Table of experimental nuclear ground state charge radii: An update. *Atomic Data and Nuclear Data Tables*, 99(1):69–95, 2013. URL: <https://www.sciencedirect.com/science/article/pii/S0092640X12000265>, doi:<https://doi.org/10.1016/j.adt.2011.12.006>.

[49] Djelloul Benzaid, Salaheddine Bentridi, Abdelkader Kerraci, and Naima Amrani. Bethe–Weizsäcker semiempirical mass formula coefficients 2019 update based on AME2016. *Nuclear Science and Techniques*, 31(1):9, 2020. doi:[10.1007/s41365-019-0718-8](https://doi.org/10.1007/s41365-019-0718-8).

[50] David J Rowe and John L Wood. *Fundamentals of Nuclear Models*. WORLD SCIENTIFIC, 2010. URL: <https://www.worldscientific.com/doi/abs/10.1142/6209>, arXiv: <https://www.worldscientific.com/doi/pdf/10.1142/6209>, doi:[10.1142/6209](https://doi.org/10.1142/6209).

- [51] O. Sorlin and M.-G. Porquet. Nuclear magic numbers: New features far from stability. *Progress in Particle and Nuclear Physics*, 61(2):602–673, 2008. URL: <https://www.sciencedirect.com/science/article/pii/S0146641008000380>, doi:<https://doi.org/10.1016/j.ppnp.2008.05.001>.
- [52] Rituparna Kanungo. A new view of nuclear shells. *Physica Scripta*, 2013(T152):014002, 2013. URL: <https://dx.doi.org/10.1088/0031-8949/2013/T152/014002>, doi:[10.1088/0031-8949/2013/T152/014002](https://doi.org/10.1088/0031-8949/2013/T152/014002).
- [53] Heiko Hergert. A guided tour of ab initio nuclear many-body theory. *Frontiers in Physics*, 8, 2020. URL: <https://www.frontiersin.org/article/10.3389/fphy.2020.00379>, doi:[10.3389/fphy.2020.00379](https://doi.org/10.3389/fphy.2020.00379).
- [54] Luigi Coraggio, Saori Pastore, and Carlo Barbieri. Editorial: The future of nuclear structure: Challenges and opportunities in the microscopic description of nuclei. *Frontiers in Physics*, 8, 2021. URL: <https://www.frontiersin.org/articles/10.3389/fphy.2020.626976>, doi:[10.3389/fphy.2020.626976](https://doi.org/10.3389/fphy.2020.626976).
- [55] Zohreh Davoudi. Light Nuclei from Lattice QCD: Spectrum, Structure and Reactions. In N. A. Orr, M. Płoszajczak, F. M. Marqués, and J. Carbonell, editors, *Recent Progress in Few-Body Physics*, pages 597–606, Cham, 2020. Springer International Publishing.
- [56] R. Machleidt and D.R. Entem. Chiral effective field theory and nuclear forces. *Physics Reports*, 503(1):1–75, 2011. URL: <https://www.sciencedirect.com/science/article/pii/S0370157311000457>, doi:<https://doi.org/10.1016/j.physrep.2011.02.001>.
- [57] Stefano Gandolfi, Diego Lonardoni, Alessandro Lovato, and Maria Piarulli. Atomic nuclei from quantum monte carlo calculations with chiral eft interactions. *Frontiers in Physics*, 8, 2020. URL: <https://www.frontiersin.org/articles/10.3389/fphy.2020.00117>, doi:[10.3389/fphy.2020.00117](https://doi.org/10.3389/fphy.2020.00117).
- [58] G Hagen, T Papenbrock, M Hjorth-Jensen, and D J Dean. Coupled-cluster computations of atomic nuclei. *Reports on Progress in Physics*, 77(9):096302, 2014. URL: <https://dx.doi.org/10.1088/0034-4885/77/9/096302>, doi:[10.1088/0034-4885/77/9/096302](https://doi.org/10.1088/0034-4885/77/9/096302).
- [59] H. Hergert, S.K. Bogner, T.D. Morris, A. Schwenk, and K. Tsukiyama. The in-medium similarity renormalization group: A novel ab initio method for nuclei. *Physics Reports*, 621:165–222, 2016. Memorial Volume in Honor of Gerald E. Brown. URL: <https://www.sciencedirect.com/science/article/pii/S0370157315005414>, doi:<https://doi.org/10.1016/j.physrep.2015.12.007>.
- [60] Ernst W. Otten. *Nuclear Radii and Moments of Unstable Isotopes*, pages 517–638. Springer US, Boston, MA, 1989. doi:[10.1007/978-1-4613-0713-6\\_7](https://doi.org/10.1007/978-1-4613-0713-6_7).
- [61] B Cheal and K T Flanagan. Progress in laser spectroscopy at radioactive ion beam facilities. *Journal of Physics G: Nuclear and Particle Physics*, 37(11):113101, 2010. doi:[10.1088/0954-3899/37/11/113101](https://doi.org/10.1088/0954-3899/37/11/113101).
- [62] Klaus Blaum, Jens Dilling, and Wilfried Nörtershäuser. Precision atomic physics techniques for nuclear physics with radioactive beams. *Physica Scripta*, 2013(T152):014017, 2013. URL: <http://stacks.iop.org/1402-4896/2013/i=T152/a=014017>.
- [63] P. Campbell, I.D. Moore, and M.R. Pearson. Laser spectroscopy for nuclear structure physics. *Progress in Particle and Nuclear Physics*, 86:127 – 180, 2016. URL: <http://>

[www.sciencedirect.com/science/article/pii/S0146641015000915](http://www.sciencedirect.com/science/article/pii/S0146641015000915), doi:<https://doi.org/10.1016/j.ppnp.2015.09.003>.

- [64] R Neugart, J Billowes, M L Bissell, K Blaum, B Cheal, K T Flanagan, G Neyens, W Nörtershäuser, and D T Yordanov. Collinear laser spectroscopy at ISOLDE: new methods and highlights. *Journal of Physics G: Nuclear and Particle Physics*, 44(6):064002, 2017. doi:[10.1088/1361-6471/aa6642](https://doi.org/10.1088/1361-6471/aa6642).
- [65] A. Nieminen, P. Campbell, J. Billowes, D. H. Forest, J. A. R. Griffith, J. Huikari, A. Jokinen, I. D. Moore, R. Moore, G. Tungate, and J. Äystö. On-line ion cooling and bunching for collinear laser spectroscopy. *Phys. Rev. Lett.*, 88:094801, 2002. URL: <https://link.aps.org/doi/10.1103/PhysRevLett.88.094801>, doi:[10.1103/PhysRevLett.88.094801](https://doi.org/10.1103/PhysRevLett.88.094801).
- [66] S.L. Kaufman. High-resolution laser spectroscopy in fast beams. *Optics Communications*, 17(3):309 – 312, 1976. URL: <http://www.sciencedirect.com/science/article/pii/0030401876902674>, doi:[https://doi.org/10.1016/0030-4018\(76\)90267-4](https://doi.org/10.1016/0030-4018(76)90267-4).
- [67] X.F. Yang, S.J. Wang, S.G. Wilkins, and R.F. Garcia Ruiz. Laser spectroscopy for the study of exotic nuclei. *Progress in Particle and Nuclear Physics*, 129:104005, 2023. URL: <https://www.sciencedirect.com/science/article/pii/S0146641022000631>, doi:<https://doi.org/10.1016/j.ppnp.2022.104005>.
- [68] W.H. King. *Isotope Shifts in Atomic Spectra*. Physics of Atoms and Molecules. Springer US, 1984. URL: <https://books.google.ch/books?id=0LdIvJU-j0kC>.
- [69] G. Fricke and K. Heilig. Nuclear charge radii. Copyright 2004 Springer-Verlag Berlin Heidelberg. URL: [https://materials.springer.com/lb/docs/sm\\_lbs\\_978-3-540-45555-4\\_1](https://materials.springer.com/lb/docs/sm_lbs_978-3-540-45555-4_1), doi:[10.1007/10856314\\_1](https://doi.org/10.1007/10856314_1).
- [70] G. Bollen and S. Schwarz. Ion traps for radioactive beam manipulation and precision experiments. *Nuclear Instruments and Methods in Physics Research Section B: Beam Interactions with Materials and Atoms*, 204:466–473, 2003. 14th International Conference on Electromagnetic Isotope Separators and Techniques Related to their Applications. URL: <https://www.sciencedirect.com/science/article/pii/S0168583X0300466X>, doi:[https://doi.org/10.1016/S0168-583X\(03\)00466-X](https://doi.org/10.1016/S0168-583X(03)00466-X).
- [71] Wolfgang Paul. Electromagnetic traps for charged and neutral particles. *Rev. Mod. Phys.*, 62:531–540, 1990. URL: <https://link.aps.org/doi/10.1103/RevModPhys.62.531>, doi:[10.1103/RevModPhys.62.531](https://doi.org/10.1103/RevModPhys.62.531).
- [72] R B Moore, A M Ghalambor Dezfuli, P Varfalvy, H Zhao, and The ISOLDE Collaboration. Production, transfer and injection of charged particles in traps and storage rings. *Physica Scripta*, 1995(T59):93, 1995. URL: <https://dx.doi.org/10.1088/0031-8949/1995/T59/012>, doi:[10.1088/0031-8949/1995/T59/012](https://doi.org/10.1088/0031-8949/1995/T59/012).
- [73] Timo Dickel, Mikhail I. Yavor, Johannes Lang, Wolfgang R. Plaß, Wayne Lippert, Hans Geissel, and Christoph Scheidenberger. Dynamical time focus shift in multiple-reflection time-of-flight mass spectrometers. *International Journal of Mass Spectrometry*, 412:1–7, 2017. URL: <https://www.sciencedirect.com/science/article/pii/S1387380616302664>, doi:<https://doi.org/10.1016/j.ijms.2016.11.005>.

[74] Robert N. Wolf, Gerrit Marx, Marco Rosenbusch, and Lutz Schweikhard. Static-mirror ion capture and time focusing for electrostatic ion-beam traps and multi-reflection time-of-flight mass analyzers by use of an in-trap potential lift. *International Journal of Mass Spectrometry*, 313:8–14, 2012. URL: <https://www.sciencedirect.com/science/article/pii/S1387380611004775>, doi:<https://doi.org/10.1016/j.ijms.2011.12.006>.

[75] R. F. Garcia Ruiz, M. L. Bissell, K. Blaum, A. Ekström, N. Frömmgen, G. Hagen, M. Hammen, K. Hebeler, J. D. Holt, G. R. Jansen, M. Kowalska, K. Kreim, W. Nazarewicz, R. Neugart, G. Neyens, W. Nörtershäuser, T. Papenbrock, J. Papuga, A. Schwenk, J. Simonis, K. A. Wendt, and D. T. Yordanov. Unexpectedly large charge radii of neutron-rich calcium isotopes. *Nature Physics*, 12(6):594–598, 2016. doi:[10.1038/nphys3645](https://doi.org/10.1038/nphys3645).

[76] P.-G. Reinhard and W. Nazarewicz. Toward a global description of nuclear charge radii: Exploring the Fayans energy density functional. *Phys. Rev. C*, 95:064328, 2017. URL: <https://link.aps.org/doi/10.1103/PhysRevC.95.064328>, doi:[10.1103/PhysRevC.95.064328](https://doi.org/10.1103/PhysRevC.95.064328).

[77] K. Minamisono, D. M. Rossi, R. Beerwerth, S. Fritzsche, D. Garand, A. Klose, Y. Liu, B. Maaß, P. F. Mantica, A. J. Miller, P. Müller, W. Nazarewicz, W. Nörtershäuser, E. Olsen, M. R. Pearson, P.-G. Reinhard, E. E. Saperstein, C. Sumithrarachchi, and S. V. Tolokonnikov. Charge Radii of Neutron Deficient  $^{52,53}\text{Fe}$  Produced by Projectile Fragmentation. *Phys. Rev. Lett.*, 117:252501, 2016. URL: <https://link.aps.org/doi/10.1103/PhysRevLett.117.252501>, doi:[10.1103/PhysRevLett.117.252501](https://doi.org/10.1103/PhysRevLett.117.252501).

[78] M. Hammen, W. Nörtershäuser, D. L. Balabanski, M. L. Bissell, K. Blaum, I. Budinčević, B. Cheal, K. T. Flanagan, N. Frömmgen, G. Georgiev, Ch. Geppert, M. Kowalska, K. Kreim, A. Krieger, W. Nazarewicz, R. Neugart, G. Neyens, J. Papuga, P.-G. Reinhard, M. M. Rajabali, S. Schmidt, and D. T. Yordanov. From calcium to cadmium: Testing the pairing functional through charge radii measurements of  $^{100-130}\text{Cd}$ . *Phys. Rev. Lett.*, 121:102501, 2018. URL: <https://link.aps.org/doi/10.1103/PhysRevLett.121.102501>, doi:[10.1103/PhysRevLett.121.102501](https://doi.org/10.1103/PhysRevLett.121.102501).

[79] S. Malbrunot-Ettenauer, S. Kaufmann, S. Bacca, C. Barbieri, J. Billowes, M. L. Bissell, K. Blaum, B. Cheal, T. Duguet, R. F. Garcia Ruiz, W. Gins, C. Gorges, G. Hagen, H. Heylen, J. D. Holt, G. R. Jansen, A. Kanellakopoulos, M. Kortelainen, T. Miyagi, P. Navrátil, W. Nazarewicz, R. Neugart, G. Neyens, W. Nörtershäuser, S. J. Novario, T. Papenbrock, T. Ratajczyk, P.-G. Reinhard, L. V. Rodríguez, R. Sánchez, S. Sailer, A. Schwenk, J. Simonis, V. Somà, S. R. Stroberg, L. Wehner, C. Wraith, L. Xie, Z. Y. Xu, X. F. Yang, and D. T. Yordanov. Nuclear charge radii of the nickel isotopes  $^{58-68,70}\text{Ni}$ . *Phys. Rev. Lett.*, 128:022502, 2022. URL: <https://link.aps.org/doi/10.1103/PhysRevLett.128.022502>, doi:[10.1103/PhysRevLett.128.022502](https://doi.org/10.1103/PhysRevLett.128.022502).

[80] T. Miyagi, S. R. Stroberg, J. D. Holt, and N. Shimizu. Ab initio multishell valence-space Hamiltonians and the island of inversion. *Phys. Rev. C*, 102:034320, 2020. URL: <https://link.aps.org/doi/10.1103/PhysRevC.102.034320>, doi:[10.1103/PhysRevC.102.034320](https://doi.org/10.1103/PhysRevC.102.034320).

[81] S. J. Novario, G. Hagen, G. R. Jansen, and T. Papenbrock. Charge radii of exotic neon and magnesium isotopes. *Phys. Rev. C*, 102:051303, 2020. URL: <https://link.aps.org/doi/10.1103/PhysRevC.102.051303>, doi:[10.1103/PhysRevC.102.051303](https://doi.org/10.1103/PhysRevC.102.051303).

[82] G. Hagen, S. J. Novario, Z. H. Sun, T. Papenbrock, G. R. Jansen, J. G. Lietz, T. Duguet, and A. Tichai. Angular-momentum projection in coupled-cluster theory: structure of  $^{34}\text{Mg}$ , 2022. [arXiv:2201.07298](https://arxiv.org/abs/2201.07298).

[83] D. T. Yordanov, M. L. Bissell, K. Blaum, M. De Rydt, Ch. Geppert, M. Kowalska, J. Krämer, K. Kreim, A. Krieger, P. Lievens, T. Neff, R. Neugart, G. Neyens, W. Nörtershäuser, R. Sánchez, and P. Vingerhoets. Nuclear charge radii of  $^{21-32}\text{Mg}$ . *Phys. Rev. Lett.*, 108:042504, 2012. URL: <https://link.aps.org/doi/10.1103/PhysRevLett.108.042504>, doi:10.1103/PhysRevLett.108.042504.

[84] Takaharu Otsuka, Noritaka Shimizu, and Yusuke Tsunoda. Moments and radii of exotic Na and Mg isotopes. *Phys. Rev. C*, 105:014319, 2022. URL: <https://link.aps.org/doi/10.1103/PhysRevC.105.014319>, doi:10.1103/PhysRevC.105.014319.

[85] P A Butler, J Cederkall, and P Reiter. Nuclear-structure studies of exotic nuclei with mini-ball. *Journal of Physics G: Nuclear and Particle Physics*, 44(4):044012, mar 2017. URL: <https://dx.doi.org/10.1088/1361-6471/aa5c4e>, doi:10.1088/1361-6471/aa5c4e.

[86] B. H. Wildenthal and W. Chung. Collapse of the conventional shell-model ordering in the very-neutron-rich isotopes of Na and Mg. *Phys. Rev. C*, 22:2260–2262, 1980. URL: <https://link.aps.org/doi/10.1103/PhysRevC.22.2260>, doi:10.1103/PhysRevC.22.2260.

[87] V. Manea, J. Karthein, D. Atanasov, M. Bender, K. Blaum, T. E. Cocolios, S. Eliseev, A. Herlert, J. D. Holt, W. J. Huang, Yu. A. Litvinov, D. Lunney, J. Menéndez, M. Mougeot, D. Neidherr, L. Schweikhard, A. Schwenk, J. Simonis, A. Welker, F. Wienholtz, and K. Zuber. First Glimpse of the  $N = 82$  Shell Closure below  $Z = 50$  from Masses of Neutron-Rich Cadmium Isotopes and Isomers. *Phys. Rev. Lett.*, 124:092502, 2020. URL: <https://link.aps.org/doi/10.1103/PhysRevLett.124.092502>, doi:10.1103/PhysRevLett.124.092502.

[88] T. D. Morris, J. Simonis, S. R. Stroberg, C. Stumpf, G. Hagen, J. D. Holt, G. R. Jansen, T. Papenbrock, R. Roth, and A. Schwenk. Structure of the lightest tin isotopes. *Phys. Rev. Lett.*, 120:152503, 2018. URL: <https://link.aps.org/doi/10.1103/PhysRevLett.120.152503>, doi:10.1103/PhysRevLett.120.152503.

[89] J. Z. Han, C. Pan, K. Y. Zhang, X. F. Yang, S. Q. Zhang, J. C. Berengut, S. Goriely, H. Wang, Y. M. Yu, J. Meng, J. W. Zhang, and L. J. Wang. Isotope shift factors for the  $\text{Cd}^+ 5s^2 S_{1/2} \rightarrow 5p^2 P_{3/2}$  transition and determination of Cd nuclear charge radii. *Phys. Rev. Res.*, 4:033049, 2022. URL: <https://link.aps.org/doi/10.1103/PhysRevResearch.4.033049>, doi:10.1103/PhysRevResearch.4.033049.

[90] T.E. Cocolios, H.H. Al Suradi, J. Billowes, I. Budinçevifá, R.P. de Groote, S. De Schepper, V.N. Fedossev, K.T. Flanagan, S. Franchoo, R.F. Garcia Ruiz, H. Heylen, F. Le Blanc, K.M. Lynch, B.A. Marsh, P.J.R. Mason, G. Neyens, J. Papuga, T.J. Procter, M.M. Rajabali, R.E. Rossel, S. Rothe, G.S. Simpson, A.J. Smith, I. Strashnov, H.H. Stroke, D. Verney, P.M. Walker, K.D.A. Wendt, and R.T. Wood. The Collinear Resonance Ionization Spectroscopy (CRIS) experimental setup at CERN-ISOLDE. *Nuclear Instruments and Methods in Physics Research Section B: Beam Interactions with Materials and Atoms*, 317:565 – 569, 2013. XVIth International Conference on ElectroMagnetic Isotope Separators and Techniques Related to their Applications, December 2, Äì7, 2012 at Matsue, Japan. URL: <http://www.sciencedirect.com/science/article/pii/S0168583X13007088>, doi:<https://doi.org/10.1016/j.nimb.2013.05.088>.

[91] R. P. de Groote, J. Billowes, C. L. Binnersley, M. L. Bissell, T. E. Cocolios, T. Day Goodacre, G. J. Farooq-Smith, D. V. Fedorov, K. T. Flanagan, S. Franchoo, R. F. Garcia Ruiz, W. Gins, J. D. Holt, Á. Koszorús, K. M. Lynch, T. Miyagi, W. Nazarewicz, G. Neyens, P. G. Reinhard, S. Rothe, H. H. Stroke, A. R. Vernon, K. D. A. Wendt, S. G. Wilkins, Z. Y. Xu, and X. F. Yang. Measurement and microscopic description of odd–even staggering of charge radii of exotic copper isotopes. *Nature Physics*, 16(6):620–624, 2020. [doi:10.1038/s41567-020-0868-y](https://doi.org/10.1038/s41567-020-0868-y).

[92] Á. Koszorús, X. F. Yang, W. G. Jiang, S. J. Novario, S. W. Bai, J. Billowes, C. L. Binnersley, M. L. Bissell, T. E. Cocolios, B. S. Cooper, R. P. de Groote, A. Ekström, K. T. Flanagan, C. Forssén, S. Franchoo, R. F. Garcia Ruiz, F. P. Gustafsson, G. Hagen, G. R. Jansen, A. Kanellakopoulos, M. Kortelainen, W. Nazarewicz, G. Neyens, T. Papenbrock, P. G. Reinhard, C. M. Ricketts, B. K. Sahoo, A. R. Vernon, and S. G. Wilkins. Charge radii of exotic potassium isotopes challenge nuclear theory and the magic character of  $n = 32$ . *Nature Physics*, 2021. [doi:10.1038/s41567-020-01136-5](https://doi.org/10.1038/s41567-020-01136-5).

[93] R. Heinke, T. Kron, S. Raeder, T. Reich, P. Schönberg, M. Trümper, C. Weichhold, and K. Wendt. High-resolution in-source laser spectroscopy in perpendicular geometry. Development and application of the PI-LIST. *Hyperfine Interactions*, 238:6, 2017. URL: <https://link.springer.com/article/10.1007/s10751-016-1386-2>, [doi:https://doi.org/10.1007/s10751-016-1386-2](https://doi.org/10.1007/s10751-016-1386-2).

[94] R. Ferrer, A. Barzakh, B. Bastin, R. Beerwerth, M. Block, P. Creemers, H. Grawe, R. de Groote, P. Delahaye, X. Fléchard, S. Franchoo, S. Fritzsche, L. P. Gaffney, L. Ghys, W. Gins, C. Granados, R. Heinke, L. Hijazi, M. Huyse, T. Kron, Yu. Kudryavtsev, M. Laatiaoui, N. Lecesne, M. Loiselet, F. Lutton, I. D. Moore, Y. Martínez, E. Mogilevskiy, P. Naubereit, J. Piot, S. Raeder, S. Rothe, H. Savajols, S. Sels, V. Sonnenschein, J.-C. Thomas, E. Traykov, C. Van Beveren, P. Van den Bergh, P. Van Duppen, K. Wendt, and A. Zadvornaya. Towards high-resolution laser ionization spectroscopy of the heaviest elements in supersonic gas jet expansion. *Nature Communications*, 8(1):14520, 2017. [doi:10.1038/ncomms14520](https://doi.org/10.1038/ncomms14520).

[95] S. Raeder, M. Block, P. Chhetri, R. Ferrer, S. Kraemer, T. Kron, M. Laatiaoui, S. Nothhelfer, F. Schneider, P. Van Duppen, M. Verlinde, E. Verstraelen, Th. Walther, and A. Zadvornaya. A gas-jet apparatus for high-resolution laser spectroscopy on the heaviest elements at SHIP. *Nuclear Instruments and Methods in Physics Research Section B: Beam Interactions with Materials and Atoms*, 463:272–276, 2020. URL: <https://www.sciencedirect.com/science/article/pii/S0168583X19303209>, [doi:https://doi.org/10.1016/j.nimb.2019.05.016](https://doi.org/10.1016/j.nimb.2019.05.016).

[96] R F Garcia Ruiz, C Gorges, M Bissell, K Blaum, W Gins, H Heylen, K Koenig, S Kauffmann, M Kowalska, J Krämer, P Lievens, S Malbrunot-Ettenauer, R Neugart, G Neyens, W Nörtershäuser, D T Yordanov, and X F Yang. Development of a sensitive setup for laser spectroscopy studies of very exotic calcium isotopes. *Journal of Physics G: Nuclear and Particle Physics*, 44(4):044003, 2017. [doi:10.1088/1361-6471/aa5a24](https://doi.org/10.1088/1361-6471/aa5a24).

[97] P. Plattner. The charge radius of  $^{26m}\text{Al}$  and the design of an advanced optical detection region for collinear laser spectroscopy. PhD thesis, University Innsbruck, 2022.

[98] C. Kanitz. Construction and characterization of a Paul trap for laser spectroscopy of exotic radionuclides in an MR-ToF device. M.Sc. thesis, Friedrich-Alexander-University Erlangen-Nürnberg, 2021.

[99] L. Croquette. Commissioning of a Paul trap for Collinear Laser Spectroscopy of Exotic Radionuclides performed in a 30-keV MR-ToF device . M.Sc. thesis, McGill University, Canada, 2023.

[100] M. Rosenbusch, S. Kemnitz, R. Schneider, L. Schweikhard, R. Tschiersch, and R. N. Wolf. Towards systematic investigations of space-charge phenomena in multi-reflection ion traps. *AIP Conference Proceedings*, 1521(1):53–62, 2013. URL: <https://aip.scitation.org/doi/abs/10.1063/1.4796061>, arXiv:<https://aip.scitation.org/doi/pdf/10.1063/1.4796061>, doi:10.1063/1.4796061.

[101] M. Rosenbusch, P. Chauveau, P. Delahaye, G. Marx, L. Schweikhard, F. Wienholtz, and R. N. Wolf. Delayed bunching for multi-reflection time-of-flight mass separation. *AIP Conference Proceedings*, 1668(1):050001, 2015. URL: <https://aip.scitation.org/doi/abs/10.1063/1.4923120>, arXiv:<https://aip.scitation.org/doi/pdf/10.1063/1.4923120>, doi:10.1063/1.4923120.

[102] M. Lange, M. Froese, S. Menk, J. Varju, R. Bastert, K. Blaum, J. R. Crespo Lopez-Urrutia, F. Fellenberger, M. Grieser, R. von Hahn, O. Heber, K.-U. Kühnel, F. Laux, D. A. Orlov, M. L. Rappaport, R. Repnow, C. D. Schröter, D. Schwalm, A. Shornikov, T. Sieber, Y. Toker, J. Ullrich, A. Wolf, and D. Zajfman. A cryogenic electrostatic trap for long-time storage of keV ion beams. *Review of Scientific Instruments*, 81(5):055105, 2010. arXiv:<https://doi.org/10.1063/1.3372557>, doi:10.1063/1.3372557.

[103] H. Wollnik and M. Przewloka. Time-of-flight mass spectrometers with multiply reflected ion trajectories. *International Journal of Mass Spectrometry and Ion Processes*, 96(3):267 – 274, 1990. URL: <http://www.sciencedirect.com/science/article/pii/016811769085127N>, doi:[https://doi.org/10.1016/0168-1176\(90\)85127-N](https://doi.org/10.1016/0168-1176(90)85127-N).

[104] D. Zajfman, O. Heber, L. Vejby-Christensen, I. Ben-Itzhak, M. Rappaport, R. Fishman, and M. Dahan. Electrostatic bottle for long-time storage of fast ion beams. *Phys. Rev. A*, 55:R1577–R1580, 1997. URL: <https://link.aps.org/doi/10.1103/PhysRevA.55.R1577>, doi:10.1103/PhysRevA.55.R1577.

[105] W. Henry Benner. A gated electrostatic ion trap to repetitiously measure the charge and m/z of large electrospray ions. *Analytical Chemistry*, 69(20):4162–4168, 1997. doi:10.1021/ac970163e.

[106] Paul Fischer, Stefan Knauer, Gerrit Marx, and Lutz Schweikhard. In-depth study of in-trap high-resolution mass separation by transversal ion ejection from a multi-reflection time-of-flight device. *Review of Scientific Instruments*, 89(1):015114, 2018. arXiv:<https://doi.org/10.1063/1.5009167>, doi:10.1063/1.5009167.

[107] Christian Breitenfeldt, Michael Wayne Froese, Klaus Blaum, Sebastian George, Manfred Grieser, Michael Lange, Sebastian Menk, Roland Repnow, Dirk Schwalm, Lutz Schweikhard, Robert von Hahn, and Andreas Wolf. Spreading times of ion-bunches in the cryogenic trap for fast ion beams. *International Journal of Mass Spectrometry*, 396:1–4, 2016. URL: <https://www.sciencedirect.com/science/article/pii/S1387380615004030>, doi:<https://doi.org/10.1016/j.ijms.2015.11.011>.

[108] W. Nörterhäuser, D. Tiedemann, M. Žáková, Z. Andjelkovic, K. Blaum, M. L. Bissell, R. Cazan, G. W. F. Drake, Ch. Geppert, M. Kowalska, J. Krämer, A. Krieger, R. Neugart, R. Sánchez, F. Schmidt-Kaler, Z.-C. Yan, D. T. Yordanov, and C. Zimmermann. Nuclear charge radii of  $^{7,9,10}\text{Be}$  and the one-neutron halo nucleus  $^{11}\text{Be}$ . *Phys. Rev. Lett.*, 102:062503,

2009. URL: <https://link.aps.org/doi/10.1103/PhysRevLett.102.062503>, doi:10.1103/PhysRevLett.102.062503.

[109] J. A. Behr, A. Gorelov, T. Swanson, O. Häusser, K. P. Jackson, M. Trinczek, U. Giesen, J. M. D'Auria, R. Hardy, T. Wilson, P. Choboter, F. Leblond, L. Buchmann, M. Dombsky, C. D. P. Levy, G. Roy, B. A. Brown, and J. Dilling. Magneto-optic Trapping of  $\beta$ -Decaying  $^{38}K^m$ ,  $^{37}K$  from an on-line Isotope Separator. *Phys. Rev. Lett.*, 79:375–378, Jul 1997. URL: <https://link.aps.org/doi/10.1103/PhysRevLett.79.375>, doi:10.1103/PhysRevLett.79.375.

[110] E. Mané, A. Voss, J. A. Behr, J. Billowes, T. Brunner, F. Buchinger, J. E. Crawford, J. Dilling, S. Ettenauer, C. D. P. Levy, O. Shelbaya, and M. R. Pearson. First experimental determination of the charge radius of  $^{74}\text{Rb}$  and its application in tests of the unitarity of the cabibbo-kobayashi-maskawa matrix. *Phys. Rev. Lett.*, 107:212502, 2011. URL: <https://link.aps.org/doi/10.1103/PhysRevLett.107.212502>, doi:10.1103/PhysRevLett.107.212502.

[111] M. S. Safronova, S. G. Porsev, M. G. Kozlov, J. Thielking, M. V. Okhapkin, P. Głowacki, D. M. Meier, and E. Peik. Nuclear charge radii of  $^{229}\text{Th}$  from isotope and isomer shifts. *Phys. Rev. Lett.*, 121:213001, Nov 2018. URL: <https://link.aps.org/doi/10.1103/PhysRevLett.121.213001>, doi:10.1103/PhysRevLett.121.213001.

[112] V. A. Dzuba, W. R. Johnson, and M. S. Safronova. Calculation of isotope shifts for cesium and francium. *Phys. Rev. A*, 72:022503, Aug 2005. URL: <https://link.aps.org/doi/10.1103/PhysRevA.72.022503>, doi:10.1103/PhysRevA.72.022503.

[113] Adriana Pálffy. Nuclear effects in atomic transitions. *Contemporary Physics*, 51(6):471–496, 2010. arXiv:<https://doi.org/10.1080/00107514.2010.493325>, doi:10.1080/00107514.2010.493325.

[114] Á Koszorús, X. F. Yang, W. G. Jiang, S. J. Novario, S. W. Bai, J. Billowes, C. L. Binnersley, M. L. Bissell, T. E. Cocolios, B. S. Cooper, R. P. de Groote, A. Ekström, K. T. Flanagan, C. Forssén, S. Franchoo, R. F. Garcia Ruiz, F. P. Gustafsson, G. Hagen, G. R. Jansen, A. Kanellakopoulos, M. Kortelainen, W. Nazarewicz, G. Neyens, T. Papenbrock, P.-G. Reinhard, C. M. Ricketts, B. K. Sahoo, A. R. Vernon, and S. G. Wilkins. Charge radii of exotic potassium isotopes challenge nuclear theory and the magic character of  $N = 32$ . *Nature Physics*, 17(4):439–443, 2021. doi:10.1038/s41567-020-01136-5.

[115] David J Pegg. Structure and dynamics of negative ions. *Reports on Progress in Physics*, 67(6):857, 2004. URL: <https://dx.doi.org/10.1088/0034-4885/67/6/R02>, doi:10.1088/0034-4885/67/6/R02.

[116] Moa Kristiansson. *Precision measurements on negative ions*. PhD thesis, Stockholm University, Department of Physics, 2022.

[117] T. Andersen. Atomic negative ions: structure, dynamics and collisions. *Physics Reports*, 394(4):157–313, 2004. URL: <https://www.sciencedirect.com/science/article/pii/S0370157304000316>, doi:<https://doi.org/10.1016/j.physrep.2004.01.001>.

[118] David Leimbach, Julia Karls, Yangyang Guo, Rizwan Ahmed, Jochen Ballof, Lars Bengtsson, Ferran Boix Pamies, Anastasia Borschevsky, Katerina Chrysalidis, Ephraim Eliav, Dmitry Fedorov, Valentin Fedosseev, Oliver Forstner, Nicolas Galland, Ronald Fernando Garcia Ruiz, Camilo Granados, Reinhard Heinke, Karl Johnston, Agota Koszorus, Ulli

Köster, Moa K. Kristiansson, Yuan Liu, Bruce Marsh, Pavel Molkanov, LukášF. Pašteka, João Pedro Ramos, Eric Renault, Mikael Reponen, Annie Ringvall-Moberg, Ralf Erik Rossel, Dominik Studer, Adam Vernon, Jessica Warbinek, Jakob Welander, Klaus Wendt, Shane Wilkins, Dag Hanstorp, and Sebastian Rothe. The electron affinity of astatine. *Nature Communications*, 11(1):3824, 2020. [doi:10.1038/s41467-020-17599-2](https://doi.org/10.1038/s41467-020-17599-2).

[119] John C. Wheeler. Electron affinities of the alkaline earth metals and the sign convention for electron affinity. *Journal of Chemical Education*, 74(1):123, Jan 1997. [doi:10.1021/ed074p123](https://doi.org/10.1021/ed074p123).

[120] V A Dzuba and G F Gribakin. - low-lying shape resonance rather than a bound state. *Journal of Physics B: Atomic, Molecular and Optical Physics*, 31(11):L483, jun 1998. URL: <https://dx.doi.org/10.1088/0953-4075/31/11/002>, [doi:10.1088/0953-4075/31/11/002](https://doi.org/10.1088/0953-4075/31/11/002).

[121] Xiaoxi Fu, Yuzhu Lu, Rulin Tang, and Chuangang Ning. Electron affinity measurements of lanthanide atoms: Pr, nd, and tb. *Phys. Rev. A*, 101:022502, Feb 2020. URL: <https://link.aps.org/doi/10.1103/PhysRevA.101.022502>, [doi:10.1103/PhysRevA.101.022502](https://doi.org/10.1103/PhysRevA.101.022502).

[122] Ephraim Eliav, Stephan Fritzsche, and Uzi Kaldor. Electronic structure theory of the superheavy elements. *Nuclear Physics A*, 944:518–550, 2015. Special Issue on Superheavy Elements. URL: <https://www.sciencedirect.com/science/article/pii/S0375947415001463>, [doi:https://doi.org/10.1016/j.nuclphysa.2015.06.017](https://doi.org/10.1016/j.nuclphysa.2015.06.017).

[123] T Carette and M R Godefroid. Isotope shift on the chlorine electron affinity revisited by an MCHF/CI approach. *Journal of Physics B: Atomic, Molecular and Optical Physics*, 46(9):095003, 2013. URL: <https://dx.doi.org/10.1088/0953-4075/46/9/095003>, [doi:10.1088/0953-4075/46/9/095003](https://doi.org/10.1088/0953-4075/46/9/095003).

[124] U. Berzinsh, M. Gustafsson, D. Hanstorp, A. Klinkmüller, U. Ljungblad, and A.-M. Mårtensson-Pendrill. Isotope shift in the electron affinity of chlorine. *Phys. Rev. A*, 51:231–238, 1995. URL: <https://link.aps.org/doi/10.1103/PhysRevA.51.231>, [doi:10.1103/PhysRevA.51.231](https://doi.org/10.1103/PhysRevA.51.231).

[125] Sebastian Rothe, Julia Sundberg, Jakob Welander, Katerina Chrysalidis, Thomas Day Goodacre, Valentin Fedosseev, Spyridon Fiotakis, Oliver Forstner, Reinhard Heinke, Karl Johnston, Tobias Kron, Ulli Köster, Yuan Liu, Bruce Marsh, Annie Ringvall-Moberg, Ralf Erik Rossel, Christoph Seiffert, Dominik Studer, Klaus Wendt, and Dag Hanstorp. Laser photodetachment of radioactive  $^{128}\text{I}$ . *Journal of Physics G: Nuclear and Particle Physics*, 44(10):104003, 2017. URL: <https://dx.doi.org/10.1088/1361-6471/aa80aa>, [doi:10.1088/1361-6471/aa80aa](https://doi.org/10.1088/1361-6471/aa80aa).

[126] J. Warbinek, D. Leimbach, D. Lu, K. Wendt, D. J. Pegg, A. Yurgens, D. Hanstorp, and J. Welander. A graphene-based neutral particle detector. *Applied Physics Letters*, 114(6):061902, 2019. [arXiv:https://doi.org/10.1063/1.5080517](https://arxiv.org/abs/https://doi.org/10.1063/1.5080517), [doi:10.1063/1.5080517](https://doi.org/10.1063/1.5080517).

[127] Eugene P. Wigner. On the behavior of cross sections near thresholds. *Phys. Rev.*, 73:1002–1009, 1948. URL: <https://link.aps.org/doi/10.1103/PhysRev.73.1002>, [doi:10.1103/PhysRev.73.1002](https://doi.org/10.1103/PhysRev.73.1002).

[128] Moa K. Kristiansson, Kiattichart Chartkunchand, Gustav Eklund, Odd M. Hole, Emma K. Anderson, Nathalie de Ruette, Magdalena Kamińska, Najeeb Punnakayathil, José E. Navarro-Navarrete, Stefan Sigurdsson, Jon Grumer, Ansgar Simonsson, Mikael Björkhage, Stefan Rosén, Peter Reinhard, Mikael Blom, Anders Källberg, John D. Alexander, Henrik Cederquist, Henning Zettergren, Henning T. Schmidt, and Dag Hanstorp. High-precision electron affinity of oxygen. *Nature Communications*, 13(1):5906, 2022. [doi:10.1038/s41467-022-33438-y](https://doi.org/10.1038/s41467-022-33438-y).

[129] D. Leimbach. Radioactive negative ions: Production and laser spectroscopy at ISOLDE. PhD thesis, Johannes Gutenberg-University Mainz, 2021.

[130] V. Radojević, H. P. Kelly, and W. R. Johnson. Photodetachment of negative halogen ions. *Phys. Rev. A*, 35:2117–2121, Mar 1987. URL: <https://link.aps.org/doi/10.1103/PhysRevA.35.2117>, doi:10.1103/PhysRevA.35.2117.

[131] Christopher J. Johnson, Ben B. Shen, Berwyck L. J. Poad, and Robert E. Continetti. Photoelectron-photofragment coincidence spectroscopy in a cryogenically cooled linear electrostatic ion beam trap. *Review of Scientific Instruments*, 82(10):105105, 2011. arXiv:<https://doi.org/10.1063/1.3641875>, doi:10.1063/1.3641875.

[132] T.W. Hänsch and A.L. Schawlow. Cooling of gases by laser radiation. *Optics Communications*, 13(1):68–69, 1975. URL: <https://www.sciencedirect.com/science/article/pii/0030401875901595>, doi:[https://doi.org/10.1016/0030-4018\(75\)90159-5](https://doi.org/10.1016/0030-4018(75)90159-5).

[133] D. J. Wineland and Wayne M. Itano. Laser cooling of atoms. *Phys. Rev. A*, 20:1521–1540, 1979. URL: <https://link.aps.org/doi/10.1103/PhysRevA.20.1521>, doi:10.1103/PhysRevA.20.1521.

[134] G. D. Sprouse and L. A. Orozco. Laser trapping of radioactive atoms. *Annual Review of Nuclear and Particle Science*, 47:429–461, 1997. arXiv:<https://doi.org/10.1146/annurev.nucl.47.1.429>, doi:10.1146/annurev.nucl.47.1.429.

[135] J. A. Behr, A. Gorelov, T. Swanson, O. Häusser, K. P. Jackson, M. Trinczek, U. Giesen, J. M. D'Auria, R. Hardy, T. Wilson, P. Choboter, F. Leblond, L. Buchmann, M. Dombsky, C. D. P. Levy, G. Roy, B. A. Brown, and J. Dilling. Magneto-optic trapping of  $\beta$ -decaying  $^{38}K^m$ ,  $^{37}k$  from an on-line isotope separator. *Phys. Rev. Lett.*, 79:375–378, 1997. URL: <https://link.aps.org/doi/10.1103/PhysRevLett.79.375>, doi:10.1103/PhysRevLett.79.375.

[136] M. Trinczek, A. Gorelov, D. Melconian, W. P. Alford, D. Asgeirsson, D. Ashery, J. A. Behr, P. G. Bricault, J. M. D'Auria, J. Deutsch, J. Dilling, M. Dombsky, P. Dubé, S. Eaton, J. Fingler, U. Giesen, S. Gu, O. Häusser, K. P. Jackson, B. Lee, J. H. Schmid, T. J. Stocki, T. B. Swanson, and W. Wong. Novel search for heavy  $\nu$  mixing from the  $\beta^+$  decay of  $^{38m}K$  confined in an atom trap. *Phys. Rev. Lett.*, 90:012501, 2003. URL: <https://link.aps.org/doi/10.1103/PhysRevLett.90.012501>, doi:10.1103/PhysRevLett.90.012501.

[137] P. A. Vetter, J. R. Abo-Shaeer, S. J. Freedman, and R. Maruyama. Measurement of the  $\beta-\nu$  correlation of  $^{21}Na$  using shakeoff electrons. *Phys. Rev. C*, 77:035502, 2008. URL: <https://link.aps.org/doi/10.1103/PhysRevC.77.035502>, doi:10.1103/PhysRevC.77.035502.

[138] J. R. A. Pitcairn et al. Tensor interaction constraints from beta decay recoil spin asymmetry of trapped atoms. *Phys. Rev. C*, 79:015501, 2009. arXiv:0811.0052, doi:10.1103/PhysRevC.79.015501.

[139] B. Fenker, A. Gorelov, D. Melconian, J. A. Behr, M. Anholm, D. Ashery, R. S. Behling, I. Cohen, I. Craiciu, G. Gwinner, J. McNeil, M. Mehlman, K. Olchanski, P. D. Shidling, S. Smale, and C. L. Warner. Precision measurement of the  $\beta$  asymmetry in spin-polarized  $^{37}\text{K}$  decay. *Phys. Rev. Lett.*, 120:062502, 2018. URL: <https://link.aps.org/doi/10.1103/PhysRevLett.120.062502>, doi:10.1103/PhysRevLett.120.062502.

[140] A. Takamine, M. Wada, K. Okada, T. Sonoda, P. Schury, T. Nakamura, Y. Kanai, T. Kubo, I. Katayama, S. Ohtani, H. Wollnik, and H. A. Schuessler. Hyperfine Structure Constant of the Neutron Halo Nucleus  $^{11}\text{Be}^+$ . *Phys. Rev. Lett.*, 112:162502, 2014. URL: <https://link.aps.org/doi/10.1103/PhysRevLett.112.162502>, doi:10.1103/PhysRevLett.112.162502.

[141] L.-B. Wang, P. Mueller, K. Bailey, G. W. F. Drake, J. P. Greene, D. Henderson, R. J. Holt, R. V. F. Janssens, C. L. Jiang, Z.-T. Lu, T. P. O'Connor, R. C. Pardo, K. E. Rehm, J. P. Schiffer, and X. D. Tang. Laser spectroscopic determination of the  $^6\text{He}$  nuclear charge radius. *Phys. Rev. Lett.*, 93:142501, 2004. URL: <https://link.aps.org/doi/10.1103/PhysRevLett.93.142501>, doi:10.1103/PhysRevLett.93.142501.

[142] P. Mueller, I. A. Sulai, A. C. C. Villari, J. A. Alcántara-Núñez, R. Alves-Condé, K. Bailey, G. W. F. Drake, M. Dubois, C. Eléon, G. Gaubert, R. J. Holt, R. V. F. Janssens, N. Lecesne, Z.-T. Lu, T. P. O'Connor, M.-G. Saint-Laurent, J.-C. Thomas, and L.-B. Wang. Nuclear charge radius of  $^8\text{He}$ . *Phys. Rev. Lett.*, 99:252501, 2007. URL: <https://link.aps.org/doi/10.1103/PhysRevLett.99.252501>, doi:10.1103/PhysRevLett.99.252501.

[143] C.J. Foot. *Atomic Physics*. Oxford Master Series in Physics. OUP Oxford, 2005. URL: [https://books.google.ch/books?id=\\_CoSDAAAQBAJ](https://books.google.ch/books?id=_CoSDAAAQBAJ).

[144] B Ohayon, S Hofsäss, J E Padilla-Castillo, S C Wright, G Meijer, S Truppe, K Gibble, and B K Sahoo. Isotope shifts in cadmium as a sensitive probe for physics beyond the standard model. *New Journal of Physics*, 24(12):123040, 2022. URL: <https://dx.doi.org/10.1088/1367-2630/acacbb>, doi:10.1088/1367-2630/acacbb.

[145] Julian C. Berengut, Dmitry Budker, Cédric Delaunay, Victor V. Flambaum, Claudia Frugueule, Elina Fuchs, Christophe Grojean, Roni Harnik, Roee Ozeri, Gilad Perez, and Yotam Soreq. Probing new long-range interactions by isotope shift spectroscopy. *Phys. Rev. Lett.*, 120:091801, 2018. URL: <https://link.aps.org/doi/10.1103/PhysRevLett.120.091801>, doi:10.1103/PhysRevLett.120.091801.

[146] Tom Manovitz, Ravid Shaniv, Yotam Shapira, Roee Ozeri, and Nitzan Akerman. Precision measurement of atomic isotope shifts using a two-isotope entangled state. *Phys. Rev. Lett.*, 123:203001, Nov 2019. URL: <https://link.aps.org/doi/10.1103/PhysRevLett.123.203001>, doi:10.1103/PhysRevLett.123.203001.

[147] V. Batteiger, S. Knünz, M. Herrmann, G. Saathoff, H. A. Schüssler, B. Bernhardt, T. Wilken, R. Holzwarth, T. W. Hänsch, and Th. Udem. Precision spectroscopy of the  $3s-3p$  fine-structure doublet in  $\text{Mg}^+$ . *Phys. Rev. A*, 80:022503, 2009. URL: <https://link.aps.org/doi/10.1103/PhysRevA.80.022503>, doi:10.1103/PhysRevA.80.022503.

[148] Takaharu Otsuka, Alexandra Gade, Olivier Sorlin, Toshio Suzuki, and Yutaka Utsuno. Evolution of shell structure in exotic nuclei. *Rev. Mod. Phys.*, 92:015002, 2020. URL: <https://link.aps.org/doi/10.1103/RevModPhys.92.015002>, doi:10.1103/RevModPhys.92.015002.

[149] D. T. Yordanov, D. L. Balabanski, M. L. Bissell, K. Blaum, I. Budinčević, B. Cheal, K. Flanagan, N. Frömmgen, G. Georgiev, Ch. Geppert, M. Hammen, M. Kowalska, K. Kreim, A. Krieger, J. Meng, R. Neugart, G. Neyens, W. Nörtershäuser, M. M. Rajabali, J. Papuga, S. Schmidt, and P. W. Zhao. Simple nuclear structure in  $^{111-129}\text{Cd}$  from atomic isomer shifts. *Phys. Rev. Lett.*, 116:032501, 2016. URL: <https://link.aps.org/doi/10.1103/PhysRevLett.116.032501>, doi:10.1103/PhysRevLett.116.032501.

[150] Takaharu Otsuka, Toshio Suzuki, Michio Honma, Yutaka Utsuno, Naofumi Tsunoda, Koshiroh Tsukiyama, and Morten Hjorth-Jensen. Novel features of nuclear forces and shell evolution in exotic nuclei. *Phys. Rev. Lett.*, 104:012501, 2010. URL: <https://link.aps.org/doi/10.1103/PhysRevLett.104.012501>, doi:10.1103/PhysRevLett.104.012501.

[151] S. Eliseev, K. Blaum, M. Block, A. Dörr, C. Droese, T. Eronen, M. Goncharov, M. Höcker, J. Ketter, E. Minaya Ramirez, D. A. Nesterenko, Yu. N. Novikov, and L. Schweikhard. A phase-imaging technique for cyclotron-frequency measurements. *Applied Physics B*, 114(1):107–128, 2014. doi:10.1007/s00340-013-5621-0.

[152] M. Rosenbusch, M. Wada, S. Chen, A. Takamine, S. Iimura, D. Hou, W. Xian, S. Yan, P. Schury, Y. Hirayama, Y. Ito, H. Ishiyama, S. Kimura, T. Kojima, J. Lee, J. Liu, S. Michimasa, H. Miyatake, J.Y. Moon, M. Mukai, S. Nishimura, S. Naimi, T. Niwase, T. Sonoda, Y.X. Watanabe, and H. Wolnik. The new MRTOF mass spectrograph following the ZeroDegree spectrometer at RIKEN’s RIBF facility. *Nuclear Instruments and Methods in Physics Research Section A: Accelerators, Spectrometers, Detectors and Associated Equipment*, page 167824, 2022. URL: <https://www.sciencedirect.com/science/article/pii/S0168900222011160>, doi:<https://doi.org/10.1016/j.nima.2022.167824>.

[153] P.A. Bolotskikh, D.E. Grinfeld, A.A. Makarov, and M.A. Monastyrskiy. Coulomb dynamics of ion bunches in multi-reflection electrostatic traps. *Nuclear Instruments and Methods in Physics Research Section A: Accelerators, Spectrometers, Detectors and Associated Equipment*, 645(1):146–152, 2011. The Eighth International Conference on Charged Particle Optics. URL: <https://www.sciencedirect.com/science/article/pii/S0168900210029724>, doi:<https://doi.org/10.1016/j.nima.2010.12.170>.

[154] Dhanoj Gupta, Raj Singh, Ryan Ringle, Catherine R. Nicoloff, Igor Rahinov, Oded Heber, and Daniel Zajfman. Particle-in-cell techniques for the study of space charge effects in an electrostatic ion beam trap. *Phys. Rev. E*, 104:065202, 2021. URL: <https://link.aps.org/doi/10.1103/PhysRevE.104.065202>, doi:10.1103/PhysRevE.104.065202.

[155] Personal Communications with Frank Wienholtz, ISOLTRAP collaboration. 2018.

[156] C. Izzo, J. Bergmann, K. A. Dietrich, E. Dunling, D. Fusco, A. Jacobs, B. Kootte, G. Kripkó-Koncz, Y. Lan, E. Leistenschneider, E. M. Lykiardopoulou, I. Mukul, S. F. Paul, M. P. Reiter, J. L. Tracy, C. Andreoiu, T. Brunner, T. Dickel, J. Dilling, I. Dillmann, G. Gwinner, D. Lascar, K. G. Leach, W. R. Plaß, C. Scheidenberger, M. E. Wieser, and A. A. Kwiatkowski. Mass measurements of neutron-rich indium isotopes for *r*-process studies. *Phys. Rev. C*, 103:025811, 2021. URL: <https://link.aps.org/doi/10.1103/PhysRevC.103.025811>, doi:10.1103/PhysRevC.103.025811.

[157] S. F. Paul, J. Bergmann, J. D. Cardona, K. A. Dietrich, E. Dunling, Z. Hockenberry, C. Hornung, C. Izzo, A. Jacobs, A. Javaji, B. Kootte, Y. Lan, E. Leistenschneider, E. M. Lykiardopoulou, I. Mukul, T. Murböck, W. S. Porter, R. Silwal, M. B. Smith, J. Ringuette, T. Brunner, T. Dickel, I. Dillmann, G. Gwinner, M. MacCormick, M. P. Reiter, H. Schatz,

N. A. Smirnova, J. Dilling, and A. A. Kwiatkowski. Mass measurements of  $^{60-63}\text{Ga}$  reduce x-ray burst model uncertainties and extend the evaluated  $T = 1$  isobaric multiplet mass equation. *Phys. Rev. C*, 104:065803, 2021. URL: <https://link.aps.org/doi/10.1103/PhysRevC.104.065803>, doi:10.1103/PhysRevC.104.065803.

[158] R. Hipple and S.M. Lund. Modeling of Space-Charge Effects in the ORISS MRTOF Device for Applications to FRIB. *Proc. NAPAC'19*, (4):786–788, 2019. <https://doi.org/10.18429/JACoW-NAPAC2019-WEPLS10>. URL: <http://jacow.org/napac2019/papers/weplls10.pdf>, doi:10.18429/JACoW-NAPAC2019-WEPLS10.

[159] T. Aumann, W. Bartmann, O. Boine-Frankenheim, A. Bouvard, A. Broche, F. Butin, D. Calvet, J. Carbonell, P. Chiggiato, H. De Gersem, R. De Oliveira, T. Dobers, F. Ehm, J. Ferreira Somoza, J. Fischer, M. Fraser, E. Friedrich, A. Frotscher, M. Gomez-Ramos, J.-L. Grenard, A. Hobl, G. Hupin, A. Husson, P. Indelicato, K. Johnston, C. Klink, Y. Kubota, R. Lazauskas, S. Malbrunot-Ettenauer, N. Marsic, W. F. O Müller, S. Naimi, N. Nakatsuka, R. Necca, D. Neidherr, G. Neyens, A. Obertelli, Y. Ono, S. Pasinelli, N. Paul, E. C. Pollacco, D. Rossi, H. Scheit, M. Schlaich, A. Schmidt, L. Schweikhard, R. Seki, S. Sels, E. Siesling, T. Uesaka, M. Vilén, M. Wada, F. Wienholtz, S. Wycech, and S. Zacarias. PUMA, antiProton unstable matter annihilation. *The European Physical Journal A*, 58(5):88, 2022. doi:10.1140/epja/s10050-022-00713-x.

[160] B. Blank, M. Aouadi, P. Ascher, M. Gerbaux, J. Giovinazzo, S. Grévy, T. Kurtukian Nieto, M. R. Dunlop, R. Dunlop, A. T. Laffoley, G. F. Grinyer, and P. Finlay. Branching ratio of the super-allowed  $\beta$  decay of  $^{10}\text{C}$ . *The European Physical Journal A*, 56(6):156, 2020. doi:10.1140/epja/s10050-020-00165-1.

[161] Cristina Müller, Konstantin Zhernosekov, Ulli Köster, Karl Johnston, Holger Dorrer, Alexander Hohn, Nico T van der Walt, Andreas Türler, and Roger Schibli. A unique matched quadruplet of terbium radioisotopes for PET and SPECT and for  $\alpha$ - and  $\beta$ -radionuclide therapy: an in vivo proof-of-concept study with a new receptor-targeted folate derivative. *J Nucl Med*, 53(12):1951–1959, 2012.

[162] Cristina Müller, Christiaan Vermeulen, Karl Johnston, Ulli Köster, Raffaella Schmid, Andreas Türler, and Nicholas P. van der Meulen. Preclinical in vivo application of  $^{152}\text{Tb}$ -DOTANOC: a radiolanthanide for PET imaging. *EJNMMI Research*, 6(1):35, 2016. doi:10.1186/s13550-016-0189-4.

[163] Cristina Müller, Christiaan Vermeulen, Ulli Köster, Karl Johnston, Andreas Türler, Roger Schibli, and Nicholas P. van der Meulen. Alpha-pet with terbium-149: evidence and perspectives for radiotheragnostics. *EJNMMI Radiopharmacy and Chemistry*, 1(1):5, 2016. doi:10.1186/s41181-016-0008-2.

[164] F. Wienholtz. Measurements of exotic calcium isotopes by multi-reflection time-of-flight mass spectrometry and further developments and applications. PhD thesis, University Greifswald, 2019.

[165] H. B. Pedersen, D. Strasser, S. Ring, O. Heber, M. L. Rappaport, Y. Rudich, I. Sagi, and D. Zajfman. Ion motion synchronization in an ion-trap resonator. *Phys. Rev. Lett.*, 87:055001, 2001. URL: <https://link.aps.org/doi/10.1103/PhysRevLett.87.055001>, doi:10.1103/PhysRevLett.87.055001.

[166] D. Zajfman, O. Heber, M. L. Rappaport, H. B. Pedersen, D. Strasser, and S. Goldberg. Self-bunching effect in an ion trap resonator. *J. Opt. Soc. Am. B*, 20(5):1028–1032, 2003.

URL: <http://opg.optica.org/josab/abstract.cfm?URI=josab-20-5-1028>, doi:10.1364/JOSAB.20.001028.

[167] H. B. Pedersen, D. Strasser, B. Amarant, O. Heber, M. L. Rappaport, and D. Zajfman. Diffusion and synchronization in an ion-trap resonator. *Phys. Rev. A*, 65:042704, 2002. URL: <https://link.aps.org/doi/10.1103/PhysRevA.65.042704>, doi:10.1103/PhysRevA.65.042704.

[168] D. Strasser, T. Geyer, H. B. Pedersen, O. Heber, S. Goldberg, B. Amarant, A. Diner, Y. Rudich, I. Sagi, M. Rappaport, D. J. Tannor, and D. Zajfman. Negative Mass Instability for Interacting Particles in a 1D Box: Theory and Application. *Phys. Rev. Lett.*, 89:283204, 2002. URL: <https://link.aps.org/doi/10.1103/PhysRevLett.89.283204>, doi:10.1103/PhysRevLett.89.283204.

[169] M W Froese, M Lange, S Menk, M Grieser, O Heber, F Laux, R Repnow, T Sieber, Y Toker, R von Hahn, A Wolf, and K Blaum. The decay of ion bunches in the self-bunching mode. *New Journal of Physics*, 14(7):073010, 2012. doi:10.1088/1367-2630/14/7/073010.

[170] A. Jacobs, C. Andreoiu, J. Bergmann, T. Brunner, T. Dickel, I. Dillmann, E. Dunling, J. Flowerdew, L. Graham, G. Gwinner, Z. Hockenberry, B. Kootte, Y. Lan, K.G. Leach, E. Leistenschneider, E.M. Lykiardopoulou, V. Monier, I. Mukul, S.F. Paul, W.R. Plaß, M.P. Reiter, C. Scheidenberger, R. Thompson, J.L. Tracy, C. Will, M.E. Wieser, M. Yavor, J. Dilling, and A.A. Kwiatkowski. Collision-induced dissociation at triumf's ion trap for atomic and nuclear science. *International Journal of Mass Spectrometry*, 482:116931, 2022. URL: <https://www.sciencedirect.com/science/article/pii/S1387380622001361>, doi:<https://doi.org/10.1016/j.ijms.2022.116931>.

[171] Florian Greiner, Timo Dickel, Samuel Ayet San Andrés, Julian Bergmann, Paul Constantin, Jens Ebert, Hans Geissel, Emma Haettner, Christine Hornung, Ivan Miskun, Wayne Lippert, Israel Mardor, Iain Moore, Wolfgang R. Plaß, Sivaji Purushothaman, Ann-Kathrin Rink, Moritz P. Reiter, Christoph Scheidenberger, and Helmut Weick. Removal of molecular contamination in low-energy ribs by the isolation-dissociation-isolation method. *Nuclear Instruments and Methods in Physics Research Section B: Beam Interactions with Materials and Atoms*, 463:324–326, 2020. URL: <https://www.sciencedirect.com/science/article/pii/S0168583X19302563>, doi:<https://doi.org/10.1016/j.nimb.2019.04.072>.

## 8 Cumulative Thesis Articles

### **Article I:** Doppler and Sympathetic Cooling for the Investigation of Short-Lived Radioactive Ions

S. Sels, F.M.Maier, M. Au, P. Fischer, C. Kanitz, V. Lagaki, S. Lechner, E. Leistenschneider, D. Leimbach, E.M. Lykiardopoulou, A. A. Kwiatkowski, T. Manovitz, Y. N. Vila Gracia, G. Neyens, P. Plattner, S. Rothe, L. Schweikhard, M. Vilen, R.N. Wolf and S. Malbrunot-Ettenauer, Phys. Rev. Research 4, 033229 (2022).

The author contribution list is reprinted from the acknowledgement section of the manuscript: S.S. and S.M.-E. conceived the measurement idea following discussions with T.M. The experimental characterization of laser and buffer-gas cooling were conducted by S.S. and F.M., who also carried out the MR-ToF measurements together with C.K. Sympathetic cooling of other ion species was performed by F.M. and C.K. M.A. participated in a set of measurements utilizing buffer-gas cooling. The initial setup combining a Paul trap and an MR-ToF mass spectrometer has been built by R.W., P.F., and L.S. It was modified for laser applications by V.L., F.M., and S.M.-E. with contributions from P.F., S.L., P.P., and S.S. The potassium ion source and injection beamline was conceived and setup by D.L. and S.R. who coupled it to the ion-trap system together with C.K., V.L., F.M., Y.N.V.G., P.P., and M.V. The central laser system was built by S.L., who maintained it together with P.P. Modifications were implemented by S.S. with contributions by S.L. and F.M. The simulation and calculation tools for laser cooling were developed by F.M. and S.S. F.M. performed the 3D simulations and S.S. carried out the calculations in the 1D model. T.M. reviewed the calculation approach. The PI-ICR simulations were performed by E.L. and E.M.L. utilizing a code which they developed together with A.A.K. S.S., F.M., and S.M.-E. regularly discussed the progress and directions of the project and reviewed the results together with L.S. and the entire collaboration. S.M.-E., L.S., S.R., G.N., and A.A.K. secured funding and/or resources to pursue the present project. S.S. led the writing of the paper, which was done together with S.M.-E and F.M. with contributions by E.L. All authors carefully reviewed the paper.

### **Article II:** Simulation Studies of a 30-keV MR-ToF Device for Highly Sensitive Collinear Laser Spectroscopy

F.M. Maier, M. Vilen, I. Belosevic, F. Buchinger, C. Kanitz, S. Lechner, E. Leistenschneider, W. Nörtershäuser, P. Plattner, L. Schweikhard, S. Sels, F. Wienholtz, S. Malbrunot-Ettenauer, Nuclear Instrum. Meth. A, Vol 1048, 167927 (2023).

F.M. was largely involved in the conceptual design of the apparatus. She developed the simulation code, performed all the simulations and the analysis. She also thought about possible systematic effects and measures to minimize them. Supported by S.M.-E., F.M. wrote the manuscript.

**Article III:** Increased Beam Energy as a Pathway Towards a Highly Selective and High-Flux MR-ToF Mass Separator (submitted)

F.M. Maier, F. Buchinger, L. Croquette, P. Fischer, H. Heylen, F. Hummer, C. Kanitz, A.A. Kwiatkowski, V. Lagaki, S. Lechner, E. Leistenschneider, G. Neyens, P. Plattner, A. Roitman, M. Rosenbusch, L. Schweikhard, S. Sels, M. Vilen, F. Wienholtz, S. Malbrunot-Ettenauer, Nuclear Instrum. Meth. A.

F.M. took the lead in performing the mass resolving power measurements, corresponding optimizations and some of the collisional excitation measurements. She wrote most of the simulation and analysis codes, carried out the simulations and the analysis of simulation and experimental data. Supported by S.M.-E., F.M. wrote the manuscript.

Confirmed:

Franziska Maier

Lutz Schweikhard

## **8.1 Doppler and Sympathetic Cooling for the Investigation of Short-Lived Radioactive Ions**

## Doppler and sympathetic cooling for the investigation of short-lived radioactive ions

S. Sels<sup>1,2,\*</sup>, F. M. Maier,<sup>1,3</sup> M. Au<sup>1,4</sup>, P. Fischer<sup>1,5</sup>, C. Kanitz,<sup>1</sup> V. Lagaki<sup>1,3</sup>, S. Lechner<sup>1,5</sup>, E. Leistenschneider<sup>1,5</sup>, D. Leimbach<sup>1,6,7</sup>, E. M. Lykiardopoulou,<sup>8,9</sup> A. A. Kwiatkowski,<sup>8</sup> T. Manovitz<sup>10</sup>, Y. N. Vila Gracia,<sup>1</sup> G. Neyens<sup>1,2</sup>, P. Plattner<sup>1,11</sup>, S. Rothe,<sup>1</sup> L. Schweikhard,<sup>3</sup> M. Vilen,<sup>1</sup> R. N. Wolf<sup>1,12</sup> and S. Malbrunot-Ettenauer<sup>1</sup>

<sup>1</sup>CERN, CH-1211 Geneve 23, Switzerland

<sup>2</sup>Instituut voor kern- en stralingsphysica, KU Leuven, Celestijnenlaan 200D, Leuven, Belgium

<sup>3</sup>Institut für Physik, Universität Greifswald, 17487 Greifswald, Germany

<sup>4</sup>Johannes Gutenberg-Universität Mainz, Department Chemie, Standort TRIGA, Fritz-Strassmann-Weg 2, 55128 Mainz, Germany

<sup>5</sup>Technische Universität Wien, Karlsplatz 13, 1040 Wien, Austria

<sup>6</sup>Department of Physics, University of Gothenburg, SE-412 96 Gothenburg, Sweden

<sup>7</sup>Institut für Physik, Johannes Gutenberg-Universität, 55099 Mainz, Germany

<sup>8</sup>TRIUMF, 4004 Wesbrook Mall, Vancouver, British Columbia, Canada V6T 2A3

<sup>9</sup>Department of Physics and Astronomy, University of British Columbia, Vancouver, British Columbia, Canada V6T 1Z1

<sup>10</sup>Department of Physics of Complex Systems, Weizmann Institute of Science, Rehovot 76100, Israel

<sup>11</sup>Universität Innsbruck, Innrain 52, 6020 Innsbruck, Austria

<sup>12</sup>ARC Centre of Excellence for Engineered Quantum Systems, The University of Sydney, New South Wales 2006, Australia



(Received 9 February 2022; accepted 15 June 2022; published 23 September 2022)

At radioactive ion beam (RIB) facilities, ions of short-lived radionuclides are cooled and bunched in buffer-gas-filled Paul traps to improve the ion-beam quality for subsequent experiments. To deliver even colder ions, beneficial to RIB experiments' sensitivity or accuracy, we employ Doppler and sympathetic cooling in a Paul trap cooler-buncher. The improved emittance of  $Mg^+$ ,  $K^+$ , and  $O_2^+$  ion beams is demonstrated by a reduced time-of-flight spread of the extracted ion bunches with respect to room-temperature buffer-gas cooling. Cooling externally-produced hot ions with energies of at least 7 eV down to a few Kelvin is achieved in a timescale of  $O(100\text{ ms})$  by combining a low-pressure helium background gas with laser cooling. This is sufficiently short to cool short-lived radioactive ions. As an example of this technique's use for RIB research, the mass-resolving power in a multireflection time-of-flight mass spectrometer is shown to increase by up to a factor of 4.6 with respect to buffer-gas cooling. Simulations show good agreement with the experimental results and guide further improvements and applications. These results open a path to a significant emittance improvement and, thus, unprecedented ion-beam qualities at RIB facilities, achievable with standard equipment readily available. The same method provides opportunities for future high-precision experiments with radioactive cold trapped ions.

DOI: [10.1103/PhysRevResearch.4.033229](https://doi.org/10.1103/PhysRevResearch.4.033229)

### I. INTRODUCTION

Radioactive ion beam (RIB) facilities around the world specialize in producing beams of short-lived radioactive nuclides for a broad range of scientific experiments [1–9]. Studies of these exotic radionuclides extend our knowledge of the nuclear forces which bind protons and neutrons together to form atomic nuclei, guide nuclear astrophysics in its understanding of the formation of the chemical elements, and enable precision experiments on nuclear probes to search for new physics beyond the standard model of particle physics [10–12]. Moreover, modern RIB facilities play a central role in nuclear applications for solid state, bio-, and medical

physics, in particular, in the quest for innovative medical isotopes [13–16].

To meet the ion-beam requirements of RIB experiments, ions are often cooled and bunched to improve the beam quality before being transported to dedicated experimental instruments. Typically, this cooling is performed by buffer-gas-filled linear Radio Frequency (RF) ion traps, also called Paul traps [17–25]. In the context of RIB facilities, these ion traps are commonly referred to as cooler bunchers. They are able to capture, accumulate, bunch, cool, and eject virtually all species of ions, making them versatile and often indispensable tools. The cooling limit achievable in such a linear Paul trap is on the order of the buffer-gas temperature [26–28]. In most operational cooler-bunchers at RIB facilities, this corresponds to room temperature of about 300 K, and a few instruments can operate at liquid nitrogen temperature [21,29].

However, in other fields of research, experiments take advantage of much colder ensembles. For instance, laser cooling of trapped neutral and ionized atoms and molecules has revolutionized the field of experimental quantum physics. Since its inception in the 1970s [30–33], it has been a

\*Simon.Sels@cern.ch

Published by the American Physical Society under the terms of the Creative Commons Attribution 4.0 International license. Further distribution of this work must maintain attribution to the author(s) and the published article's title, journal citation, and DOI.

cornerstone in several Nobel-prize-winning experiments [33–35] as it allows for a precise preparation and quantum coherent control of cold trapped atoms and molecules. In the meantime, various laser-cooling techniques have been developed [36] and laser cooling has become a standard tool for high-precision research and applications such as atomic clocks [37], quantum information science [38], the search for physics beyond the standard model [39], and the study of antimatter [40,41]. In contrast to buffer-gas cooling, temperatures achievable with Doppler laser cooling [36] are several orders of magnitude lower and only restricted by the Doppler cooling limit,  $T = \hbar\Gamma/2k_B$  [42]. Here,  $\hbar$  is the reduced Planck's constant,  $\Gamma$  is the atomic transition linewidth, and  $k_B$  is Boltzmann's constant. For instance, in singly charged magnesium ions, the cooling limit becomes  $T \approx 1$  mK when utilizing the D1 and D2 cooling transitions [43].

The beam quality of an ion bunch extracted from a Paul trap, expressed quantitatively as the ion beam emittance, scales with the temperature of the ion ensemble [44]. The relation between the temperature  $T$  of cooled, trapped ions and the longitudinal emittance of a subsequently extracted ion bunch can be quantified at the time-focus point in terms of the latter's energy spread  $\Delta E$  and temporal width  $\Delta t$ , following [21]

$$(\Delta E \Delta t)_{95\%} \approx 2\pi \ln(20) k_B T \sqrt{\frac{m}{2qC_2}}. \quad (1)$$

Here,  $m$  and  $q$  represent the mass and charge of the ions, respectively, while the trapping parameter  $C_2$  is related to the axial trap depth (for details, see Ref. [21]).

Next-generation experiments at RIB facilities will have increased demands on the quality of the RIBs. In this context, laser cooling could provide the necessary reduction of ion temperature for the formation of RIBs with hitherto unmatched qualities. By way of sympathetic cooling of cotrapped (radioactive) ions, this temperature reduction will not be limited to the few laser-coolable ions, but will lead to a universal availability of cold RIBs of any atomic or molecular species.

In this paper, we report on direct laser cooling of magnesium ions and sympathetic cooling of cotrapped atomic and molecular ions in a Paul-trap cooler-buncher with the goal of improving ion-beam emittance within a timescale that is compatible with experiments involving short-lived radioactive ions. To this end, we systematically study the properties of extracted ion bunches following laser and sympathetic cooling in the ion trap. Our results show a significantly reduced temporal ion-bunch width, indicating an improved longitudinal beam emittance with respect to room-temperature buffer-gas cooled ion bunches. The experimental results are in good agreement with accompanying three-dimensional (3D) cooling simulations of the experimental setup and procedures. In addition, these simulations are benchmarked against a one-dimensional (1D) numerical cooling model. Both tools, 3D simulation and the 1D model, are employed to extend the cooling dynamics beyond the experimentally accessible ion-bunch properties. Thereby, we are able to envision and study applications of this cooling method for various RIB experiments.

Laser-cooled ion bunches at RIB facilities will allow for an increased sensitivity in collinear laser spectroscopy experiments on exotic atoms or molecules [10,45–47]. Likewise,

this cooling scheme will increase the resolving power of mass measurements of radionuclides. First, we experimentally demonstrate the latter by inserting a laser-cooled ion bunch into a multireflection time-of-flight mass spectrometer (MR-ToF MS) [48–50], resulting in an improved mass-resolving power. Second, we simulate how this cooling technique can be used for the phase-imaging ion-cyclotron resonance (PI-ICR) method in Penning-trap-based mass measurements [51,52]. Here, the simulation results promise an improvement in precision of up to two orders of magnitude. Finally, we show, as an experimental validity check, that this cooling technique can also be used for measuring isotope shifts between different laser-coolable isotopes by observing the time-of-flight (ToF) width of the extracted ion bunches as a function of cooling-laser frequency.

Laser cooling at RIB facilities has been utilized for dedicated trapped-ion or atom experiments [2,53–58], but never, to our knowledge, for the delivery of high-quality (short-lived) ion beams. Like-minded applications of laser cooling have recently been pursued for improving the mass-resolving power  $R = m/\Delta m$  for ToF mass separation of stable nuclides [59–62]. Our paper distinguishes itself in two aspects: First, we report on the improvement of  $R$  by another two orders of magnitude enabled by our unique combination of laser cooling and MR-ToF mass spectrometry. Second, and more importantly, we focus on laser-cooling applications of externally produced hot ions, as is the case for cooler bunchers at RIB facilities. More generally, our paper discusses the potential use of laser and sympathetic cooling for various RIB experiments and demonstrates the feasibility of cooling hot, energetic ions to few-Kelvin temperatures within time constraints imposed by experiments with short-lived radionuclides. We thus propose this technique for future cooling of RIBs. As demonstrated in the present paper, by utilizing an unmodified cooler buncher, many laser-cooling applications can be readily implemented in existing linear Paul traps at RIB facilities despite their original design being focused on buffer-gas cooling. In fact, buffer-gas cooling at low gas pressures followed by laser cooling represents an attractive combination to reduce the temperature of hot injected ions (demonstrated here for  $E > 7$  eV at the entrance of the Paul trap) to (sub-)Kelvin level within a timescale compatible with half-lives of radionuclides with  $T_{1/2} < 1$  s. We also note the significance of this step for future cold trapped-ion experiments at RIB facilities. Cooling techniques, analogous to the ones demonstrated in this paper, are critical prerequisites for laser-spectroscopy experiments on cold trapped ions with short-lived radioactive isotopes which aim to improve on the current precision frontier in nuclear structure or beyond-standard-model physics, as, for example, in fifth-force searches from precision isotope-shift measurements [63,64].

## II. EXPERIMENTAL SETUP AND METHOD

The main components of the experimental setup, sketched in Fig. 1, are two ion sources that provide low-energy beams of either magnesium ( $Mg^+$ ) or potassium ( $K^+$ ) ions and are connected via a quadrupole bender to a linear segmented Paul-trap cooler buncher, an MR-ToF device, and the laser

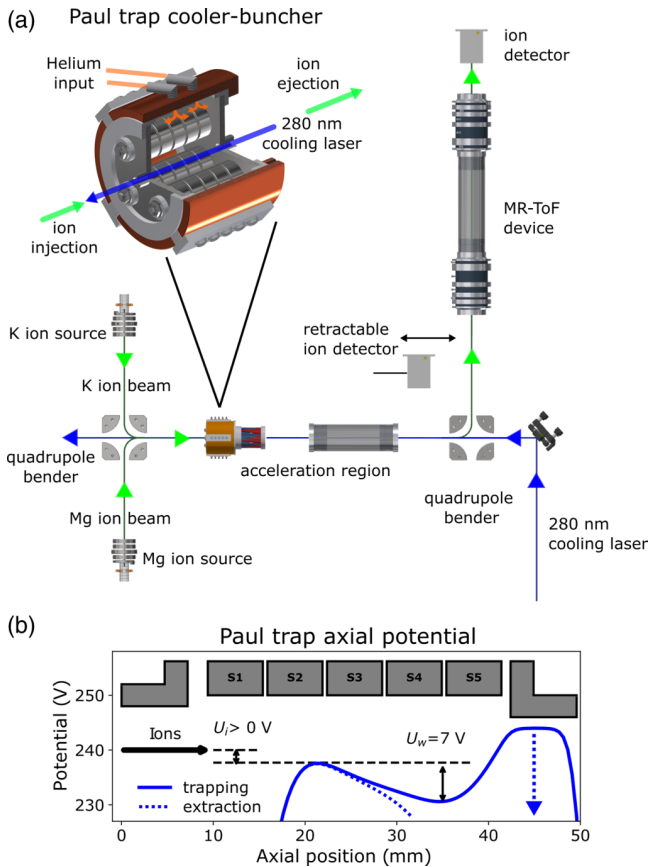


FIG. 1. (a) Layout of the experimental setup showing the main components with an enlarged, detailed view of the Paul trap cooler buncher. There,  $Mg^+$  ions are Doppler cooled by 280-nm laser light for direct or sympathetic laser cooling of other ions species. See text for details. (b) dc potential along the Paul-trap axis during trapping (solid blue) and extraction (dashed blue). The position of the individual dc trap electrodes is indicated in gray. The axial well depth  $U_w$  and ions' excess energy  $U_i$  are shown as vertical arrows.

system. This apparatus is part of the MIRACLS project at CERN-ISOLDE, detailed in previous publications [65–69].

Singly charged ions of stable magnesium isotopes,  $^{24,25,26}Mg^+$ , with relative natural abundances of approximately 80, 10, and 10%, respectively, are produced by electron-impact ionization of magnesium vapor from a resistively heated crucible [70], similar to Ref. [71]. The positively charged  $Mg^+$  ions are extracted from the ion source by a 240-V potential difference. When another species is co-trapped with the magnesium ions, they can either be ionized simultaneously in the same ion source or can be delivered by a separate surface ion source of the standard ISOLDE design [72–74]. The former is used in the case of dioxygen ions  $O_2^+$ , where the ion source is operated under different conditions and the latter is utilized for the production of singly charged potassium ions,  $K^+$ . After extraction from the ion source(s), the ions pass into a  $90^\circ$  electrostatic quadrupole bender which is controlled by high-voltage (HV) switches to selectively deflect ions from one of the two ion sources toward the Paul trap.

The Paul trap cooler buncher consists of four rods that provide the RF fields for radial ion confinement. They are each

split into five longitudinal segments of equal length to which additional dc voltages are applied to create an axial potential well. The characteristic Paul-trap dimension  $r_0$  of the minimum distance of the rod surfaces to the trap axis is 6.2 mm. The trap is operated in ac-only mode at an RF frequency of 2 MHz and voltage amplitude of 140 V. Surrounding the Paul trap electrodes is a grounded metallic housing for spatial confinement of the helium buffer gas as well as two end-cap electrodes with a 4 mm (2 mm) diameter aperture for injection (extraction) of ions.

An electrostatic steerer upstream of the Paul trap, controlled by a HV switch, acts as a beamgate; i.e., ions pass into the cooler buncher during a well-defined ion-loading time. This loading time typically ranges from  $10\ \mu s$  to 500 ms. Subsequently, the ion beam is deflected away from the ion trap's entrance. The period after ion injection, during which no additional ions are entering the trap, is referred to as cooling time.

In full analogy to cooler bunchers at RIB facilities, the Paul-trap electrodes are floated to a potential just below the ions' initial acceleration potential. This reduces the energy of the incoming ion beam to a few electronvolts at the entrance of the trap, i.e.,  $E = eU_i$  as illustrated in Fig. 1(b). The remaining energy is dissipated in the cooler buncher via room-temperature helium buffer gas cooling, laser cooling, or a combination of both. The ions are cooled into the bottom of the Paul-trap's potential well, which is in these studies typically  $U_w \approx 7$  eV below the potential barrier at the trap entrance, shown in Fig. 1(b). Thus, a total energy of  $E = e(U_i + U_w)$  has to be dissipated by the ion-cooling process before the equilibrium temperature is reached. Note that  $U_w$  in our application is of similar value to potential wells typically employed in cooler bunchers at RIB facilities.

A precision needle valve controls the flow of helium gas into the Paul trap to typical pressures ranging from a residual pressure of  $10^{-8}$  mbar, when the valve is closed, to  $10^{-5}$  mbar, as measured by a pressure gauge connected to the vacuum chamber housing the Paul trap. According to gas-flow simulations performed in Molflow+ [75], a helium pressure of  $10^{-5}$  mbar in the vacuum chamber corresponds to  $10^{-2}$  mbar inside the Paul trap, when helium is being leaked in.

When laser cooling is applied, a continuous-wave laser beam with a wavelength of 280 nm with typical laser powers of 0.25 to 20 mW and a diameter of 2 mm is directed into the Paul trap during the entire measurement sequence. Due to the lack of transversal optical access in the present setup, the laser direction is limited to the longitudinal axis of the Paul trap. For Doppler cooling, the frequency of the laser is set below the resonance frequency (i.e., red-detuned) of the  $3s\ ^2S_{1/2} \rightarrow 3p\ ^2P_{3/2}$  transition (D2 line) of the singly charged  $Mg^+$  ions. The addition of low-pressure buffer gas speeds up the initial ion-energy reduction from higher energies ( $>7$  eV at the point of injection) to energies at which laser cooling can be efficiently applied.

The laser light used for Doppler cooling of  $Mg^+$  ions is generated by the setup detailed in Ref. [65]. In short, a Spectra Physics 20 W Millennia eV laser (Nd-YAG) produces 532 nm laser light that pumps a Sirah MATISSE dye laser to create 560 nm output light. The latter is coupled into a high-power, large-mode-area 25-m-long optical fiber

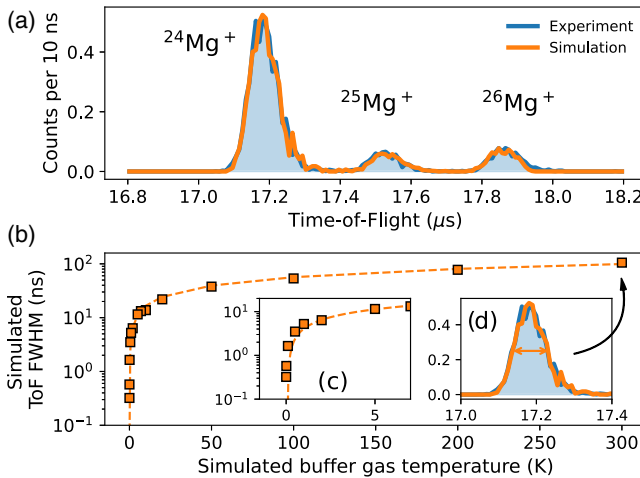


FIG. 2. (a) Time-of-flight spectrum of  $^{24,25,26}\text{Mg}^+$  ions from ion optical simulations including 300 K buffer-gas cooling (orange) and experimental data (blue). The simulation is normalized in intensity to the experimental data. (b) Simulated FWHM values of time-of-flight spectra as a function of buffer-gas temperature fitted to a square-root function (dashed orange line). (c) shows a zoom of (b) at lower temperatures. (d) shows a zoom of (a), with additional arrows indicating the FWHM and corresponding data point.

for transport of the laser light from the laser room to the ion-trap laboratory. Here, the second-harmonic laser light at 280 nm is generated utilizing a SIRAH WaveTrain-2 frequency doubler. The output of the doubler is then focused and directed along the axis of the Paul trap cooler buncher, where the Doppler cooling takes place. The wavelength meter (HighFinesse ANGSTROM WS/U-10) used in the experiment was calibrated with a reference wavelength provided by a stabilized diode laser (Toptica DL PRO 780). The laser linewidth of  $\sim 1$  MHz is small compared to the 41 MHz natural linewidth of the D2 line [43].

The  $\text{Mg}^+$  ions are cooled for the full duration of the time the ions spend in the trap. As a result of the cooling process, the ions end up close to the axial potential minimum near the ejection side of the Paul trap. The ion bunch is subsequently ejected, accelerated to an energy of 2.2 keV and directed toward the MR-ToF device by a second 90° quadrupole bender. The ions are detected on one of two MagneTOF ion-ToF detectors, positioned in front and behind the MR-ToF device. While the ions are stored in the MR-ToF device [48], they perform up to several thousand revolutions, being reflected back and forth between two electrostatic mirrors. This increases their overall flight time, during which ions of different masses separate. The three outermost mirror electrodes are passively stabilized and the second outermost one is additionally actively stabilized to reduce fluctuations in the ions' ToF as described in Refs. [76,77]. A more detailed description of the operational principles of MR-ToF devices can be found in Refs. [48,78].

An example of a ToF spectrum obtained after room-temperature buffer-gas cooling without trapping in the MR-ToF instrument is shown in Fig. 2(a). The ions' ToF values are depicted with respect to the extraction trigger of the Paul trap. The experimental data is compared to ion-optical simulations

of the ion trajectories in the Paul trap and subsequent ion transport following the procedures explained in Ref. [66]. Overall, the simulations yield excellent agreement with the experimental data.

The full width at half maximum (FWHM) of the ToF spectrum after ion extraction from the Paul trap cooler buncher is indicative of the temperature of the ion ensemble in the trap and closely follows a square-root dependence on temperature [50,79]. This was reproduced in ion optical simulations: The reduction of the buffer-gas temperature results in a reduced FWHM of the ToF peaks following the expected trend, as shown in Fig. 2(b). The FWHM of the ToF peak structures as measured on the ion detector is used in the following sections to compare buffer-gas and Doppler cooling.

### III. EXPERIMENTAL RESULTS

The effectiveness of Doppler cooling in reducing the ion-ensemble temperature below those achievable by room-temperature buffer-gas cooling becomes apparent in Fig. 3. Here, the experimental ToF spectra are presented for three cases: (1) He buffer gas cooling at 300 K and  $5 \times 10^{-7}$  mbar as measured in the surrounding vacuum chamber (green). Ions were loaded into the trap for a 100- $\mu\text{s}$ -long loading time and cooled for the duration of 500 ms, leading to a FWHM of the ToF spectrum of 100(8) ns. (2) Neither buffer-gas nor laser cooling of the ion bunch, with only the background residual gas present in the system at a pressure of  $3 \times 10^{-8}$  mbar (orange). Due to the reduced capture efficiency with respect to standard buffer-gas cooling, the loading time was adjusted to 10 ms. The FWHM after extraction of the ion bunches was 103(10) ns. (3) Doppler cooling with an on-axis laser of 6 mW in the presence of the background residual gas (blue), performed under the same conditions as for the residual-gas cooling data alone. In this case, the cooling laser was detuned by  $-150$  MHz with respect to the D2 transition frequency in  $^{24}\text{Mg}^+$  ions and applied for the full duration of the cooling

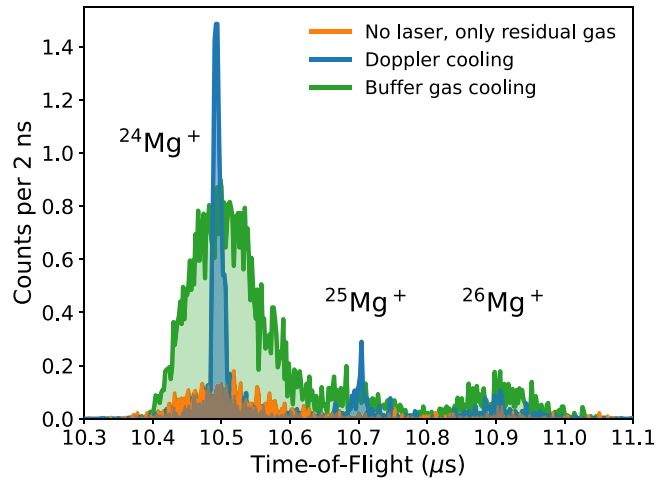


FIG. 3. Time-of-flight spectrum of  $^{24,25,26}\text{Mg}^+$  ions after extraction from the Paul trap cooler-buncher as measured on the retractable ion detector in front of the MR-ToF device using Doppler cooling (blue), buffer-gas cooling (green), and residual gas cooling (orange).

time of 500 ms after injection as described in Sec. II. A reduction in FWHM from 100(8) ns for buffer-gas cooling to 12(1) ns for laser cooling is obtained for  $^{24}\text{Mg}^+$  ions. According to the results of the ion-thermometry simulations in Fig. 2, a buffer gas of 6 K would be required to achieve a similar ToF width as obtained with Doppler cooling in this example.<sup>1</sup> In addition, ion-optical simulations show that, by optimizing the ion-acceleration section downstream of the Paul trap, a ToF spread of 4(1) ns would be achievable under the same experimental conditions for laser-cooled ion bunches. The time spread of buffer-gas cooled ions would barely be affected by these changes and, in the simulation, result in a ToF spread of 107(4) ns for the optimized acceleration potentials compared to 105(4) ns for the experimentally used ones.

### A. Cooling systematics

The theoretical photon scattering rate of ions at rest for different detuning frequencies with respect to  $^{24}\text{Mg}^+$  ions is shown in Fig. 4(a). For  $^{24,25,26}\text{Mg}^+$  ions, the area of each peak is scaled to their natural abundance ratio and single-transition, angular-momentum coupling estimates of transition intensity (i.e., Racah transition intensities). The width of all peaks corresponds to the natural line width of 41 MHz [43]. The insert shows the relevant transitions for  $^{24,26}\text{Mg}^+$  and  $^{25}\text{Mg}^+$  ions in blue and orange colors, respectively.

Since Doppler cooling is based on red-detuning of the cooling laser from the transition frequency and all three stable isotope species of magnesium are co-trapped in the Paul trap cooler buncher during the cooling process, the isotope shift  $\delta\nu^{A,A'} = \nu^{A'} - \nu^A$  between them determines that each isotope will experience a different frequency detuning. This implies that at a fixed laser frequency, the different isotopes show varying photon scattering and thus cooling rates. Additionally, the only stable magnesium isotope with nuclear spin  $I \neq 0$  is  $^{25}\text{Mg}$  ( $I = 5/2$ ), where the hyperfine interaction gives rise to six hyperfine levels, as shown in the insert of Fig. 4(a).

By scanning the frequency detuning of the cooling laser, the effect of the differing cooling rates for  $^{24,25,26}\text{Mg}^+$  ions becomes apparent, indicated by the width of the corresponding ToF signals shown in Fig. 4(b). The influence of increased laser power and cooling time are shown in Figs. 4(c) and 4(d), respectively. For all experimental results shown here, a residual gas pressure of  $\approx 10^{-8}$  mbar was measured in the vacuum chamber.

From Fig. 4(c), it becomes apparent that an increased laser power for a fixed frequency and cooling time has a positive effect on the number of laser-cooled ions. At intermediate laser powers, we observe a distinct separation of laser-cooled ions, represented by a narrow ToF width on top of a wide ToF distribution due to hot ions. The latter is of similar

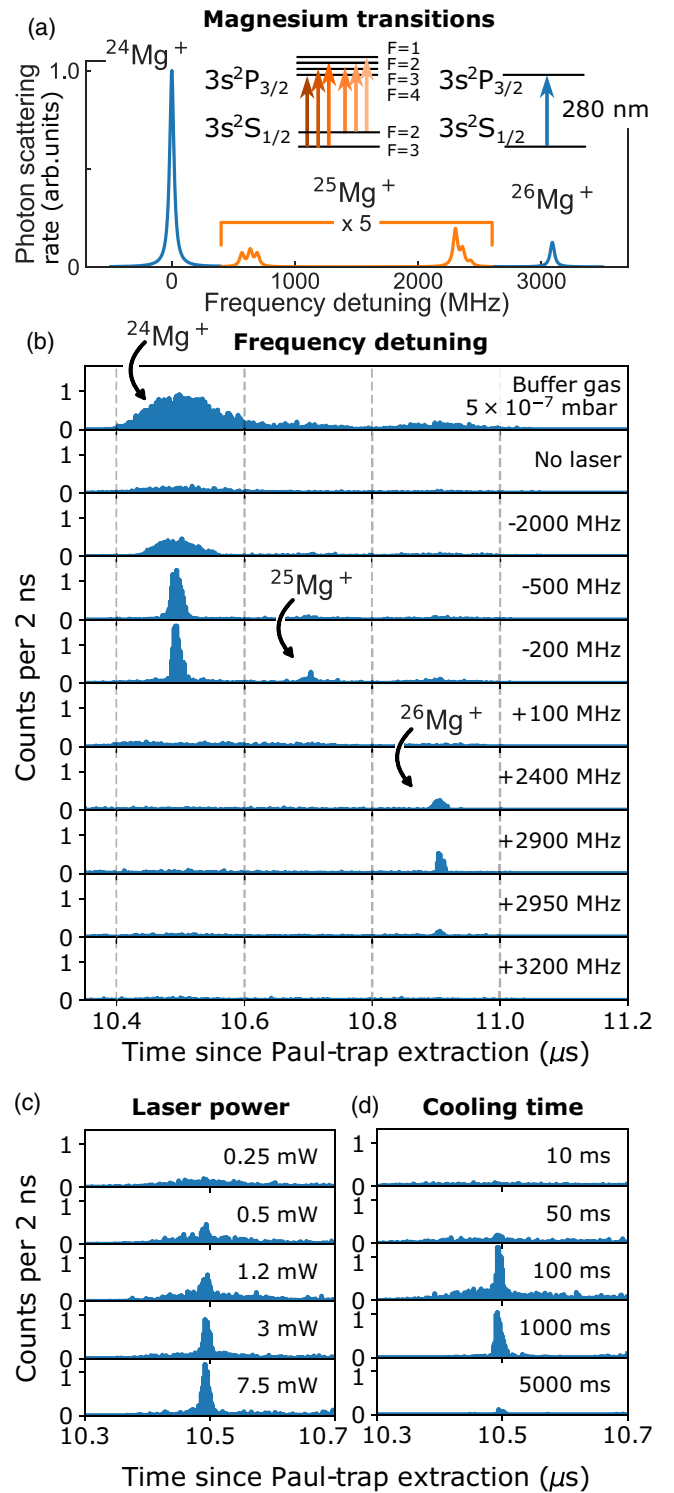


FIG. 4. (a) Photon-scattering rates calculated as a function of laser-frequency detuning from the D2 transition in  $^{24}\text{Mg}^+$  ions. ToF spectra for laser-cooling systematics at residual gas pressures as a function of (b) laser detuning at 3 mW and 500 ms cooling, (c) laser power at 200 ms cooling and  $-200$  MHz detuning, (d) cooling time at 3 mW and  $-200$  MHz detuning, as measured on the first, retractable ion detector.

<sup>1</sup>We note that the ion optical simulations indicate that the time-focus point for cooling at varying buffer-gas temperatures and laser-cooled ions occur at different spatial positions. Thus, the comparison of the ToF widths for different cooling schemes at a fixed detector position may provide an incomplete picture. In fact, the energy distribution of the simulated laser-cooled ions suggests that the (longitudinal) ion-cloud temperature is actually  $< 1$  K.

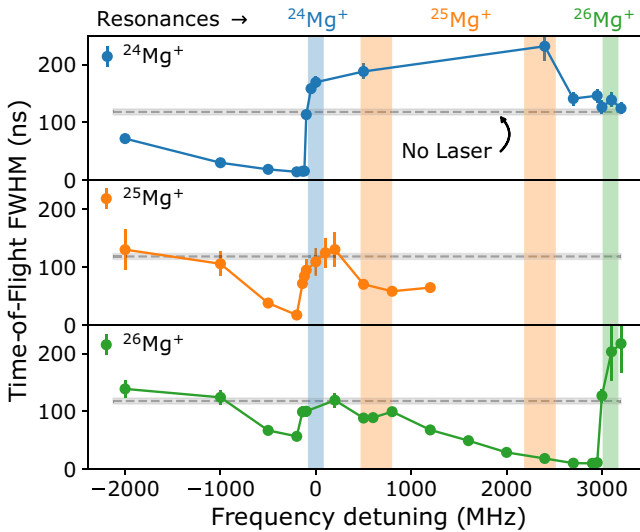


FIG. 5. FWHM of the time-of-flight spectra for  $^{24,25,26}\text{Mg}^+$  ions as a function of laser-frequency detuning with respect to the D2 transition in  $^{24}\text{Mg}^+$  ions. Resonance frequencies for  $^{24,25,26}\text{Mg}^+$  are represented as colored bands.

width as in the case of buffer-gas or residual-gas cooling, which indicates that these ions have experienced only a few absorption-emission cycles, if any. When the laser power is increased from 0.25 mW to 7.5 mW, the total ion count rate stays nearly constant at 12 counts per bunch while the fraction of laser-cooled ions increases significantly from 1.6 to 7.5 counts per bunch. The cooling time variation shown in Fig. 4(d) shows similar behavior; laser cooled ions are first observed for cooling times as low as 50 ms. With increasing cooling time, the fraction of laser-cooled ions becomes larger while the background of noncooled ions decreases. Cooling longer than 1 s increases the overall ion losses, most likely due to collisions or charge exchange with residual gas atoms.

When the laser is red detuned with respect to the ion species' respective transition frequencies, Doppler cooling takes place and the FWHM of the ToF signal drops for each magnesium isotope. Trapped ions interacting with a blue detuned laser frequency experience heating. This effect is observed as a sudden increase of the FWHM in measured ToF signals to values larger than without laser-ion interaction. Both effects of laser cooling and heating are visible in Fig. 5, where the width of the ToF peaks extracted from Gaussian fits of the ToF spectrum is shown as a function of frequency detuning for each of the three magnesium isotopes.

The cooling effect is observed below the transition frequencies, indicated as vertical colored bands, as the FWHM sinks below the gray reference line, i.e., the ToF width without any laser beam present. The hyperfine splitting in the D2 transition in  $^{25}\text{Mg}^+$  ions complicates the laser interaction with this isotope as the ion population is transferred between the two hyperfine levels of the  $3s\ ^2\text{S}_{1/2}$  fine structure state. Hence, laser cooling can proceed exclusively with a single laser frequency if it is red detuned to all six transitions in the D2 line, albeit at a reduced cooling rate. This might (partially) explain the higher ToF width at frequencies close to the

lower-frequency multiplet compared to the other magnesium isotopes on their respective resonance frequencies.

The FWHM increase due to heating is visible in Fig. 5 when the laser frequency is varied from below to above the resonance frequency around 0 MHz and  $+3000$  MHz for  $^{24}\text{Mg}^+$  and  $^{26}\text{Mg}^+$  ions respectively. Because of the shift in resonance frequency for different isotopes, a single laser frequency can be blue detuned for one species, but red detuned for another. It is thus possible for a laser to heat  $^{24}\text{Mg}^+$  ions while cooling  $^{25,26}\text{Mg}^+$  ions. This is the case for frequency values between 0 and  $+3000$  MHz in Figs. 4(a) and 5. However, the cooling of  $^{26}\text{Mg}^+$  ions is strong enough to overcome the interaction with the heated  $^{24}\text{Mg}^+$  ions. This is seen from the reduced ToF FWHM values at detuning frequencies closer to the resonance frequency of  $^{26}\text{Mg}^+$  ions, i.e., from  $+1000$  MHz to  $+3000$  MHz in Fig. 5. The data for  $^{25}\text{Mg}^+$  are limited to the region up to 1200 MHz. Above that value, laser heating of  $^{24}\text{Mg}^+$  ions leads to its signal overlapping with  $^{25}\text{Mg}^+$  ions which prevents a reliable determination of the latter's ToF width.

Because of the simultaneous trapping of all magnesium isotopes, laser-heated  $^{24}\text{Mg}^+$  ions may also influence the temperature of cotrapped  $^{25,26}\text{Mg}^+$  ions through ion-ion interactions. In particular, a clear cooling feature for all isotopes is observed on the red-detuned side of the transition frequency of  $^{24}\text{Mg}^+$  ions, likely indicating sympathetic cooling of  $^{25,26}\text{Mg}^+$  ions induced by the more abundant  $^{24}\text{Mg}^+$  ions. Indeed, the ToF width reduction in  $^{25,26}\text{Mg}^+$  ions as shown in Fig. 5 is close to the one found for  $^{24}\text{Mg}^+$  ions. This would not be expected for direct laser cooling of  $^{25}\text{Mg}^+$  ions at this detuning frequency. Nevertheless, contributions due to direct laser cooling of  $^{25,26}\text{Mg}^+$  ions at a less efficient cooling rate cannot be excluded.

## B. Sympathetic cooling of $\text{K}^+$ and $\text{O}_2^+$ ions

Since Doppler cooling requires a closed level system, its applicability is limited to isotopes with a suitable ionic level structure. This would limit the technique to only a select number of ion species. As already indicated by the results of the previous section, this restriction can be overcome by sympathetic cooling, where cotrapped ion species are cooled down through interactions with laser-cooled trapped ions. Indications of sympathetic cooling of  $^{25,26}\text{Mg}^+$  are present in Fig. 5. However, as pointed out above, we cannot exclude a potential contribution of direct Doppler cooling of  $^{25,26}\text{Mg}^+$  ions. As demonstration of the sympathetic cooling technique in the present apparatus, either potassium  $\text{K}^+$  ions or molecular oxygen ions  $\text{O}_2^+$  were thus cotrapped with laser-cooled  $^{24}\text{Mg}^+$  ions. For laser powers, cooling times, and buffer-gas pressures similar to those described above, we observe a clear increase in trapping and cooling efficiency of both co-trapped species as shown in Fig. 6.

As expected, the final temperature reduction for similar cooling times and laser powers is not as high as in the case of direct Doppler cooling. Nevertheless, we observe a reduction in ToF FWHM for  $^{16}\text{O}_2^+$  ions from 113(5) to 58(4) ns and for  $^{39}\text{K}^+$  ions from 180(13) to 145(5) ns. Additionally, the number of trapped ions per bunch increases by a factor of 2.6 for oxygen and a factor of 2 for potassium. In the present paper,

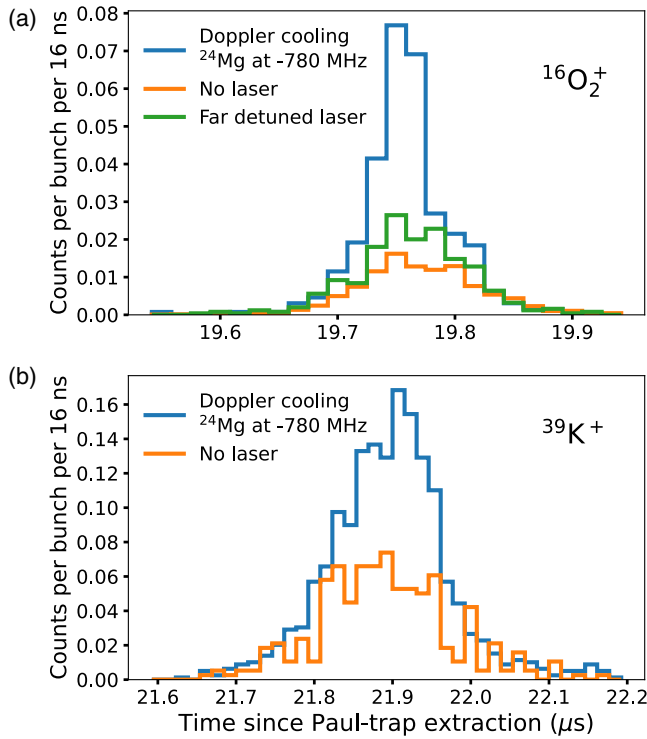


FIG. 6. Sympathetic cooling of molecular oxygen,  $^{16}\text{O}_2^+$ , and atomic potassium,  $^{39}\text{K}^+$  ions. Sympathetic cooling of oxygen at 800 ms loading time and 600 ms cooling time with 20 mW of laser power. Same settings for potassium. See text for details.

sympathetic cooling experiments have been limited by reliable tuning of the intensity ratios of injected isotope species. With further improvements, sympathetic cooling performance similar to the results in more specialized work [80,81] can be expected. This way, ion temperatures approaching the one of the directly Doppler cooled ions are expected. Monitoring the cooling dynamics of the ions using a photon detector, not available in this work, could provide additional guidance in such a program. However, the present results already show that sympathetic cooling of atomic and molecular ions is applicable at RIB facilities.

#### IV. COOLING SIMULATIONS AND MODEL

##### A. Ion optical simulations

The trajectories of trapped magnesium ions are simulated using the ion-optical software package SIMION 8.2 [82]. The simulations include ion dynamics inside the Paul trap, subsequent ejection from the trap, and transport up to the ion detector, similarly to the implementation in Ref. [66]. To obtain an initial ion distribution for laser-cooling simulations, ions are first left to thermalize in a room-temperature buffer gas modeled by SIMION's hard-sphere interaction HS1 [83]. The ion ensemble obtained at the end of this simulation is then used as a starting point for further laser-cooling simulations, also performed with SIMION.

The laser-cooling simulation starts with the prethermalized magnesium ions already inside the cooler buncher. The effect of the laser-ion interaction on trapped-ion dynamics

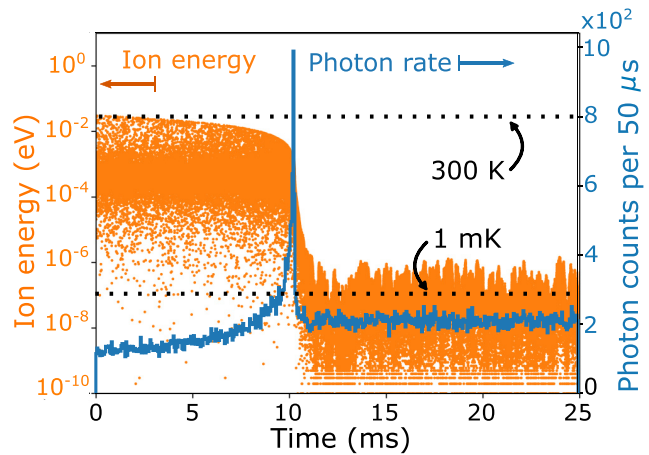


FIG. 7. Simulated energy for a single  $^{24}\text{Mg}^+$  ion (orange) at each time when a photon-ion interaction takes place. The photon scattering rate per  $50\ \mu\text{s}$  (blue) is indicated on the right y axis. The simulation is performed for an ion with 0.03 eV initial energy being cooled by a 200 MHz red-detuned cooling laser with 25 mW power and 2 mm diameter.

is modeled in a semiclassical Monte Carlo manner. At each time step of the simulation, the ion's instantaneous velocity with respect to the laser-beam direction was used as an input parameter for a calculation of the Doppler-shifted frequency detuning from resonance  $\Delta$ , i.e., the laser-frequency detuning from resonance as perceived by the ion, as well as the photon scattering rate [42],

$$\mathcal{R}(\Delta) = \frac{\Gamma}{2} \frac{I/I_{\text{sat}}}{1 + I/I_{\text{sat}} + 4\Delta^2/\Gamma^2}, \quad (2)$$

where  $\Gamma$  is the transition width,  $I$  is the laser power density, and  $\tau = \Gamma^{-1}$

$$I_{\text{sat}} = \frac{\pi}{3} \frac{hc}{\lambda^3 \tau} \quad (3)$$

is the saturation power density of the transition,  $h$  represents Planck's constant,  $c$  the speed of light, the transition wavelength is given by  $\lambda$  and the lifetime  $\tau = \Gamma^{-1}$  [42]. The calculated scattering rate is converted into a photon-ion interaction probability. A random number generator signals a photon event when the returned value is smaller than the interaction probability. In such an event, the photon momentum is subtracted from the magnesium ion momentum in the direction of the absorption. The momentum kick due to the re-emission of a photon is set to be prompt and in a random direction. Stimulated emission of photons is not taken into account.

An example of the result of the kinetic-energy evolution of a single trapped ion and photon scattering rate as a function of time are shown in Fig. 7. Here, an ion with initial energy of 0.03 eV interacts with a 25-mW and 2-mm diameter laser beam that is red detuned by  $-200\ \text{MHz}$  in the absence of buffer gas. In Sec. V B 1, examples will be presented where buffer gas is included as well. Each point on the ion-energy scatter plot represents the ion energy at the time of interaction with a laser photon. The blue curve represents the instantaneous photon scattering rate. The largest drop in ion energy

takes place in a short time range when the overlap between ion energy and laser-frequency detuning matches. This coincides with a maximal photon scattering rate, seen as a distinct photopeak under the right cooling conditions.

### B. Numerical cooling model

A second approach to describing the cooling dynamics models the energy evolution and photon scattering rate of a trapped ion being laser cooled in the presence of a buffer gas using a 1D numerical approach. Here, Doppler cooling of a single trapped ion in the weak binding regime [32], where  $\Gamma$  is larger than the oscillation frequency in the ion trap, is assumed [84] and buffer-gas cooling is added as an exponential decay term to the equation describing the ions energy evolution as a function of time [85]. The model applied in these simulations and the equations shown in this section were adopted from Refs. [84,85]. This 1D numerical model does not take into account any micromotion or RF-heating effects in the Paul trap, nor does it consider ion-ion interactions or stimulated emission effects.

The ion energy is determined by numerically solving a differential equation in reduced variables for ion energy  $E$ , frequency detuning  $\Delta$ , and recoil energy  $E_r = (\hbar k)^2/(2m)$  as  $\{\varepsilon, \delta, r\} \equiv \{E, \hbar\Delta, E_r\}/E_0$ , where  $E_0 \equiv \hbar\Gamma\sqrt{1+s_0}/2$ , and  $\Gamma\sqrt{1+s_0}$  describes the power-broadened linewidth with the saturation parameter  $s_0 = I/I_{\text{sat}}$ . The variation of the reduced energy  $\varepsilon$  is described with respect to a reduced time  $\mathcal{T} = t/t_0$ , where  $t$  denotes time and  $t_0 = (\frac{\Gamma}{2}\frac{s_0}{1+s_0})^{-1}$ . The differential equation describing the energy evolution is given by

$$\begin{aligned} \frac{d\varepsilon}{d\mathcal{T}} = & -\gamma(\varepsilon - \varepsilon_1) + \frac{4}{3}r\frac{1}{2\sqrt{\varepsilon r}} \text{Im}(Z) \\ & + \frac{1}{2\sqrt{\varepsilon r}}(\text{Re}(Z) + \delta \text{Im}(Z)), \end{aligned} \quad (4)$$

with  $Z = i\sqrt{1 - (\delta + i)^2/4\varepsilon r}$ . The first term describes the buffer-gas interaction using the mobility  $\gamma$  [85,86] and the difference between instantaneous reduced energy  $\varepsilon$  and the reduced energy attainable by buffer gas cooling  $\varepsilon_1 = k_B T/E_0$ . The second term describes the stochastic recoil heating effect after photon emission, while the final term is used to model the laser-ion interaction. The fluorescence photon emission rate is given by

$$\frac{dN}{d\mathcal{T}} = \frac{1}{2\sqrt{\varepsilon r}} \text{Im}(Z). \quad (5)$$

The derivation of this equation is described in Appendix A of Ref. [84]. In contrast to Sec. IV A, where the laser-ion interaction was only included after room-temperature buffer-gas thermalization, Fig. 8 shows the energy evolution and photon scattering rate as a function of time for a  $^{24}\text{Mg}^+$  ion with 10 eV initial energy being cooled simultaneously by a 300 K helium buffer gas at  $1 \times 10^{-5}$  mbar and a 200 MHz red-detuned cooling laser with 25 mW of laser power and 2 mm diameter. The mobility of magnesium ions in helium buffer gas is taken as  $2.3 \times 10^{-3} \text{ m}^2 \text{ s}^{-1} \text{ V}^{-1}$  [85,87].

The initial cooling is dominated by the exponential buffer-gas cooling effect until the ion velocity distribution matches the laser detuning frequency and Doppler cooling becomes

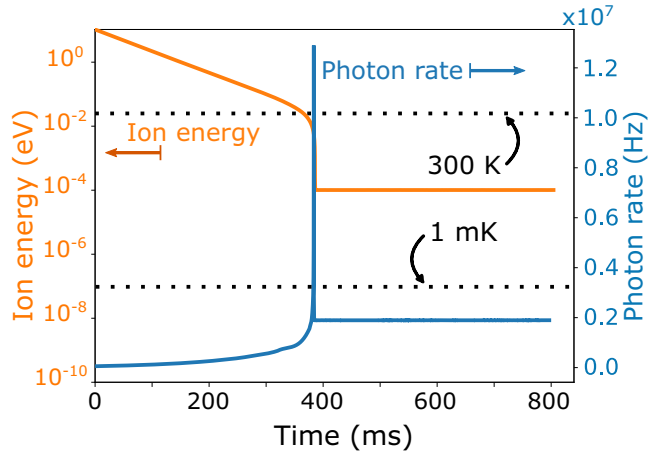


FIG. 8. Calculated energy for a single  $^{24}\text{Mg}^+$  ion (orange) and instantaneous photon scattering rate (blue) as a function of time for an ion with 10 eV initial energy being cooled by a 300 K helium buffer gas at  $10^{-5}$  mbar and a 200 MHz red-detuned cooling laser with 25 mW power and 2 mm diameter.

very efficient. This point is indicated by the photon fluorescence peak around 0.38 s in Fig. 8. This agrees well with the experimental data as shown in Fig. 4(d), where a significant fraction of the ions is cooled within 100 ms, considering the limited knowledge of the exact initial ion energies, buffer-gas pressure, and laser-ion overlap in experimental conditions. Under similar conditions, but in the absence of buffer gas, the photopeak would occur only after 137 s according to the numerical cooling model.

This indicates the importance of the background buffer gas in reducing the overall cooling time of the ion. The cooling times in the absence of a buffer gas would be prohibitively long for use at RIB facilities. The limit of 300 K in the case of buffer-gas cooling is indicated by the horizontal dashed lines in Figs. 7 and 8. The final energy reachable according to this numerical model is a balance between the buffer-gas and laser-cooling effects and depends on variables such as buffer-gas pressure, temperature, laser frequency detuning, and power density.

The findings in Refs. [84,85] show that laser cooling is most efficient when the laser-frequency detuning corresponds to half the width of the velocity distribution of the ions. As an alternative for speeding up the cooling process of hot trapped ions using low-pressure buffer gas, one could in principle use a fast-scanning laser that matches the ions' instantaneous velocity distribution [88]. With a fixed laser frequency and no added buffer gas, laser cooling of a 10-eV magnesium ion would take  $>100$  s. However, according to the numerical cooling model, matching the laser-frequency at every moment in the cooling process would reduce this time down to  $<50$  ms. This would require a laser with output power of 25 mW to chirp the laser frequency in a controlled manner over a range from  $-32$  GHz detuning down to near 0 MHz detuning within 50 ms according to the time dependence as shown in Fig. 9. In this small time-step calculation, the frequency detuning was adjusted to the optimal one for the ion's instantaneous energy. This allows for a high photon scattering rate and strong ion-energy reduction during the full cooling time.

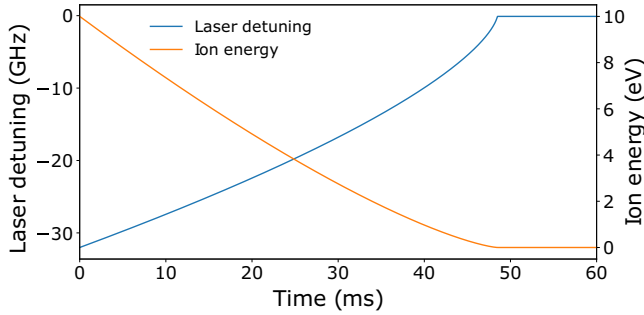


FIG. 9. Optimal laser-frequency detuning (blue) and corresponding ion energy (orange) as a function of time needed for cooling down a 10 eV  $^{24}\text{Mg}^+$  ion in absence of a buffer gas as obtained from the 1D numerical model.

### C. Comparison of both approaches

Results of the laser interaction introduced in ion-optical Monte Carlo simulations were benchmarked against the 1D numerical cooling model without buffer gas as shown in Fig. 10. In this comparison, the initial position and velocities of ions in the simulation were fixed to the axial direction of the Paul trap cooler buncher to reduce SIMION's 3D model to 1D only. Both the ions' kinetic energy, starting from 0.03 eV and the photon scattering rates are presented for different laser-frequency detuning settings. The agreement between the two methods, despite their different modeling, is excellent.

As can be seen from Fig. 10, the time needed for cooling the ions strongly depends on the laser frequency: The cooling efficiency for red-detuned laser frequencies depends on the photon-scattering probabilities over time. In the absence of a frequency-detuning, the ion energy remains unaffected [Fig. 10(a)]. Data in Figs. 10(b)–10(d) showing the laser-cooling effect of red-detuned laser frequencies of  $-20$ ,  $-200$ ,

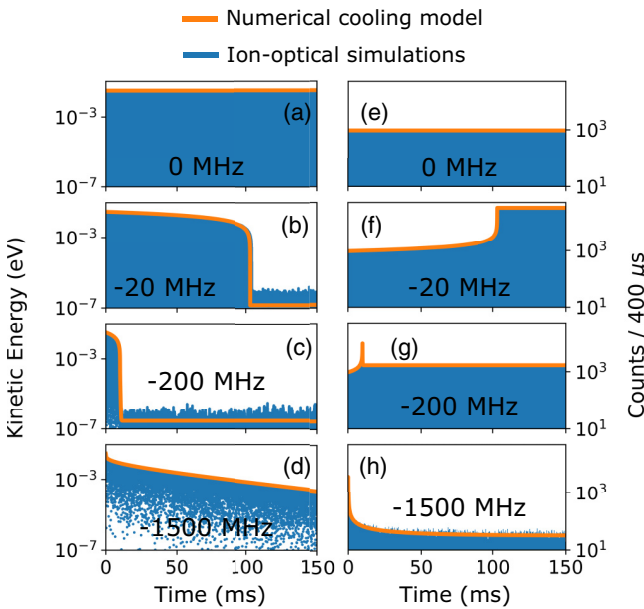


FIG. 10. (a)–(d) Kinetic energy and (e)–(h) scattered photon rate for the 1D numerical model (orange) and ion-optical simulations (blue) as a function of time for different laser detuning frequencies.

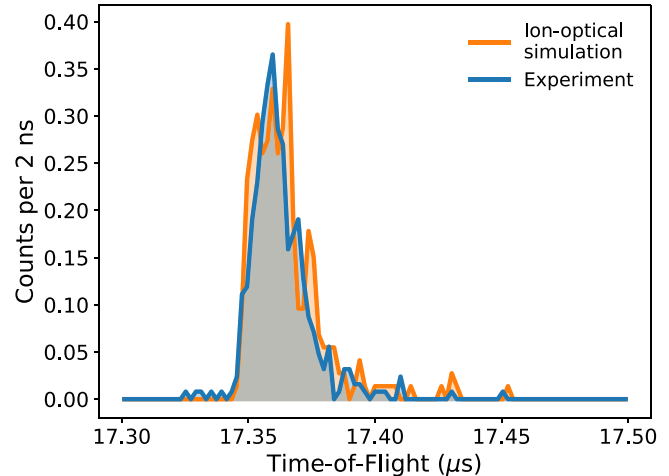


FIG. 11. Time-of-flight spectrum of Doppler-cooled  $^{24}\text{Mg}^+$  ions. The experimental data are compared to ion-optical simulations. Both are obtained for a laser frequency detuning of  $-600$  MHz with respect to the D2 transition, a laser power of 25 mW, and a cooling time of 150 ms. No residual gas is considered in the simulation. The only free simulation parameters are the ToF offset and the ion intensity, which were matched to experiment for better comparison.

and  $-1500$  MHz indicate a significant cooling-time difference. This agrees with the experimental observations from Sec. III, where the laser-detuning frequency is identified as a key parameter for laser cooling efficiency.

### D. Experimental benchmark of simulation and model

To evaluate the quality of the 3D ion-optical simulation, its results in terms of obtained ToF distributions are compared to experimental data. Under varying experimental conditions, ions are cooled, extracted from the Paul trap, and their flight time recorded at the position of the ion detector, see Fig. 1. Previous studies established good agreement between experiment and simulation when exclusively buffer-gas cooling is performed [66]. This conclusion is confirmed by the present paper, see for instance Fig. 2(a). An example of a ToF distribution for Doppler-cooled  $^{24}\text{Mg}^+$  ions is shown in Fig. 11. The simulated data reproduces the shape and width of the experimental ToF peak, including a tail toward longer times. This provides evidence for the validity of our simulation approach when also considering the laser-ion interactions.

A more comprehensive comparison is given in Fig. 12. It summarizes the obtained FWHM of ToF spectra such as the one shown in Fig. 11 when varying the laser frequency detuning. Here, the experimental data are compared to results of (a) the numerical cooling model and (b) ion-optical simulations, where the effect of buffer-gas and laser cooling are simultaneously included for both. To reduce the computation time, both approaches start from room-temperature ions that are subsequently cooled by a laser with a saturation parameter  $s_0 = 3.27$  for the duration of 150 ms. This differs from experiment, where the ions are injected into the cooler buncher with an estimated initial energy of  $>7$  eV and are cooled for 600 ms. Note that, in the simulation, the exact cooling time has no influence on the results, provided that the equilibrium state

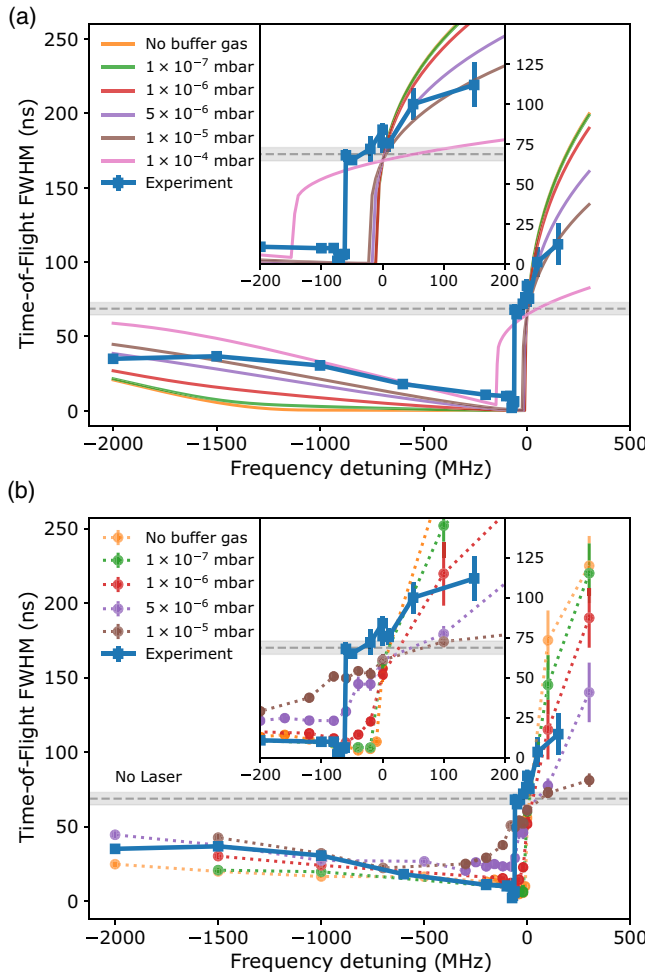


FIG. 12. Width of the experimental ToF signal of  $^{24}\text{Mg}^+$  ions as a function of the cooling-laser frequency at a residual buffer-gas pressure of  $1 \times 10^{-8}$  mbar. Experimental data are shown as blue squares. Results from (a) the numerical model described in Sec. IV B and (b) ion-optical simulations described in Sec. IV A for different buffer-gas pressures. To obtain (a), the ion temperature obtained from the 1D Model is translated into a ToF width by employing the found relationship of Fig. 2(b). For reference, the experimental ToF width without injecting the laser beam into the Paul trap is shown as a grey band.

has been reached. This can also be seen in Figs. 7 and 8, where the ion energy remains constant once the cooling equilibrium is obtained.

As indicated in Fig. 12, the results of the 1D model and 3D simulation qualitatively agree with the experiment over the entire frequency range. As the most prominent feature in the data, a strong increase in the FWHM of the ToF signals the change from laser cooling to laser heating. This effect is clearly visible in the experimental data as well as in the 1D model and 3D simulation when low residual gas pressures are used. If the laser frequency matches the transition frequency of the D2 line exactly, the laser has no net effect on the ion energy [Figs. 10(a) and 10(e)]. Thus, at this frequency, all curves in Fig. 12(c) cross the grey band which represents the experimental ToF width for room-temperature buffer-gas

cooling without a laser injected into the Paul trap. This is also the case for the experimental data, but the sharp increase in the ToF width is shifted by a few tens of megahertz to red-detuned laser frequencies, see inserts of Fig. 12. This is attributed to potentially two reasons. First, the accuracy of the employed wavelength meter for the 560 nm fundamental laser light is 30 MHz, given the used calibration wavelength. This leads to a 60 MHz uncertainty on the absolute frequency of the cooling laser. Second, incomplete ion cooling before reaching equilibrium or the presence of residual gas smear out the otherwise sharp cooling-heating transition. The latter effect can be seen in both the 1D model as well as the 3D simulation for pressures exceeding  $\sim 1 \times 10^{-5}$  mbar, although the exact shape of this transition differs slightly in the two methods.

More generally, the buffer-gas interactions reduce the effect of the laser-cooling. This is also visible on the red-detuned, laser-cooling side. It results in a higher ToF FWHM when buffer-gas interactions are included in simulations and the opposite effect is present for a blue-detuned laser frequency. Far from the transition frequency, where the relative importance of buffer-gas cooling is the largest, 3D ion-optical simulations agree better with experimental findings than the 1D numerical model. This is likely due to the more accurate implementation of buffer-gas cooling by use of the hard-sphere modeling.

In summary, both the 1D model and 3D simulations reproduce the experimental ToF data, which indicates that the relevant cooling physics is well captured. This provides confidence that other ion-bunch properties, not accessible in experiment, can be reliably studied by means of the developed cooling models. Moreover, the same tools can be employed to evaluate the implications of laser cooling of RIBs for specific experiments.

## V. EXPERIMENTAL APPLICATIONS

The technique for cooling an ion ensemble using a combination of low-pressure background gas and laser cooling as presented here is beneficial for many RIB applications. Such applications using short-lived radioactive ions include, for instance, trapping and laser or sympathetic cooling for high precision spectroscopy, (collinear) laser spectroscopy on atomic and molecular ions, or mass measurements.

### A. Mass spectrometry

#### 1. Demonstration of an improved mass-resolving power in a multireflection time-of-flight device

To demonstrate the improved beam emittance and the potential use for mass measurements at RIB facilities, Doppler-cooled ion bunches are injected into a 1.5-keV MR-ToF device [65–69] and the mass-resolving power after laser cooling is compared with buffer-gas and residual-gas cooled ions. To this end, the mass-resolving power  $R$  is investigated as a function of storage duration in the MR-ToF spectrometer. The obtained data shown in Fig. 13 is compared to a fit using the following equation:

$$R_{N_a} = \frac{m}{\Delta m} = \frac{t}{2\Delta t} = \frac{t_0/N_a + t_a}{2\sqrt{\Delta t_a^2 + (\Delta t_0/N_a)^2}}, \quad (6)$$

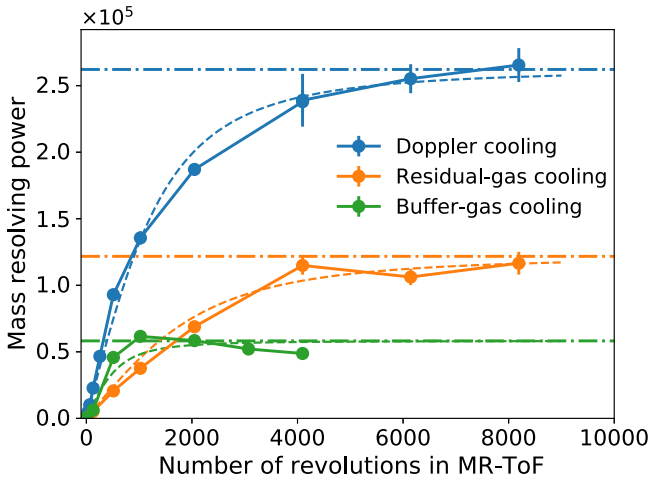


FIG. 13. Mass resolving power for the  $^{24}\text{Mg}^+$  ion signal as a function of storage time in the MR-ToF device for three different cooling mechanisms. Solid lines are fits of Eq.(6) to the data. Dashed lines denote the saturation resolving power  $R_\infty$ .

describing the mass-resolving power in an MR-ToF spectrometer [50]. Here  $N_a$  is the number of turns in the MR-ToF instrument and  $t_0 = 17.35 \mu\text{s}$  represents the time it takes for the ions to reach the ToF detector without trapping in the MR-ToF device.  $\Delta t_0$  denotes the FWHM of the ToF signal due to initial conditions (20 ns for laser cooling and 80 ns for buffer- and residual gas cooling) and  $t_a = 6.7 \mu\text{s}$  the period of a single revolution in the spectrometer, which are both measured.  $\Delta t_a$  describes the increment in ToF-distribution width induced during each period due to aberrations and was left as the only free fitting parameter.

For Doppler-cooled magnesium ions, an improvement of a factor 4.6 in mass-resolving power  $R_\infty$  from 57 000 for standard buffer-gas cooled ions to 261 000 was observed. A mass-resolving power of 50 000 is reached after 250 revolutions for laser cooling, which is five times faster than for residual gas cooling and 2.6 times faster than for standard buffer-gas cooling. We note in passing that the present limit of the mass-resolving power for buffer-gas cooled ions seems to be due to collisions between ions and residual gas in the MR-ToF device: Adding buffer gas in the cooler buncher increases the pressure in the MR-ToF region as well, where collisions increase beam losses, very similar to the effects described in Ref. [89]. Therefore, the mass-resolving power can only be determined up to about 30 ms of storage time, corresponding to roughly 4500 revolutions in the MR-ToF mass spectrometer. Additionally, if the cooling in the Paul trap is only due to collisions with residual-gas atoms, the pressure in the MR-ToF device is lower, and hence larger mass-resolving powers can be reached than for standard buffer gas cooling. The resolving power obtained for residual-gas cooled ions is  $R_\infty = 125 000$ . An adverse effect, on the other hand, is that the storage efficiency of magnesium ions in the Paul trap is strongly reduced for residual-gas cooling as compared with buffer-gas and Doppler cooling.

The ToF spread of an ion bunch in an MR-ToF device not only relies on the temperature of the ion ensemble but can also be affected by other variables such as the strength of

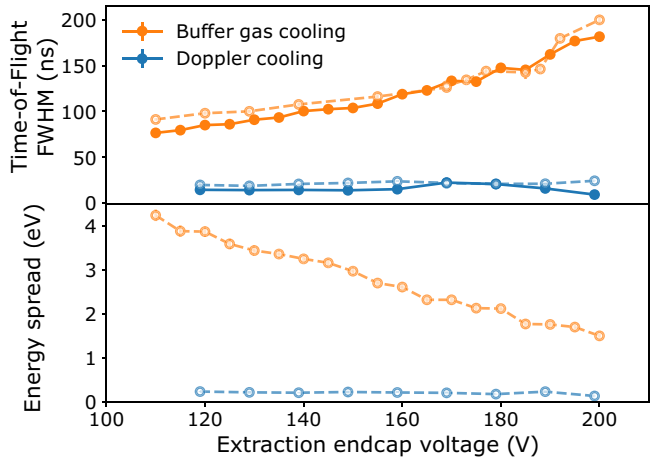


FIG. 14. Simulation (dashed) and experimental (full) ToF and energy-spread results for varying Paul-trap extraction field strengths of Doppler and buffer-gas cooled ions. Both observables are evaluated at the ion-detector position without trapping in the MR-ToF device.

the electric field used for extraction from the Paul trap [90] or whether the MR-ToF instrument is operated in a so-called isochronous mode [91]. In this mode, the MR-ToF electrode potentials are tuned to minimize the ToF dependence on ion energy. The measurements shown here were all performed in isochronous operation and using the same Paul-trap extraction field of about 2 V/mm.

We note that when minimizing the ToF spread by varying the extraction field from the Paul trap, a trade-off happens between ToF- and energy spread as emittance remains conserved. This is confirmed in the ion-optical simulations shown in Fig. 14. There it is shown that a reduction in ToF peak width by variation of the extraction field significantly increases the energy spread of the ions. Once the energy spread is too large and stretches beyond the isochronous region of the MR-ToF operation, the resulting mass-resolving power is eventually decreased.

The central advantage of laser cooling for MR-ToF mass spectrometry is that both the ToF and energy spread of the ion bunch are strongly diminished at the same time. Figure 14 illustrates the significant improvement in both ion-bunch properties by laser cooling over buffer gas. Once again, the experimental data on the ToF width are well reproduced by ion-optical simulation. Recalling that the longitudinal emittance equals to  $\Delta E \Delta t$  at the time-focus point, it is a consequence of the reduced overall ion-beam emittance facilitated by laser cooling which enables an improved MR-ToF performance as compared to standard room-temperature buffer gas.

## 2. Impact on phase-imaging-based Penning-trap mass spectrometry

Penning trap mass spectrometry is currently the most precise and accurate approach to determine the mass of charged particles, stable or radioactive [92]. It is based on the measurement of the cyclotron frequency of an ion confined in a strong and uniform magnetic field. Among the techniques

available for cyclotron frequency determination, the PI-ICR technique [52] provides a superior resolving power and precision compared to other techniques under typical experimental conditions. In essence, PI-ICR relies on measuring the phase evolution of an ion's motion inside the Penning trap. The ion is ejected from the Penning trap onto a position-sensitive detector, which enables the reconstruction of the phase of the motion and, thus, its cyclotron frequency. Accordingly, the mass-resolving power is directly proportional to the spatial spread of the ions hitting the detector [92]. Therefore, by reducing the ion beam's radial spread, the application of novel beam preparation and cooling techniques has the potential to greatly impact the precision and resolving power obtained through PI-ICR.

To verify the conceivable impact of the techniques described in this paper to PI-ICR measurements, we perform simulations of a hypothetical PI-ICR procedure where  $^{24}\text{Mg}^+$  ions are isotropically cooled to a given temperature inside the Paul trap employed in this experiment. The ions are sent to a Penning trap, where they are captured, accumulate a phase for a fixed amount of time, and are subsequently released toward a detector, where their spatial distribution is recorded. The Penning trap is modeled after the measurement Penning trap, operated by the TITAN Collaboration at TRIUMF [93], whose preceding simulations for employing the PI-ICR technique are described in Ref. [94]. The injection into the Penning trap is optimized for best trapping efficiency using an ion cloud of  $T = 300$  K as reference, and an analysis of the spatial distribution of ions hitting the detector is performed with several beam temperatures down to 1 mK, the Doppler limit for cooling  $^{24}\text{Mg}^+$  ions using the D2 line. It is important to note that PI-ICR's performance is highly reliant on the transversal emittance of the beam. Therefore, unlike the strictly longitudinal cooling performed in the experiment described in this paper, PI-ICR requires such cooling to be performed in all dimensions.

The results of the simulations are presented in Fig. 15. Overall, the FWHM of the detected beam image is proportional to the square root of the beam temperature. At 300 K, our simulations yield a beam spot FWHM of 1.75 mm, similarly as observed in well-established PI-ICR systems [52,95]. At sub-Kelvin temperatures, the beam spot FWHM is reduced by more than one order of magnitude, down to 220 times at 1 mK, which translates to a similar improvement in precision ( $\delta m/m$ ), not having considered possible systematic effects. The improvement in mass precision and resolving power in a PI-ICR measurement should scale accordingly until other uncertainty contributions become equally or more relevant, such as the detector's spatial resolution, and imperfections and instabilities of the ion extraction field.

## B. Laser spectroscopy

### 1. Demonstration of isotope shift measurements through observation of laser cooling-heating transition in time-of-flight measurements

The abrupt transition from laser cooling to laser heating takes place at the resonance frequency that corresponds to the isotope-dependent energy difference between the two involved electronic states. In our paper, this transition from

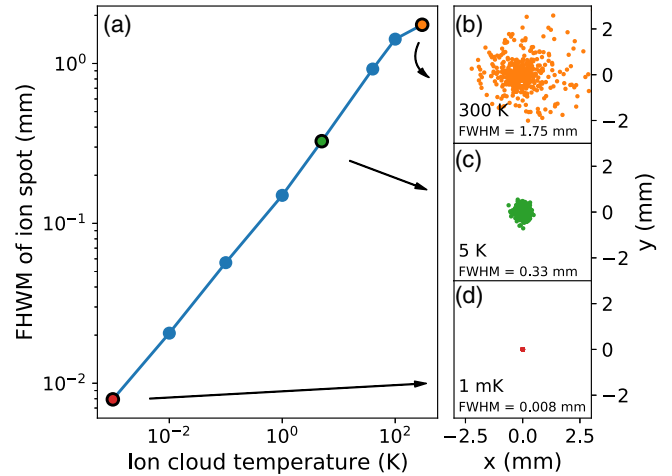


FIG. 15. (a) The spatial FWHM of the detected beam image after extraction from the Penning trap, as a function of beam temperature. In comparison to room temperature beam preparation, sub-Kelvin beam temperatures can yield an improvement in the precision of a PI-ICR measurement of well over an order of magnitude. (b)–(d) Example of simulated ion beamspots on the detector for three different ion cloud temperatures with their respective beam-spot sizes.

cooling to heating is visible as a steep increase in ToF width as seen in Figs. 5 and 12. This abrupt change in ToF width can thus be used to determine the resonance frequency and, consequently, also isotope shifts between different magnesium isotopes with nuclear spin  $I = 0$ . Unlike conventional isotope-shift measurements, this method does not require photon detection or extra laser steps for photoionization [47]. This method relies on the laser-frequency-dependent effect of Doppler cooling on the trapped ion momentum distribution, and probing that distribution through ToF measurements.

A scan of the cooling-laser frequency over cooling and heating transitions of both  $^{24}\text{Mg}^+$  and  $^{26}\text{Mg}^+$  ions is shown in Fig. 16. The sudden rises in FWHM are marked as the positions of the respective resonance frequencies. Their frequency difference corresponds to the isotope shift between the two nuclides.

The isotope shift extracted from this measurement,  $\delta\nu^{26,24} = 3090(4)_{\text{stat}}\{26\}_{\text{sys}} \text{ MHz}$ , is in good agreement with the literature value  $\delta\nu_{\text{lit}}^{26,24} = 3087.560(87) \text{ MHz}$ , obtained from a high-precision spectroscopy experiment [96], and our value is comparable in precision to collinear laser spectroscopy with fast ion beams at RIB facilities.

The systematic error quoted in our result stems from two contributions. First, the (relative) accuracy of the employed wavelength meter to which we have assigned a systematic uncertainty of 20 MHz in isotope shifts between  $\text{Mg}^+$  ions following Ref. [68]. Second, it also stems from the pressure and mass-dependent offset of the cooling-to-heating transition from the absolute transition frequency. As discussed in Sec. IV D and shown in Fig. 12, the ion-optical simulations and the numerical model both predict a small pressure-dependent shift in the transition from cooling to heating. Our calculations confirm that this shift is very similar for isotopes that are close in mass and are measured in the same pressure conditions, as is the case for the current experiment.

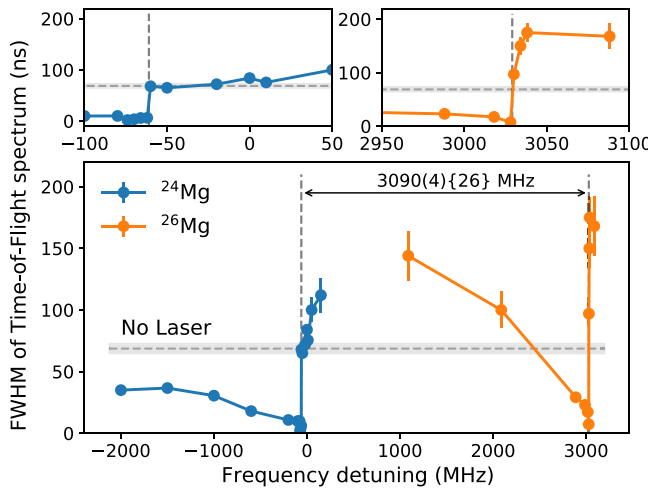


FIG. 16. Width of the experimental ToF signal as a function of the cooling-laser frequency, spanning laser cooling and heating of  $^{24}\text{Mg}^+$  and  $^{26}\text{Mg}^+$  ions. The  $x$ -axis offset is taken as the literature value for the absolute frequency of the  $D_2(3s\ ^2S_{1/2} \rightarrow 3p\ ^2P_{3/2})$  transition in  $^{24}\text{Mg}^+$  ions,  $\nu_{24} = 1\,072\,082\,934.33(16)$  MHz [96]. Two inserts on top show a zoom in near the regions of interest of the data shown in the bottom part.

For isotopes that have larger mass differences, a systematic shift might occur due to different mass- and pressure-dependent cooling dynamics. The quoted systematic error contribution was estimated from the numerical cooling model, which returns the largest shift. For example, according to this model, a difference of 10 MHz from the actual isotope shift is expected between  $^{20}\text{Mg}$  and  $^{34}\text{Mg}$  at a pressure of  $10^{-5}$  mbar (initial energy 10 eV,  $s_0 = 3.27$ , and 600 ms cooling). The shift between  $^{24}\text{Mg}$  and  $^{26}\text{Mg}$  remains within 16 MHz over the whole pressure range from  $10^{-6}$  mbar to  $10^{-4}$  mbar. Therefore, we estimate the systematic uncertainty due to the pressure and mass-dependent offset as such. The total systematic error adds up to 26 MHz.

Both the numerical cooling model and ion optical simulations shown in Fig. 12 suggest that the systematic error on the transition frequency and isotope shift determination could be reduced in future experiments by performing laser scans at different background pressures, since the different FWHM curves would cross at the resonance frequency when the cooling equilibrium is reached. Moreover, the systematic uncertainty due to the wavemeter can be decreased to a few megahertz by employing high-end models characterized in Refs. [97,98]. This technique can in principle be applied in online RIB conditions for all laser-coolable ions with sufficiently long half-lives to reach the cooling equilibrium. Some examples include the isotopic chains of Be, Mg, Ca, Sr, Ba, Ra, Hg, Yb, and Cd, that can either be laser cooled by a single laser or with the addition of a second repumping laser. The physics interest in these isotopic chains ranges from studying exotic nuclear shapes such as halo-nuclei [99] and the shell evolution [100–104] to King-plot nonlinearities and physics beyond the standard model [105]. If we focus on the case of  $^{98}\text{Cd}$ , for instance, a 10-eV ion would be cooled in 800 ms in a  $10^{-5}$  mbar helium buffer gas by a 214 nm laser of 2 mW laser power and 2 mm beam diameter. This cooling time is

significantly shorter than the 9.2(3) s half-life. Taking into account standard RIB efficiencies and a yield of 10 ions/ $\mu\text{C}$  [106], such an experiment is feasible. For isotopes of these elements with very short half-lives ( $\lesssim 500$  ms) and low yields, other approaches such as the MIRACLS technique of performing collinear laser spectroscopy in a 30-keV MR-ToF device [65,66,68] or the CRIS technique of collinear laser ionization spectroscopy [107] are better-suited high-resolution techniques.

## 2. Collinear laser spectroscopy

Collinear laser spectroscopy is a leading technique for precision laser spectroscopy at RIB facilities [46,108]. In this method, a narrow-band laser beam is overlapped with a fast ion beam. Counting emitted photons from laser-excited atoms or ions as a function of the laser frequency reveals the hyperfine structure of the studied transition and nuclide. The typically used ion beam energy of 30 to 60 keV results in a velocity compression which minimizes the Doppler broadening  $\delta\nu$  due to the ions' energy spread  $\delta E$  according to  $\delta\nu \propto \delta E/\sqrt{E}$  [109].

Modern applications of the technique employ cooler bunchers to accumulate and bunch the ion beam before the ions are sent into the laser spectroscopy beamline. This allows for a significant suppression of the photon background due to laser-stray light and detector dark counts by several orders of magnitude when gating the photon counting on the ion bunch's passage through the ion-laser-interaction and optical-detection region. Usual time spreads of ion bunches at RIB facilities are on the order of several microseconds [110].

As shown by our results, this can be readily reduced down to several nanoseconds when employing laser and sympathetic cooling in the cooler buncher. The ion bunch's significantly smaller temporal width, while maintaining a low-energy spread, will allow for an enhanced sensitivity by a factor of  $O(10^3)$ , narrowing the time-gating of ions passing through the optical-detection region. In practice, this will work best with axially segmented detection regions. Then, the flight time through a single segment is of similar order as the temporal bunch width itself while the cumulative laser-interaction and detection time remains of similar order as in contemporary CLS applications. Additionally, collinear laser spectroscopy could also benefit from an improved transverse emittance of a 3D-laser-cooled ion beam. This would maximize the overlap of the spectroscopy laser and the ion bunch and could improve the experimental sensitivity further.

## C. Optimal future laser-cooling setup

While many of the proposed applications can be directly implemented in cooler bunchers which are operational in today's RIB facilities, the cooling performance could be fully optimized in a dedicated ion-trap system. Based on the proof-of-principle results from this Paul trap cooler-buncher, we propose a potential future device for delivering low-emittance bunched beams of radioactive ions. In the small Paul trap used in this experiment, the trapping efficiency during injection was significantly reduced when only residual buffer gas was present in the trap. Most likely, this was caused by insufficient cooling during the initial injection into and first oscillations

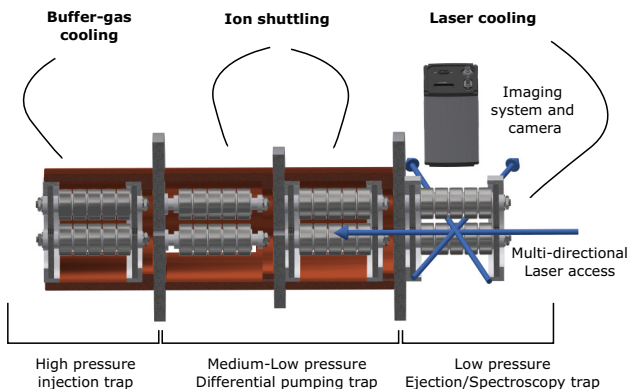


FIG. 17. Sketch of a future proposed cooler-buncher design for delivering low-emittance ion bunches and performing laser spectroscopy.

in the trap, causing a significant fraction of the injected ions to be lost at the start of the cooling cycle. Additionally, the combination of buffer gas and laser cooling in the same Paul trap speeds up the cooling with respect to laser cooling alone, but the presence of buffer gas also limits the achievable temperature. This would be undesired and even detrimental for experiments with cold trapped ions. Therefore, a future optimized setup should extend further in the axial direction and consist of several separate stages for cooling, where the buffer gas cooling is used primarily for initial cooling after which the ions are transmitted to a low-pressure Paul trap for subsequent laser cooling.

The envisioned cooler buncher, shown in a conceptual sketch in Fig. 17, would therefore consist of three segmented Paul-trap sections: a higher-pressure buffer gas cooling section, a two-stage differential pumping trap for ion shuttling at intermediate buffer-gas pressures, and, finally, a buffer-gas-free Paul trap dedicated to laser- and sympathetic cooling to achieve the low temperatures desired. The final section includes a photodetector for *in situ* monitoring of the cooling dynamics through detection of scattered photons. This will also allow this section of the device to be used for dedicated laser-spectroscopy studies using cold, trapped radioactive ions. These demands require the final stage trap to have an open structure with photon detection and multiaxis laser access, e.g., for laser cooling in all three dimensions. Additionally, the last stage has to be equipped with an ion source of stable, laser-coolable isotopes of different masses for sympathetic cooling purposes of a broad range of co-trapped ion species. An ion crystal of stable ions can then be formed before short-lived radioactive ions are injected for sympathetic cooling, similar as is done for stable (highly-charged) ions [111,112]. These short-lived ions would at this point have gone through the previous buffer-gas cooling stage. This proposed trap spatially separates the buffer gas and laser cooling, using different trap sections. An alternative approach might be considered where buffer gas and laser cooling happen in the same trap, but are separated temporally rather than spatially. Here, a burst of buffer gas fills the trap for a short time during injection of the ions. Subsequently, the buffer gas dissipates from the trap, which allows laser

cooling to take place at low gas pressures. Such a burst of gas could be controlled using a piezo-actuated valve. A similar development as the latter proposal has been successfully achieved in Ref. [113], albeit at a timescale of 30 s to reach  $3 \times 10^{-11}$  mbar.

Experiments on cold trapped ions using radioactive species are of potential use for standard-model tests, fifth force, and dark matter candidate searches as well as for nuclear structure physics [57,63,64]. Realizing a setup as described above would form a first step toward such studies with short-lived radioactive isotopes at RIB facilities.

## VI. CONCLUSIONS

We have introduced and studied, by corresponding experiments and calculations, the cooling of initially hot RIBs to sub-K temperatures, making use of laser- and sympathetic cooling in a cooler buncher in the presence of a low-pressure background gas. This technique was demonstrated to be fast enough for experiments with short-lived isotopes and can be readily implemented in current devices at RIB facilities. By use of these techniques, an improved beam emittance of Doppler-cooled magnesium and sympathetically cooled molecular oxygen and potassium ions was achieved. By combining Doppler cooling with a low-pressure helium background gas, the cooling time for ions with initial energies of at least 7 eV is reduced to suitable timescales for experiments at RIB facilities. Based on the reduction in ToF spread after extraction from a Paul trap cooler buncher, we estimate a temperature reduction factor of at least 50 after 200 ms of cooling, using ion-thermometry techniques. Additionally, our simulations show that this could be improved even further.

The improved ion bunch properties were further demonstrated by measuring an enhanced mass resolving power in an MR-ToF device. The experimental results were in good agreement with simulations performed in parallel, which in turn can guide future applications and improvements. As such, it was shown that the mass-resolving power in PI-ICR mass measurements could potentially be improved by up to two orders of magnitude. Other RIB experiments, such as (collinear) laser spectroscopy are also expected to significantly benefit from the improved ion beam emittance. Furthermore, it was shown that this technique can also be used for measuring isotope shifts of Doppler-coolable ions without the need for photon detection or additional laser steps for ionization.

Overall, the present results open possibilities for future high-precision experiments with cold trapped ions and significantly improved beam emittance at RIB facilities. By means of sympathetic cooling with co-trapped laser-coolable ions, this approach is universally applicable in providing cold ion samples and beams to subsequent RIB experiments. This includes sympathetic cooling of radioactive molecules which have recently been introduced as attractive new probes for searches of new physics [10].

As demonstrated in the present paper, the techniques can be readily implemented in existing instrumentation at RIB facilities. This will be the focus of our work in the near future. Ultimately, we envision a dedicated ion trap for laser and sympathetic cooling in all mass ranges which, in addition to its function as a next-generation RIB cooler buncher, could serve

as a platform for high-precision studies for nuclear structure and fundamental symmetries with trapped, radioactive ions.

### ACKNOWLEDGMENTS

The research leading to these results has received funding from the European Research Council (ERC) under the European Unions Horizon 2020 research and innovation program under Grant Agreement No. 679038. Part of the work of S. Sels has been funded by Interne Fondsen KU Leuven/Internal Funds KU Leuven. The work of F. Maier has been sponsored by the Wolfgang Gentner Programme of the German Federal Ministry of Education and Research. P. F. and L.S. acknowledge support by the German Ministry for Education and Research (BMBF, No. 05P18HGCIA and No. 05P21HGCI1). R.N.W. acknowledges support by the Australian Research Council under the Discovery Early Career Researcher Award scheme (Award No. DE190101137). E.M.L and A.A.K. acknowledge support from the Natural Sciences and Engineering Research Council of Canada and the National Research Council of Canada through TRIUMF. M.A. acknowledges support from the European Union Horizon 2020 Research and Innovation Program under Grant Agreement No. 861198 project LISA (Laser Ionization and Spectroscopy of Actinides) Marie Skłodowska-Curie Innovative Training Network (ITN). We are thankful to W. Nörtershäuser and M. Mugeot for fruitful discussions and input to the paper. We are grateful for the support of the ISOLTRAP, COLLAPS, and RILIS collaborations at ISOLDE and, in particular, M. Mugeot, K. Crysaldis, and S. Wilkins for providing essential equipment and help. We

thank the CRIS collaboration for providing the diode laser for laser wavelength calibration, in particular, A. Koszorus and A. Vernon.

S.S. and S.M.-E. conceived the measurement idea following discussions with T.M. The experimental characterization of laser and buffer-gas cooling were conducted by S.S. and F.M., who also carried out the MR-ToF measurements together with C.K. Sympathetic cooling of other ion species was performed by F.M. and C.K. M.A. participated in a set of measurements utilizing buffer-gas cooling. The initial setup combining a Paul trap and an MR-ToF mass spectrometer has been built by R.W., P.F., and L.S. It was modified for laser applications by V.L., F.M., and S.M.-E. with contributions from P.F., S.L., P.P., and S.S. The potassium ion source and injection beamline was conceived and setup by D.L. and S.R. who coupled it to the ion-trap system together with C.K., V.L., F.M., Y.N.V.G., P.P., and M.V. The central laser system was built by S.L., who maintained it together with P.P. Modifications were implemented by S.S. with contributions by S.L. and F.M. The simulation and calculation tools for laser cooling were developed by F.M. and S.S. F.M. performed the 3D simulations and S.S. carried out the calculations in the 1D model. T.M. reviewed the calculation approach. The PI-ICR simulations were performed by E.L. and E.M.L. utilizing a code which they developed together with A.A.K. S.S., F.M., and S.M.-E. regularly discussed the progress and directions of the project and reviewed the results together with L.S. and the entire collaboration. S.M.-E., L.S., S.R., G.N., and A.A.K. secured funding and/or resources to pursue the present project. S.S. led the writing of the paper, which was done together with S.M.-E and F.M. with contributions by E.L. All authors carefully reviewed the paper.

- [1] M. J. G. Borge and B. Jonson, ISOLDE past, present and future, *J. Phys. G: Nucl. Part. Phys.* **44**, 044011 (2017).
- [2] G. C. Ball, G. Hackman, and R. Krücken, The TRIUMF-ISAC facility: Two decades of discovery with rare isotope beams, *Phys. Scr.* **91**, 093002 (2016).
- [3] J. Äystö, T. Eronen, A. Jokinen, A. Kankainen, I. D. Moore, and H. Penttilä, *Three Decades of Research Using IGISOL Technique at the University of Jyväskylä* (Springer, Dordrecht, Netherlands, 2013).
- [4] J. Gerl, M. Górska, and H. J. Wollersheim, Towards detailed knowledge of atomic nuclei—the past, present and future of nuclear structure investigations at GSI, *Phys. Scr.* **91**, 103001 (2016).
- [5] G. Gaubert, C. Baru  , C. Canet, J. C. Cornell, M. Dubois, M. Dupuis, C. Eleon, J. L. Flambard, R. Frigot, P. Jardin, C. Leboucher, N. Lecesne, P. Leherissier, F. Lemagnen, R. Leroy, and J. Y. Pacquet, Status report of stable and radioactive ion beam production at GANIL, *Rev. Sci. Instrum.* **79**, 02A309 (2008).
- [6] A. Gade and B. M. Sherrill, NSCL and FRIB at Michigan State University: Nuclear science at the limits of stability, *Phys. Scr.* **91**, 053003 (2016).
- [7] H. Okuno, T. Dantsuka, M. Fujimaki, N. Fukunishi, H. Hasebe, Y. Higurashi, E. Ikezawa, N. Ikoma, H. Imao, O. Kamigaito, M. Kidera, M. Komiyama, K. Kumagai, T. Maie,
- M. Nagase, T. Nagatomo, T. Nakagawa, M. Nakamura, J. Ohnishi, K. Ozeki *et al.*, Present status of and recent developments at RIKEN RI beam factory, *J. Phys.: Conf. Ser.* **1401**, 012005 (2020).
- [8] G. Savard, A. Levand, R. Pardo, R. Vondrasek, and B. Zabransky, The CARIBU Facility, in *Proceedings of the Conference on Advances in Radioactive Isotope Science (ARIS2014)* (The Physical Society of Japan, Tokyo, Japan, 2015).
- [9] Y. Blumenfeld, T. Nilsson, and P. V. Duppen, Facilities and methods for radioactive ion beam production, *Phys. Scr.* **2013**, 014023 (2013).
- [10] R. F. Garcia Ruiz, R. Berger, J. Billowes, C. L. Binnersley, M. L. Bissell, A. A. Breier, A. J. Brinson, K. Chrysalidis, T. E. Cocolios, B. S. Cooper, K. T. Flanagan, T. F. Giesen, R. P. de Groot, S. Franchoo, F. P. Gustafsson, T. A. Isaev,   . Koszorus, G. Neyens, H. A. Perrett, C. M. Ricketts *et al.*, Spectroscopy of short-lived radioactive molecules, *Nature (London)* **581**, 396 (2020).
- [11] L. P. Gaffney, P. A. Butler, M. Scheck, A. B. Hayes, F. Wenander, M. Albers, B. Bastin, C. Bauer, A. Blazhev, S. B  nig, N. Bree, J. Cederk  ll, T. Chupp, D. Cline, T. E. Cocolios, T. Davinson, H. De Witte, J. Diriken, T. Grahn, A. Herzan *et al.*, Studies of pear-shaped nuclei using accelerated radioactive beams, *Nature (London)* **497**, 199 (2013).

[12] D. G. Jenkins, Recent advances in nuclear physics through online isotope separation, *Nat. Phys.* **10**, 909 (2014).

[13] R. M. Dos Santos Augusto, L. Buehler, Z. Lawson, S. Marzari, M. Stachura, T. Stora, and CERN-MEDICIS collaboration, CERN-MEDICIS (Medical Isotopes Collected from ISOLDE): A new facility, *Appl. Sci.* **4**, 265 (2014).

[14] C. Müller, K. Zhernosekov, U. Köster, K. Johnston, H. Dorrer, A. Hohn, N. T. van der Walt, A. Türler, and R. Schibli, A unique matched quadruplet of terbium radioisotopes for PET and SPECT and for alpha- and beta-radionuclide therapy: An in vivo proof-of-concept study with a new receptor-targeted folate derivative, *J. Nucl. Med.* **53**, 1951 (2012).

[15] A. K. H. Robertson, C. F. Ramogida, P. Schaffer, and V. Radchenko, Development of  $^{225}\text{Ac}$  radiopharmaceuticals: TRIUMF perspectives and experiences, *Curr. Radiopharm.* **11**, 156 (2018).

[16] C. Duchemin, J. P. Ramos, T. Stora, E. Ahmed, E. Aubert, N. Audouin, E. Barbero, V. Barozier, A.-P. Bernardes, P. Bertreix, A. Boscher, F. Bruchertseifer, R. Catherall, E. Chevallay, P. Christodoulou, K. Chrysalidis, T. E. Cocolios, J. Comte, B. Crepieux, M. Deschamps *et al.*, CERN-MEDICIS: A review since commissioning in 2017, *Front. Med.* **8**, 693682 (2021).

[17] F. Herfurth, J. Dilling, A. Kellerbauer, G. Bollen, S. Henry, H.-J. Kluge, E. Lamour, D. Lunney, R. Moore, C. Scheidenberger, S. Schwarz, G. Sikler, and J. Szerypo, A linear radiofrequency ion trap for accumulation, bunching, and emittance improvement of radioactive ion beams, *Nucl. Instrum. Methods Phys. Res. Sect. A* **469**, 254 (2001).

[18] P. Campbell, A. Nieminen, J. Billowes, P. Dendooven, K. T. Flanagan, D. H. Forest, Y. Gangrsky, J. A. R. Griffith, J. Huikari, A. Jokinen, I. D. Moore, R. Moore, H. L. Thayer, G. Tungate, S. G. Zemlyanoi, and J. Äystö, First results from laser spectroscopy on bunched radioactive beams from the JYFL ion-beam cooler, *Eur. Phys. J. A* **15**, 45 (2002).

[19] E. Mané, J. Billowes, K. Blaum, P. Campbell, B. Cheal, P. Delahaye, K. T. Flanagan, D. H. Forest, H. Franberg, C. Geppert, T. Giles, A. Jokinen, M. Kowalska, R. Neugart, G. Neyens, W. Nörterhäuser, I. Podadera, G. Tungate, P. Vingerhoets, and D. T. Yordanov, An ion cooler-buncher for high-sensitivity collinear laser spectroscopy at ISOLDE, *Eur. Phys. J. A* **42**, 503 (2009).

[20] T. Brunner, M. Smith, M. Brodeur, S. Ettenauer, A. Gallant, V. Simon, A. Chaudhuri, A. Lapierre, E. Mané, R. Ringle, M. Simon, J. Vaz, P. Delheij, M. Good, M. Pearson, and J. Dilling, TITAN's digital RFQ ion beam cooler and buncher, operation and performance, *Nucl. Instrum. Methods Phys. Res. Sect. A* **676**, 32 (2012).

[21] S. Schwarz, G. Bollen, R. Ringle, J. Savory, and P. Schury, The LEBIT ion cooler and buncher, *Nucl. Instrum. Methods Phys. Res. Sect. A* **816**, 131 (2016).

[22] B. Barquest, G. Bollen, P. Mantica, K. Minamisono, R. Ringle, S. Schwarz, and C. Sumithrarachchi, RFQ beam cooler and buncher for collinear laser spectroscopy of rare isotopes, *Nucl. Instrum. Methods Phys. Res. Sect. A* **866**, 18 (2017).

[23] B. Barquest, J. Bale, J. Dilling, G. Gwinner, R. Kanungo, R. Krücken, and M. Pearson, Development of a new RFQ beam cooler and buncher for the CANREB project at TRIUMF, *Nucl. Instrum. Methods Phys. Res. Sect. B* **376**, 207 (2016), Proceedings of the XVIIth International Conference on Electromagnetic Isotope Separators and Related Topics (EMIS2015), Grand Rapids, MI, USA, 11-15 May 2015.

[24] E. Haettner, W. R. Plaß, U. Czok, T. Dickel, H. Geissel, W. Kinsel, M. Petrick, T. Schäfer, and C. Scheidenberger, A versatile triple radiofrequency quadrupole system for cooling, mass separation and bunching of exotic nuclei, *Nucl. Instrum. Methods Phys. Res. Sect. A* **880**, 138 (2018).

[25] A. Valverde, M. Brodeur, J. Clark, D. Lascar, and G. Savard, A cooler-buncher for the  $N = 126$  factory at Argonne National Laboratory, *Nucl. Instrum. Methods Phys. Res. Sect. B* **463**, 330 (2020).

[26] D. Lunney, F. Buchinger, and R. Moore, The temperature of buffer-gas cooled ions in a Paul trap, *J. Mod. Opt.* **39**, 349 (1992).

[27] A. Kellerbauer, T. Kim, R. Moore, and P. Varfalvy, Buffer gas cooling of ion beams, *Nucl. Instrum. Methods Phys. Res. Sect. A* **469**, 276 (2001).

[28] P. Delahaye, Analytical model of an ion cloud cooled by collisions in a Paul trap, *Eur. Phys. J. A* **55**, 83 (2019).

[29] J. Van Schelt, D. Lascar, G. Savard, J. A. Clark, P. F. Bertone, S. Caldwell, A. Chaudhuri, A. F. Levand, G. Li, G. E. Morgan, R. Orford, R. E. Segel, K. S. Sharma, and M. G. Sternberg, First Results from the CARIBU Facility: Mass Measurements on the  $r$ -Process Path, *Phys. Rev. Lett.* **111**, 061102 (2013).

[30] T. W. Hänsch and A. Schawlow, Cooling of gases by laser radiation, *Opt. Commun.* **13**, 68 (1975).

[31] D. Wineland and H. Dehmelt, Proposed laser fluorescence spectroscopy on Tl+ mono-ion oscillator, *Bull. Am. Phys. Soc.* **20** (1975).

[32] D. J. Wineland and W. M. Itano, Laser cooling of atoms, *Phys. Rev. A* **20**, 1521 (1979).

[33] D. J. Wineland, Nobel Lecture: Superposition, entanglement, and raising Schrödinger's cat, *Rev. Mod. Phys.* **85**, 1103 (2013).

[34] W. D. Phillips, Nobel lecture: Laser cooling and trapping of neutral atoms, *Rev. Mod. Phys.* **70**, 721 (1998).

[35] W. Ketterle, Nobel lecture: When atoms behave as waves: Bose-Einstein condensation and the atom laser, *Rev. Mod. Phys.* **74**, 1131 (2002).

[36] J. Eschner, G. Morigi, F. Schmidt-Kaler, and R. Blatt, Laser cooling of trapped ions, *J. Opt. Soc. Am. B* **20**, 1003 (2003).

[37] A. D. Ludlow, M. M. Boyd, J. Ye, E. Peik, and P. O. Schmidt, Optical atomic clocks, *Rev. Mod. Phys.* **87**, 637 (2015).

[38] C. D. Bruzewicz, J. Chiaverini, R. McConnell, and J. M. Sage, Trapped-ion quantum computing: Progress and challenges, *Appl. Phys. Rev.* **6**, 021314 (2019).

[39] M. S. Safronova, D. Budker, D. DeMille, D. F. Jackson Kimball, A. Derevianko, and C. W. Clark, Search for new physics with atoms and molecules, *Rev. Mod. Phys.* **90**, 025008 (2018).

[40] C. J. Baker, W. Bertsche, A. Capra, C. Carruth, C. L. Cesar, M. Charlton, A. Christensen, R. Collister, A. C. Mathad, S. Eriksson, A. Evans, N. Evetts, J. Fajans, T. Friesen, M. C. Fujiwara, D. R. Gill, P. Grandemange, P. Granum, J. S. Hangst, W. N. Hardy *et al.*, Laser cooling of antihydrogen atoms, *Nature (London)* **592**, 35 (2021).

[41] M. Bohman, V. Grunhofer, C. Smorra, M. Wiesinger, C. Will, M. J. Borchert, J. A. Devlin, S. Erlewein, M. Fleck, S. Gavranovic, J. Harrington, B. Latacz, A. Mooser, D. Popper,

E. Wursten, K. Blaum, Y. Matsuda, C. Ospelkaus, W. Quint, J. Walz *et al.*, Sympathetic cooling of a trapped proton mediated by an LC circuit, *Nature (London)* **596**, 514 (2021).

[42] C. J. Foot, *Atomic Physics*, Oxford Master Series in Atomic, Optical, and Laser Physics (Oxford University Press, Oxford, 2007).

[43] A. Kramida, Y. Ralchenko, and J. Reader, NIST ASD Team, National Institute of Standards and Technology, NIST Atomic Spectra Database, version 5.8 (2020), <https://physics.nist.gov/asd> (accessed May 31, 2021).

[44] R. B. Moore, A. M. G. Dezfuli, P. Varfalvy, and H. Zhao, The ISOLDE Collaboration, Production, transfer and injection of charged particles in traps and storage rings, *Phys. Scr.* **1995**, 93 (1995).

[45] K. Blaum, J. Dilling, and W. Nörtershäuser, Precision atomic physics techniques for nuclear physics with radioactive beams, *Phys. Scr.* **2013**, 014017 (2013).

[46] P. Campbell, I. Moore, and M. Pearson, Laser spectroscopy for nuclear structure physics, *Prog. Part. Nucl. Phys.* **86**, 127 (2016).

[47] R. Neugart, J. Billowes, M. L. Bissell, K. Blaum, B. Cheal, K. T. Flanagan, G. Neyens, W. Nörtershäuser, and D. T. Yordanov, Collinear laser spectroscopy at ISOLDE: New methods and highlights, *J. Phys. G: Nucl. Part. Phys.* **44**, 064002 (2017).

[48] R. Wolf, D. Beck, K. Blaum, C. Böhm, C. Borgmann, M. Breitenfeldt, F. Herfurth, A. Herlert, M. Kowalska, S. Kreim, D. Lunney, S. Naimi, D. Neidherr, M. Rosenbusch, L. Schweikhard, J. Stanja, F. Wienholtz, and K. Zuber, On-line separation of short-lived nuclei by a multi-reflection time-of-flight device, *Nucl. Instrum. Methods Phys. Res. Sect. A* **686**, 82 (2012).

[49] W. R. Plaß, T. Dickel, and C. Scheidenberger, Multiple-reflection time-of-flight mass spectrometry, *Int. J. Mass Spectrom.* **349-350**, 134 (2013), 100 years of Mass Spectrometry.

[50] T. Dickel, W. Plaß, A. Becker, U. Czok, H. Geissel, E. Haettner, C. Jesch, W. Kinsel, M. Petrick, C. Scheidenberger, A. Simon, and M. Yavor, A high-performance multiple-reflection time-of-flight mass spectrometer and isobar separator for the research with exotic nuclei, *Nucl. Instrum. Methods Phys. Res. Sect. A* **777**, 172 (2015).

[51] S. Eliseev, K. Blaum, M. Block, C. Droese, M. Goncharov, E. Minaya Ramirez, D. A. Nesterenko, Y. N. Novikov, and L. Schweikhard, Phase-Imaging Ion-Cyclotron-Resonance Measurements for Short-Lived Nuclides, *Phys. Rev. Lett.* **110**, 082501 (2013).

[52] S. Eliseev, K. Blaum, M. Block, A. Dörr, C. Droese, T. Eronen, M. Goncharov, M. Höcker, J. Ketter, E. M. Ramirez, D. A. Nesterenko, Y. N. Novikov, and L. Schweikhard, A phase-imaging technique for cyclotron-frequency measurements, *Appl. Phys. B* **114**, 107 (2014).

[53] L.-B. Wang, P. Mueller, K. Bailey, G. W. F. Drake, J. P. Greene, D. Henderson, R. J. Holt, R. V. F. Janssens, C. L. Jiang, Z.-T. Lu, T. P. O'Connor, R. C. Pardo, K. E. Rehm, J. P. Schiffer, and X. D. Tang, Laser Spectroscopic Determination of the  ${}^6\text{He}$  Nuclear Charge Radius, *Phys. Rev. Lett.* **93**, 142501 (2004).

[54] P. Mueller, I. A. Sulai, A. C. C. Villari, J. A. Alcántara-Núñez, R. Alves-Condé, K. Bailey, G. W. F. Drake, M. Dubois, C. Eléon, G. Gaubert, R. J. Holt, R. V. F. Janssens, N. Lecesne, Z.-T. Lu, T. P. O'Connor, M.-G. Saint-Laurent, J.-C. Thomas, and L.-B. Wang, Nuclear Charge Radius of  ${}^8\text{He}$ , *Phys. Rev. Lett.* **99**, 252501 (2007).

[55] D. Melconian, J. Behr, D. Ashery, O. Aviv, P. Bricault, M. Dombsky, S. Fostner, A. Gorelov, S. Gu, V. Hanemaayer, K. Jackson, M. Pearson, and I. Vollrath, Measurement of the neutrino asymmetry in the  $\beta$ -decay of laser-cooled, polarized  ${}^{37}\text{K}$ , *Phys. Lett. B* **649**, 370 (2007).

[56] K. Okada, M. Wada, T. Nakamura, A. Takamine, V. Lioubimov, P. Schury, Y. Ishida, T. Sonoda, M. Ogawa, Y. Yamazaki, Y. Kanai, T. M. Kojima, A. Yoshida, T. Kubo, I. Katayama, S. Ohtani, H. Wollnik, and H. A. Schuessler, Precision Measurement of the Hyperfine Structure of Laser-Cooled Radioactive  ${}^7\text{Be}^+$  Ions Produced by Projectile Fragmentation, *Phys. Rev. Lett.* **101**, 212502 (2008).

[57] J. A. Behr and G. Gwinner, Standard model tests with trapped radioactive atoms, *J. Phys. G: Nucl. Part. Phys.* **36**, 033101 (2009).

[58] W. Jiang, W. Williams, K. Bailey, A. M. Davis, S.-M. Hu, Z.-T. Lu, T. P. O'Connor, R. Purtschert, N. C. Sturchio, Y. R. Sun, and P. Mueller,  ${}^{39}\text{Ar}$  Detection at the  $10^{-16}$  Isotopic Abundance Level with Atom Trap Trace Analysis, *Phys. Rev. Lett.* **106**, 103001 (2011).

[59] C. Schneider, S. J. Schowalter, K. Chen, S. T. Sullivan, and E. R. Hudson, Laser-Cooling-Assisted Mass Spectrometry, *Phys. Rev. Appl.* **2**, 034013 (2014).

[60] C. Schneider, S. J. Schowalter, P. Yu, and E. R. Hudson, Electronics of an ion trap with integrated time-of-flight mass spectrometer, *Int. J. Mass Spectrom.* **394**, 1 (2016).

[61] P. C. Schmid, J. Greenberg, M. I. Miller, K. Loeffler, and H. J. Lewandowski, An ion trap time-of-flight mass spectrometer with high mass resolution for cold trapped ion experiments, *Rev. Sci. Instrum.* **88**, 123107 (2017).

[62] N. Deb, L. L. Pollum, A. D. Smith, M. Keller, C. J. Rennick, B. R. Heazlewood, and T. P. Softley, Coulomb crystal mass spectrometry in a digital ion trap, *Phys. Rev. A* **91**, 033408 (2015).

[63] T. Manovitz, R. Shani, Y. Shapira, R. Ozeri, and N. Akerman, Precision Measurement of Atomic Isotope Shifts using a Two-Isotope Entangled State, *Phys. Rev. Lett.* **123**, 203001 (2019).

[64] P.-G. Reinhard, W. Nazarewicz, and R. F. Garcia Ruiz, Beyond the charge radius: The information content of the fourth radial moment, *Phys. Rev. C* **101**, 021301(R) (2020).

[65] S. Sels, P. Fischer, H. Heylen, V. Lagaki, S. Lechner, F. Maier, P. Plattner, M. Rosenbusch, F. Wienholtz, R. Wolf, W. Nörtershäuser, L. Schweikhard, and S. Malbrunot-Ettenauer, First steps in the development of the multi ion reflection apparatus for collinear laser spectroscopy, *Nucl. Instrum. Methods Phys. Res. Sect. B* **463**, 310 (2020).

[66] F. M. Maier, P. Fischer, H. Heylen, V. Lagaki, S. Lechner, P. Plattner, S. Sels, F. Wienholtz, W. Nörtershäuser, L. Schweikhard, and S. Malbrunot-Ettenauer, Simulations of a proof-of-principle experiment for collinear laser spectroscopy within a multi-reflection time-of-flight device, *Hyperfine Interact.* **240**, 54 (2019).

[67] V. Lagaki, P. Fischer, H. Heylen, F. Hummer, S. Lechner, M. F.M., P. Plattner, M. Rosenbusch, F. Wienholtz, R. Wolf, W. Nörtershäuser, L. Schweikhard, and S. Malbrunot-Ettenauer,

Stray-light suppression for the MIRACLS proof-of-principle experiment, *Acta Phys. Pol. B* **51**, 571 (2020).

[68] V. Lagaki, H. Heylen, I. Belosevic, P. Fischer, C. Kanitz, S. Lechner, F. Maier, W. Nörtershäuser, P. Plattner, M. Rosenbusch, S. Sels, L. Schweikhard, M. Vilen, F. Wienholtz, R. Wolf, and S. Malbrunot-Ettenauer, An accuracy benchmark of the MIRACLS apparatus: Conventional, single-passage collinear laser spectroscopy inside a MR-ToF device, *Nucl. Instrum. Methods Phys. Res. Sect. A* **1014**, 165663 (2021).

[69] S. Lechner, P. Fischer, H. Heylen, V. Lagaki, F. Maier, P. Plattner, M. Rosenbusch, S. Sels, F. Wienholtz, R. N. Wolf, W. Nörtershäuser, L. Schweikhard, and S. Malbrunot-Ettenauer, Fluorescence detection as a new diagnostics tool for electrostatic ion beam traps, *Hyperfine Interact.* **240**, 95 (2019).

[70] L. M. Bartels, Increasing electron emission rates in an offline electron impact  $Mg^+$  ion source for laser spectroscopy of radioactive ions, bachelor's thesis, Georg-August-Universität Göttingen, Germany 2018.

[71] T. Murböck, S. Schmidt, Z. Andelkovic, G. Birk, W. Nörtershäuser, and M. Vogel, A compact source for bunches of singly charged atomic ions, *Rev. Sci. Instrum.* **87**, 043302 (2016).

[72] D. Leimbach, Radioactive negative ions: Production and laser spectroscopy at ISOLDE, Ph.D. thesis, Johannes Gutenberg Universitaet Mainz, 2021.

[73] U. Köster, ISOLDE target and ion source chemistry, *Radiochimica Acta* **89**, 749 (2001).

[74] E. Kugler, The ISOLDE facility, *Hyperfine Interact.* **129**, 23 (2000).

[75] R. Kersevan and J.-L. Pons, Introduction to MOLFLOW+: New graphical processing unit-based Monte Carlo code for simulating molecular flows and for calculating angular coefficients in the compute unified device architecture environment, *J. Vac. Sci. Technol. A* **27**, 1017 (2009).

[76] F. Wienholtz, K. Blaum, J. Karthein, D. Lunney, S. Malbrunot-Ettenauer, V. Manea, M. Mougeot, L. Schweikhard, T. Steinsberger, and R. Wolf, Improved stability of multi-reflection time-of-flight mass spectrometers through passive and active voltage stabilization, *Nucl. Instrum. Methods Phys. Res. Sect. B* **463**, 348 (2020).

[77] P. Fischer and L. Schweikhard, Multiple active voltage stabilizations for multi-reflection time-of-flight mass spectrometry, *Rev. Sci. Instrum.* **92**, 063203 (2021).

[78] R. Wolf, F. Wienholtz, D. Atanasov, D. Beck, K. Blaum, C. Borgmann, F. Herfurth, M. Kowalska, S. Kreim, Y. A. Litvinov, D. Lunney, V. Manea, D. Neidherr, M. Rosenbusch, L. Schweikhard, J. Stanja, and K. Zuber, ISOLTRAP's multi-reflection time-of-flight mass separator/spectrometer, *Int. J. Mass Spectrom.* **349-350**, 123 (2013).

[79] M. Nötzold, S. Z. Hassan, J. Tauch, E. Endres, R. Wester, and M. Weidemüller, Thermometry in a multipole ion trap, *Appl. Sci.* **10**, 5264 (2020).

[80] J. B. Wübbena, S. Amairi, O. Mandel, and P. O. Schmidt, Sympathetic cooling of mixed-species two-ion crystals for precision spectroscopy, *Phys. Rev. A* **85**, 043412 (2012).

[81] M. Guggemos, D. Heinrich, O. A. Herrera-Sancho, R. Blatt, and C. F. Roos, Sympathetic cooling and detection of a hot trapped ion by a cold one, *New J. Phys.* **17**, 103001 (2015).

[82] D. Manura and D. Dahl, SIMION 8.1 User Manual (2008).

[83] D. Manura, SIMION HS1 collision model REV4 (2007).

[84] J. H. Wesenberg, R. J. Epstein, D. Leibfried, R. B. Blakestad, J. Britton, J. P. Home, W. M. Itano, J. D. Jost, E. Knill, C. Langer, R. Ozeri, S. Seidelin, and D. J. Wineland, Fluorescence during Doppler cooling of a single trapped atom, *Phys. Rev. A* **76**, 053416 (2007).

[85] T. Murböck, S. Schmidt, G. Birk, W. Nörtershäuser, R. C. Thompson, and M. Vogel, Rapid crystallization of externally produced ions in a Penning trap, *Phys. Rev. A* **94**, 043410 (2016).

[86] S. George, K. Blaum, M. Block, M. Breitenfeldt, M. Dworschak, F. Herfurth, A. Herlert, M. Kowalska, M. Kretzschmar, E. M. Ramirez, D. Neidherr, S. Schwarz, and L. Schweikhard, Damping effects in Penning trap mass spectrometry, *Int. J. Mass Spectrom.* **299**, 102 (2011).

[87] L. M. Chanin and M. A. Biondi, Mobilities of mercury ions in helium, neon, and argon, *Phys. Rev.* **107**, 1219 (1957).

[88] W. Ertmer, R. Blatt, J. L. Hall, and M. Zhu, Laser Manipulation of Atomic Beam Velocities: Demonstration of Stopped Atoms and Velocity Reversal, *Phys. Rev. Lett.* **54**, 996 (1985).

[89] M. Reiter, S. A. S. Andrés, J. Bergmann, T. Dickel, J. Dilling, A. Jacobs, A. Kwiatkowski, W. Plaß, C. Scheidenberger, D. Short, C. Will, C. Babcock, E. Dunling, A. Finlay, C. Hornung, C. Jesch, R. Klawitter, B. Koote, D. Lascar, E. Leistenschneider *et al.*, Commissioning and performance of TITAN's multiple-reflection time-of-flight mass-spectrometer and isobar separator, *Nucl. Instrum. Methods Phys. Res. Sect. A* **1018**, 165823 (2021).

[90] T. Dickel, M. I. Yavor, J. Lang, W. R. Plaß, W. Lippert, H. Geissel, and C. Scheidenberger, Dynamical time focus shift in multiple-reflection time-of-flight mass spectrometers, *Int. J. Mass Spectrom.* **412**, 1 (2017).

[91] R. N. Wolf, G. Marx, M. Rosenbusch, and L. Schweikhard, Static-mirror ion capture and time focusing for electrostatic ion-beam traps and multi-reflection time-of-flight mass analyzers by use of an in-trap potential lift, *Int. J. Mass Spectrom.* **313**, 8 (2012).

[92] J. Dilling, K. Blaum, M. Brodeur, and S. Eliseev, Penning-trap mass measurements in atomic and nuclear physics, *Annu. Rev. Nucl. Part. Sci.* **68**, 45 (2018).

[93] M. Brodeur, V. Ryjkov, T. Brunner, S. Ettenauer, A. Gallant, V. Simon, M. Smith, A. Lapierre, R. Ringle, P. Delheij, M. Good, D. Lunney, and J. Dilling, Verifying the accuracy of the TITAN Penning-trap mass spectrometer, *Int. J. Mass Spectrom.* **310**, 20 (2012).

[94] E. M. Lykiardopoulou, C. Izzo, E. Leistenschneider, A. A. Kwiatkowski, and J. Dilling, Towards high precision mass measurements of highly charged ions using the phase-imaging ion-cyclotron-resonance technique at TITAN, *Hyperfine Interact.* **241**, 37 (2020).

[95] D. A. Nesterenko, T. Eronen, A. Kankainen, L. Canete, A. Jokinen, I. D. Moore, H. Penttilä, S. Rinta-Antila, A. de Roubin, and M. Vilen, Phase-imaging ion-cyclotron-resonance technique at the JYFLTRAP double Penning trap mass spectrometer, *Eur. Phys. J. A* **54**, 154 (2018).

[96] V. Batteiger, S. Knünz, M. Herrmann, G. Saathoff, H. A. Schüssler, B. Bernhardt, T. Wilken, R. Holzwarth, T. W. Hänsch, and T. Udem, Precision spectroscopy of the  $3s-3p$  fine-structure doublet in  $Mg^+$ , *Phys. Rev. A* **80**, 022503 (2009).

[97] K. König, P. Ingram, J. Krämer, B. Maaß, K. Mohr, T. Ratajczyk, F. Sommer, and W. Nörtershäuser, On the performance of wavelength meters: Part 2- frequency-comb based characterization for more accurate absolute wavelength determinations, *Appl. Phys. B* **126**, 86 (2020).

[98] M. Verlinde, K. Dockx, S. Geldhof, K. König, D. Studer, T. E. Cocolios, R. P. de Groot, R. Ferrer, Y. Kudryavtsev, T. Kieck, I. Moore, W. Nörtershäuser, S. Raeder, P. Van den Bergh, P. Van Duppen, and K. Wendt, On the performance of wavelength meters: Part 1-consequences for medium-to-high-resolution laser spectroscopy, *Appl. Phys. B* **126**, 85 (2020).

[99] W. Nörtershäuser, D. Tiedemann, M. Žáková, Z. Andjelkovic, K. Blaum, M. L. Bissell, R. Cazan, G. W. F. Drake, C. Geppert, M. Kowalska, J. Krämer, A. Krieger, R. Neugart, R. Sánchez, F. Schmidt-Kaler, Z.-C. Yan, D. T. Yordanov, and C. Zimmermann, Nuclear Charge Radii of  $^{7,9,10}\text{Be}$  and the One-Neutron Halo Nucleus  $^{11}\text{Be}$ , *Phys. Rev. Lett.* **102**, 062503 (2009).

[100] T. Otsuka, A. Gade, O. Sorlin, T. Suzuki, and Y. Utsuno, Evolution of shell structure in exotic nuclei, *Rev. Mod. Phys.* **92**, 015002 (2020).

[101] B. H. Wildenthal and W. Chung, Collapse of the conventional shell-model ordering in the very-neutron-rich isotopes of Na and Mg, *Phys. Rev. C* **22**, 2260 (1980).

[102] M. Hammen, W. Nörtershäuser, D. L. Balabanski, M. L. Bissell, K. Blaum, I. Budinčević, B. Cheal, K. T. Flanagan, N. Frömmgen, G. Georgiev, C. Geppert, M. Kowalska, K. Kreim, A. Krieger, W. Nazarewicz, R. Neugart, G. Neyens, J. Papuga, P. G. Reinhard, M. M. Rajabali, S. Schmidt, and D. T. Yordanov, From Calcium to Cadmium: Testing the Pairing Functional Through Charge Radii Measurements of  $^{100-130}\text{Cd}$ , *Phys. Rev. Lett.* **121**, 102501 (2018).

[103] D. T. Yordanov, D. L. Balabanski, M. L. Bissell, K. Blaum, I. Budinčević, B. Cheal, K. Flanagan, N. Frömmgen, G. Georgiev, C. Geppert, M. Hammen, M. Kowalska, K. Kreim, A. Krieger, J. Meng, R. Neugart, G. Neyens, W. Nörtershäuser, M. M. Rajabali, J. Papuga, S. Schmidt, and P. W. Zhao, Simple Nuclear Structure in  $^{111-129}\text{Cd}$  from Atomic Isomer Shifts, *Phys. Rev. Lett.* **116**, 032501 (2016).

[104] T. Otsuka, T. Suzuki, M. Honma, Y. Utsuno, N. Tsunoda, K. Tsukiyama, and M. Hjorth-Jensen, Novel Features of Nuclear Forces and Shell Evolution in Exotic Nuclei, *Phys. Rev. Lett.* **104**, 012501 (2010).

[105] I. Counts, J. Hur, D. P. L. Aude Craik, H. Jeon, C. Leung, J. C. Berengut, A. Geddes, A. Kawasaki, W. Jhe, and V. Vuletić, Evidence for Nonlinear Isotope Shift in  $\text{Yb}^+$  Search for New Boson, *Phys. Rev. Lett.* **125**, 123002 (2020).

[106] Isolde Target Team, ISOLDE Yield database (2020).

[107] R. P. de Groot, J. Billowes, C. L. Bintersley, M. L. Bissell, T. E. Cocolios, T. Day Goodacre, G. J. Farooq-Smith, D. V. Fedorov, K. T. Flanagan, S. Franchoo, R. F. Garcia Ruiz, W. Gins, J. D. Holt, Á. Koszorús, K. M. Lynch, T. Miyagi, W. Nazarewicz, G. Neyens, P.-G. Reinhard, S. Rothe *et al.*, Measurement and microscopic description of odd-even staggering of charge radii of exotic copper isotopes, *Nat. Phys.* **16**, 620 (2020).

[108] R. Neugart, Lasers in nuclear physics—a review, in *Exotic Nuclei and Atomic Masses*, edited by J. Åystö, P. Dendooven, A. Jokinen, and M. Leino (Springer, Berlin, 2003), pp. 69–73.

[109] S. Kaufman, High-resolution laser spectroscopy in fast beams, *Opt. Commun.* **17**, 309 (1976).

[110] H. Heylen, C. S. Devlin, W. Gins, M. L. Bissell, K. Blaum, B. Cheal, L. Filippin, R. F. Garcia Ruiz, M. Godefroid, C. Gorges, J. D. Holt, A. Kanellakopoulos, S. Kaufmann, A. Koszorús, K. König, S. Malbrunot-Ettenauer, T. Miyagi, R. Neugart, G. Neyens, W. Nörtershäuser *et al.*, High-resolution laser spectroscopy of  $^{27-32}\text{Al}$ , *Phys. Rev. C* **103**, 014318 (2021).

[111] P. Micke, T. Leopold, S. A. King, E. Benkler, L. J. Spieß, L. Schmöger, M. Schwarz, J. R. Crespo López-Urrutia, and P. O. Schmidt, Coherent laser spectroscopy of highly charged ions using quantum logic, *Nature (London)* **578**, 60 (2020).

[112] Y. Meng and L. Du, Study on the high-efficiency sympathetic cooling of mixed ion system with a large mass-to-charge ratio difference in a dual radio-frequency field by numerical simulations, *Eur. Phys. J. D* **75**, 19 (2021).

[113] C. J. Campbell, A. V. Steele, L. R. Churchill, M. V. DePalatis, D. E. Naylor, D. N. Matsukevich, A. Kuzmich, and M. S. Chapman, Multiply Charged Thorium Crystals for Nuclear Laser Spectroscopy, *Phys. Rev. Lett.* **102**, 233004 (2009).

## **8.2 Simulation Studies of a 30-keV MR-ToF Device for Highly Sensitive Collinear Laser Spectroscopy**



## Simulation studies of a 30-keV MR-ToF device for highly sensitive collinear laser spectroscopy

F.M. Maier <sup>a,b,\*</sup>, M. Vilen <sup>a</sup>, I. Belosevic <sup>c</sup>, F. Buchinger <sup>d</sup>, C. Kanitz <sup>a,e</sup>, S. Lechner <sup>a,d</sup>, E. Leistenschneider <sup>a</sup>, W. Nörtershäuser <sup>f</sup>, P. Plattner <sup>a,g</sup>, L. Schweikhard <sup>b</sup>, S. Sels <sup>a</sup>, F. Wienholtz <sup>a,f</sup>, S. Malbrunot-Ettenauer <sup>a</sup>

<sup>a</sup> Experimental Physics Department, CERN, CH-1211, Geneva 23, Switzerland

<sup>b</sup> Institut für Physik, Universität Greifswald, 17487 Greifswald, Germany

<sup>c</sup> TRIUMF, 4004 Wesbrook Mall, Vancouver, BC V6T 2A3, Canada

<sup>d</sup> McGill University, Montréal, Québec, H3A 2T8, Canada

<sup>e</sup> Department für Physik, Friedrich-Alexander-Universität Erlangen-Nürnberg, 91058 Erlangen, Germany

<sup>f</sup> Institut für Kernphysik, Technische Universität Darmstadt, Schlossgartenstr. 9, 64289 Darmstadt, Germany

<sup>g</sup> Universität Innsbruck, Inrain 52, 6020 Innsbruck, Austria



### ARTICLE INFO

#### Keywords:

Collinear laser spectroscopy

MR-ToF device

Short-lived radionuclides

MIRACLS

Simlon simulations

Ion trapping

### ABSTRACT

The Multi Ion Reflection Apparatus for Collinear Laser Spectroscopy (MIRACLS) seeks to extend the reach of high-resolution collinear laser spectroscopy (CLS) to more exotic radionuclides. In this novel technique, ion bunches of short-lived radioisotopes are trapped between two electrostatic mirrors of a Multi-Reflection Time-of-Flight (MR-ToF) device at 30-keV kinetic energy. The same ion bunch can be probed by a spectroscopy laser for thousands of times compared to a single probing in the traditional CLS measurement scheme. Thus, the experimental sensitivity is increased by more than one to two orders of magnitude. Extensive simulations are presented, demonstrating the feasibility of high-resolution collinear laser spectroscopy (CLS) in the newly envisioned MR-ToF apparatus operating at ion energies of 30 keV. Once the mechanical design and operational parameters are optimized for the requirements of CLS, the spectral line is neither significantly broadened nor distorted by the combination of CLS and MR-ToF operation. According to the simulations, the storage efficiency and the ion-laser overlap are suitable for laser excitation of the majority of the trapped ions. In summary, > 90% injection and storage efficiency, > 75% ion-laser overlap and a line width approaching the natural line width of the transition of interest are reached in the simulation.

### 1. Introduction

For more than four decades fluorescence-based Collinear Laser Spectroscopy (CLS) has been employed to determine ground-state properties of short-lived radionuclides [1–5]. In this technique, a beam of ionic or neutral atoms is superimposed with a continuous-wave, narrow-band laser beam. Fluorescence photons from excited ionic or neutralized atoms are detected by photomultiplier tubes. By scanning the laser around the resonance frequency, the hyperfine structure of the optical transition is obtained. To increase the signal-to-noise ratio, current state-of-the-art CLS experiments employ bunched ion beams formed in a Paul trap cooler-buncher [2,6]. Due to its high precision, accuracy and resolution, CLS is a powerful experimental technique for accessing nuclear spins, electromagnetic moments and mean square charge radii of short-lived radionuclides and hence provides insight into the nuclear structure far away from stability.

However, conventional fluorescence-based CLS is limited to nuclides with production yields of typically more than several thousands or even ten-thousands ions per second [5]. Hence, there is a strong demand to extend the reach of high-resolution laser spectroscopy to the most exotic radionuclides with very low production yields as available at radioactive ion beam facilities. To this end, innovative methods such as Collinear Resonance Ionization Spectroscopy (CRIS) [7–9], high-resolution in-source laser spectroscopy [10], in-gas jet spectroscopy [11,12], laser cooling of radioactive ions [13] or more specialized techniques [14] have been or are being developed. Most recently, the novel Multi Ion Reflection Apparatus for CLS (MIRACLS), currently under construction at ISOLDE/CERN, has been envisioned to improve the experimental sensitivity of fluorescence-based CLS itself [15–19]. In this setup, 30-keV ion bunches will be trapped between two electrostatic mirrors of a multi-reflection time-of-flight (MR-ToF)

\* Corresponding author at: Experimental Physics Department, CERN, CH-1211, Geneva 23, Switzerland.

E-mail address: [franziska.marie.maier@cern.ch](mailto:franziska.marie.maier@cern.ch) (F.M. Maier).

device, allowing the laser beam to probe the ions during each revolution. Thus, the observation time will be extended and the experimental sensitivity will be increased by more than one to two orders of magnitude [20]. The actual improvement depends on the half-life and mass of the nuclide, the ionic transition and the achievable trapping time in the MR-ToF device without significant beam losses through collisions with residual gas or loss of the bunched-beam structure.

Over the years, MR-ToF instruments have become indispensable tools for precision mass measurements and mass separation of short-lived radionuclides at radioactive ion beam facilities throughout the world, see e.g. [21–30]. As a novel application of MR-ToF devices, the MIRACLS project aims to extend the reach of fluorescence-based collinear laser spectroscopy techniques.

As first science cases for MIRACLS, neutron-rich Magnesium (Mg) isotopes in the  $N = 20$  island of inversion [31] and Cadmium (Cd) isotopes at and beyond the  $N=50$  and  $N=82$  neutron shell closures will be studied, extending previous measurements with traditional CLS [32,33]. Nuclear charge radii obtained in these measurements will serve as important benchmarks for modern nuclear theory, such as the Fayans-based nuclear density functional theory [32,34–37] or leading ab-initio methods, which have made remarkable progress over the last decade [34,35,37,38] and are now capable to predict electromagnetic ground state properties of exotic radionuclides even in mid-shell regions [39–41].

In both, Mg and Cd, even–even isotopes form a closed two-level system in their ionic structure in which laser-excited ions decay back to the ionic ground state. As a consequence, they can in principle be probed indefinitely by a laser beam. Hence, without any pumping to other (hyper)fine structure states, these isotopes are ideal first science cases with maximal sensitivity for the novel MIRACLS approach. Additionally, development work is ongoing to extend the MIRACLS technique beyond closed-two level systems [42]. For instance, an additional (broad-band) laser beam can be utilized to depopulate a dark, metastable (fine-structure) state or to redistribute the population among the available hyperfine states.

In previous studies, a MIRACLS proof-of-principle experimental campaign was successfully performed to demonstrate the potential of CLS within a 1.5-keV MR-ToF device [15–20]. Additionally, its results have established the validity of ion-optical simulation tools for CLS in this setup [15,20]. Hence, the same simulation approach is applied to design a high-resolution MIRACLS. In order to obtain a spectral resolution that approaches the natural line width in conventional CLS, fast ion beams with a kinetic energy  $E$  of tens of keV are employed. This minimizes the Doppler broadening  $\sigma_f$  of the measured transition frequency according to  $\sigma_f \propto \sigma_E/\sqrt{E}$  [43], where  $\sigma_E$  is the energy spread of the ions. However, MR-ToF devices built so far utilize ion beam kinetic energies around a few keV and mirror potentials of less than 8 kV [21–30,44–47]. Therefore, a MR-ToF device capable of trapping ions with 30-keV kinetic energy is envisioned for a high-resolution MIRACLS.

In the present work, extensive simulation studies of this new device and its injection optics are performed to guide physical design and initial operation of the setup. Different geometries and combinations of the electric potentials for the injection optics as well as MR-ToF mirrors are explored. The design with the best performance achieved that simultaneously meets the space requirements of the experimental hall at ISOLDE/CERN is discussed in more detail. Special emphasis is given to the parameters relevant for CLS at MIRACLS. These are the ion-storage efficiency, the ion-laser overlap and the Doppler broadening governed by the energy spread as well as the angular spread of the ions' motion with respect to the laser beam axis. Moreover, several sources of systematic effects are investigated in this manuscript. The simulation results for CLS in the envisioned 30-keV MR-ToF apparatus show the conceptual feasibility and potential of high-resolution CLS in an MR-ToF device. This offers a strong foundation for realizing the planned apparatus.

## 2. Experimental setup

A schematic overview of the MIRACLS setup currently being under construction at ISOLDE/CERN is presented in Fig. 1. After formation of the radioactive ion beam at the ISOLDE target station, electrostatic acceleration and mass selection by a magnetic mass separator, the ions are injected into MIRACLS' linear buffer-gas-filled Paul trap for cooling and bunching of the ion beam [48,49]. The Paul trap is floated to 50 kV. Following the extraction of the ions from the Paul trap as ion bunches, the ions are accelerated to a kinetic energy of 2 keV, i.e. the beamline beyond the Paul trap is floated to 48 kV, accordingly. Afterwards the ion beam is focused by three electrostatic einzel lenses (L1–L3) enabling parallel-to-parallel focusing and bent by a 30-degree deflector to overlap it with the laser beam. Subsequently, the ions pass through two more einzel lenses (L4 and L5) and are reaccelerated to 50 keV shortly before they reach the MR-ToF device. Lens L5 differs from the other einzel lenses L1–L4 by its much larger focusing capability given its higher field strength. The reacceleration region consisting of a conical electrode is modelled after Refs. [50,51]. The 2-keV section of the transfer beamline is floated to 48 kV, see above, while the vacuum chambers around the MR-ToF device remain on ground potential. Hence a HV break is installed between the high-voltage lens L5 and the reacceleration cone, which is shielded by an inner cylinder to which a potential of 48 kV is applied.

After reacceleration to 50 keV, the ions are captured at 30-keV beam energy in an MR-ToF device via the technique of in-trap lift switching [52]. A 20-kV potential difference has been chosen such that the ions will easily overcome the maximum in the electric potentials applied to the mirror electrodes (around 40 kV) when the ions are injected into the MR-ToF device (see Section 3). Mirror switching is a technical challenge for a 30-keV MR-ToF device due to the high potentials needed at the individual mirror electrodes. This motivates the choice of the in-trap lift for the ion capture and extraction.

The MR-ToF device (see also Section 3) consists of two opposing electrostatic mirrors with a central drift tube in between (electrode 7, see Fig. 2(top)). Each electrostatic mirror consists of six electrodes (1–6). The two mirror electrodes (1–2) that are closest to the central drift tube provide radial refocusing of the ion cloud. The axial trapping potential is realized by the four outermost mirror electrodes (3–6). Between the central drift tube and the mirror electrodes two additional electrodes (8–9) are installed, which can be used as electrodes for ion monitoring and diagnostics by pickup of image-charge signals [53] or, if azimuthally segmented, as deflector electrodes [54]. The inner diameter of electrodes 7–9 is reduced to 40 mm compared to the inner diameter of the mirror electrodes of 80 mm in order to maximize the size of the field-free region in the central drift tube. Given the sensitivity of the ions' trajectories to field distortions at the point where the ions are reflected, the so-called turn-around point, the outermost mirror electrode 6 is reduced at its outer end to an inner diameter of 40 mm to shield the MR-ToF region from external electric fields. Grounded electrodes (0) in front and behind the MR-ToF device provide an additional shielding from fringe fields [20]. The planned beamline geometry provides spaces for ion diagnostics along the ions' path, including a retractable ion detector downstream of the MR-ToF device.

## 3. The 30-keV MR-ToF device: design and simulations<sup>1</sup>

To find suitable MR-ToF geometries and potentials applied to individual electrodes, trajectories of the ions are simulated using the ion-optical software package SimIon, version 8.1 [55]. Firstly, the geometry of all electrodes is defined in a three dimensional grid with constant node spacing. On every grid point, the Laplace equation is solved numerically to obtain the electric potential. After definition of

<sup>1</sup> This section and the last paragraph of the previous section are partly reproduced from chapter 5 of the MSc thesis of F.M. Maier, see [20].

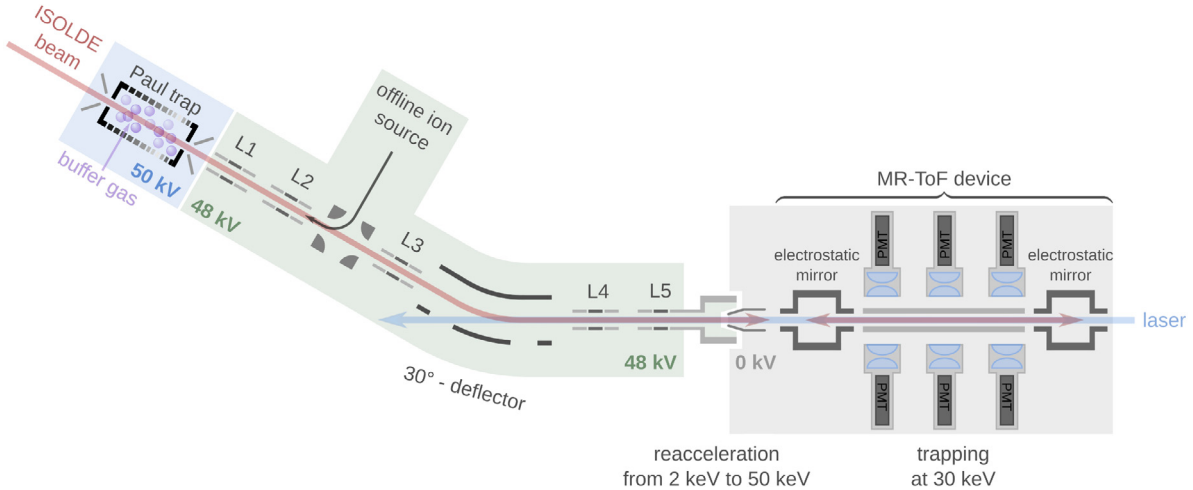


**Fig. 1.** Schematic overview of the MIRACLS setup for high-resolution laser spectroscopy at ISOLDE, which takes up a floor space of around  $1.5 \text{ m} \times 4.4 \text{ m}$ . After ion preparation of the incoming ISOLDE beam in a Paul trap, ion bunches are transported to the MR-ToF device via a  $\approx 1.9\text{-m}$  long transfer beamline consisting of totally 5 einzel lenses and a 30-degree deflector. The Paul trap section is floated to 50 kV (blue shaded region), the 2-keV section of the transfer beamline is floated to 48 kV (green shaded region) and the beamline around the MR-ToF device is on ground potential (grey shaded region). A quadrupole bender installed between the einzel lenses L2 and L3 facilitates injection of stable ions from an offline ion source for testing and calibration of the MR-ToF components and the ion-laser interaction. The optical detection region consisting of six photo multiplier tubes (PMTs) is located between the two electrostatic mirrors of the MR-ToF device. The figure is not to scale. See text for details.

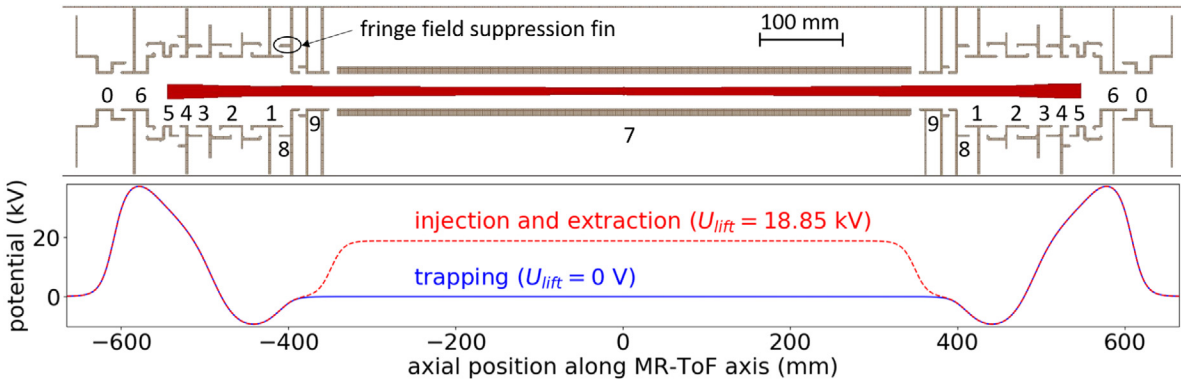


**Fig. 2.** MIRACLS 30-keV MR-ToF device: (Top) Cut view of its electrode structure together with the ions' simulated trajectories (in red) for 300 ions performing 300 revolutions. (Bottom) Electric potential along the central axis of the MR-ToF device once for trapping (blue) and once for injection and extraction (red) with an in-trap lift potential of  $U_{\text{lift}} = 18.85 \text{ kV}$ .

the ions' initial conditions such as the ion mass, position and energy, the ion trajectories are calculated for every time step in the previously calculated fields. It is possible to modify certain aspects of the simulation during the ions' flight via user programming in Lua, e.g. to include buffer-gas collisions [56] or time-dependent fields. The resulting ion parameters such as velocity or position can be recorded at user-defined planes. Coulomb interactions between ions and between ions and image charges on the electrodes are not taken into account in the simulations discussed in the present work. These so-called space-charge effects are neglected since due to the low yields only up to a few 100 ions will be stored simultaneously in the 30-keV MR-ToF device in CLS mode. For the neutron-rich Mg isotopes isobaric contamination is not expected to be present in notable amounts in the ion beam. In case of sizeable amounts of contamination, MIRACLS can take advantage of the MR-ToF's capability for mass separation. For example, the deflector electrodes between the central drift tube and the mirror electrodes will allow to remove unwanted contaminants, see e.g. [54]. Further details of the simulation procedure and investigations of the accuracy achieved can be found in the [Appendix](#).

The simulation is started with  $^{24}\text{Mg}^+$  ions positioned at the middle plane of the MR-ToF device, i.e. the plane at the centre of the drift tube perpendicular to the axis. The ion beam has a transversal rms emittance of  $3 \pi \text{ mm mrad}$ . The kinetic energy is Gaussian distributed

around a centre of 30 keV with a standard deviation of 0.4 eV. Note that the simulations of the MIRACLS Paul trap predict a standard deviation of the energy of around 0.4 eV and a transversal rms emittance of  $< 1 \pi \text{ mm mrad}$  [48]. Existing Paul traps (e.g. [57–59]) such as ISCOOL at ISOLDE show a transversal rms emittance of around  $2 \pi \text{ mm mrad}$  [60]. Hence the chosen rms emittance of  $3 \pi \text{ mm mrad}$  depicts a worse case scenario in the simulations.

The potentials of the six mirror electrodes are optimized in a Monte-Carlo manner similarly as performed in Ref. [15]. Due to the risk of electric discharges across the mirror electrodes, we limit our choice to potential sets in which the difference in electric potentials between neighbouring electrodes is less than 40 kV. To reduce the size of the parameter space of the system the potential of the two innermost mirror electrodes (1–2) are chosen to be identical. At a later stage, different potentials can be applied to these two electrodes to allow some fine tuning in the experiment. The properties of the ions are recorded whenever they pass the middle plane of the MR-ToF device in collinear direction. Storage efficiency, ion-laser overlap, Doppler broadening and increase of ion-bunch width as a function of revolution number are determined. The storage efficiency is calculated as the fraction of ions that remain trapped after 100 revolutions. The ion-laser overlap is computed as an average over all 300 simulated revolutions of the fraction of ions with a transversal displacement from the MR-ToF axis

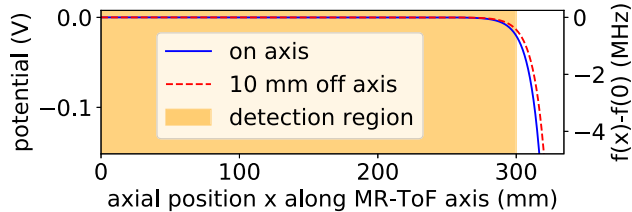


**Fig. 3.** Electric potential and the change of the Doppler-shifted frequency  $f(x) - f(0)$  (D2 line in  $Mg^+$  ions) for a kinetic energy of 30 keV, once for a  $^{24}Mg^+$  ion flying along the central axis and once on a parallel line shifted 10 mm off axis. The length of the optical detection region is marked in orange. The central drift tube itself is extending from -345 to 345 mm.

smaller than the assumed laser beam radius of either 2 mm or 4 mm at the middle plane. For simplicity it is assumed that the laser beam is homogeneous within the assumed radius. The Doppler broadening is given by the FWHM of the Doppler-shifted resonance frequencies  $f$  calculated in the laboratory frame,

$$f = f_0 \frac{\sqrt{1 - \left(\frac{v}{c}\right)^2}}{1 - \frac{v \cos \alpha}{c}}, \quad (1)$$

where  $f_0$  is the resonance frequency in the rest frame of the ions,  $c$  is the speed of light,  $v$  the velocity of individual ions and  $\alpha$  is the angle between an individual ion path and the laser beam axis. The latter is assumed to be identical to the central axis of the MR-ToF device.

The Monte-Carlo optimization of the potentials applied to the individual electrodes is repeated for different geometries of the MR-ToF device, which are all guided by the design of the Greifswald MR-ToF device operating at 1.3 keV [54,61]. The lengths of the six mirror electrodes are kept fixed to the values of the Greifswald MR-ToF device while the inner electrode diameters are enlarged by a factor 2.7 for better field conformity in radial direction and hence reduced aberrations [62]. Fringe-field suppression fins are added to the individual mirror electrodes to prevent any fringe fields from outside reaching into the MR-ToF device, see Fig. 2 (top). The simulations show that the existence and design of the fringe field suppression fins as well as the gap dimensions between the individual electrodes have minimal to no effect on ion-laser overlap or Doppler broadening whereas they can significantly alter the evolution of an ion-bunch's temporal width over revolution number. After modifying the gap size and redesigning the fringe field suppression fins the bunched-beam structure is preserved for almost a factor 3 higher revolution number. This is beneficial for the boost in sensitivity at MIRACLS to suppress background, see Section 5.3.

Only in a field-free region the ion velocity is fully independent of an ion's position in the central drift tube. In practice, remaining potential gradients result in slightly different velocities and hence different Doppler-shifted laser frequencies in the rest frame of the ion. Hence, the length of the central drift tube (electrode 7 in Fig. 2) is chosen to be 690 mm, such that the change in electric potential along the MR-ToF axis is less than 0.1 V within a region with a length of 62 cm (see Fig. 3). For the  $3s\ ^2S_{1/2} \rightarrow 3p\ ^2P_{3/2}$  (D2) transition in  $^{24}Mg^+$  ions, for instance, a 0.1-V potential change corresponds to a change of the Doppler-shifted frequency of less than 3 MHz for an ion with 30-keV kinetic energy. In the case of the  $5s\ ^2S_{1/2} \rightarrow 5p\ ^2P_{3/2}$  (D2) transition in the  $Cd^+$  ions a 0.1 V change corresponds to less than 2 MHz change. This is significantly smaller than the systematic uncertainties of traditional single-passage CLS, see for instance Ref. [33] for measurements of exotic Mg isotopes. Given the lifetime of around 3.8 ns of the excited state in the D1 and D2 transitions for the  $Mg^+$  ions [63] and the kinetic energy in the MR-ToF device, an excited ion will typically travel less than 2 mm until it decays back to the ground state. For the selected transition in  $Cd^+$ , the lifetime of the excited state is around 2.6 ns [64],

**Table 1**

Potentials for the MR-ToF mirror electrodes as obtained in the Monte-Carlo approach for  $^{24}Mg^+$  ions with 30-keV beam energy. See text and Fig. 2.

Respective electrode	Potential (V)
1 (innermost mirror)	-12,469.3
2	-12,469.3
3	23,002.6
4	25,966.4
5	29,648.9
6 (outermost mirror)	39,013.0

hence the travelling distance is even smaller. Thus photons emitted by ions excited outside the optical detection region at different velocities (and therefore other resonance frequencies in the laboratory frame) will not be detected.

A suitable MR-ToF geometry leading to high storage efficiency, high ion-laser overlap, small Doppler broadening and a small increase of temporal bunch width over revolution number is presented in Fig. 2 (top). The resulting potential distribution along the MR-ToF axis is shown in Fig. 2 (bottom) and the individual electrostatic potentials are listed in Table 1.

#### 4. Simulations of the injection beamline

In the second step of the simulations, suitable injection optics for the 30-keV MR-ToF device is obtained. To start with a realistic initial ion distribution in phase space, simulations of the ion preparation in a dedicated MIRACLS Paul trap cooler-buncher [48] are performed. Ions are positioned at the potential minimum of the Paul trap and left to thermalize with room-temperature buffer gas. The buffer-gas cooling is modelled with SimIon's built-in hard-sphere interaction model [56]. For a similar Paul trap at the MIRACLS proof-of-principle apparatus, the buffer-gas cooling simulations show an excellent agreement with experimental data [13,15]. After extraction of the ion bunches from the Paul trap, they pass the ion optical elements as described in Section 2. Subsequently, they are trapped in the MR-ToF device via the in-trap lift switching technique [52].

The potentials applied to ion-optical elements along the transport beamline from the Paul trap to the MR-ToF device are optimized via SimIon's built-in Nelder-Mead algorithm [65]. The MR-ToF mirror potentials are kept fixed to the values obtained in Section 3. The objective function of the optimization has been tailored for minimal ion losses in the transport beamline and for a maximal storage efficiency in the MR-ToF device, simultaneously. Once good settings are found for these, the individual potentials of the transport beamline elements are varied in the next optimization step around their previous values to additionally obtain a high ion-laser overlap and a small Doppler broadening while maintaining the best storage efficiency as obtained before.

In principle, a small radial ion-beam size is desired in CLS which allows for an optimal ion-laser overlap with reduced laser diameters and, thus, little laser stray light and higher power densities. At the same time, one aims for ion trajectories which are as parallel as possible to minimize the contribution of diverging ion-beam propagation to the Doppler broadening. In practice, however, the ion bunch's angular divergence and transversal spatial width are related to each other through the conserved transversal emittance. The latter is governed by the beam preparation in the Paul trap. The repeated reflections in the MR-ToF device couple the ion's radial displacement and the angles of their trajectories. Thus, when observed over many revolutions in the MR-ToF instrument, one generally obtains a suboptimal laser-ion overlap, an increased Doppler broadening or both. As a consequence, many combinations of injection beamline potentials lead to a large storage efficiency, but only a few of them also result in a good performance for CLS operation.

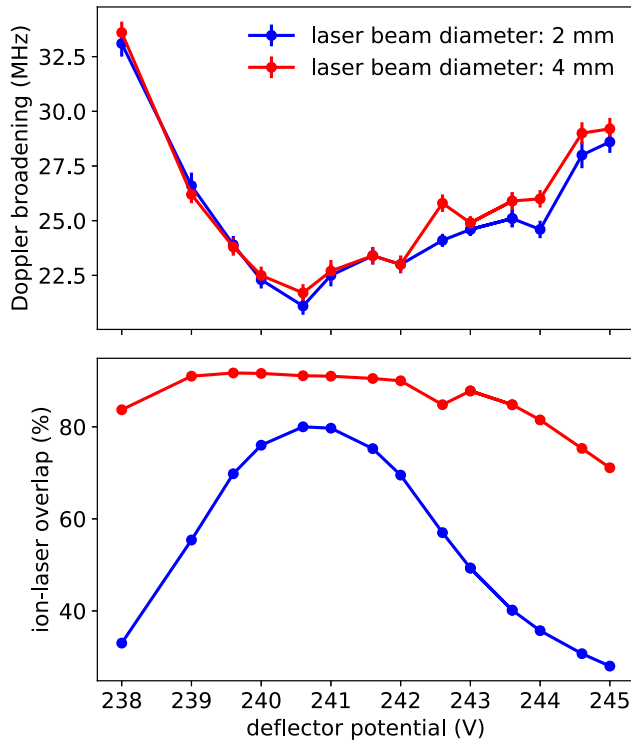


Fig. 4. Doppler broadening (FWHM) and ion-laser overlap for varying deflector potentials of the 30-degree bender for laser beam diameters of 2 mm and 4 mm. The points are connected to guide the eyes. Both observables are evaluated at the transversal middle plane of the MR-ToF device for 300  $^{24}\text{Mg}^+$  ions summed over 100 revolutions.

The reacceleration region consisting of a conical electrode leads to a focusing of the ions directly in front of the MR-ToF device. Hence the einzel lens L5 (see Fig. 1) with its large focusing strength is needed to counteract the focusing properties of the reacceleration region as well as the MR-ToF entrance mirror electrodes to provide a parallel-to-parallel ion beam injection into the MR-ToF device.

In the last optimization step, the in-trap lift potential is optimized to yield a minimal broadening of the temporal ion-bunch width. This means that the beam energy in the MR-ToF device is varied. The ideal value of the in-trap lift potential is found to be 18.85 kV. Alternatively, instead of changing the beam energy, all the potentials applied to the electrodes of the electrostatic mirrors could be scaled accordingly. The potential of the in-trap lift does not noticeably effect the Doppler broadening or ion-laser overlap, as long as most of the ions can be trapped.

The potentials obtained for the ion optical elements of the injection beamline are listed in Table 2. The potentials utilized for the einzel lenses can differ by up to 50 V from their set values without significantly altering the performance of the setup. The potentials applied to the electrodes of the 30-degree deflector are much more sensitive. Fig. 4 shows the Doppler broadening and the ion-laser overlap over the deflector potential. Details on this Doppler broadening are given in Section 5.2. Whereas the storage efficiency remains above 90% between 232 V and 245 V, the ion-laser overlap for a 2-mm laser beam diameter exceeds 70% only in a limited voltage range of 239.6 V to 242.0 V for  $^{24}\text{Mg}^+$  ions. This is also the region where the Doppler broadening is minimal.

For Cd ions the potentials of the 30-degree deflector need to be changed from 240.6 V to 243.6 V for an optimal performance of the setup whereas all the other potentials can be kept the same. This small difference is due to slightly different energies which is a consequence of different Paul-trap storage and extraction settings between the two mass ranges of Mg and Cd isotopes.

Table 2

Chosen potential combination for the injection beamline electrodes with respect to the 48-kV potential of the transfer beamline. The deflector is operated with identical voltages of opposite polarity on the two plates. The optimal potential of the deflector is different for Mg and Cd isotopes.

Electrode	Potential (V)
Lens 1	-1800
Lens 2	-1400
Lens 3	-2400
Deflector	$\pm 240.6$ (Mg) or $\pm 243.6$ (Cd)
Lens 4	-1380
Lens 5	-16950

## 5. Simulated performance of the setup

In this section the simulated performance of the envisioned MIRACLS setup will be discussed for the previously optimized potentials and geometries including the thermalization of the ions in the Paul trap, the passage of the ions along the whole transport beamline as well as their capture and storage in the MR-ToF device. 1000 ions with a selected mass between 20–34 u (Mg isotopic chain) or 96–134 u (Cd isotopic chain) are trapped in the MR-ToF instrument for 300 revolutions. In general, the simulations show that the combined injection and storage efficiency exceeds 90% and the ion-laser overlap is larger than 75% for a 2-mm laser-beam diameter. The Doppler broadening is smaller than the natural line width for all investigated isotopes with a mass between 20–34 u and 96–134 u.

In addition to the nominal case of a 50-keV ISOLDE beam and an MR-ToF device operating at 30 keV, we have also performed simulations for a 30-keV incoming ISOLDE beam, an in-trap lift of 12 kV and, thus, an 18-keV MR-ToF device. These lead to slightly worse ion-laser overlap and Doppler broadening compared to the 30-keV MR-ToF device as discussed here, but will allow high-resolution MIRACLS. In case of unexpected HV challenges, a MIRACLS operation at lower ion-beam energy is possible.

As an example, the results for  $^{24}\text{Mg}^+$  ions trapped in the 30-keV MR-ToF device are discussed in the following.

### 5.1. Storage efficiency and ion-laser overlap

The evolution of the ion-laser overlap and that of the capture and storage efficiency as a function of revolution number are presented in Figs. 5 and 6, respectively. It typically takes a few revolutions until the ions move on trajectories in the vicinity of the axis of the MR-ToF device. About 4% of the ions are lost in the MR-ToF device during the first 7 revolutions (see Fig. 6). The ion-laser overlap fluctuates around 83% for 2-mm laser-beam diameter and around 97% for 4-mm laser-beam diameter (see Fig. 5). These estimates reflect the ion properties recorded in the transversal middle plane of the MR-ToF device. However, the spatial width of the ion bunch increases the further the ion bunch is away from the transversal middle plane of the MR-ToF device as visible in Fig. 2 (top). Hence, for a laser-beam diameter of 2 mm the ion-laser overlap decreases from 83% to 68% from the middle of the MR-ToF device to the end of the optical detection region. Assuming a laser-beam diameter of 4 mm, the ion-laser overlap is reduced from 97% in the middle to 95% at the edges of the optical detection region. The visible oscillations of ion-laser overlap versus revolution number are attributed to the periodic movement of certain ions, moving in and out from the area where they can be excited by the laser beam (see also Fig. 6 in Ref. [15]). Overall, the simulated capture and storage efficiency as well as the ion-laser overlap allow to excite most of the ions.

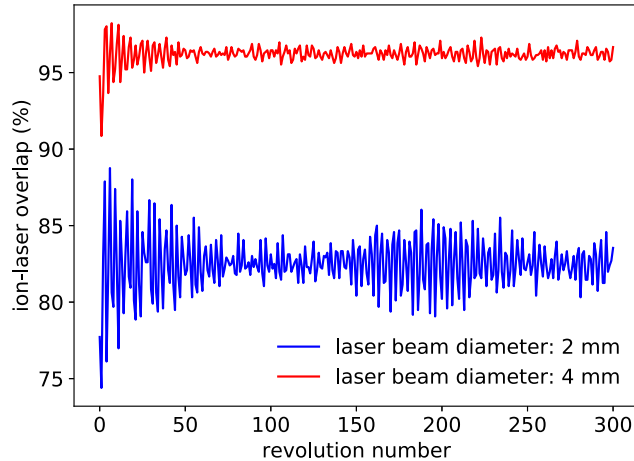


Fig. 5. Ion-laser overlap versus revolution number for 1000  $^{24}\text{Mg}^+$  ions for a laser-beam diameter of 2 mm (blue) and for 4 mm (red). Both are evaluated at the transversal middle plane of the MR-ToF device.

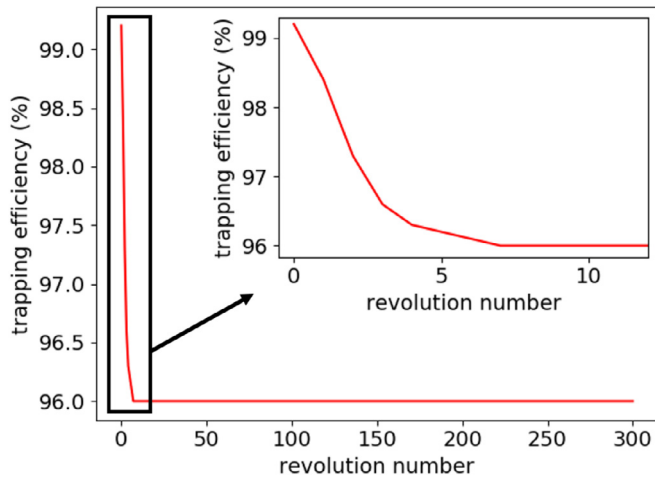


Fig. 6. Capturing and storage efficiency versus revolution number for 1000  $^{24}\text{Mg}^+$  ions. The efficiency is calculated as the fraction of ions that remain passing the middle plane of the MR-ToF during every revolution.

## 5.2. CLS spectra

In a classical fluorescence-based CLS experiment, the number of fluorescence photons is counted as a function of the laser frequency to obtain a (hyper)fine spectrum of the selected optical transition. To simulate the resonance spectrum of the D2 transition in Mg, the Doppler-shifted frequencies  $f$  are calculated in the laboratory frame based on the velocity of individual ions and the angles between an individual ion path and the laser beam axis according to Eq. (1). For the simulated 1000  $^{24}\text{Mg}^+$  ions, a histogram of the Doppler-shifted frequencies of the D2 transition summed over 300 revolutions is shown in Fig. 7. The natural line width is neglected in this simulation in order to clearly distinguish the different contributions to the experimental line-width broadenings. A histogram of the angles  $\alpha$  between an individual ion trajectory and laser-beam axis, summed over all revolutions and ions, is depicted in Fig. 8. Note that the mean ion trajectory is fully aligned with the laser-beam axis. The centroid angle is 0.08 degrees and the FWHM is 0.12 degrees.

A histogram of the kinetic energy of the ions' first passage through the middle plane of the MR-ToF device can be seen in Fig. 9. Due to the energy spread of 0.82(3) eV FWHM and the angles between ions' trajectories and laser beam, the Doppler broadening is found

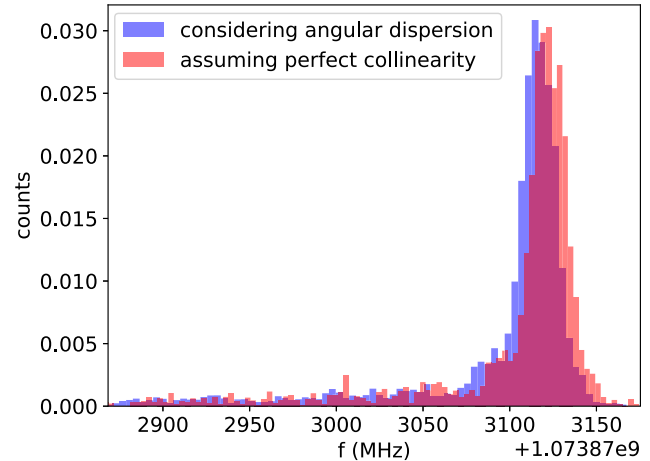


Fig. 7. Doppler-shifted frequency  $f$  of the D2 line in  $^{24}\text{Mg}^+$  ions in a collinear configuration. Data is recorded at the transversal middle plane of the MR-ToF device for 1000  $^{24}\text{Mg}^+$  ions summed over 300 revolutions. In the evaluation of  $f$  for the histogram assuming perfect collinearity, the angles  $\alpha$  are set to 0 to distinguish the effects of kinetic energy spread and angular spread on the CLS spectra. The overlapping region between the two histograms is shown in purple. The natural line width is neglected in this simulation.

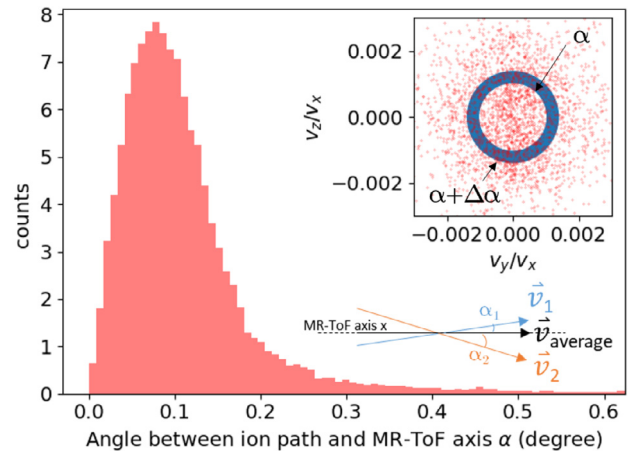


Fig. 8. Angles  $\alpha$  between ion path and MR-ToF axis evaluated at the transversal middle plane of the MR-ToF device for 1000  $^{24}\text{Mg}^+$  ions summed over 300 revolutions. The top inset shows the ratio of the respective transversal velocity component  $v_y$  and  $v_z$  and the longitudinal velocity component  $v_x$ . Each point corresponds to one ion passing the central drift tube for revolution numbers 200–202. Because of  $v_{y,z} \ll v_x$ , the angle  $\alpha$  (in mrad) can be visualized in this figure by using the approximation  $\alpha^2 \approx v_y^2/v_x^2 + v_z^2/v_x^2$ . The bottom inset shows two trajectories of ions with velocity  $\vec{v}_1$  and  $\vec{v}_2$ , that are moving with angles  $\alpha_1$  and  $\alpha_2$  in respect to the MR-ToF axis. Note that the average ion trajectory  $\vec{v}_{\text{average}}$  is fully aligned with the laser-beam axis.

to be 22.1(6) MHz for the ions excitable by a laser beam with 2-mm diameter and 23.1(6) MHz when all trapped ions are considered. According to Eq. (1), non-vanishing angles between ion trajectories and laser-beam axis will always shift the laser frequency observed in the ions' rest frame in one direction, i.e. to lower values for the collinear configuration compared to a shift to higher frequency in an anti-collinear setup. This results in a shift of the average Doppler-shifted frequency accounting to around 7.5 MHz, see Fig. 7. Note that this shift is also present when exclusively considering the first passage through the optical detection region as it would be the case in conventional CLS. Such a 7.5-MHz shift in the absolute frequency of the centroid can be neglected when isotope shifts are measured using CLS since all measured isotopes are shifted by (almost) the same amount. In the present simulation, this is verified along the isotopic chains of the Mg

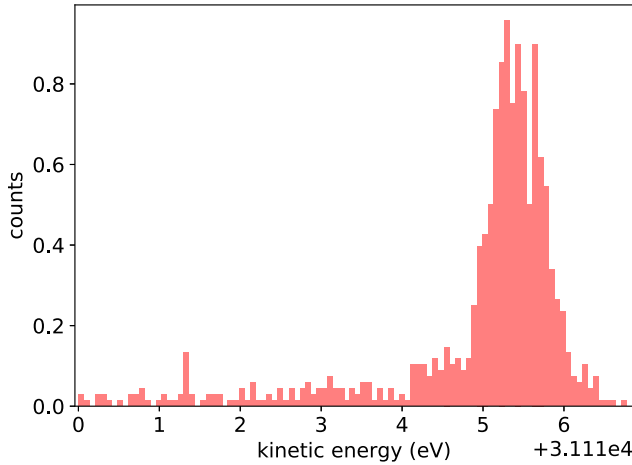


Fig. 9. Kinetic energy evaluated at the transversal middle plane of the MR-ToF device for 1000  $^{24}\text{Mg}^+$  ions for the very first passage.

and Cd ions, where any isotopic dependence is found to be less than 0.1 MHz.

The leading contribution to the asymmetric frequency lineshape, especially in the tail towards lower frequencies as depicted in Fig. 7, is shown to arise from reheating effects in the Paul trap. Some ions undergo collisions with buffer gas during extraction and reacceleration from the Paul trap and hence experience a reduction of their kinetic energy (see Fig. 9). The resulting tail in the CLS frequency spectrum is thus not specific to the MIRACLS measurement concept but a general feature of the ion preparation in buffer-gas-filled Paul traps for CLS with bunched ion beams. The asymmetry, which is arising from the angular distribution of the ions, is minimal. This can be seen in Fig. 7 where a spectrum including the effect of angular dispersion is compared with a spectrum that is assuming perfect collinearity.

Since the centroid of the Doppler-shifted resonance frequency as well as the Doppler broadening stay constant over revolution number, the CLS spectrum characteristics for 300 revolutions in the MR-ToF device are very similar to the first passage. This provides confidence that line-shape distortions due to the reflections at the mirror electrodes are well under control once the mirror potentials and ion optics for the injection into the MR-ToF device are appropriately chosen.

### 5.3. Evolution of the ion-bunch width

To reduce the influence of background originating from laser stray light or detector dark counts, current state-of-the-art CLS experiments employ bunched ion beams [2,6]. Photon signals are only accepted when the ion bunch is within the optical detection region such that a time-gated spectrum is obtained. Hence, it is of advantage to preserve the bunched structure of the beam over thousands of revolutions in the MIRACLS approach. In the present investigation we thus enforced the ion bunch to never become larger than half of the revolution period, i.e. 2.3  $\mu\text{s}$  to 3.0  $\mu\text{s}$  for Mg isotopes and 5.0  $\mu\text{s}$  to 5.9  $\mu\text{s}$  for Cd isotopes to still maintain a bunched beam structure. The given ranges are due to the mass dependence of the revolution period. The increase in ion-bunch width over revolution number can be described by the dispersion per turn and is desired to be as small as possible. For fixed mirror potentials and MR-ToF geometry, this is achieved by selecting an appropriate in-trap lift potential [52]. Due to limited computing resources, only a few hundred revolutions can be simulated with sufficient accuracy (see Appendix). In order to estimate the ion bunch width after many thousands of revolutions, the flight times of the ions in the MR-ToF apparatus are evaluated with respect to the time they first cross the transversal middle plane of the MR-ToF device. The ions are trapped for 100 revolutions and the resulting time spread

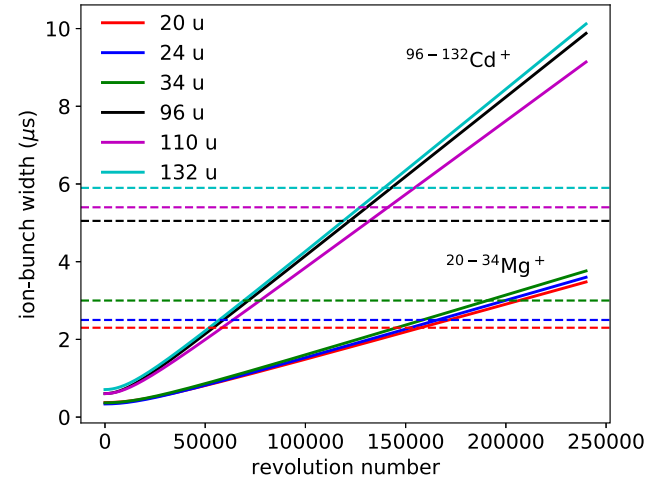


Fig. 10. Ion-bunch width (FWHM) versus revolution number for 1000 ions of various masses. To maintain the bunched ion-beam structure in the MR-ToF device the ToF peak width should remain below half of the revolution period which is indicated by horizontal lines for the different masses.

after 100 revolutions is divided by the revolution number to obtain the dispersion per turn  $\Delta t_1$ . The temporal ion bunch width  $\Delta t$  for a given revolution number  $n$  follows as [26]

$$\Delta t = \sqrt{\Delta t_0^2 + n\Delta t_1^2}, \quad (2)$$

where  $\Delta t_0$  is the initial bunch width when the ions pass the transversal middle plane for the first time. The in-trap lift potential is scanned across a broad voltage range until the region with minimal dispersion per turn is found. The evolution of the ion bunch width as a function of revolution number is shown in Fig. 10 for Mg and Cd ions.

For  $\text{Mg}^+$  ions the bunched-beam structure is maintained until 150,000 to 190,000 revolutions depending on the isotope, corresponding to a total trapping time of 690 ms to 1.1 s. The half-lives of  $^{20,21}\text{Mg}$  are around 100 ms and the half-lives of  $^{30-34}\text{Mg}$  range from 313 ms down to 20 ms [66]. They are significantly shorter than the maximal trapping time given by the loss of the bunched-beam structure.

Similarly, Cd ions keep a suitable bunch structure for 120,000 to 138,000 revolutions and hence for 1.2 to 1.6 s. The Cd isotopes around the N=82 neutron shell closures have half-lives of a few tens of ms [66] and the majority of the trapped ions is hence decayed before the bunched-beam structure is lost. Cd isotopes around the N=50 neutron shell closure have half-lives in the order of a few seconds [66] and consequently lose their bunched structure before the onset of significant radioactive losses. Based on these results, we conclude that the bunched-beam structure can be maintained over many thousands of revolutions for the first science cases allowing a significant improvement in sensitivity of the MIRACLS approach in comparison to traditional single-passage CLS.

### 5.4. Investigation of high-voltage instabilities

In order to extend the reach of the MIRACLS technique towards more exotic radionuclides, sufficient photon counts need to be accumulated over time to unambiguously locate the CLS resonance. Hence, after the measurement of one ion bunch over thousands of revolutions in the MR-ToF device, this bunch will be released and can be recorded at an ion detector behind the MR-ToF device for e.g. intensity calibration. Moreover, in the case of very rarely produced radionuclides, the data of this ion detector could in future applications be utilized to discard any measurement cycle in which no ion of interest is trapped in the MR-ToF device and, thus, to further decrease the photon background in the analysis. To this end, the ion beam needs to be guided onto an ion

detector positioned off-centred and away from the laser beam, either by the deflector electrodes in the MR-ToF device or additional ones downstream of the electrostatic mirror. Due to the MR-ToF capability to mass separate isobars, the ions of interest can in many cases be distinguished from contaminants. Subsequently, the next ion bunch will be injected into the MR-ToF device and the measurement will be repeated ideally under exactly the same experimental conditions. However, any drift or fluctuation in the potentials applied to the Paul trap extraction, the in-trap lift or MR-ToF mirror electrodes, can alter the kinetic energy of the ions and can hence lead to a shift of the CLS centroid frequency or to a broadening of the spectral line.

Commercially available power supplies suitable for the proposed system provide peak-to-peak voltage stabilities  $\Delta V/V < 10^{-5}$  within 8 h and residual ripples of less than  $10^{-5} \cdot V + 10$  mV, where  $V$  is the maximal voltage of the anticipated power supplies, i.e. 35 or 65 kV depending on the potential of the respective electrode in the MIRACLS apparatus. We expect to have three different types of voltage fluctuations, those on a time scale much below the revolution period of the MR-ToF device, those on the time scale of a few revolutions in the MR-ToF device as e.g. 50-Hz electrical pick-up and those on a time scale larger than the full measurement cycle.

The latter can be addressed by regular reference scans. Thus, corrections can be made such that voltage drifts over a time period of a few hours are well under control, similarly as for traditional CLS. However, the other two types representing short-term voltage fluctuations can significantly reduce the performance of the setup.

To estimate the reduction in CLS performance due to these, the potentials of the individual mirror electrodes in the simulations are changed every time step while the ions are trapped in the MR-ToF device, either by adding Gaussian white noise or sinusoidal pick-up to the MR-ToF mirror potentials.

The Gaussian white noise is implemented via the polar form of the Box-Muller transformation [67] with a standard deviation of 0.15, 0.25 and 0.5 V. Note that since each ion is simulated independently and the potentials are changed for each ion, individual ions experience different fields during their flight time. Neither the storage efficiency nor the ion-laser overlap are found to be influenced by the added instabilities. No significant increase of temporal ion-bunch width over revolution number is observed when Gaussian white noise with up to 0.25 V standard deviation is added to the individual potentials of the mirror electrodes.

While there is hardly any visible difference for the centroid frequency, the Doppler broadening starts increasing over revolution number as visible in Fig. 11. Because of the statistical nature of this process, the linewidth may temporarily even decrease as visible, for instance, between revolution number 140 and 180 for the shown simulation considering fluctuations with a standard deviation of 0.5 V. Thus, in the scenario of a 0.15-V standard deviation, which is slightly exceeding the quoted peak-to-peak voltage fluctuations of available power supplies, 20 independent simulations are carried out and the worst case over 300 revolution is considered. This highest increase of Doppler broadening is found to be 0.009 MHz per revolution. Hence, high-resolution CLS measurements up to a few thousand revolutions are expected to be possible without any significant reduction in performance of the setup.

The sinusoidal pick-up is implemented with an amplitude of 0.4 V and frequencies between 50 Hz and 200 kHz. The amplitude is motivated by the expected residual ripples of the MR-ToF mirror power supplies. Arbitrary phases between the individual mirror electrodes are assumed, including the case in which the sinusoidal pick-up has the same phase for all electrodes. Neither the storage efficiency nor the ion-laser overlap are influenced by the instabilities described above. The centroid frequency follows the sinusoidal behaviour of the mirror potentials (see Fig. 12 for some selected frequencies), while the Doppler broadening is nearly constant. As long as the sinusoidal period is longer than the revolution period and hence the frequency smaller than 200 kHz, the peak-to-peak changes in resonance centroid are the same

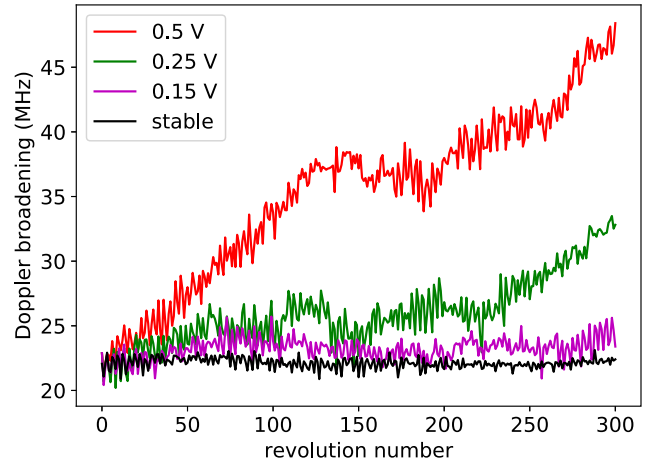


Fig. 11. Doppler broadening (FWHM) versus revolution number for the addition of Gaussian white noise to the potentials of the MR-ToF mirror electrodes. Only ions excitable by a laser with 2-mm beam diameter are taken into account when 300  $^{24}\text{Mg}^+$  ions are evaluated at the transversal middle plane of the MR-ToF device. The consequences are studied for Gaussian white noise with different standard deviations.

and in the order of 8 MHz for the tested frequencies and phases. This is also found when a multiple of the revolution period  $T$  is chosen for the sinusoidal period. Due to the fact that the photon signal of all revolutions are added up, a broadening of the line shape will occur, which is expected to be in the order of 8 MHz.

While for ions within the same ion bunch the phase of the sinusoidal pick-up is always the same, in the experiment the photon signals of more ion bunches will be added up to improve statistics and hence an additional broadening of the line shape will occur in the experiment. This broadening will be smaller than the natural line width up to a few 1000 revolutions and hence high-resolution CLS measurements are expected to be possible even without additional stabilization of the power supplies.

Voltage fluctuations of the potentials applied to the Paul trap extraction electrodes as well as to the central drift tube of the MR-ToF device can lead to a broadening of the line shape or a shift in centroid frequency. Both are however also present in traditional CLS measurements and are thus not expected to degrade the MIRACLS performance in comparison to the conventional technique.

If the stability of the power supplies is unexpectedly worse than their manufacturer's specifications, similar stabilization techniques as discussed in [68–70] can be applied to the 30-keV MR-ToF device power supplies to minimize the increase in Doppler broadening.

### 5.5. Modelling of a realistic in-trap lift switching

Up to this point an ideal high-voltage (HV) switching for the operation of the in-trap lift is assumed, e.g. instantaneous switching from 18.85 kV to ground potential. However, any real HV switch circuit exhibits a non-vanishing time constant in the switching process. To investigate the influence of a realistic HV switch circuit on the performance of MIRACLS, we employ two different circuit models to obtain electrode response functions which can qualitatively describe the trend in the transient behaviour. Firstly, the voltage behaviour over time is measured for the in-trap lift switch used at the 1.5-keV MR-ToF device with  $U_l = 700$  V in MIRACLS' proof-of-principle experiment [18,19] and scaled to  $U_l = 18.85$  kV. Secondly, electronic circuit simulations for a simplified model of the in-trap lift switch of the 30-keV MR-ToF device are performed with the software LTspice [71]. To obtain response functions that can be used in SimIon, the potential curves  $U(t)$  are fitted with the following function for both models:

$$U(t) = \begin{cases} U_l & \text{for } t < 0 \\ U_l \cdot (a \cdot e^{-t/t_f} + (1 - a) \cdot e^{-t/t_s}) & \text{for } t > 0, \end{cases} \quad (3)$$

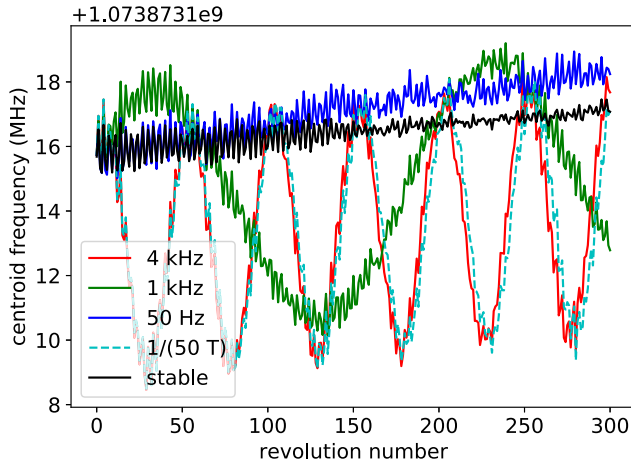


Fig. 12. CLS centroid frequency versus revolution number for the application of sinusoidal voltage variations for 300  $^{24}\text{Mg}^+$  ions evaluated at the transversal middle plane of the MR-ToF device. Sinusoidal voltage fluctuations of 0.4 V amplitude with different frequencies are added to the potentials of the individual MR-ToF mirror electrodes. The dashed light-blue line shows the case when the sinusoidal period  $T$  multiplied with a factor of 50. The slight increase in centroid frequency over revolution number is explained by the chosen geometrical resolution in this simulation, see Appendix.

Table 3

Fit constants as used for the modelling of the high voltage switch, as defined in Eq. (3). The second column (measured) shows the parameters for the in-trap lift at the MIRACLS proof-of-principle experiment, which are measured for  $U_l = 700$  V and scaled to  $U_l = 18.85$  kV. The third column (simulated) lists the parameters for the planned HV switch configuration for the 30-keV MR-ToF device simulated in LTspice. See text for details.

Parameter	Measured	Simulated
$a$	0.992549	1
$t_f$	45.8 ns	42.6 ns
$t_s$	12.84 $\mu$ s	–

The respective fit parameters  $a, t_f, t_s$  can be found in Table 3 and the different switch functions are compared to each other in Fig. 13. We assume two time constants  $t_s$  and  $t_f$ . The fast component  $a \cdot e^{-t/t_f}$  is very similar between scaled measurement and LTspice simulation. However, the scaled measurement shows an additional slow component  $(1 - a) \cdot e^{-t/t_s}$  which is not present in the LTspice simulations. The most likely explanation to the observed difference is the incomplete description of the internal structure of the commercial switch in the simulations and the resulting uncertainty on the involved electrical parasitics.

On closer inspection of the simulated centroid frequency and Doppler broadening over revolution number for 100  $^{24}\text{Mg}^+$  ions (see Fig. 14) no noticeable differences between the ideal switch and the switch simulated in LTspice are observed. For the measurement-based response function, it takes up to 20 revolutions until a stable centroid frequency and Doppler broadening are reached. This is a consequence of the slow component in the HV switching of the in-trap lift potential. Moreover, the centroid frequency and Doppler broadening are significantly larger for the measurement-based switching function compared to the ideal switch as shown in Fig. 14. Within the first 20 revolutions the ions see different potentials of the central drift tube for each revolution, which causes changes in the kinetic energy of the ions over revolution number and hence a change in centroid frequency of almost 2 GHz. When assuming the measurement-based response function, the Doppler broadening accounts for around 42.5 MHz which is in the order of the natural line width. Hence, high-resolution CLS is also possible with the measurement-based in-trap lift switching function.

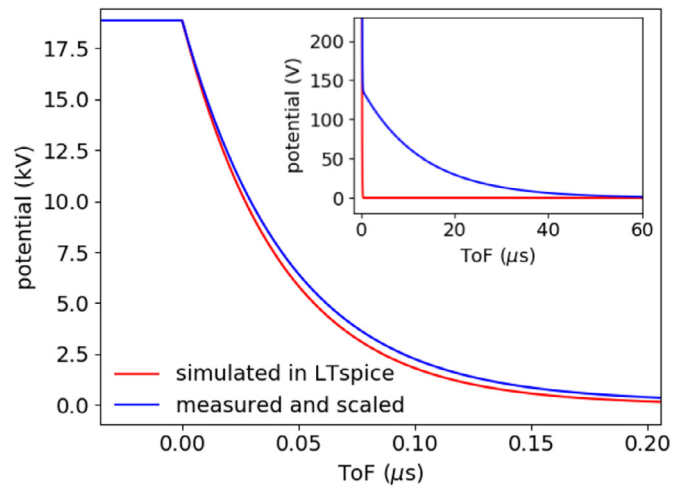


Fig. 13. Different models for the HV switching of the central drift tube are compared. Blue curve: The voltage behaviour over time is measured for the in-trap lift switch used at the MIRACLS proof-of-principle 1.5-keV MR-ToF device and the result is scaled to  $U_l = 18.85$  kV. Red curve: LTspice simulations are performed for the components to be used in the planned configuration of the in-trap lift switch for the 30-keV MR-ToF device. The inset shows a low-voltage region for several tens of microseconds.

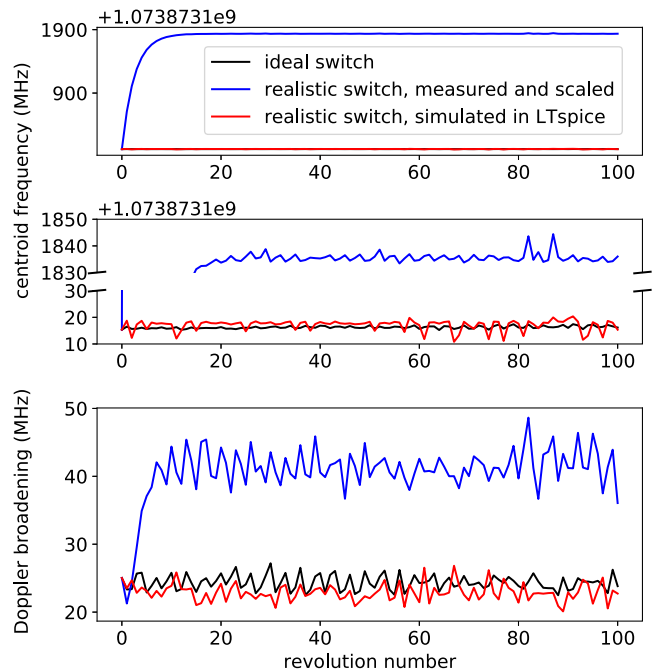
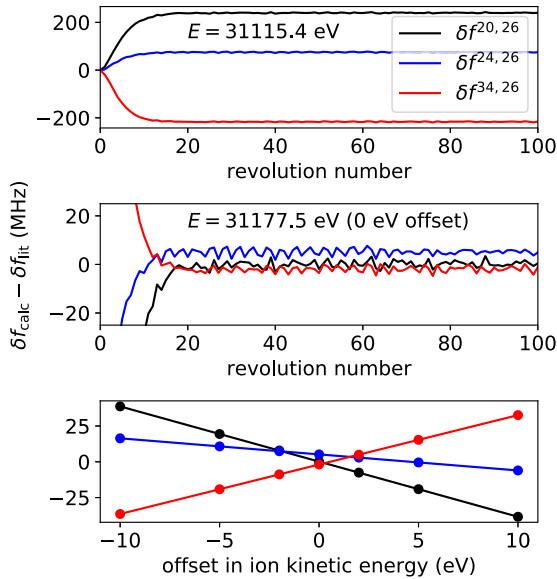


Fig. 14. (Top) Simulated CLS centroid frequency versus revolution number for 100  $^{24}\text{Mg}^+$  ions evaluated at the transversal middle plane of the MR-ToF device for different potential-over-time functions of the in-trap lift switch. In the case of the ideal switch the simulation is done with 1000  $^{24}\text{Mg}^+$  ions. (Middle) A zoom of the top panel. (Bottom) Doppler broadening (FWHM) versus revolution number taking only ions excitable by a laser with 2-mm beam diameter into account for different in-trap lift switching functions. The ions need around 5.05  $\mu$ s to complete one revolution.

The ions' kinetic energy after 20 revolutions (corresponding to a storage time of around 100  $\mu$ s) is approximately 62 eV larger for the measured and scaled in-trap lift switch compared to the ideal case. To obtain the isotope shifts from the experimental data, the measured Doppler-shifted resonance frequencies  $f$  in the laboratory frame as shown in, e.g., Fig. 14 need to be converted to the resonance frequencies  $f_0$  in the rest frame of the ions. This can be done via equation (1) with  $\alpha = 0$ . As usually the case in the analysis of CLS data, the ions



**Fig. 15.** Difference between the calculated isotope shift  $\delta f_{\text{calc}}$  and the (extrapolated) literature value [33,72]  $\delta f_{\text{lit}}$  for different assumed ion energies in the determination of  $\delta f_{\text{calc}}$  in the D1 line. The top figure shows this difference versus revolution number for  $^{20,24,34}\text{Mg}^+$  vs  $^{26}\text{Mg}^+$  ions if the determination of the beam energy assumes an ideal in-trap lift switch ( $E = 31115.4$  eV), while the actual ion energy is governed by a realistic HV switching. The middle figure shows the isotope shift difference as function of revolution number for the actual energy  $E = 31177.5$  eV which the ions end up to have after 25 revolutions in the simulations. The bottom figure shows the mean difference in isotope-shift determination versus offset from the actual energy  $E = 31177.5$  eV, taking all revolutions between 25 and 100 into account. As switching function for the in-trap lift, the measurement-based switching behaviour is used. See text for details.

are assumed to move fully parallel to the laser beam axis, hence  $\alpha = 0$ , since the angles of individual ion trajectories are not experimentally accessible. The velocity of the ions  $v$  is given by

$$v = c \sqrt{1 - \frac{m^2 c^4}{(E + mc^2)^2}} \quad (4)$$

with  $E$  the energy and  $m$  the mass of the ions.

The calculation of the rest frame frequencies requires precise knowledge of the ions' energy. For a switch with a slow time constant, the ions' energy is a priori not well known and can lead to systematic deviations in the order of up to a few 100 MHz in isotope-shift measurements [19]. Indeed, by assuming the ion kinetic energy that the ions would have in case of an ideal lift switching, one would make a systematic error of up to 240 MHz between  $^{20,24,34}\text{Mg}^+$  versus  $^{26}\text{Mg}^+$  as shown in Fig. 15 (top).

When using the actual ion kinetic energy that the ions have after 25 revolutions in the simulations and when neglecting the first 20 revolutions we have systematic deviations of less than 5 MHz in the simulated isotope shifts between  $^{20,24,34}\text{Mg}^+$  versus  $^{26}\text{Mg}^+$  as shown in Fig. 15 (middle). Fig. 15 (bottom) shows the systematic error in the isotope shift for different offsets in the assumed ion energy compared to its literature value. A 5-eV offset in ion kinetic energy leads to a systematic error of up to 20 MHz.

If the transient behaviour of the in-trap lift switch circuit is well understood, the shift in energy due to the realistic HV switching could in principle be corrected in the analysis of the isotope shift. However, in practice an accurate characterization of a fast 20-kV HV switch remains a technical challenge which cannot be easily resolved by a purely simulation approach of the switch circuit.

For this reason, the kinetic energy after a few tens of revolutions in the MR-ToF device needs to be determined by other means. Once the kinetic energy is known for one isotope it can be used for the isotope

**Table 4**

Expected line width broadenings for MIRACLS measurements of the D1 and D2 line in  $\text{Mg}^+$  ions. See text for details.

Cause of broadening	Broadening (MHz)
Natural line width	42
Doppler broadening (depending on in-trap lift switching behaviour)	23–42.5
Gaussian white noise on mirror electrodes	<0.009 MHz per revolution
Sinusoidal noise on mirror electrodes	<8
Total (5000 revolutions)	<75
Total (10,000 revolutions)	<108

shift calculation along the entire isotopic chain as long as there are no additional energy shifts between the individual isotopes, as holds true in the simulations. The beam energy can also be determined via CLS measurements: The very precisely measured resonance frequencies  $f_0$  of the D1 and D2 line in the ions' rest frame of either  $^{24}\text{Mg}^+$  or  $^{26}\text{Mg}^+$  ions can be taken from literature [72]. The kinetic energy can then be calculated according to Eq. (1) from the measured resonance frequency in the laboratory frame of the respective stable isotope. Alternatively, one can determine the rest frame transition frequency  $f_0$  via collinear and anticollinear measurements performed on one specific isotope within the MIRACLS apparatus itself. Once  $f_0$  is known it can be used to determine the beam energy in combination with any collinear or anticollinear measurement carried out at later times. If the same wavemeter for measuring the laser frequency is used, the wavemeter uncertainty is almost eliminated and the beam energy can be determined with a relative uncertainty of  $10^{-5}$  [73]. This would correspond to around 0.3 eV at MIRACLS which is a sufficiently accurate estimation of the experimental ion beam energy for MIRACLS, see Fig. 15 (bottom).

We note that the timing between Paul trap extraction and switching of the in-trap lift needs to be adjusted for each individual isotope, such that the isotope of interest is within the field-free region when the lift is switched for trapping. In the following it is investigated for one specific isotope, namely  $^{24}\text{Mg}^+$ , how the energy is changed when the ion of interest is not exactly in the middle of the in-trap lift when its HV switching for trapping takes place. In the case of the measurement-based switching function, a 0.1- $\mu\text{s}$  offset in the switch timing leads to an offset in the energy of 0.5 eV, corresponding to a systematic error of 16 MHz in the D1 line of Mg (see Fig. 16). In the case of the simulated switch circuit in LTspice, a 0.1- $\mu\text{s}$  offset switch timing just changes the centroid energy by 0.15 eV, corresponding to a systematic error of 4.5 MHz. The change in the centroid energy due to the offset switch timing is in the simulations observed to be mass independent in a range from 20 to 134 u. Provided careful adjustment of the in-trap lift switch timing for each isotope, no significant systematic deviations are expected in CLS measurements at MIRACLS. Appropriate timings can be deduced from the ions' ToF spectra as recorded on a MagneToF detector downstream of the MR-ToF device. Once known for one mass, a scaling to other isotopes is feasible. We investigate this effect nevertheless since there might be (small) uncertainties in the scaling or inaccuracies in the timing signals.

In Table 4 a short summary of the expected line broadenings as relevant for the MIRACLS technique is given, while Table 5 lists the expected systematic deviations on the isotope shift.

The systematic error on the isotope shift arising due to a limited knowledge on the kinetic energy on the 5-eV level is less than 20 MHz. If the switch timing is oppositely offset by 0.1  $\mu\text{s}$  for both isotopes or if it is offset for only one isotope by 0.2  $\mu\text{s}$  a systematic error of 32 MHz originates. This results in a total systematic error of 38 MHz for a future measurement of the isotope shift of  $^{20}\text{Mg}$  to  $^{34}\text{Mg}$  in the most conservative application of MIRACLS. This is comparable in magnitude to systematic uncertainties of previous measurements on exotic Mg isotopes [33]. More recent work in traditional, single-passage CLS reports systematic errors for isotope shifts over the same mass

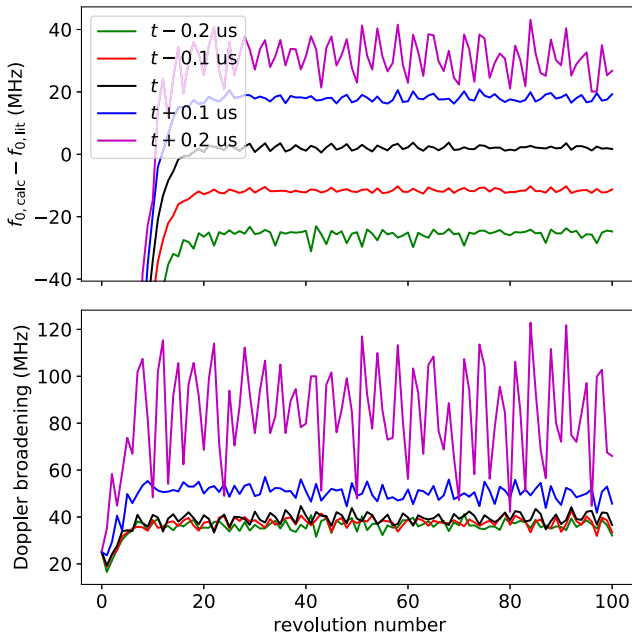


**Fig. 16.** (Top) Difference between the calculated resonance frequency in the ions' rest frame according to Eq. (1) and the literature value [72] versus revolution number for 100  $^{24}\text{Mg}^+$  ions in the D1 line. The simulations are evaluated at the transversal middle plane of the MR-ToF device for different timings between Paul trap extraction and in-trap lift switching. At time  $t$  the ion bunch is exactly in the middle of the central drift tube, when the HV switching is activated. (Bottom) Doppler broadening (FWHM) versus revolution number taking only ions excitable by a laser with 2-mm beam diameter into account for different timings between Paul trap extraction and in-trap lift switching. The measurement-based function for the in-trap lift switch is used.

**Table 5**

Simulated upper limit of the investigated systematic deviations of the MIRACLS technique on the isotope shifts for  $\text{Mg}^+$  ions of mass  $A = 20\text{--}34$  versus  $^{26}\text{Mg}$ . Note that the limited knowledge of the beam energy is both given by the Paul trap acceleration potential as well as by the realistic HV switching of the in-trap lift of the MR-ToF device. By performing simultaneous collinear-anticollinear measurements the systematic error due to the ion energy is eliminated. See text for details.

Cause of error	Uncertainty on isotope shift (MHz)
Limited knowledge of energy on 5-eV level	20
Non-ideal switch timings of in-trap lift	32

difference by a factor of 2 to 10 smaller, e.g. [37,74–77]. There, they are related to the uncertainty of the acceleration potential. Given that an offset in acceleration potential equally effects the kinetic energy of all studied isotopes, an uncertainty in its determination leads to errors in the isotope shifts which are correlated along the entire isotopic chain and increase in size as function of the mass difference to the reference ion. This effect is common to both, MIRACLS as well as traditional single-passage CLS. If absolute, nuclear charge radii are known for at least three isotopes along the studied isotopic chain, a King-plot analysis can be performed. As a result, the systematic error due to incomplete knowledge of the acceleration potential is eliminated in the determination of the other charge radii from the measured isotope shifts.

For MIRACLS, however, an additional systematic error arises due to inaccurate settings in the timings of the HV switching. This can lead to shifts in resonance-centroid frequencies which may vary in size and direction from isotope to isotope and which are not eliminated in the extraction of charge radii via a King-plot analysis. In order to minimize this effect, the consequences of the switch timing on the isotope shift will be studied for the well-known (stable) isotopes before an online experiment. Moreover, the correct switch timings can be precisely determined for abundant (stable) ion species and, then, scaled to its

value for an exotic nuclide. Thus, within the systematic uncertainties estimated above, we do not expect any significant reduction in the performance or accuracy of the MIRACLS technique even when a slow in-trap lift switching is employed.

Finally, if simultaneous collinear-anticollinear laser spectroscopy measurements are performed, the uncertainties on the ions' energies are eliminated [78]. Due to the trapping of the ions in the MR-ToF device, collinear and anticollinear probing of the ions can be done within the same measurement and hence no additional time is required, provided a second laser system is available.

## 6. Conclusion and outlook

The simulation of CLS in the envisioned 30-keV MR-ToF apparatus in combination with the first experimental results of MIRACLS' proof-of-principle experiment [15–19] demonstrate the feasibility of high-resolution CLS in an MR-ToF device and highlight the potential of the novel concept of MIRACLS. Building on the successful benchmarking of the simulation approach against the experimental 1.5-keV proof-of-principle data, extensive simulations of the new 30-keV device and its injection optics have been performed in the present work. Taking the space constraints in the ISOLDE experimental hall into account, suitable geometries and potentials for ion beam preparation and transfer as well as MR-ToF injection and operation have been found.

These allow for > 90% injection and storage efficiency, > 75% ion-laser overlap and a line width approaching the natural line width of the transition of interest. When the electrostatic potentials applied to the MR-ToF mirror electrodes and ion optical elements of the transport beamline are optimized for the requirements of CLS, the shape of the simulated spectral line is neither significantly broadened nor distorted by the combination of CLS and MR-ToF operation. Additional systematic effects such as high-voltage instabilities or non-ideal high-voltage switches do not lead to any significant reduction in performance of the MIRACLS technique in the simulations. This indicates that accuracy and resolution for MIRACLS will be close to traditional single-passage CLS. However, by trapping the ions in the 30-keV MR-ToF device the sensitivity of traditional CLS will be enhanced by more than one to two orders of magnitude.

The construction of the 30-keV MR-ToF device as simulated in this work is currently ongoing and its commissioning will be topic of a future publication. The first MIRACLS measurements are foreseen to be performed on neutron-rich Magnesium isotopes in the island of inversion and Cadmium isotopes at and beyond the  $N=50$  and  $N=82$  neutron shell closures. Following a similar simulation approach but focused on mass separation, we are currently investigating a 30-keV MR-ToF device with the aim to provide high purity radioactive beams to downstream experiments.

## Declaration of competing interest

The authors declare that they have no known competing financial interests or personal relationships that could have appeared to influence the work reported in this paper.

## Data availability

Input data and datasets generated and analysed during the current study are available from the corresponding author on request. The simulation package SimIon itself is available at <https://simion.com/>.

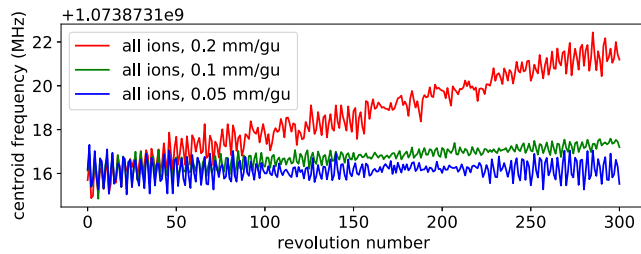


Fig. 17. Simulated CLS centroid frequency versus revolution number for 1000  $^{24}\text{Mg}^+$  ions evaluated at the transversal middle plane of the MR-ToF device for different chosen grid resolutions.

## Acknowledgements

The research leading to these results has received funding from the European Research Council (ERC) under the European Union's Horizon 2020 research and innovation programme under grant agreement No. 679038. The work was additionally supported by the Canadian Natural Science and Engineering Council (NSERC). Part of the work of F.M.M. has been sponsored by the Wolfgang Gentner Programme of the German Federal Ministry of Education and Research, Germany (grant no. 05E18CHA). We are grateful for support of the MIRACLS project from CERN, Switzerland, the ISOLDE Collaboration, Switzerland, and the Max-Planck-Institut für Kernphysik (MPI K) in Heidelberg, Germany.

## Appendix

To improve the accuracy in SimIon the following steps are undertaken in this work: A 3D solid geometry modelling language is used to define the respective geometries of the setup in an ASCII file with .gem extension, which can be directly read in by SimIon. A simplified model of the beamline is included in the simulations to properly define the boundary conditions of the potentials. SimIon's surface enhancement feature is enabled to better model curved surfaces.

The simulations are split into three different geometrical segments. In the simulation segments between Paul trap and Lens 4, a geometrical resolution of 0.5 mm per grid unit is used together with a convergence objective of  $1e-5$  V in electric field refinement. For the final, fully cylindrical symmetric simulation segment including Lens 5 and the MR-ToF device, 0.1 mm per grid unit and  $1e-7$  V are used to minimize computational errors. The maximal size of a time step is given by the time the ions need to travel one grid unit, but a dynamical reduction of its size is enabled to improve accuracy when needed, e.g. close to the electrode surfaces or during the reversal of the axial velocity of the ions in the MR-ToF device.

The ion parameters are passed on to the next simulation segment at user-defined planes, perpendicular to beam propagation, via a Python routine which is executing the respective SimIon simulations for all geometrical segments. In order to ensure smooth transitions, it is required that the adjacent segments have identical fields at the common plane. For the calculation of the ion trajectories relativistic corrections are enabled in SimIon. However, no differences are noticeable for the results presented in this work if a fully classical treatment is chosen.

When trapping the ions for multiple revolutions in the MR-ToF device computational errors may accumulate leading to significant errors after many revolutions. Hence the simulations in this work are limited to the first 300 revolutions.

The inaccuracy of the simulations for too large grid spacing is also evident by a nonphysical change of the energy of individual ions. By comparing different grid resolutions it is verified that the simulations have indeed converged as exemplarily shown for the evolution of the centroid frequency and the ion-bunch width over revolution number in Figs. 17 and 18. While for a geometrical resolution of 0.2 mm per grid unit the centroid frequency increases with revolution number, the

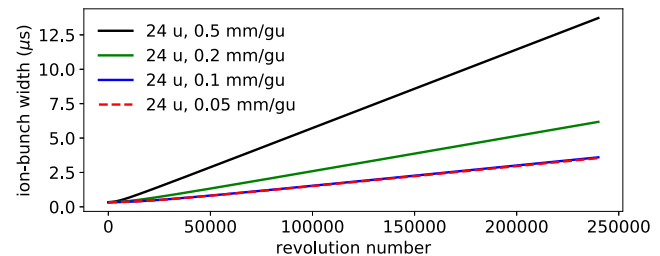


Fig. 18. Ion-bunch width (FWHM) versus revolution number for 1000  $^{24}\text{Mg}^+$  ions with various grid resolutions.

simulations using 0.1 mm per grid unit are almost constant, yielding results close to the ones for 0.05 mm per grid unit. In the case of the evolution of the ion-bunch width over revolution number 0.05 and 0.1 mm per grid unit lead to the same overall behaviour, while 0.2 and 0.5 mm per grid unit would predict a too large increase of ion-bunch width over revolution number. Hence, 0.1 mm grid spacing provides a suitable accuracy for our purposes while the setup and run times of the simulations are still kept reasonably small.

## References

- [1] E.W. Otten, Nuclear radii and moments of unstable isotopes, in: *Treatise on Heavy Ion Science: Volume 8: Nuclei Far from Stability*, Springer US, Boston, MA, 1989, pp. 517–638.
- [2] B. Cheal, K.T. Flanagan, Progress in laser spectroscopy at radioactive ion beam facilities, *J. Phys. G: Nucl. Part. Phys.* 37 (11) (2010) 113101.
- [3] K. Blaum, J. Dilling, W. Nörtershäuser, Precision atomic physics techniques for nuclear physics with radioactive beams, *Phys. Scr.* 2013 (T152) (2013) 014017.
- [4] P. Campbell, I. Moore, M. Pearson, Laser spectroscopy for nuclear structure physics, *Prog. Part. Nucl. Phys.* 86 (2016) 127–180.
- [5] R. Neugart, J. Billowes, M.L. Bissell, K. Blaum, B. Cheal, K.T. Flanagan, G. Neyens, W. Nörtershäuser, D.T. Yordanov, Collinear laser spectroscopy at ISOLDE: new methods and highlights, *J. Phys. G: Nucl. Part. Phys.* 44 (6) (2017) 064002.
- [6] A. Nieminen, P. Campbell, J. Billowes, D.H. Forest, J.A.R. Griffith, J. Huikari, A. Jokinen, I.D. Moore, R. Moore, G. Tungate, J. Äystö, On-line ion cooling and bunching for collinear laser spectroscopy, *Phys. Rev. Lett.* 88 (2002) 094801.
- [7] T. Cocolios, H. Al Suradi, J. Billowes, I. Budinçeviç, R. de Groot, S. De Schepper, V. Fedossev, K. Flanagan, S. Franchoo, R. Garcia Ruiz, H. Heylen, F. Le Blanc, K. Lynch, B. Marsh, P. Mason, G. Neyens, J. Papuga, T. Procter, M. Rajabali, R. Rossel, S. Rothe, G. Simpson, A. Smith, I. Strashnov, H. Stroke, D. Verney, P. Walker, K. Wendt, R. Wood, The Collinear Resonance Ionization Spectroscopy (CRIS) experimental setup at CERN-ISOLDE, *Nucl. Instrum. Methods Phys. Res. B* 317 (2013) 565–569.
- [8] R.P. de Groot, J. Billowes, C.L. Binnensley, M.L. Bissell, T.E. Cocolios, T. Day Goodacre, G.J. Farooq-Smith, D.V. Fedorov, K.T. Flanagan, S. Franchoo, R.F. Garcia Ruiz, W. Gins, J.D. Holt, Á. Koszorús, K.M. Lynch, T. Miyagi, W. Nazarewicz, G. Neyens, P.G. Reinhard, S. Rothe, H.H. Stroke, A.R. Vernon, K.D.A. Wendt, S.G. Wilkins, Z.Y. Xu, X.F. Yang, Measurement and microscopic description of odd–even staggering of charge radii of exotic copper isotopes, *Nat. Phys.* 16 (6) (2020) 620–624.
- [9] Á. Koszorús, X.F. Yang, W.G. Jiang, S.J. Novario, S.W. Bai, J. Billowes, C.L. Binnensley, M.L. Bissell, T.E. Cocolios, B.S. Cooper, R.P. de Groot, A. Ekström, K.T. Flanagan, C. Forssén, S. Franchoo, R.F.G. Ruiz, F.P. Gustafsson, G. Hagen, G.R. Jansen, A. Kanellakopoulos, M. Kortelainen, W. Nazarewicz, G. Neyens, T. Papenbrock, P.G. Reinhard, C.M. Ricketts, B.K. Sahoo, A.R. Vernon, S.G. Wilkins, Charge radii of exotic potassium isotopes challenge nuclear theory and the magic character of N=32, *Nat. Phys.* 17 (2021) 439–443.
- [10] R. Heinke, T. Kron, S. Raeder, T. Reich, P. Schönberg, M. Trümper, C. Weichhold, K. Wendt, High-resolution in-source laser spectroscopy in perpendicular geometry. Development and application of the PI-LIST, *Hyperfine Interact.* 238 (2017) 6.
- [11] R. Ferrer, A. Barzakh, B. Bastin, R. Beerwerth, M. Block, P. Creemers, H. Grawe, R. de Groot, P. Delahaye, X. Fléchard, S. Franchoo, S. Fritzsche, L.P. Gaffney, L. Ghys, W. Gins, C. Granados, R. Heinke, L. Hijazi, M. Loiselet, F. Lutton, I.D. Moore, Y. Martínez, E. Mogilevskiy, P. Naubereit, J. Piot, S. Raeder, S. Rothe, H. Savajols, S. Sels, V. Sonnenschein, J.-C. Thomas, E. Traykov, C. Van Beveren, P. Van den Bergh, P. Van Duppen, K. Wendt, A. Zadvornaya, Towards high-resolution laser ionization spectroscopy of the heaviest elements in supersonic gas jet expansion, *Nature Commun.* 8 (1) (2017) 14520.

[12] S. Raeder, M. Block, P. Chhetri, R. Ferrer, S. Kraemer, T. Kron, M. Laatiaoui, S. Nothhelfer, F. Schneider, P. Van Duppen, M. Verlinde, E. Verstraelen, T. Walther, A. Zadvornaya, A gas-jet apparatus for high-resolution laser spectroscopy on the heaviest elements at SHIP, *Nucl. Instrum. Methods Phys. Res. B* 463 (2020) 272–276.

[13] S. Sels, F.M. Maier, M. Au, P. Fischer, C. Kanitz, V. Lagaki, S. Lechner, E. Leistenschneider, D. Leimbach, E.M. Lykiardopoulou, A.A. Kwiatkowski, T. Manovitz, Y.N. Vila Gracia, G. Neyens, P. Plattner, S. Rothe, L. Schweikhard, M. Vilen, R.N. Wolf, S. Malbrunot-Ettenauer, Doppler and sympathetic cooling for the investigation of short-lived radioactive ions, *Phys. Rev. Res.* 4 (2022) 033229.

[14] R.F.G. Ruiz, C. Gorges, M. Bissell, K. Blaum, W. Gins, H. Heylen, K. Koenig, S. Kaufmann, M. Kowalska, J. Krämer, P. Lievens, S. Malbrunot-Ettenauer, R. Neugart, G. Neyens, W. Nörterhäuser, D.T. Yordanov, X.F. Yang, Development of a sensitive setup for laser spectroscopy studies of very exotic calcium isotopes, *J. Phys. G: Nucl. Part. Phys.* 44 (4) (2017) 044003.

[15] F.M. Maier, P. Fischer, H. Heylen, V. Lagaki, S. Lechner, P. Plattner, S. Sels, F. Wienholtz, W. Nörterhäuser, L. Schweikhard, S. Malbrunot-Ettenauer, Simulations of a proof-of-principle experiment for collinear laser spectroscopy within a multi-reflection time-of-flight device, *Hyperfine Interact.* 240 (1) (2019) 54.

[16] S. Lechner, P. Fischer, H. Heylen, V. Lagaki, F. Maier, P. Plattner, M. Rosenbusch, S. Sels, F. Wienholtz, R.N. Wolf, W. Nörterhäuser, L. Schweikhard, S. Malbrunot-Ettenauer, Fluorescence detection as a new diagnostics tool for electrostatic ion beam traps, *Hyperfine Interact.* 240 (1) (2019) 95.

[17] V. Lagaki, P. Fischer, H. Heylen, F. Hummer, S. Lechner, S. Sels, F. Maier, P. Plattner, M. Rosenbusch, F. Wienholtz, R. Wolf, W. Nörterhäuser, L. Schweikhard, S. Malbrunot-Ettenauer, Stray-light suppression for the MIRACLS proof-of-principle experiment, *Acta Phys. Polon. B* 51 (2020) 571–576.

[18] S. Sels, P. Fischer, H. Heylen, V. Lagaki, S. Lechner, F. Maier, P. Plattner, M. Rosenbusch, F. Wienholtz, R. Wolf, W. Nörterhäuser, L. Schweikhard, S. Malbrunot-Ettenauer, First steps in the development of the Multi Ion Reflection Apparatus for Collinear Laser Spectroscopy, *Nucl. Instrum. Methods Phys. Res. B* 463 (2020) 310–314.

[19] V. Lagaki, H. Heylen, I. Belosevic, P. Fischer, C. Kanitz, S. Lechner, F. Maier, W. Nörterhäuser, P. Plattner, M. Rosenbusch, S. Sels, L. Schweikhard, M. Vilen, F. Wienholtz, R. Wolf, S. Malbrunot-Ettenauer, An accuracy benchmark of the MIRACLS apparatus: Conventional, single-passage collinear laser spectroscopy inside a MR-ToF device, *Nucl. Instrum. Methods Phys. Res. A* 1014 (2021) 165663.

[20] F.M. Maier, Laser Spectroscopy of Short-Lived- Radionuclides in an Ion Trap: MIRACLS' Proof-of-Principle Experiment and the Simulation of the Future 30-keV MR-ToF Device (M.Sc. thesis), Johannes Kepler University Linz, 2019.

[21] A. Piechaczek, V. Shchepunov, H.K. Carter, J.C. Batchelder, E.F. Zganjar, S.N. Liddick, H. Wollnik, Y. Hu, B.O. Griffith, Development of a high resolution isobar separator for study of exotic decays, *Nucl. Instrum. Methods Phys. Res. B* 266 (19) (2008) 4510–4514.

[22] W.R. Plaß, T. Dickel, U. Czok, H. Geissel, M. Petrick, K. Reinheimer, C. Scheidenberger, M. I.Yavor, Isobar separation by time-of-flight mass spectrometry for low-energy radioactive ion beam facilities, *Nucl. Instrum. Methods Phys. Res. B* 266 (19–20) (2008) 4560–4564.

[23] P. Schury, K. Okada, S. Shchepunov, T. Sonoda, A. Takamine, M. Wada, H. Wollnik, Y. Yamazaki, Multi-reflection time-of-flight mass spectrograph for short-lived radioactive ions, *Eur. Phys. J. B* 42 (3) (2009) 343.

[24] F. Wienholtz, D. Beck, K. Blaum, C. Borgmann, M. Breitenfeldt, R.B. Cakirli, S. George, F. Herfurth, J.D. Holt, M. Kowalska, S. Kreim, D. Lunney, V. Manea, J. Menéndez, D. Neidherr, M. Rosenbusch, L. Schweikhard, A. Schwenk, J. Simonis, J. Stanja, R.N. Wolf, K. Zuber, Masses of exotic calcium isotopes pin down nuclear forces, *Nature* 498 (7454) (2013) 346–349.

[25] R.N. Wolf, D. Beck, K. Blaum, C. Böhm, C. Borgmann, M. Breitenfeldt, F. Herfurth, A. Herlert, M. Kowalska, S. Kreim, D. Lunney, S. Naimi, D. Neidherr, M. Rosenbusch, L. Schweikhard, J. Stanja, F. Wienholtz, K. Zuber, On-line separation of short-lived nuclei by a multi-reflection time-of-flight device, *Nucl. Instrum. Methods Phys. Res. A* 686 (2012) 82–90.

[26] R. Wolf, F. Wienholtz, D. Atanasov, D. Beck, K. Blaum, C. Borgmann, F. Herfurth, M. Kowalska, S. Kreim, Y.A. Litvinov, D. Lunney, V. Manea, D. Neidherr, M. Rosenbusch, L. Schweikhard, J. Stanja, K. Zuber, ISOLTRAP's multi-reflection time-of-flight mass separator/spectrometer, *Int. J. Mass Spectrom.* 349–350 (2013) 123–133, 100 years of Mass Spectrometry.

[27] T. Dickel, W. Plaß, A. Becker, U. Czok, H. Geissel, E. Haettner, C. Jesch, W. Kinsel, M. Petrick, C. Scheidenberger, A. Simon, M. Yavor, A high-performance multiple-reflection time-of-flight mass spectrometer and isobar separator for the research with exotic nuclei, *Nucl. Instrum. Methods Phys. Res. A* 777 (2015) 172–188.

[28] M. Reiter, S.A.S. Andrés, J. Bergmann, T. Dickel, J. Dilling, A. Jacobs, A. Kwiatkowski, W. Plaß, C. Scheidenberger, D. Short, C. Will, C. Babcock, E. Dunling, A. Finlay, C. Hornung, C. Jesch, R. Klawitter, B. Kootte, D. Lascar, E. Leistenschneider, T. Murböck, S. Paul, M. Yavor, Commissioning and performance of TITAN's Multiple-Reflection Time-of-Flight Mass-Spectrometer and isobar separator, *Nucl. Instrum. Methods Phys. Res. A* 1018 (2021) 165823.

[29] P. Chauveau, P. Delahaye, G. De France, S. El Abir, J. Lory, Y. Merrer, M. Rosenbusch, L. Schweikhard, R. Wolf, PILGRIM, a multi-reflection time-of-flight mass spectrometer for Spiral2-S3 at GANIL, *Nucl. Instrum. Methods Phys. Res. B* 376 (2016) 211–215, Proceedings of the XVIth International Conference on Electromagnetic Isotope Separators and Related Topics, EMIS2015, Grand Rapids, MI, U.S.A., 11–15 May 2015.

[30] B. Liu, M. Brodeur, D. Burdette, J. Kelly, T. Kim, J. Long, P. O'Malley, The performance of the commissioned Notre Dame multi-reflection time-of-flight mass spectrometer, *Nucl. Instrum. Methods Phys. Res. A* 985 (2021) 164679.

[31] F. Nowacki, A. Obertelli, A. Poves, The neutron-rich edge of the nuclear landscape: Experiment and theory, *Prog. Part. Nucl. Phys.* 120 (2021) 103866.

[32] M. Hammen, W. Nörterhäuser, D.L. Balabanski, M.L. Bissell, K. Blaum, I. Budinčević, B. Cheal, K.T. Flanagan, N. Frömmgen, G. Georgiev, C. Geppert, M. Kowalska, K. Kreim, A. Krieger, W. Nazarewicz, R. Neugart, G. Neyens, J. Papuga, P.-G. Reinhard, M.M. Rajabali, S. Schmidt, D.T. Yordanov, From calcium to cadmium: Testing the pairing functional through charge radii measurements of  $^{100-130}\text{Cd}$ , *Phys. Rev. Lett.* 121 (2018) 102501.

[33] D.T. Yordanov, M.L. Bissell, K. Blaum, M. De Rydt, C. Geppert, M. Kowalska, J. Krämer, K. Kreim, A. Krieger, P. Lievens, T. Neff, R. Neugart, G. Neyens, W. Nörterhäuser, R. Sánchez, P. Vingerhoets, Nuclear charge radii of  $^{21-32}\text{Mg}$ , *Phys. Rev. Lett.* 108 (2012) 042504.

[34] R.F. García Ruiz, M.L. Bissell, K. Blaum, A. Ekström, N. Frömmgen, G. Hagen, M. Hammen, K. Hebeler, J.D. Holt, G.R. Jansen, M. Kowalska, K. Kreim, W. Nazarewicz, R. Neugart, G. Neyens, W. Nörterhäuser, T. Papenbrock, J. Papuga, A. Schwenk, J. Simonis, K.A. Wendt, D.T. Yordanov, Unexpectedly large charge radii of neutron-rich calcium isotopes, *Nat. Phys.* 12 (6) (2016) 594–598.

[35] P.-G. Reinhard, W. Nazarewicz, Toward a global description of nuclear charge radii: Exploring the Fayans energy density functional, *Phys. Rev. C* 95 (2017) 064328.

[36] K. Minamisono, D.M. Rossi, R. Beerwerth, S. Fritzsche, D. Garand, A. Klose, Y. Liu, B. Maas, P.F. Mantica, A.J. Miller, P. Müller, W. Nazarewicz, W. Nörterhäuser, E. Olsen, M.R. Pearson, P.-G. Reinhard, E.E. Saperstein, C. Sumithrarachchi, S.V. Tolokonnikov, Charge radii of neutron deficient  $^{52,53}\text{Fe}$  produced by projectile fragmentation, *Phys. Rev. Lett.* 117 (2016) 252501.

[37] S. Malbrunot-Ettenauer, S. Kaufmann, S. Bacca, C. Barbieri, J. Billowes, M.L. Bissell, K. Blaum, B. Cheal, T. Duguet, R.F.G. Ruiz, W. Gins, C. Gorges, G. Hagen, H. Heylen, J.D. Holt, G.R. Jansen, A. Kanellakopoulos, M. Kortelainen, T. Miyagi, P. Navrátil, W. Nazarewicz, R. Neugart, G. Neyens, W. Nörterhäuser, S.J. Novario, T. Papenbrock, T. Ratajczyk, P.-G. Reinhard, L.V. Rodríguez, R. Sánchez, S. Sailer, A. Schwenk, J. Simonis, V. Somá, S.R. Stroberg, L. Wehner, C. Wraith, L. Xie, Z.Y. Xu, X.F. Yang, D.T. Yordanov, Nuclear charge radii of the nickel isotopes  $^{58-68,70}\text{Ni}$ , *Phys. Rev. Lett.* 128 (2022) 022502.

[38] H. Hergert, A guided tour of ab initio nuclear many-body theory, *Front. Phys.* 8 (2020).

[39] T. Miyagi, S.R. Stroberg, J.D. Holt, N. Shimizu, Ab initio multishell valence-space Hamiltonians and the island of inversion, *Phys. Rev. C* 102 (2020) 034320.

[40] S.J. Novario, G. Hagen, G.R. Jansen, T. Papenbrock, Charge radii of exotic neon and magnesium isotopes, *Phys. Rev. C* 102 (2020) 051303.

[41] G. Hagen, S.J. Novario, Z.H. Sun, T. Papenbrock, G.R. Jansen, J.G. Lietz, T. Duguet, A. Tichai, Angular-momentum projection in coupled-cluster theory: structure of  $^{34}\text{Mg}$ , 105, 2022, 064311.

[42] P. Plattner, The Charge Radius of  $^{26m}\text{Al}$  and the Design of an Advanced Optical Detection Region for Collinear Laser Spectroscopy (Ph.D. thesis), University Innsbruck, 2022.

[43] S. Kaufman, High-resolution laser spectroscopy in fast beams, *Opt. Commun.* 17 (3) (1976) 309–312.

[44] M. Lange, M. Froese, S. Menk, J. Varju, R. Bastert, K. Blaum, J.R.C. Lopez-Urrutia, F. Fellenberger, M. Grieser, R. von Hahn, O. Heber, K.-U. Kühnel, F. Laux, D.A. Orlov, M.L. Rappaport, R. Repnow, C.D. Schröter, D. Schwalm, A. Shornikov, T. Sieber, Y. Toker, J. Ullrich, A. Wolf, D. Zajfman, A cryogenic electrostatic trap for long-time storage of keV ion beams, *Rev. Sci. Instrum.* 81 (5) (2010) 055105.

[45] H. Wollnik, M. Przewloka, Time-of-flight mass spectrometers with multiply reflected ion trajectories, *Int. J. Mass Spectrom. Ion Process.* 96 (3) (1990) 267–274.

[46] D. Zajfman, O. Heber, L. Vejby-Christensen, I. Ben-Itzhak, M. Rappaport, R. Fishman, M. Dahan, Electrostatic bottle for long-time storage of fast ion beams, *Phys. Rev. A* 55 (1997) R1577–R1580.

[47] W.H. Benner, A gated electrostatic ion trap to repetitiously measure the charge and m/z of large electrospray ions, *Anal. Chem.* 69 (20) (1997) 4162–4168.

[48] C. Kanitz, Construction and Characterization of a Paul Trap for Laser Spectroscopy of Exotic Radionuclides in an MR-ToF Device (M.Sc. thesis), Friedrich-Alexander-University Erlangen-Nürnberg, 2019.

[49] S. Lechner, Laser Spectroscopy of Antimony Isotopes and the Design of a Cryogenic Paul Trap (Ph.D. thesis), Technical University Vienna, 2021.

[50] Y. Kudryavtsev, P. Creemers, R. Ferrer, C. Granados, L. Gaffney, M. Huyse, E. Mogilevskiy, S. Raeder, S. Sels, P. Van den Berg, P. Van Duppen, A. Zadvornaya, A new in-gas-laser ionization and spectroscopy laboratory for off-line studies at KU Leuven, *Nucl. Instrum. Methods Phys. Res. B* 376 (2016) 345–352, Proceedings of the XVIth International Conference on Electromagnetic Isotope Separators and Related Topics, EMIS2015, Grand Rapids, MI, U.S.A., 11–15 May 2015.

[51] V. Fedossev, K. Chrysalidis, T. Goodacre, B. Marsh, S. Rothe, C. Seiffert, K. Wendt, Ion beam production and study of radioactive isotopes with the laser ion source at ISOLDE, *J. Phys. G: Nucl. Part. Phys.* 44 (2017) 084006.

[52] R.N. Wolf, G. Marx, M. Rosenbusch, L. Schweikhard, Static-mirror ion capture and time focusing for electrostatic ion-beam traps and multi-reflection time-of-flight mass analyzers by use of an in-trap potential lift, *Int. J. Mass Spectrom.* 313 (2012) 8–14.

[53] C. Breitenfeldt, M.W. Froese, K. Blaum, S. George, M. Grieser, M. Lange, S. Menk, R. Repnow, D. Schwalm, L. Schweikhard, R. von Hahn, A. Wolf, Spreading times of ion-bunches in the cryogenic trap for fast ion beams, *Int. J. Mass Spectrom.* 396 (2016) 1–4.

[54] P. Fischer, S. Knauer, G. Marx, L. Schweikhard, In-depth study of in-trap high-resolution mass separation by transversal ion ejection from a multi-reflection time-of-flight device, *Rev. Sci. Instrum.* 89 (1) (2018) 015114.

[55] D. Manura, D. Dahl, SIMION 8.1 User Manual, 2008.

[56] D. Manura, SIMION HSI collision model REV4, 2007.

[57] H. Frånberg, P. Delahaye, J. Billowes, K. Blaum, R. Catherall, F. Duval, O. Gianfrancesco, T. Giles, A. Jokinen, M. Lindroos, D. Lunney, E. Mane, I. Podadera, Off-line commissioning of the ISOLDE cooler, *Nucl. Instrum. Methods Phys. Res. B* 266 (19) (2008) 4502–4504, Proceedings of the XVth International Conference on Electromagnetic Isotope Separators and Techniques Related to their Applications.

[58] S. Schwarz, G. Bollen, R. Ringle, J. Savory, P. Schury, The LEBIT ion cooler and buncher, *Nucl. Instrum. Methods Phys. Res. A* 816 (2016) 131–141.

[59] B. Barquest, G. Bollen, P. Mantica, K. Minamisono, R. Ringle, S. Schwarz, C. Sumithrarachchi, RFQ beam cooler and buncher for collinear laser spectroscopy of rare isotopes, *Nucl. Instrum. Methods Phys. Res. A* 866 (2017) 18–28.

[60] I. Podadera, M. Lindroos, R. Catherall, T. Giles, H. Franberg, J. Billowes, F. Duval, E. Mane, P. Delahaye, A. Jokinen, ISCOOL: cooled and bunched beams for ISOLDE, 2007.

[61] P. Fischer, S. Knauer, G. Marx, L. Schweikhard, Non-isobaric time-of-flight correction for isobar resolving in MR-ToF mass spectrometry, *Int. J. Mass Spectrom.* 432 (2018) 44–51.

[62] M. Rosenbusch, M. Wada, P. Schury, Y. Ito, H. Ishiyama, S. Ishizawa, Y. Hirayama, S. Kimura, T. Kojima, H. Miyatake, J. Moon, T. Niwase, T. Sonoda, A. Takamine, Y. Watanabe, H. Wollnik, A new multi-reflection time-of-flight mass spectrograph for the SLOWRI facility, *Nucl. Instrum. Methods Phys. Res. B* 463 (2020) 184–188.

[63] W. Ansborcher, Y. Li, E. Pinnington, Precision lifetime measurement for the 3p levels of Mg II using frequency-doubled laser radiation to excite a fast ion beam, *Phys. Lett. A* 139 (3) (1989) 165–169.

[64] D.L. Moehring, B.B. Blinov, D.W. Gidley, R.N. Kohn, M.J. Madsen, T.D. Sanderson, R.S. Vallery, C. Monroe, Precision lifetime measurements of a single trapped ion with ultrafast laser pulses, *Phys. Rev. A* 73 (2006) 023413.

[65] D. Manura, SIMION Simplex optimizer, 2007.

[66] National Nuclear Data Center, Brookhaven National Laboratory, 2022.

[67] G.E.P. Box, M.E. Muller, A note on the generation of random normal deviates, *Ann. Math. Stat.* 29 (2) (1958) 610–611.

[68] F. Wienholtz, K. Blaum, J. Karthein, D. Lunney, S. Malbrunot-Ettenauer, V. Manea, M. Mougeot, L. Schweikhard, T. Steinsberger, R. Wolf, Improved stability of multi-reflection time-of-flight mass spectrometers through passive and active voltage stabilization, *Nucl. Instrum. Methods Phys. Res. B* 463 (2020) 348–356.

[69] P. Fischer, L. Schweikhard, Multiple active voltage stabilizations for multi-reflection time-of-flight mass spectrometry, *Rev. Sci. Instrum.* 92 (6) (2021) 063203.

[70] P. Schury, M. Wada, H. Wollnik, J.-Y. Moon, T. Hashimoto, M. Rosenbusch, High-stability, high-voltage power supplies for use with multi-reflection time-of-flight mass spectrographs, *Rev. Sci. Instrum.* 91 (1) (2020) 014702.

[71] Analog Devices, LTspice simulation software, 2007.

[72] V. Batteiger, S. Knünz, M. Herrmann, G. Saathoff, H.A. Schüssler, B. Bernhardt, T. Wilken, R. Holzwarth, T.W. Hänsch, T. Udem, Precision spectroscopy of the  $3s - 3p$  fine-structure doublet in  $Mg^+$ , *Phys. Rev. A* 80 (2009) 022503.

[73] K. König, K. Minamisono, J. Lantis, S. Pineda, R. Powel, Beam energy determination via collinear laser spectroscopy, *Phys. Rev. A* 103 (2021) 032806.

[74] C. Gorges, L.V. Rodríguez, D.L. Balabanski, M.L. Bissell, K. Blaum, B. Cheal, R.F. García Ruiz, G. Georgiev, W. Gins, H. Heylen, A. Kanellakopoulos, S. Kaufmann, M. Kowalska, V. Lagaki, S. Lechner, B. Maaß, S. Malbrunot-Ettenauer, W. Nazarewicz, R. Neugart, G. Neyens, W. Nörtershäuser, P.-G. Reinhard, S. Sailer, R. Sánchez, F. Schmidt, L. Wehner, C. Wraith, L. Xie, Z.Y. Xu, X.F. Yang, D.T. Yordanov, Laser spectroscopy of neutron-rich tin isotopes: A discontinuity in charge radii across the  $N = 82$  shell closure, *Phys. Rev. Lett.* 122 (2019) 192502.

[75] H. Heylen, C.S. Devlin, W. Gins, M.L. Bissell, K. Blaum, B. Cheal, L. Filippin, R.F.G. Ruiz, M. Godefroid, C. Gorges, J.D. Holt, A. Kanellakopoulos, S. Kaufmann, Á. Koszorús, K. König, S. Malbrunot-Ettenauer, T. Miyagi, R. Neugart, G. Neyens, W. Nörtershäuser, R. Sánchez, F. Sommer, L.V. Rodríguez, L. Xie, Z.Y. Xu, X.F. Yang, D.T. Yordanov, High-resolution laser spectroscopy of  $^{27-32}Al$ , *Phys. Rev. C* 103 (2021) 014318.

[76] S.V. Pineda, K. König, D.M. Rossi, B.A. Brown, A. Incorvati, J. Lantis, K. Minamisono, W. Nörtershäuser, J. Piekarewicz, R. Powel, F. Sommer, Charge radius of neutron-deficient  $^{54}Ni$  and symmetry energy constraints using the difference in mirror pair charge radii, *Phys. Rev. Lett.* 127 (2021) 182503.

[77] A.J. Miller, K. Minamisono, A. Klose, D. Garand, C. Kujawa, J.D. Lantis, Y. Liu, B. Maaß, P.F. Mantica, W. Nazarewicz, W. Nörtershäuser, S.V. Pineda, P.-G. Reinhard, D.M. Rossi, F. Sommer, C. Sumithrarachchi, A. Teigelhöfer, J. Watkins, Proton superfluidity and charge radii in proton-rich calcium isotopes, *Nat. Phys.* 15 (5) (2019) 432–436.

[78] W. Nörtershäuser, D. Tiedemann, M. Žáková, Z. Andjelkovic, K. Blaum, M.L. Bissell, R. Cazan, G.W.F. Drake, C. Geppert, M. Kowalska, J. Krämer, A. Krieger, R. Neugart, R. Sánchez, F. Schmidt-Kaler, Z.-C. Yan, D.T. Yordanov, C. Zimmermann, Nuclear charge radii of  $^{7,9,10}Be$  and the one-neutron halo nucleus  $^{11}Be$ , *Phys. Rev. Lett.* 102 (2009) 062503.

### **8.3 Increased Beam Energy as a Pathway Towards a Highly Selective and High-Flux MR-ToF Mass Separator**

# Increased Beam Energy as a Pathway Towards a Highly Selective and High-Flux MR-ToF Mass Separator

F.M. Maier<sup>a,b,\*</sup>, F. Buchinger<sup>c</sup>, L. Croquette<sup>c</sup>, P. Fischer<sup>b</sup>, H. Heylen<sup>a</sup>, F. Hummer<sup>a,c</sup>, C. Kanitz<sup>a</sup>, A.A. Kwiatkowski<sup>h</sup>, V. Lagaki<sup>a</sup>, S. Lechner<sup>a,c</sup>, E. Leistenschneider<sup>a</sup>, G. Neyens<sup>a,d</sup>, P. Plattner<sup>a,e</sup>, A. Roitman<sup>c</sup>, M. Rosenbusch<sup>b,f</sup>, L. Schweikhard<sup>b</sup>, S. Sels<sup>a</sup>, M. Vilen<sup>a</sup>, F. Wienholtz<sup>a,g</sup>, S. Malbrunot-Ettenauer<sup>a,h,i</sup>

<sup>a</sup>*Experimental Physics Department, CERN, CH-1211 Geneva 23, Switzerland*

<sup>b</sup>*Institut für Physik, Universität Greifswald, 17487 Greifswald, Germany*

<sup>c</sup>*McGill University, Montréal, Québec, H3A 2T8, Canada*

<sup>d</sup>*Instituut voor kern- en stralingsfysica, KU Leuven, Celestijnenlaan 200D, Leuven, Belgium*

<sup>e</sup>*Universität Innsbruck, Innrain 52, 6020 Innsbruck, Austria*

<sup>f</sup>*Wako Nuclear Science Center (WNSC), Institute of Particle and Nuclear Studies (IPNS), High Energy Accelerator Research Organization (KEK), Wako, Saitama 351-0198, Japan*

<sup>g</sup>*Institut für Kernphysik, Technische Universität Darmstadt, Schlossgartenstr. 9, 64289 Darmstadt, Germany*

<sup>h</sup>*TRIUMF, 4004 Wesbrook Mall, Vancouver, BC V6T 2A3, Canada*

<sup>i</sup>*Department of Physics, University of Toronto, 60 St. George St., Toronto, Ontario, Canada*

## Abstract

Many experiments at radioactive ion beam (RIB) facilities suffer from isobaric contamination, i.e. unwanted ions of similar mass. During the last decade, Multi-Reflection Time-of-Flight (MR-ToF) devices have gained remarkable attention for mass separation of short-lived, low-intensity beams of radionuclides at RIB facilities throughout the world. They exceed mass resolving powers  $m/\Delta m$  of  $10^5$  within a processing time of some (tens of) milliseconds. Due to space-charge effects, however, the mass separation remains an experimental challenge when many ions are simultaneously confined in the MR-ToF device. This limits the wider application of MR-ToF mass separators at RIB facilities. By performing ion-optical simulations including space-charge effects, we investigate different schemes of ion preparation in a Paul trap upstream of the MR-ToF device as well as MR-ToF operation and study their influence on mass separation and maximal ion flux. The validity of these simulations are benchmarked by time-of-flight and collision-induced fluorescence measurements with a 1.5-keV MR-ToF device. More advanced ion-beam preparation techniques such as the use of laser cooling, buffer-gas cooling at cryogenic temperatures or specific electric-field parameters for ion trapping and ejection from the Paul trap can significantly reduce the processing time needed to reach a given mass resolving power. However, the simulations of these methods also indicate that space-charge effects in the MR-ToF device become relevant at lower ion numbers compared to 'standard' ion preparation. Thus, the overall amount of mass separated ions per unit of time remains essentially the same. In contrast, the simulations suggest that increasing the kinetic energy of typically just a few kiloelectronvolts in present MR-ToF instruments to 30 keV results in a significant increase of the attainable maximal ion flux.

## 1. Introduction

Many experiments at radioactive ion beam (RIB) facilities require pure ion beams with high intensity. Existing mass separators, such as the high-resolution mass separator at ISOLDE/CERN [1], use dipole magnets and achieve mass resolving powers  $R = m/\Delta m$  in the order of a few 1000. Next-generation magnetic mass separators such as the high-resolution isobar separator for the CARIBU project [2, 3], the SPIRAL2/DESIR high resolution mass separator [4, 5] or the CANREB high-resolution separator at TRIUMF [6] are in the process of reaching mass resolving powers of up to 20,000-30,000. There remain, however, many applications which require an even higher

mass resolving power to suppress isobaric contamination, i.e. unwanted ions of similar mass.

Recently, Multi-Reflection Time-of-Flight (MR-ToF) devices have significantly gained in importance for the mass separation of short-lived radionuclides at RIB facilities throughout the world [7–17]. Since they exceed mass resolving powers  $R$  of  $10^5$  within just some (tens of) milliseconds they are capable of providing isobaric-purified ion beams to subsequent experiments. In an MR-ToF device ions are separated in time-of-flight (ToF) according to their mass-over-charge ratio  $m/q$ . Compared to conventional ToF separation, the high mass resolving power is achieved as ion bunches are bouncing back and fourth between two electrostatic mirrors. Hence, a flight path of several kilometers is realised while the ions are confined in a table-top instrument. MR-ToF mass separation at high  $R$  is, however, only possible up to a limited number of ions.

\*Corresponding author

Email address: [franziska.marie.maier@cern.ch](mailto:franziska.marie.maier@cern.ch) (F.M. Maier)

At large ion densities, the Coulomb interactions between the ions can no longer be neglected and, thus, so-called space-charge effects degrade the otherwise superb mass separation capabilities. In particular, phenomena such as selfbunching [18–25] and peak coalescence [22, 25–27] at increased numbers of stored ions have been reported in MR-ToF devices. As a consequence, the ion species do not separate in  $m/q$  any longer when too many ions are simultaneously confined.

However, virtually all fields of rare isotope science pursued at low-energy branches of RIB facilities would benefit from isobaric pure beams with a high ion intensity. For some initiatives such as the antiProton Unstable Matter Annihilation (PUMA) project [28] for the study of the interaction of anti-matter with radioactive nuclides, pure radioactive ion beams are an indispensable prerequisite. Even applications closer to stability like the production of innovative medical isotopes [29, 30] suffer from isobaric contamination. An advanced beam purification apparatus with a large ion flux could reduce the need of chemical separation and would hence reduce the radioactive activity during transport and handling as well as the radioactive waste.

Magnetic separators are expected to continue exceeding MR-ToF systems in ion flux while the latter remain superior in attainable mass resolving power. The ultimate configuration would, thus, combine mass separation in stages in which a high resolution magnetic separator delivers a ‘pre-separated’ RIB to an MR-ToF device ideally with a higher ion throughput compared to current state-of-the-art MR-ToF instruments. Magnetic dipole separation and MR-ToF separation differ in their time structure of operation. While magnetic mass separators work for a continuous beam of ions, a bunched beam structure is required for MR-ToF operation. Hence a Paul trap acting as a cooler-buncher is typically installed upstream of an MR-ToF system.

Employing ion optical simulations including ion-ion interactions, the present work investigates options to increase the mass resolving power of MR-ToF devices and the maximal ion flux while maintaining the large mass resolving power. Our findings suggest that, while the ion preparation in a cooler-buncher prior to the MR-ToF device has for most applications no significant influence on the maximal ion flux possible at a given resolving power, increasing the kinetic energy of the stored ions from 1.5 keV to 30 keV could substantially increase the number of mass separated ions per unit of time.

To benchmark the validity of the simulation approach, time-of-flight studies of ion bunches extracted from the MR-ToF device as well as collisional-induced fluorescence measurements with a 1.5-keV MR-ToF device [24, 26, 27, 31, 35, 36] are carried out. For the latter, we take advantage of inelastic collisions between ions and residual gas particles leading to fluorescence [24, 37]. The detection of the emitted photons enables the tracking of the evolution of the ion bunch’s temporal spread over revolution num-

ber [24] and thereby understand the ion dynamics within the MR-ToF device for varying numbers of stored ions.

The next section introduces general characteristics of MR-ToF systems and section 3 describes the experimental setup consisting of a 1.5-keV MR-ToF device used for benchmarking the simulation code. In section 4 the simulated mass resolving power is compared with and validated by the experimental one. Afterwards the simulation code is employed to investigate the advantages of a 30-keV MR-ToF mass separator in the context of single-ion counting experiments where ion-ion interactions are negligible. In section 5 space-charge effects are taken into account between the ensemble of one single ion species and between two different ion species. The simulation results are benchmarked against the collisional excitation data from the 1.5-keV MR-ToF device. In section 6 we study the ion flux in MR-ToF devices and explore and simulate different possibilities to increase it. Our simulation results indicate that a significantly higher ion throughput is possible when the ion-beam energy is increased from 1.5 keV to 30 keV. Section 7 introduces such a novel 30-keV MR-ToF apparatus, which is currently under construction at ISOLDE/CERN as part of the MIRACLS project.

## 2. General Characteristics of MR-ToF systems

Typically an MR-ToF system consists of a Paul trap forming bunched beams, some injection optics and the MR-ToF device itself, in which the ion bunch is reflected back and forth between two electrostatic mirrors (see figure 1). After some revolutions within the confining electrostatic fields in the MR-ToF device the ions are ejected onto a downstream detector either by lowering the potentials of the mirror electrodes or by raising the kinetic energy of the ions via the technique of in-trap lift switching [38].

Important performance characteristics are mass resolving power, processing time and maximal ion flux. The mass resolving power (also see equation 2) describes the capability of the device to mass separate two ion species with masses  $m$  and  $m + \Delta m$  with abundance ratio  $r_{ab} = N_1/N_2$ , where  $N_1$  is the number of ions with mass  $m$  and  $N_2$  is the number of ions with mass  $m + \Delta m$ .

The processing time  $t_{\text{proc}}$  describes how long it takes to mass separate the stored ions, so the needed time until a given mass resolving power is reached. It is a sum of the preparation time  $t_{\text{prep}}$  of the ion bunch in the Paul trap (typically 2 ms) and the storage time  $t_s$  in the MR-ToF device required to achieve the desired mass separation (typically a few (tens of) milliseconds). In case of parallel preparation of an ion bunch in the Paul trap and mass separation of another ion bunch in the MR-ToF device  $t_{\text{proc}}$  is given by  $\max(t_s, t_{\text{prep}})$ .

The maximal ion flux  $\phi$  is given by the number of ions which can be mass separated per unit of time,

$$\phi = \frac{N_{\text{max}}}{t_{\text{proc}}} = \frac{N_{\text{max}}}{\max(t_s, t_{\text{prep}})} \quad (1)$$

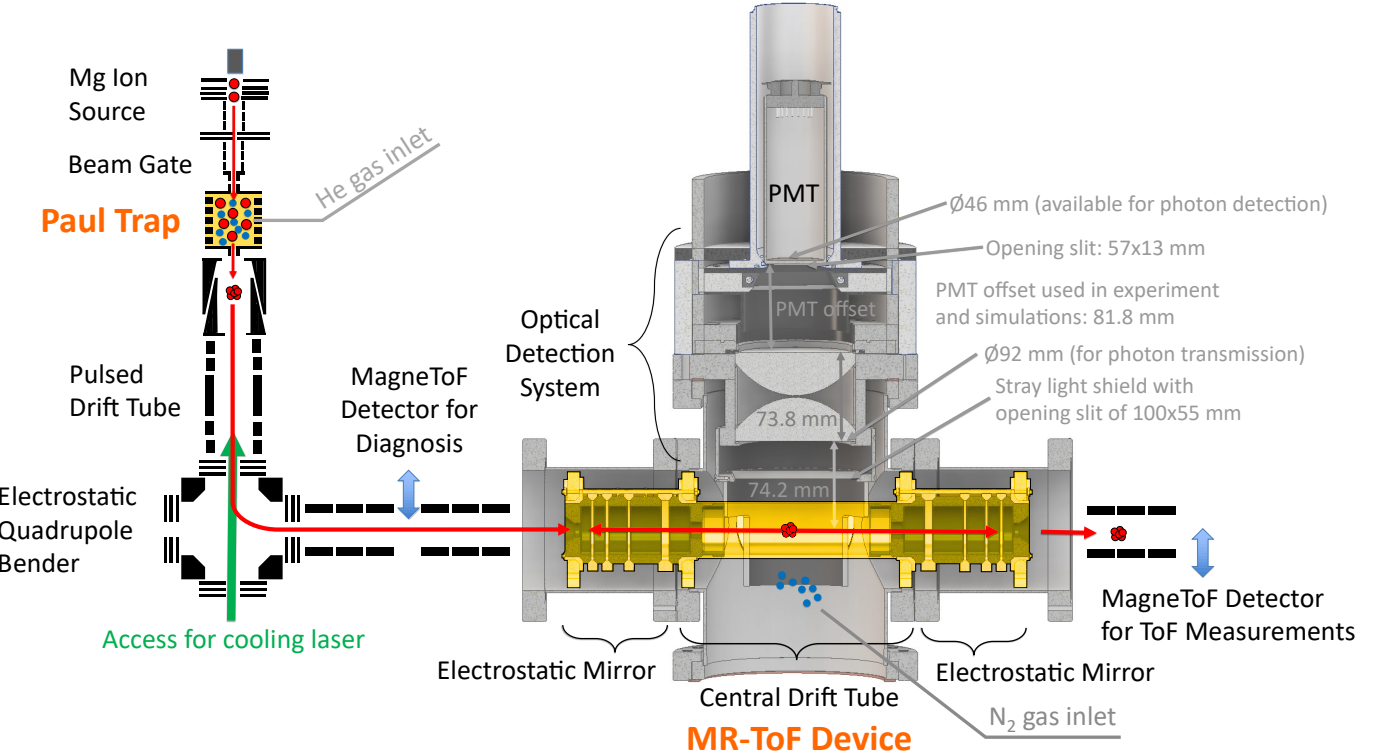


Figure 1: Schematic overview of the MIRACLS low-energy setup at ISOLDE, which operates at 1.5-keV beam energy and takes up a floor space of around 1.5 m x 2 m. Only the MR-ToF section and the optical detection system located above the central drift tube of the MR-ToF device are to scale. The central drift tube is made out of a conductive mesh as discussed in [31]. An optical lens system, adapted from [32, 33], images the collisional-induced fluorescence photons onto a photomultiplier tube (PMT). For the laser cooling measurements a second quadrupole bender was installed between the ion source and the Paul trap allowing to monitor the cooling laser passing through the Paul trap openings, see [34]. For an explanation of the ions' path see text. The dimensions stated are relevant for optical ray tracing simulations as discussed in section 5.1.

It is limited by the processing time  $t_{\text{proc}}$  as well as by the maximal ion number  $N_{\text{max}}$  that can be confined simultaneously in the MR-ToF device without notable space-charge effects between the ions due to repulsive Coulomb interactions.

The mass resolving power at the detector plane follows [12]

$$R = \frac{m}{\Delta m} = \frac{t}{2\Delta t} = \frac{t_0 + rt_1 + t_d}{2\sqrt{\Delta t_0^2 + (r\Delta t_1)^2}}, \quad (2)$$

where  $t$  is the ions' total flight time upon extraction from the Paul trap and  $\Delta t$  is the temporal spread of the ion bunch at the detector. The total flight time  $t$  is the sum of the time  $t_0$  required to transport the ions from the Paul trap to the middle of the MR-ToF device, the storage time  $t_s = rt_1$ , and the time  $t_d$  the ions travel from the middle of the MR-ToF device to the ion detector after ejection.  $r$  is the number of revolutions and  $t_1$  is the duration of a full revolution i.e. the period.  $\Delta t_0$  is the initial bunch width when the ions pass the transversal middle plane of the MR-ToF device for the first time. Finally,  $\Delta t_1$  is the ToF peak-width broadening per revolution in the MR-ToF device. In the limit of infinite revolutions, the mass resolving power is given by  $R_{\text{inf}} = t_1/(2\Delta t_1)$ . The initial time spread  $\Delta t_0$

mainly determines the processing time, so how long it takes to reach a certain mass resolving power  $R < R_{\text{inf}}$ .  $\Delta t$ ,  $\Delta t_0$  and  $\Delta t_1$  are given as the full-width-at-half-maximum (FWHM) of the ToF peak width throughout this work.

Note that equation 2 strictly holds true only when the time-focus plane<sup>1</sup> is set close to the detector plane [38] without trapping in the MR-ToF device. In this case, starting from  $\Delta t_0$ , the ion bunch width is steadily increasing with revolution number caused by unwanted ion-optical aberrations.  $\Delta t_0$  is given by the turn-around time in the Paul trap [13] and an additional contribution in case the time-focus point is not set exactly to the middle plane of the MR-ToF device. The mass resolving power hence increases almost linearly for the first few milliseconds, until it approaches  $R_{\text{inf}}$ .

The spatial location of the time-focus plane depends on the extraction field strength in the Paul trap. The stronger the extraction field gradient from the Paul trap, the more the time-focus point shifts closer towards the Paul trap [39]. Thus, in order to place this time-focus point

<sup>1</sup>The time-focus point corresponds to the moment when the faster ions, which are initially at the end of the ion bunch, overtake the slower ions, which left the Paul trap first.

close to the detector plane, as necessary for application of equation 2, the extraction field strength is limited to a certain range depending on the distance between Paul trap and MR-ToF device [39]. This allows to keep the potential tune of the MR-ToF mirror electrodes largely independent of the number of revolutions in the MR-ToF device. This approach is followed in the present work. Alternatively, the initial voltage of the central drift tube can be varied in the in-trap lift technique to adjust the position of the time focus onto the detector plane for each revolution number separately [38]. Moreover, the dynamical time-focus-shift technique [39] can be applied to keep the potential tune independent of the number of revolutions in the MR-ToF device.

### 3. Experimental Setup

In the following the MIRACLS low-energy MR-ToF setup at ISOLDE/CERN [24, 31, 34–36, 40], a typical MR-ToF system operating at 1.5-keV beam energy, is introduced. This setup is used for the experimental studies in this work, which allow to benchmark the simulation code and to illustrate and understand important MR-ToF characteristics. Figure 1 shows an overview of the setup. It includes an electron-impact ionization source similar to reference [41], producing a continuous beam of singly-charged ions of stable magnesium isotopes  $^{24,25,26}\text{Mg}^+$ . These ions are injected into a linear Paul trap which acts as a cooler-buncher to accumulate ions and obtain bunched beams. An electrostatic steerer upstream of the Paul trap is used as a beam gate to control the number of ions injected into the Paul trap. In the Paul trap, the ions can either be cooled by Helium buffer gas at room-temperature and  $\approx 3\text{e-}6$  mbar Helium pressure as measured in the surrounding vacuum chamber or by performing a combination of buffer-gas and laser cooling in which the former is done with the background residual gas present in the system. If only 300-K beam temperature is required, standard buffer-gas cooling can be applied and a cooling time of 2 ms is normally sufficient, depending on the buffer-gas pressure in the Paul trap. For Doppler cooling a continuous-wave laser beam with a wavelength of 280 nm is sent into the Paul trap. Within around 100 ms of ion-storage time in the Paul trap, the  $\text{Mg}^+$  ions can be laser-cooled down to a few Kelvin. More details about Paul-trap operation and laser cooling in this setup are found in reference [34].

After ion extraction from the Paul trap, the ion bunch is deflected by an electrostatic quadrupole bender onto the axis of the MR-ToF device. There, it is captured by the in-trap lift [38] and trapped for thousands of revolutions at a beam energy of around 1.5 keV. After a given storage time in the MR-ToF device, the ions are ejected (again by activating the in-trap lift [38]) and impinge on a MagneToF detector for time-of-flight measurements. Another MagneToF detector is installed in front of the MR-ToF device to allow improved diagnostics of its capture efficiency. The MR-ToF component itself consists of two opposing

electrostatic mirrors and a central drift tube. Each mirror is made out of four concentric ring electrodes. The MR-ToF device has a total length of 384 mm and the central drift tube has a length of 212 mm. More details can be found in references [31, 35, 36].

For studies of the device's mass resolving power, the outermost three mirror electrodes are passively stabilized and the second outermost one is also actively stabilized. This reduces the impact of voltage fluctuations on the ions' flight time, following a similar stabilization procedure as discussed in [42, 43].

For collision-induced fluorescence studies, above the central drift tube of the MR-ToF device an optical lens system adapted from references [32, 33] and a photomultiplier tube are mounted for detection of the emitted photons. In order to increase the collision probability of the  $\text{Mg}^+$  ions with residual gas particles, the background pressure in the MR-ToF device can be increased to  $1\text{e-}7$  mbar by leaking in nitrogen gas. For this purpose, a precision needle valve is installed at the vacuum chamber close to the central drift tube.

## 4. Studies of the Mass Resolving Power

### 4.1. Simulations of the mass resolving power

To investigate the advantages of an increased beam energy on the mass resolving power and processing time, a dedicated simulation code is developed and validated by experimental measurements of the mass resolving power as a function of the storage time  $t_s$  in MIRACLS' low-energy MR-ToF setup. The measurements are performed in single-ion counting mode where ion-ion interactions are negligible, hence space-charge effects are also neglected in the simulations. (In section 5 Coulomb interactions will be added to the simulation code.)

The simulations targeting the mass resolving power are carried out with the software package SIMION following the procedure described in reference [31]. Firstly, simulations of the ion preparation in the Paul trap are performed by employing SIMION's built-in hard-sphere interaction model [44] and/or a custom-made code for Doppler cooling [34]. A thousand  $^{24}\text{Mg}^+$  ions are positioned around the potential minimum of the Paul trap and left to thermalize with room-temperature or 5-K buffer-gas and/or are Doppler cooled. After extraction of the ion bunches from the Paul trap, they pass the ion optical elements and are captured in the MR-ToF device.

Each time the ions pass the middle plane of the MR-ToF device, their time-of-flight is recorded. The release of the ions from the MR-ToF device is not taken into account. It is shown for some selected settings that the time  $t_d$  the ions travel from the middle of the MR-ToF device to the ion detector after ejection can be neglected in the simulations as well as in the experiment for this particular geometry and chosen extraction field strengths.

To evaluate equation 2 for simulated data, the times  $t_0$  and  $t_1$  as well as the initial time spread  $\Delta t_0$  follow directly from the simulated ion distribution. In principle,  $\Delta t$  after many thousands of revolutions and, thus, the peak width broadening per revolution  $\Delta t_1$  would follow from the simulated ion distribution, too. In practice, however, only a few hundred revolutions can be simulated with sufficient accuracy. Hence the ions are studied for only up to 100 revolutions. The peak-width broadening  $\Delta t_1$  over 100 revolutions is very small for optimized settings. To observe the small changes of the ion bunch width  $\Delta t$  over revolution number in the simulated data, the flight time of each ion in the MR-ToF device is evaluated with respect to the time the ion first crosses the transversal middle plane of the MR-ToF device. This means for the determination of the peak-width broadening  $\Delta t_1$ , the initial time spread  $\Delta t_0$  is artificially set to zero when the ions are captured in the MR-ToF device, see also reference [45]. The resulting time spread  $\Delta t$  considering all ions after 100 revolutions is divided by the revolution number to obtain  $\Delta t_1$ . For a given scenario (Paul-trap operation, transfer beam line, MR-ToF mirrors) all required input values for equation 2 are thus extracted from the simulations and the corresponding mass resolving power is obtained.

#### 4.2. Optimization of the mass resolving power

To optimize the mass resolving power a similar optimization procedure as described in reference [46] is followed. Firstly, the potentials of the four mirror electrodes constituting one MR-ToF mirror are varied in a Monte Carlo approach [31] for a fixed initial ion distribution. Secondly, the potential combinations leading to the largest  $R_{\text{inf}}$  are further optimized employing SIMION's built-in Nelder-Mead algorithm [47]. The ion injection simulation for the best mirror potentials is then optimized via the Nelder-Mead algorithm for a large transport and trapping efficiency. Finally, the in-trap lift potential is chosen such that the time for one revolution  $t_1$  is fairly independent of the potential applied to the in-trap lift and hence the energy of the ions. Operating the MR-ToF device in this so-called isochronous mode boosts  $R_{\text{inf}}$ . The obtained potentials are stated in table 1.

Table 1: Potentials for the MR-ToF mirror electrodes and the in-trap lift as obtained in the optimization procedure described in the text. The in-trap lift potential needs to be readjusted for different extraction field strengths from the Paul trap.

respective electrode	potential (V)
mirror electrode 1 (innermost)	-4776.6
mirror electrode 2	1215.8
mirror electrode 3	995.3
mirror electrode 4 (outermost)	1881.9
in-trap lift	778.0 to 801.0

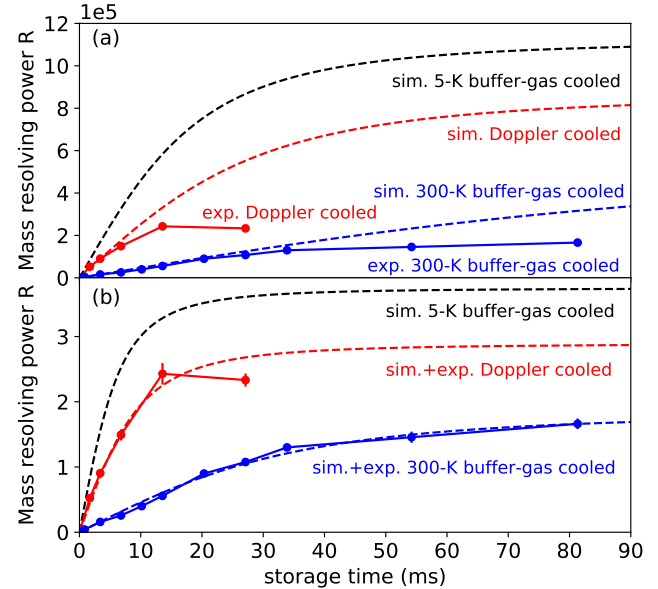


Figure 2: Mass resolving power versus storage time for 300-K buffer gas, 5-K buffer gas and Doppler cooling for  $^{24}\text{Mg}^+$  ions in MIRACLS' 1.5-keV MR-ToF device. For Doppler cooling and 300-K buffer-gas cooling the experimental (full line) as well as the simulated mass resolving power (dashed line) is shown. Figure (b) is the same as (a) but the simulated peak-width broadening per revolution is multiplied with a factor of 3 which yields a good agreement with the experimentally obtained mass resolving power curve, see text. The revolution period  $t_1$  is  $6.62\ \mu\text{s}$ .

#### 4.3. Comparison between Simulations and Experiment

In figure 2(a) the experimental and simulated mass resolving power is shown as a function of the storage time in the MR-ToF device for buffer-gas as well as Doppler cooling in the Paul trap. The measurement procedure of the mass resolving power is the same as discussed in [34]. Note that in our Doppler-cooling work only the longitudinal motion is cooled by the laser beam [34]. For comparison, an additional simulation with 5-K buffer-gas temperature in the Paul trap is depicted. The potential tune of injection electrodes and mirror electrodes has been optimized for 300-K buffer-gas cooling in the Paul trap, but also leads to very good results for 5-K buffer-gas cooling. This was confirmed by performing a dedicated potential optimization of injection and MR-ToF mirror optics for 5-K buffer-gas cooling, which yielded a similar mass resolving power as the potential tune found for 300-K buffer-gas cooling.

The initial, almost linear increase in mass resolving power can be well reproduced in simulations. It is governed by the initial peak width  $\Delta t_0$ , which shows an excellent agreement between simulations and experiment, see also references [31, 34]. For 5-K buffer-gas cooling  $\Delta t_0$  is 10 ns, for Doppler cooling it is 19 ns (corresponding to 15-K buffer-gas cooling)<sup>2</sup> and for 300-K buffer-gas cooling it is 106 ns (measurements performed with the Paul

<sup>2</sup>Note that this laser-cooling result is due to a particular combi-

trap settings at the time being, for possible improvements see section 4.4). Hence, for laser cooling a mass resolving power of 100,000 can be reached within 4 ms storage time in the MR-ToF device; for 5-K buffer-gas cooling this can be achieved in 2 ms whereas for 300-K buffer-gas cooling a storage time of 22 ms is needed. The ion preparation time in the Paul trap is for buffer-gas cooling around 2 ms, whereas it is significantly increased for laser cooling to around 100 ms given the reduced buffer-gas pressure and the power density of the cooling laser. Therefore, the total processing time for mass separation of the ions is longer for laser cooling than for buffer-gas cooling for these first laser-cooling measurements [34].

Due to the peak-width broadening per revolution  $\Delta t_1$ , the mass resolving power approaches the maximally possible  $R_{\text{inf}}$  after some ion storage time in the MR-ToF device. For 5-K buffer-gas cooling  $R_{\text{inf}}$  is larger compared to Doppler cooling or 300-K buffer-gas cooling. This is related to the smaller longitudinal emittance which scales linearly with the ion beam temperature [48]. A reduction in longitudinal emittance results both in a reduced time as well as energy spread [34]. Due to the smaller initial time spread, a specific  $R$  value is reached faster and due to the reduced energy spread the peak-width broadening per revolution  $\Delta t_1$  is decreased and  $R_{\text{inf}}$  is significantly larger compared to room-temperature buffer-gas cooling.

As visible in figure 2(a) there is a significant mismatch between simulated and measured mass resolving power for larger storage times. This can be corrected by multiplying the simulated peak-width broadening per revolution with the same factor of 3 for both buffer-gas and Doppler cooling, see figure 2(b).

The mismatch of the experimental and simulated peak-width broadening per revolution could possibly be explained by voltage instabilities of the mirror electrodes or energy fluctuations prior to the injection of the ions in the MR-ToF device. To investigate this further, Gaussian white noise is added to the potentials applied to the mirror electrodes. The Gaussian white noise is implemented via the polar form of the Box-Muller transformation [49] with varying standard deviations and the potential is changed every time step of the simulation and for each ion individually. As such, we consider voltage fluctuations occurring during the storage cycle and voltage fluctuations between different storage cycles. Figure 3 shows a decrease in  $R_{\text{inf}}$  with increasing electrical noise. However, the experimentally determined [50] voltage fluctuations have temporal standard deviations below 0.1 V in agreement with the spec-

nation of low-pressure buffer-gas and laser cooling as explained in reference [34]. Laser cooling is capable to prepare ion bunches with even smaller ToF widths and, thus, in principle, also to improve MR-ToF operation even further. The purpose of the mass resolving power measurements is to benchmark the simulations and to experimentally show that colder ion beams lead to a faster mass separation and to an increased  $R_{\text{inf}}$ . More modern MR-ToF devices exceed in  $R_{\text{inf}}$  even with conventional ion preparation, but would also benefit from colder beams for an additional boost in  $R_{\text{inf}}$ .

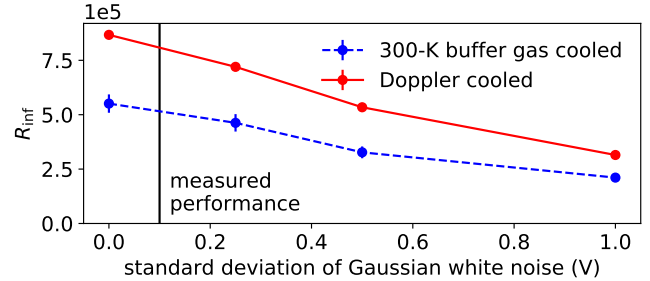


Figure 3: Simulated mass resolving power in the limit of infinite revolutions  $R_{\text{inf}}$  as a function of the standard deviation of the Gaussian white noise added to the mirror electrodes of the 1.5-keV MR-ToF device for Doppler and 300-K buffer-gas cooling. The standard deviation of the voltage fluctuations in the experiment are less than 0.1 V as indicated by the black vertical line.

ifications of the power supplies. Hence, only a minimal increase of the peak-width broadening per revolution is expected and the factor 3 mismatch cannot be explained by voltage fluctuations.

Another reason for this mismatch could be the residual gas pressure in the MR-ToF device in the experiment, whereas the MR-ToF simulations are performed assuming perfect vacuum. The importance of a good vacuum quality in the MR-ToF device has been reported repeatedly [13, 14] and is observed in the present experiment as well. If more helium buffer gas is leaked into the Paul trap, the MR-ToF vacuum quality is reduced and  $R_{\text{inf}}$  is decreased. For instance, when the Helium pressure in the MR-ToF device is increased from  $1.2\text{e-}7$  mbar to  $3\text{e-}7$  mbar,  $R_{\text{inf}}$  is reduced by a factor of 2.4 for the buffer-gas cooling case. Hence, the mismatch of the experimental and simulated peak-width broadening per revolution is most likely due to residual gas particles.<sup>3</sup>

It can be concluded that the simulations are a powerful tool to find a set of MR-ToF mirror and injection potentials which allows to reach a good mass resolving power in the experiment. While the initial increase in mass resolving power is very well reproduced, the final mass resolving power  $R_{\text{inf}}$  is for both laser and buffer-gas cooling around a factor 3 overestimated in the simulations compared to experiment, which is most likely originating from the fact that collisions with residual gas particles are not taken into account in the simulations.

<sup>3</sup>For taking collisions between ions and residual gas particles into account in the MR-ToF simulations the knowledge of the cross sections for all ion energies in the MR-ToF device ranging from 0 to 5 keV would be required. (In our MR-ToF mirror configuration, see table 1, ions are temporarily accelerated up to 5 keV in the refocusing sections (mirror electrode 1) of the electrostatic mirrors.) The hard-sphere interaction model which is employed for simulating the buffer-gas cooling of ions of a few electronvolts in the Paul trap may, however, not be sufficiently accurate for the present purpose and ion energy range.

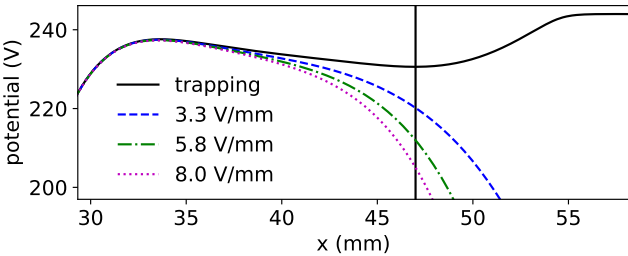


Figure 4: Electrostatic potential along the central axis of the Paul trap of MIRACLS' low-energy MR-ToF apparatus for trapping of the ions and for three different ion extraction modes. For the latter, the potential applied to the Paul-trap's endcap is switched from 244 V during trapping to a lower value which has a strong impact on the axial field experienced by the ions. Applying 169 V, 110 V and 60 V to the extraction endcap results in field gradients at the position of the potential minimum of 3.3 V/mm, 5.8 V/mm and 8.0 V/mm, respectively. The vertical black line indicates the position of the potential minimum for trapping.

#### 4.4. Operation of a 1.5-keV MR-ToF device with different Paul trap preparation schemes

For MR-ToF operation at RIB facilities with short-lived radionuclides it is important to reach a good mass resolving power in a processing time which is smaller than the nuclide's lifetime. This is a challenge for rare isotopes with halflives in the order of a few milliseconds. Therefore the initial time spread  $\Delta t_0$  needs to be as small as possible. As discussed in the previous section, laser cooling or cryogenic buffer-gas cooling lead to a much faster initial increase in mass resolving power compared to 300-K buffer-gas cooling. Nevertheless, because of its simplicity, room-temperature buffer-gas cooling is more commonly used at contemporary RIB facilities. To still reach a good mass resolving power in a short amount of time, a high extraction field strength is often applied during the Paul trap extraction [39]. The electrostatic potential along the central axis of the Paul trap in MIRACLS' low-energy apparatus is shown in figure 4 for ion trapping and three different extraction modes. The chosen cooling times in the Paul trap are always 2 ms. A higher extraction field strength reduces  $\Delta t_0$  at the cost of an increased energy spread of the ion bunch because of the conserved longitudinal emittance (see figure 14 in reference [34]).

As a consequence, the peak-width broadening per revolution  $\Delta t_1$  and thus MR-ToF performance can be degraded if the energy spread  $\Delta E$  gets too large<sup>4</sup>. Figure 5(a) illustrates this interplay between  $\Delta t_0$  and  $\Delta E$  on the mass resolving power in our simulation studies. The Paul trap extraction scheme with a field strength of 3.3 V/mm results in  $\Delta E = 2.3$  eV and  $\Delta t_0 = 106$  ns and in a relatively slow increase in  $R$  over MR-ToF storage time (blue curve). For example,  $R = 1e5$  is reached after 22 ms. A steeper extraction field with 8 V/mm yields  $\Delta t_0 = 33$  ns

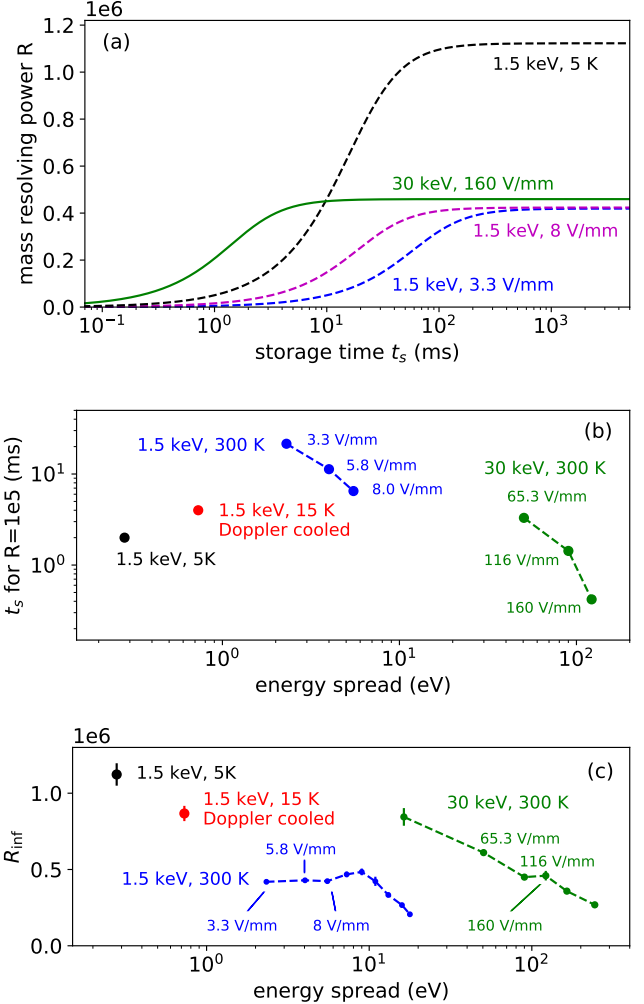


Figure 5: Results of simulation studies for 1.5-keV and 30-keV beam energy with different Paul trap settings in MIRACLS' low-energy MR-ToF setup. (a) Mass resolving power versus storage time  $t_s$  for some selected settings. The dashed blue and dashed black curve reshown the same data as depicted in figure 2(a). (b) Minimum storage time  $t_s$  for reaching  $R = 1e5$ . Note that for determination of  $t_s$  equation 2 is not applicable for extraction field strengths outside the range 3-8 V/mm for 1.5-keV beam energy or 65-160 V/mm for 30-keV beam energy (see section 4.1). (c)  $R_{\text{inf}}$  as a function of the energy spread of the ions for 1.5-keV beam energy and for 30-keV energy. For 1.5-keV beam energy the revolution period  $t_1$  is 6.62  $\mu$ s and for 30-keV beam energy it is 1.48  $\mu$ s.

and  $\Delta E = 5.5$  eV (pink curve). Thus, higher mass resolving powers are obtained in a much shorter storage time. In particular,  $R = 1e5$  is reached after 6.5 ms, around 3.4 times faster than for 3.3 V/mm. Note that for 5-K buffer gas cooling  $\Delta t_0$  does not show any dependence on the extraction field strength as also discussed in reference [34]. When increasing the extraction field strength further to achieve even smaller storage times in the MR-ToF device for 300-K buffer-gas cooling,  $R_{\text{inf}}$  will significantly decrease (see figure 5(c)).

Figure 5(b) and 5(c) show the processing time, here evaluated by the storage time  $t_s$  needed to reach  $R >$

<sup>4</sup> $\Delta E$  is in this work always given as FWHM of the energy distribution of the ions.

1e5, and the ultimate mass resolving power  $R_{\text{inf}}$ , respectively, for various energy spreads  $\Delta E$  of the ion ensemble. Note that for the calculation of  $t_s$  from the simulations (as shown in figure 5(b)) the time-focus point needs to be close to the detector, while the determination of  $R_{\text{inf}} = t_1/(2\Delta t_1)$  (in figure 5(c)) is independent of the position of the time-focus point. For room-temperature buffer-gas cooling, it is again the variation of the extraction field strength from the Paul trap which allows one to reduce  $\Delta t_0$  at the cost of the increased  $\Delta E$  and vice versa.

As expected, the processing time is shorter (smaller  $t_s$ ) the smaller  $\Delta t_0$  and, thus, the larger  $\Delta E$  (see blue curve in figure 5(b)). Similarly,  $R_{\text{inf}}$  is increasing with decreasing  $\Delta E$  (and increasing  $\Delta t_0$ ), see blue curve in figure 5(c). Interestingly, this is only true above about  $\Delta E \approx 9$  eV. There  $R_{\text{inf}}$  reaches a maximum below which  $R_{\text{inf}}$  is again decreasing with lower  $\Delta E$ . This is interpreted as a consequence of a too soft extraction field strength which has a negative impact on the transversal phase space and thus, also on the peak-width broadening per revolution  $\Delta t_1$  and  $R_{\text{inf}}$ . If we artificially change the ion ensemble's energy spread while maintaining the same transversal phase space<sup>5</sup>, then  $R_{\text{inf}}$  keeps growing for smaller and smaller  $\Delta E$ , as expected.

For comparison, figure 5 also shows the MR-ToF performance for ion bunches cooled via laser cooling or a cryogenic buffer gas. As discussed above, both methods allow one to obtain small  $\Delta t_0$  and  $\Delta E$  at the same time. Hence, a fast mass separation in combination with a large  $R_{\text{inf}}$  can be realised.

Alternatively, a fast mass separation with a high  $R_{\text{inf}}$  value may be achieved by increasing the energy-spread tolerance of MR-ToF devices while still operating the cooler-buncher at room temperature. To this end, it has been suggested that low-aberration ion mirrors may increase the energy-spread tolerances to up to 18% of the beam energy [51, 52] from the current typical  $\Delta E/E$  of around 1% for  $R_{\text{inf}} > 1\text{e}5$ . This latter value is in agreement with our simulation studies, too. To our knowledge, energy-spread tolerances of 18% have not been experimentally demonstrated so far. Alternatively, instead of increasing the relative energy-spread tolerance, the tolerance of an MR-ToF device in terms of absolute  $\Delta E$  could be raised by increasing the ion-beam energy  $E$ , thus keeping the  $\Delta E/E$  tolerance.

Such experiments have been reported for  $^{133}\text{Cs}^+$  ions stored at different ion energies within the same MR-ToF device [53]. For 1.3 keV beam energy,  $R_{\text{inf}} = 4.5\text{e}5$  was reached with an energy spread of 14.3 eV while for 750 eV

beam energy and  $\Delta E \approx 6$  eV 'only'  $R_{\text{inf}} = 2.8\text{e}5$  was obtained. Thus, the increase in beam energy from 750 eV to 1.3 keV beam energy allowed the use of a larger extraction field strength from the Paul trap which also made it possible to reach a mass resolving power of 1e5 within 2 ms<sup>6</sup> instead of 5 ms storage time.

#### 4.5. Comparison of a 1.5-keV with a 30-keV MR-ToF Device

Encouraged by these reports, we next explore the performance of an MR-ToF device operating at even higher ion-beam energies. Since our MIRACLS collaboration is building a 30-keV MR-ToF instrument for laser-spectroscopy applications at ISOLDE/CERN [45], the discussion will consider this specific ion energy as an example. For a direct comparison between 1.5-keV and 30-keV MR-ToF operation, simulations with a 30-keV beam energy are first performed within MIRACLS' low-energy setup as introduced in section 3. To this end, all the MR-ToF and injection potentials are scaled up by a factor 20. Since we find a similar focal condition at the center of the MR-ToF device as for the 1.5-keV case, adaptions of the injection fields are not necessary for the comparison. The Paul-trap electrodes retain their relative potential differences but are shifted by an overall floating potential. Such a scaling is presently not possible in practice due to high-voltage limitations, but the study will illustrate the advantages of high-energy MR-ToF instruments. For a realistic device, MIRACLS' dedicated 30-keV MR-ToF setup will be discussed in section 7.

When increasing the energy of the stored  $^{24}\text{Mg}^+$  ions to 30 keV within the simulated MIRACLS low-energy setup, the MR-ToF tolerance in  $\Delta E$  is increased such that a fast mass separation and high  $R_{\text{inf}}$  are attainable in the same settings. As shown in figure 5, the 30-keV instrument exceeds the respective low-energy room-temperature simulations on both processing time and  $R_{\text{inf}}$ . When investigating different Paul-trap extraction field strengths and thus different  $\Delta E$ , see figure 5(c), the simulation suggests that much higher  $R_{\text{inf}}$  can be reached for the higher beam energy. For an energy spread of 16 eV, for instance,  $R_{\text{inf}}$  is found to be almost twice as large in the 30-keV instrument compared to the highest  $R_{\text{inf}}$  found for an operation at 1.5 keV.

Moreover, even in the case of large extraction field strengths (e.g. 160 V/mm in Fig. 5) resulting in an energy spread as high as  $\sim 120$  eV, the obtained  $R_{\text{inf}}$  is with  $4.6\text{e}5$  still competitive to the highest  $R_{\text{inf}}$  achieved in the low-energy configuration. However, such an extraction leads to an initial time spread of  $\Delta t_0 \approx 2$  ns obtained in the middle of the MR-ToF device which would allow one

<sup>5</sup>When an ion passes the central middle plane of the MR-ToF device for the first time, the value of the total energy of this ion is exchanged with a value obtained from a Gaussian distribution. The standard deviation of the Gaussian distribution is given by the desired energy spread of the ions and the centroid is given by the average energy of all ions passing the central middle plane for the first time.

<sup>6</sup>In reference [39] a record minimum processing time of 1.7 ms is reported for reaching a mass resolving power of 1e5 for  $^{133}\text{Cs}^+$  ions. The initial time spread mainly governed by the Paul-trap preparation was 9.6 ns and the energy spread was 16.9 eV.

to achieve  $R = 1e5$  in only 0.4 ms of storage time. Operating the MR-ToF system at this extreme necessitates the availability of a Paul trap capable to accomplish an initial time spread of less than a few nanoseconds. To our knowledge, the smallest  $\Delta t_0$  reported for  $^{133}\text{Cs}^+$  ions with a room-temperature Paul trap is already as short as 5 ns corresponding to an estimated energy spread of 23 eV [13], which is slightly above the tolerance in energy spread of current state-of-the-art 1.5-keV MR-ToF devices. Hence, a 30-keV MR-ToF device coupled to a room-temperature Paul trap designed for large extraction field strengths may offer a path to improved mass resolving power and to shorter processing times for MR-ToF mass separation.

## 5. Space-Charge Studies

In addition to the attainable mass resolving power and processing time, another central MR-ToF characteristics is its maximal ion flux, i.e. the number of ions which can be mass separated per unit of time. For many simultaneously trapped ions, Coulomb interactions between the ions cannot be neglected anymore. When different ion species are simultaneously trapped, these space-charge effects manifest as a confined motion of the ions inside one single bunch, which prevents any mass separation. This so-called peak coalescence effect [22, 25–27] limits the ion flux.

Also below the space-charge limit where peak coalescence becomes obvious, space-charge effects can influence the ion-bunch properties of the trapped ions. Normally, the peak-width broadening per revolution  $\Delta t_1$  as discussed in section 4 leads over time to an increase in the temporal ion bunch width  $\Delta t$ . However, when many ions are stored in the trap  $\Delta t$  can stay almost constant with increasing revolution number for certain MR-ToF settings. This is referred to as selfbunching [18–25].

As both phenomena are caused by the same effect, it is meaningful to experimentally investigate the changes in  $\Delta t_1$  for a single species as a first approach to study the influence of the underlying space-charge effects. In the following, the experimental method of collisional-induced fluorescence will be discussed since it allows for in-situ monitoring of the ion bunch within the MR-ToF device (section 5.1), and the space-charge response of the system in simulation and measurement will be compared for  $^{24}\text{Mg}^+$  ions (section 5.2). Furthermore, a simulation of peak-coalescence phenomena using different ion masses will be discussed (section 5.3).

### 5.1. Collision-induced fluorescence method

Collision-induced fluorescence measurements provide an excellent way to observe space-charge effects experimentally as a benchmark for MR-ToF simulations including Coulomb interactions. We explore in simulation and experiment how the ion bunch structure evolves with ion number during one storage cycle in the MR-ToF device.

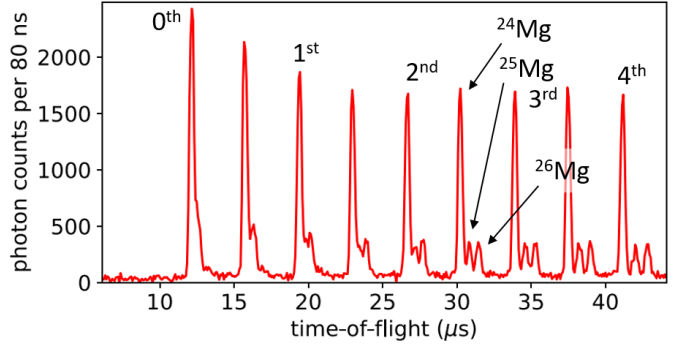


Figure 6: Measured photon count rate versus time of flight since ion extraction from the Paul trap. The corresponding revolution numbers in the 1.5-keV MR-ToF device are indicated. The data corresponds to almost 8 million measurement cycles.

For the following measurements, the pressure in the MR-ToF device is increased to  $1e-7$  mbar by leaking in nitrogen through a precision needle valve installed at the vacuum chamber housing. The higher pressure increases the probability for collisions of  $\text{Mg}^+$  ions with the gas particles. Emitted photons, following an inelastic collision, are detected by the photomultiplier tube installed above the central drift tube of the MR-ToF device. More details about the optical detection system can be found in references [32, 33, 54, 55] and in figure 1.

Figure 6 shows the photon count rate as a function of the time since extraction from the Paul trap. Every time the ions pass the optical detection region in either direction in the MR-ToF device, the emitted photons can be detected. Based on this data, the peak widths corresponding to the passage of  $^{24,25,26}\text{Mg}^+$  ions are extracted for every half revolution number, respectively.

Here, we extend previous, qualitative work [24] to facilitate a quantitative comparison of simulations and experiment for the ion bunch properties observed via collision-induced fluorescence. The extraction of the ion bunch shape from the simulated fluorescence signal requires precise knowledge about the detection efficiency of the emitted photons as a function of the axial position of the ions. To this end, the photon detection efficiency along the ion-beam axis of the MR-ToF device is obtained using optical ray-tracing calculations [33, 54, 55]. For the ray tracing, 100,000 ions are randomly displaced in transversal direction from the MR-ToF axis mimicking an ion beam of 5-mm beam diameter<sup>7</sup> as suggested by simulations [31]. The detection efficiency follows as the fraction of photons impinging on the PMT compared to the number of initially generated photons which are assumed to be emitted isotropically. Since only the relative photon detection efficiency as a function of the position along the ion beam axis of the MR-ToF device is relevant for the simulations,

<sup>7</sup>Note that there is no relevant difference in photon detection efficiency between ion beams with diameters from 2 to 12 mm, which imposes the upper geometrical limit.

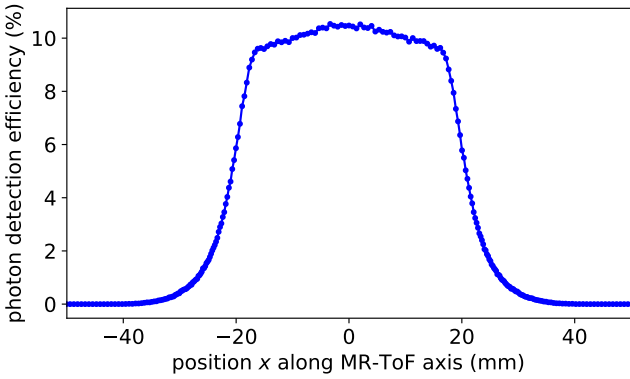


Figure 7: Photon detection efficiency versus the position  $x$  along the 1.5-keV MR-ToF axis for 5-mm ion beam diameter. The middle plane of the MR-ToF device is at 0 mm.

the quantum efficiency of the PMT is neglected. So it is assumed that every photon making it to the rectangular detection area of the PMT can be detected.

Figure 7 shows the detection efficiency as a function of the position along the ion-beam axis of the MR-ToF device. The region along the ion-beam axis of the MR-ToF device, where the photon detection efficiency is large enough for efficient detection, is significantly smaller than the region that is considered to be field free.<sup>8</sup>

For the simulations of the photon count rate versus time-of-flight, the ion distribution is in SimIon recorded whenever the simulated 1000 ions pass the transversal middle plane of the MR-ToF device. Because of the field-free region, the information of the ions' radial displacements and velocity vectors at the MR-ToF devices central plane is sufficient to calculate the entire passage through the optical detection region, which significantly speeds up the calculation time. For each chosen ion position along the ion-beam axis of the MR-ToF device the photon detection efficiency is evaluated and the detection probabilities for all ions are added up [56].

In figure 8 the simulated photon rate versus time of photon detection in the optical detection region is compared to experimental data for the zeroth and fourth revolution in the MR-ToF device. Since only the very first few revolutions are shown and less than 4000 ions are experimentally initially injected into the MR-ToF device (see paragraph below), space-charge effects can be safely neglected in these spectra. The simulated data are normalized in peakheight to the experimental data and shifted by 330 ns, an offset in time most likely originating from HV switch delays in the experiment. Peak width and peak shape of the fluorescence signal during the ions' passage through the central drift tube are very well reproduced. This provides confidence in the validity of the simulation approach combining the ion optical simulations in SIMION

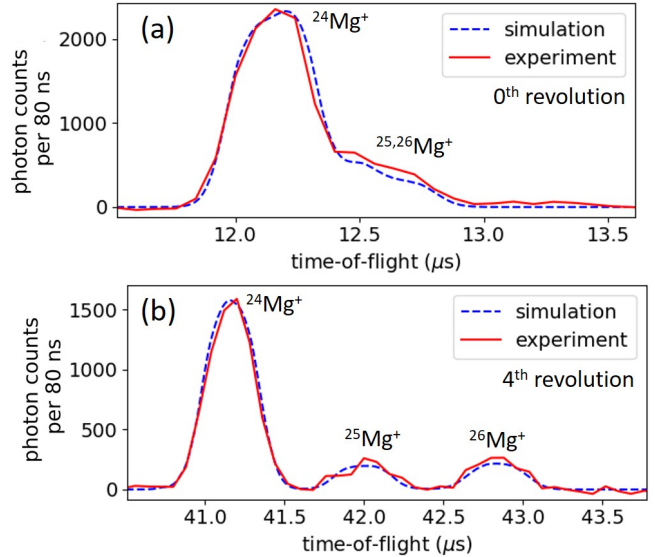


Figure 8: Photon count rate versus time-of-flight since ion extraction from the Paul trap for  $^{24,25,26}\text{Mg}^+$  ions for the very first passage through the optical detection region (a) and for the forth revolution in the 1.5-keV MR-ToF device (b). The experimental data (red) is compared to the simulated spectrum of detected photons (blue). Space-charge effects are neglected in the simulations.

with optical ray-tracing calculations of the emitted photons.

To obtain an estimate on the experimentally trapped ion number, data are recorded to count the injected ions as well as those extracted after 124 revolutions using the MagneToF detectors upstream and downstream of the MR-ToF device, respectively. These ion detectors have been calibrated for ion-number determination beyond single-ion counting following a procedure discussed in reference [56], which is assumed to be accurate up to around 10,000 ions per bunch. When an ion bunch consists of more than around 10,000 ions, non-linearities of the detector response occur [56] attributed to detector dead-time effects. Based on the measurements presented in reference [56], it is expected that the actual ion number remains within a factor 2 the same as the experimentally determined ion number up to around 50,000 ions per bunch.

## 5.2. Space-charge study of ensembles of the same species

When increasing the number of simultaneously stored ions in the MR-ToF device, the peak shape and width observed in the spectrum of photons versus time can change for higher revolution numbers. For example, figure 9 shows the measured photon response for the 34th revolution of  $^{24}\text{Mg}^+$  ions in the MR-ToF device, once for 3870(380) ions (a) and once for 18,200(1300) injected ions (b). Coulomb interactions lead to a reduction of the ToF peak width ('selfbunching') when more ions are simultaneously confined in the MR-ToF device. In both cases, the simulated photon signal is in excellent agreement with the experimental data. Between 10,000 and 20,000 ions there is no

<sup>8</sup>The region with less than 0.04 V change in electric potential is given by  $-46 \text{ mm} < x < 46 \text{ mm}$  [31].

notable difference in the photon response in the simulations.

For the simulations, Coulomb interactions between the individual ions are enabled employing SIMION's built-in factor repulsion method [57]. Each particle is treated as a point charge and the particles repel each other according to Coulomb's law. For up to 1000 ions a treatment of all individual ions is computationally tractable. For a higher number of trapped ions, one ion is treated as a sub-bunch of  $N$  ions with  $N$  being the defined charge repulsion factor. E.g. to represent 1000 actual ions with 100 simulated ions, a charge repulsion factor of 10 is needed. It is important to note that only ion-ion interactions are accounted for, i.e. interactions between image charges on the electrodes and ions are not considered. Note that ion-ion interactions are only enabled within the MR-ToF device. The simulations of the ion preparation in the Paul trap and ion-beam transport to the MR-ToF device are executed without taking Coulomb interactions between individual ions into account since space charge effects in the Paul trap for up to 50,000 injected ions into the MR-ToF device are almost negligible for the MR-ToF performance as dedicated simulation studies have shown.

### 5.2.1. Comparison between simulations and experiment

In order to benchmark the space-charge simulation code more comprehensively, collision-induced fluorescence measurements are performed for up to 124 revolutions utilising different in-trap lift potentials as well as different numbers of injected ions into the MR-ToF device. When increasing the in-trap lift potential  $U_{\text{lift}}$ , the kinetic energy of the stored ions reduces linearly,  $E_{\text{trapped}} = E_{\text{injected}} - U_{\text{lift}}$ . This allows one to operate the MR-ToF device either in dispersive, selfbunching or isochronous mode [24, 25]. The peak widths of the measured and simulated photon response to the  $^{24}\text{Mg}^+$  ion passage is shown in figure 10 as a function of revolution number for three different in-trap lift potentials and different ion numbers.

For an in-trap lift potential of 850 V, the MR-ToF device is operated in isochronous mode, in which the revolution period  $t_1$  is fairly independent of the energy  $E$  of the individual ions, hence  $dt_1/dE \approx 0$ . The peak width over revolution number remains constant in this mode, irrespective of the number of confined ions, see figure 10(a,b). For ion numbers exceeding 20,000 ions a slight increase of the peak width is visible in both simulations as well as experimental data, which indicates that it is more difficult to maintain an isochronous mode when more ions are simultaneously stored.

If an in-trap lift potential of 995 V is chosen, the MR-ToF device is operated in dispersive mode with  $dt_1/dE < 0$ . In this mode, the peak width increases over revolution number, see figure 10(c) and for a higher number of stored ions the bunch disperses faster, see figure 10(d). Note that only 400(100) of the initially 8740(520) injected ions can be extracted after 124 revolutions. The low storage efficiency in the MR-ToF device is a consequence of the vac-

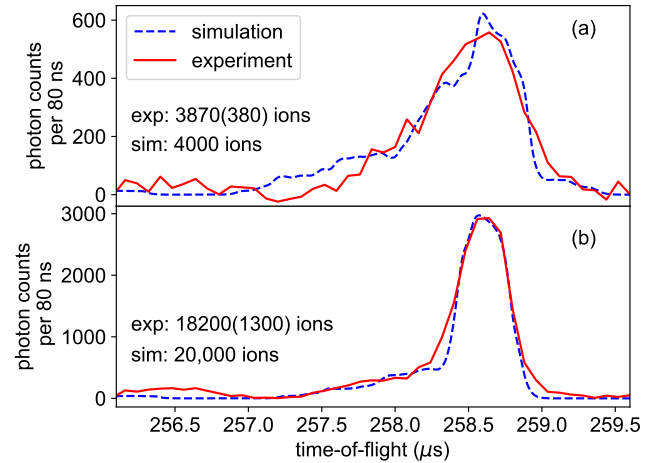


Figure 9: Photon counts versus time-of-flight since ion extraction from the Paul trap for  $^{24}\text{Mg}^+$  ions for the 34th revolution and an in-trap lift potential of 700 V in MIRACLS' low-energy MR-ToF device. The experimental data (red) is compared to the simulated ToF spectrum of detected photons (blue). For (b) the ion number is around a factor 5 larger than for (a).

uum pressure of  $1\text{e-}7$  mbar needed to increase the collision probability in order to obtain enough statistics within a few days of measurements. However, this also implies that more and more ions are lost due to ion-gas collisions the longer the ions are confined in the MR-ToF device. In the simulations assuming perfect vacuum, the storage efficiency is more than 90% irrespective of the number of simultaneously confined ions as tested for up to 25,000 ions. These 10% losses take place in the simulations during the first few revolutions only.

For an in-trap lift potential of 700 V, the relation  $dt_1/dE > 0$  holds and the ion bunch is also dispersing (figure 10(e)). However, if the charge density of stored ions is high enough, Coulomb interactions lead to the self-bunching effect and the peak width stays fairly constant over revolution number (figure 10(f)). This self-bunching phenomenon is well reproduced by the simulations. For lower numbers of stored ions in this configuration, there is a small difference between simulation and experiment, see again figure 10(e). Among all cases studied,  $U_{\text{lift}} = 700$  V with an intermediate ion number shows by far the strongest dependence of the peak-width broadening per revolution on the exact ion number, see simulation results in figure 10(e). Thus, any smaller sized inaccuracies in ion number, either in the measured ion number, intensity fluctuations or ion losses, may lead to more notable shifts in this particular configuration.

Generally, for around 20,000 injected ions the experimental peak widths are slightly larger than predicted by the simulations (see figure 10(b,f)). This effect has been studied in reference [58] and was attributed to the Coulomb repulsion in the Paul trap, which is neglected in the present simulations to keep the simulation times reasonably short.

Overall, the comparison of the simulations with experimental data with ions of the same species provides confidence in the space-charge simulations. The simulations with up to 25,000 simultaneously stored ions show a good qualitative agreement with experimental data. The charge repulsion factor method in SIMION provides a powerful tool for our purposes (for a charge repulsion factor up to at least 250, see appendix 8) while reducing the simulation time significantly. Given the good agreement between the SIMION simulations and our experimental data, we consider SIMION as an appropriate tool to estimate the onset of space-charge effects in MR-ToF devices. Thus, it can provide a qualitative guidance to reduce space-charge effects in MR-ToF systems.

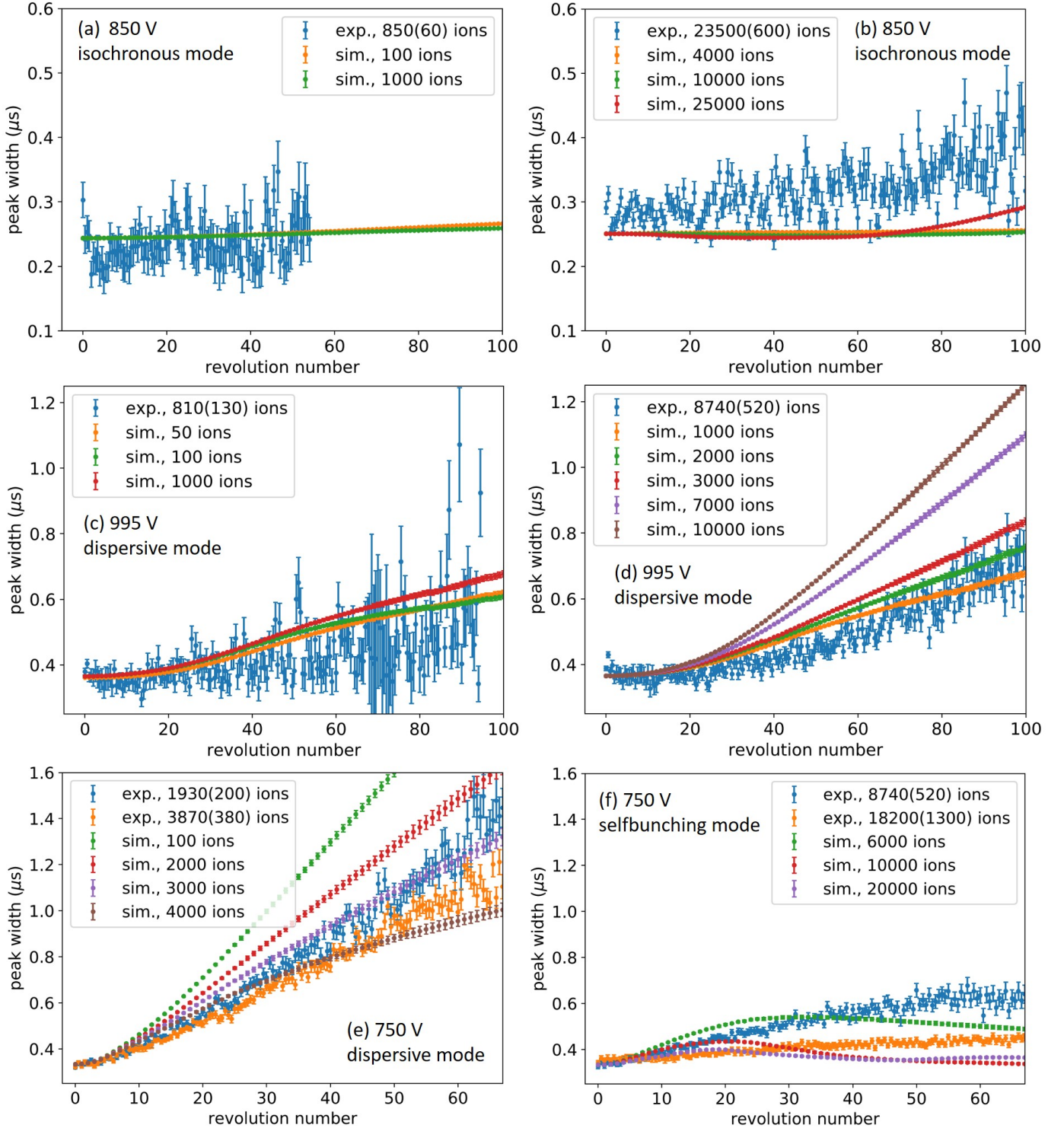


Figure 10: Simulated and measured peak widths of the photon signal during ion passage versus revolution number for different numbers of injected ions and MR-ToF in-trap lift potentials of the 1.5-keV MR-ToF device. The left column shows scenarios with a smaller number of simultaneously stored ions than the right column. Note that measurements and simulations as shown in (a) and (b) are performed with an accidentally 25-degree rotated slit in front of the PMT. While this has no overall impact on the plotted comparisons and conclusions, it explains the slightly smaller peak width for 0 revolutions in (a,b) compared to (c-f). For higher revolution numbers than shown it is not feasible to extract the peak widths due to too little statistics.

### 5.3. Study of the interaction of two ensembles of different ion species

After benchmarking the space-charge simulation code with experimental data for one ion species trapped in the MR-ToF device, it will in the following be used to investigate the peak coalescence effect in dedicated simulations. To this end, ions of hypothetical masses 24 u and 24.0096 u ( $m/\Delta m = 2500$ ) and an abundance ratio (see section 2 for a definition) of  $r_{ab} = 9$  are thermalized with 300-K buffer gas in the Paul trap, transported to the MR-ToF device and stored simultaneously for 150 revolutions at a beam energy of 1.5-keV. Figure 11 shows the simulated time-of-flight spectra of the ions after 150 revolutions as recorded at the middle plane of the MR-ToF device. For up to around 3000 stored ions the two ion species are well separated in time-of-flight after 150 revolutions. Starting from 5000 ions more than 7% of the ions of mass 24 u are overlapping in time-of-flight with ions of mass 24.0096 u and hence cannot be fully mass separated anymore. For 25,000 ions a full peak coalescence is observed. However, some ions lose synchronicity with the main ion bunch (see figure 11(f)). When the ion number is further increased less ions loose synchronicity (not shown).

The peak coalescence simulations presented in this work show a good agreement with earlier simulations performed in Simbuca [59] and experimental data from the same MR-ToF device, while it had been operated earlier at Greifswald [26, 27]. For those simulations the ion distribution was initialized directly in the axial center of the MR-ToF device. The present work goes a step further, and the full process from thermalization in the Paul trap up to ion storage in the MR-ToF device has been simulated. This comprehensive approach is required to predict and optimize the ion flux, i.e. the number of ions which are mass separated and transmitted per unit time. In the following this is investigated for various experimental conditions including different schemes in the ion preparation prior to the ion storage in the MR-ToF device itself.

## 6. Ion Flux Simulations

### 6.1. Ion flux for ion doublets with $m/\Delta m = 2500$

In this section, the maximal ion flux is evaluated for different Paul trap and MR-ToF operation modes for a storage time leading to a mass resolving power of 5000. The  $m/\Delta m$  ratio of the two ion species to mass separate is chosen with 2500 in order to fully mass separate them in the limit of single ion counting [12]. The two ion species have mass  $m = 24$  u and  $m = 24.0096$  u, respectively, and an abundance ratio  $r_{ab} = 9$ . While  $R = 5000$  is a very modest mass resolving power for which next-generation magnetic separators outperform MR-ToF devices in ion flux, it is chosen for the simulations in this section as it is still fully tractable<sup>9</sup>. It allows conclusions about the

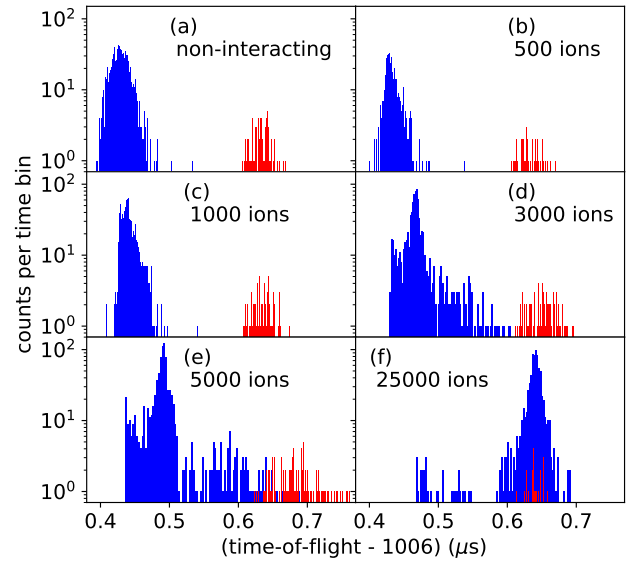


Figure 11: Simulated time-of-flight spectra of ions with mass 24 u and with mass 24.0096 u simultaneously stored in the 1.5-keV MR-ToF device after 150 revolutions. In (b) 450 ions with 24 u and 50 ions with 24.0096 u are simulated and in all other cases 900 ions with 24 u and 100 ions with 24.0096 u are simulated. In (b,c) a charge repulsion factor of 1 is used, in (d) a factor of 3, in (e) a factor of 5 and in (f) a factor of 25. 300-K buffer-gas cooling is employed and the extraction field strength in the Paul trap is 8 V/mm.

effects caused by high ion flux in MR-ToF devices at low  $R$  and low mass which are confirmed to be valid also for the experimentally more relevant larger  $R$  and ion masses, as discussed in section 6.2.

The maximal ion flux is in the following defined by  $N_{\max}/t_s$ , so it is limited by the storage time  $t_s$  in the MR-ToF device as well as by the maximal ion number  $N_{\max}$  that can be confined simultaneously in the MR-ToF device without notable peak overlap due to the peak coalescence effect. Note that a more general definition of the ion flux is given in section 2 (see equation 1), where the ion flux is defined by  $N_{\max}/t_{\text{proc}}$ . As the present work aims to characterize the behaviour of the MR-ToF mass separator itself, the processing time  $t_{\text{proc}}$  is equated with the storage time  $t_s$ .

In the case of a 300-K buffer gas and a field strength of 3.3 V/mm in the Paul trap  $R = 5000$  can be reached in MIRACLS low-energy device for 24-u ions within a storage time  $t_s$  of 1 ms. For a higher extraction field strength with either 8 V/mm or 10.6 V/mm or alternatively a reduced buffer-gas temperature, less storage time is needed to achieve the same mass resolving power due to the reduced initial time spread as already discussed in section 4.1. The initial time spread  $\Delta t_0$  and the storage time  $t_s$ , after which  $R = 5000$  is reached, are shown in

<sup>9</sup>Due to limitations in computing resources, only a few hundred revolutions can be simulated with sufficient accuracy and reasonable

run times. Hence, most of the simulations discussed in the following are limited to a storage time of 1 ms (corresponding to up to 150 revolutions for  $^{24}\text{Mg}^+$  ions with 1.5-keV beam energy).

figures 12(a,b) for different extraction field strengths and buffer-gas temperatures, respectively.

The maximum number of stored ions  $N_{\max}$ , before more than 7% of the two ion species are overlapping in time-of-flight due to peak coalescence, is shown in figure 12(c) for the different Paul trap settings<sup>10</sup>. The simulations reveal that for a smaller initial time spread fewer ions can be simultaneously stored in the MR-ToF device. This is interpreted as a consequence of ions being closer together in time-of-flight and thus also in space in longitudinal direction such that the ions will experience stronger Coulomb interactions, especially effective during their velocity reversal in the mirror electrodes.

The resulting maximal ion flux  $N_{\max}/t_s$ , is shown in figure 12(d) for the different investigated cases. Even though a given  $R$  is reached more quickly for a smaller initial time spread  $\Delta t_0$ , the ion flux remains within statistics the same. For a smaller  $\Delta t_0$  fewer ions can be stored simultaneously in the MR-ToF device due to the earlier onset of peak coalescence. Thus, as long as the half-lives of investigated nuclides are long enough to allow a mass separation within the necessary storage time, our simulations suggest that there is no notable advantage for an MR-ToF device's maximal ion flux using a Paul trap capable to obtain a small initial time spread  $\Delta t_0$ . If the ion bunch preparation time  $t_{\text{prep}}$  in the Paul trap is not neglected and one operates with settings  $t_s < t_{\text{prep}}$ , a faster mass separation (hence smaller  $\Delta t_0$ ) leads to a reduction of the ion flux defined via  $N_{\max}/\max(t_s, t_{\text{prep}})$  since for smaller  $\Delta t_0$  less ions can be simultaneously confined in the MR-ToF device.

Experimental ion flux measurements have been carried out in earlier work utilising the same MIRACLS 1.5-keV MR-ToF device for  $A = 28$  [26, 27]. These experimental studies showed that for  $1.5\text{e}7$  ions/s a separation of  $\text{N}_2^+$  and  $\text{CO}^+$  ions ( $m/\Delta m = 2500$ ) is possible, whereas for  $6.25\text{e}7$  ions/s a significant peak coalescence prevents the mass separation. The experimentally determined maximal ion flux is hence very close to the one simulated in this work, providing further confidence in our simulation approach (see inset of figure 13).

## 6.2. Ion flux for larger $m/\Delta m$

While the previous simulations illustrated that the ion preparation has no significant impact on the ion flux as long as  $t_s > t_{\text{prep}}$ , we discuss next the relationship between maximal ion flux and  $m/\Delta m$  of the ion species to be mass separated. In particular, one needs to take into account that for ions closer in mass the maximal attainable ion flux significantly drops. Figure 13 shows the maximal ion flux versus  $m/\Delta m$  of the present simulation work for MIRACLS' 1.5-keV MR-ToF device for  $A = 24$  (blue

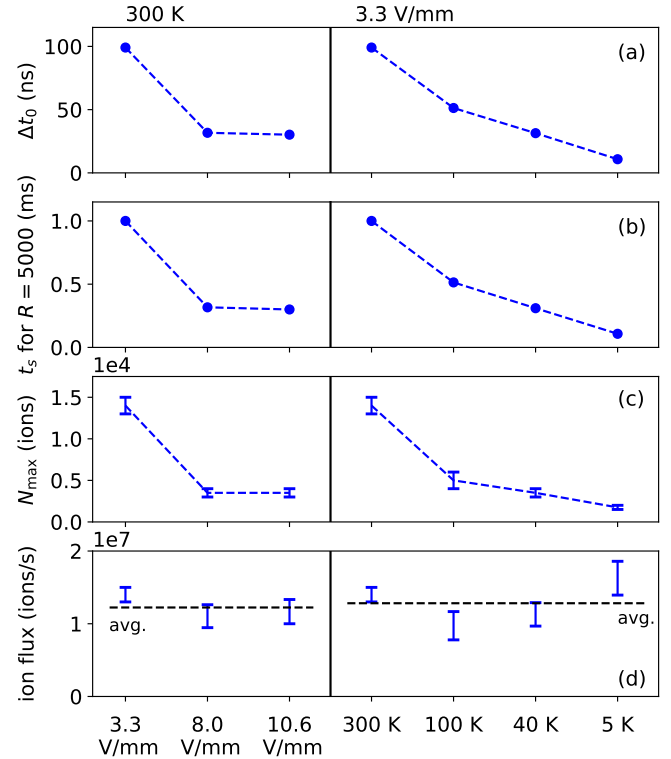


Figure 12: (a) Initial time spread  $\Delta t_0$  recorded when the ions pass the middle plane of the 1.5-keV MR-ToF device the first time for different Paul-trap preparation settings. The first three data points are performed for 300-K beam temperature and 3 different extraction field strengths, the last 4 data points are for an extraction field strength of 3.3 V/mm and different buffer gas temperatures. Error bars are smaller than the dots. (b) Necessary storage time  $t_s$  to reach the mass resolving power  $R = 5000$  for the different settings. Error bars are smaller than the dots. (c) Maximal number  $N_{\max}$  of simultaneously stored ions before more than 7% of the ions are overlapping due to the peak coalescence effect for the different settings. (d) The maximal ion flux, given by  $N_{\max}/t_s$  versus the different Paul-trap preparation settings. The average is indicated by a dashed horizontal line. The simulations are performed with ions of mass 24 u and 24.0096 u ( $m/\Delta m = 2500$ ) with an abundance ratio  $r_{\text{ab}} = 9$ . Charge repulsion factors of up to 17 are used to simulate up to 17,000 simultaneously stored ions in the MR-ToF device.

data points) compared to other experimental and/or simulation studies (gray data points). Due to too long simulation run times, we cannot easily extend our simulations in the 'standard' Paul trap operation to  $m/\Delta m > 5000$ . For larger  $m/\Delta m$ , we thus perform simulations with 5-K buffer-gas cooling. This reduces  $t_s$  to a tractable value while the maximal ion flux is comparable with the room-temperature case (see figure 12).

The ion flux simulations for the ORISS MR-ToF device planned for FRIB [60] are performed with Warp [64], an open-source particle-in-cell Python package. The simulations are carried out for  $A = 238$  and  $m/\Delta m = 238$ , thus, separating ions with 238 u from contaminants with 239 u. They show a reasonably good agreement with the ion flux simulations from the present work.

<sup>10</sup>The top of the error bar indicates the ion number for which more than 7% of the ions are overlapping while the bottom of the error bar marks the ion number where the overlap is less than 7%. The same applies for all other ion flux figures.

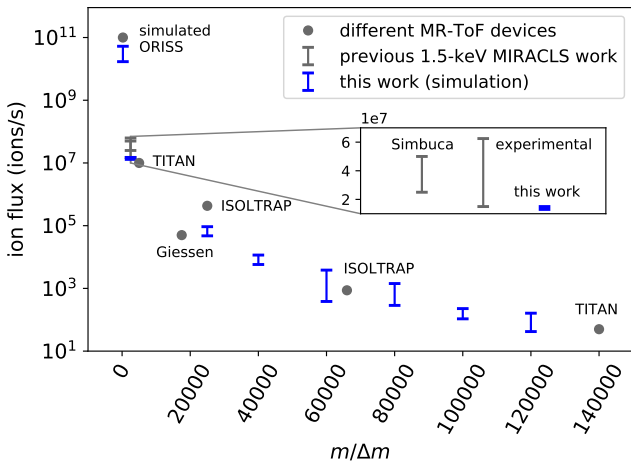


Figure 13: Maximal ion flux versus  $m/\Delta m$  for different low-energy MR-ToF devices. The simulations for the ORISS MR-ToF device are performed for  $A = 238$  [60]. The ion flux measurements from ISOLTRAP are for  $A = 152$  [61], from Giessen for  $A = 78$  [13], and from TITAN for  $A = 28, 60, 131$  and  $151$  [14, 62, 63]. The simulated ion flux values for MIRACLS’ 1.5-keV MR-ToF device for  $A = 24$  are shown in comparison (blue). For  $m/\Delta m = 2500$  also simulations in Simbuca [59] were performed for the MIRACLS 1.5-keV MR-ToF device for  $A = 28$  as well as dedicated measurements [26, 27] (see inset). All values above or equal  $m/\Delta m = 1e5$  are resulting from only confining one single ion in the MR-ToF device.

Additional information: The reported ion flux values for TITAN are the limit for high-precision mass measurements, the ones for mass separation are expected to be slightly larger. For ISOLTRAP’s ion flux measurements more than 7% of the ions are overlapping, especially for  $m/\Delta m = 27,200$ , which is most likely explaining its offset from our simulations and the ion flux reported from Giessen.

As mentioned in section 6.1, the measured maximal ion flux for MIRACLS’ low-energy MR-ToF device [26, 27] agrees with simulation studies in Simbuca [59] as well as with the present work (see inset of figure 13 and discussion in section 6.1).

Also the experimentally reported maximal ion flux values for ISOLTRAP [61], TITAN [14, 62, 63] and Giessen MR-ToF devices [13] with different  $m/\Delta m$  are in line with the simulations performed in this work. Note that at TITAN, a two-step strategy is adapted in which at first MR-ToF mass separation of  $1e6$  to  $1e7$  ions/s with  $m/\Delta m < 1e4$  is performed followed by a mass selective retrapping in the Paul trap to remove a large fraction of the contaminants. Finally, a high-precision mass measurement of the remaining 50 ions/s with up to  $m/\Delta m = 2.5e5$  is conducted in the MR-ToF device [14, 62, 63].

The overall good agreement with existing measurement data as well as other simulation codes provides additional confidence in the present simulation approach. Interestingly, the maximal ion flux seems to be within a factor of 4 fairly independent of the different MR-ToF designs, different masses ranging from  $A = 24$  to  $A = 238$  and different abundance ratios between ions of interest and contaminants. For a more detailed discussion on the influence of mass and abundance ratios on the maximal ion flux see

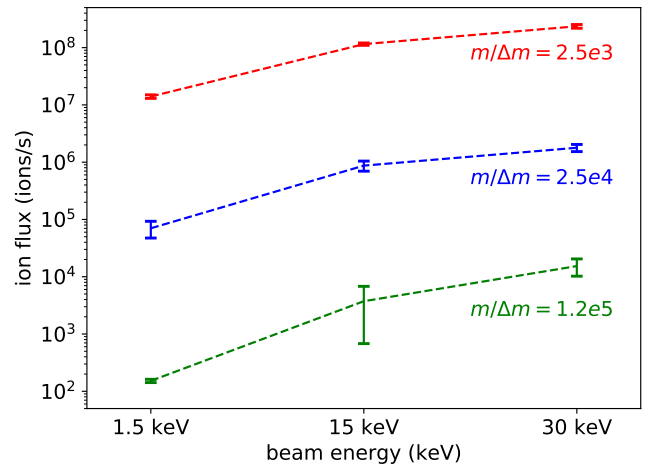


Figure 14: Maximal attainable ion flux for different beam energies and mass differences in MIRACLS’ low-energy MR-ToF setup. For 1.5-keV beam energy the simulations are performed with an extraction field strength of 3.3 V/mm, for 15-keV beam energy with 33 V/mm and for 30-keV beam energy with 65.3 V/mm. Simulations with  $m/\Delta m = 2500$  are performed with mass 24 u and 24.0096 u, simulations with  $m/\Delta m = 25,000$  with 24 u and 24.0096 u and simulations with  $m/\Delta m = 1.2e5$  are performed with 24 u and 24.0002 u. The abundance ratio is always 9. Charge repulsion factors of up to 80 are used to simulate up to 40,000 simultaneously stored ions.

section 7.3.

### 6.3. Boosting the ion flux with a higher-energy MR-ToF device

For many applications at RIB facilities it is required to be able to provide isobarically pure beams with higher ion flux. For this purpose, one may consider to perform the mass separation very fast and only have maximally one ion stored in the MR-ToF device at a given time. In practice, such an approach will face a technical limit either by the involved electronics or the ion preparation in the Paul trap. As an alternative path, one may identify an MR-ToF configuration allowing to store more ions simultaneously in the MR-ToF device without significant space-charge effects.

As we have shown above, due to its larger tolerance in energy spread a 30-keV MR-ToF device can be advantageous for a faster mass separation of isobars. As another, possibly even more important benefit, our simulations indicate that the ion-flux can be significantly boosted when increasing the MR-ToF ion-beam energy. To this end all the potentials in the MIRACLS low-energy setup are scaled up in the simulations to allow ion storage in the MR-ToF device with either 15 keV or 30 keV in analogy to the discussion in section 4.4. Figure 14 summarises the results in terms of maximal ion flux for 1.5-keV, 15-keV and 30-keV beam energies. In all cases, the abundance ratio between ions of interest and contaminants is 9.

For 1.5-keV beam energy, 5-K buffer-gas temperature and  $m/\Delta m = 1.2e5$ , space-charge effects become dominant as soon as only a few ions are simultaneously stored

in the MR-ToF device. Thus, the maximal ion flux is simply calculated by  $1/t_s$  with a storage time  $t_s$  of 6.2 ms necessary to reach  $R = 2.4e5$ . For 15-keV beam energy, 5-K buffer-gas temperature and  $m/\Delta m = 1.2e5$  peak coalescence is observed for 10 interacting ions (upper limit in figure 14). The lower ion flux limit is given by storing only one ion at a time in the MR-ToF device. For 30-keV beam energy, 5-K buffer gas temperature and  $m/\Delta m = 1.2e5$ , no peak coalescence is visible for 10 interacting ions (lower limit), but for 20 interacting ions effects towards peak-coalescence become visible (upper limit in figure 14).

Confirming our previous conclusion once more, configurations which only differ in their ion preparation yield a similar maximal ion flux (not shown). When comparing the ion flux simulations for the three different beam energies however, it becomes apparent that a factor 6 to 12 higher maximal ion flux is achieved when increasing the beam energy from 1.5 keV to 15 keV. At 30 keV the increase is even a factor of 13 to 25. Hence, our simulations suggest that an increase in beam energy of the stored ions will allow to reach a significantly higher ion flux. This can be attributed to the observation that for the same temporal ion bunch width  $\Delta t$  a 30-keV ion beam is further spatially spread in longitudinal direction compared to a 15-keV or 1.5-keV ion beam.

## 7. A 30-keV MR-ToF mass separator

### 7.1. Conceptual Design and Operational Parameters

A dedicated 30-keV MR-ToF system is currently in development at ISOLDE/CERN for the purpose of highly sensitive, high-resolution collinear laser spectroscopy at MIRACLS [45]. Reflecting its potential for highly selective mass separation, we propose an MR-ToF system by reconfiguring the components of MIRACLS' 30-keV apparatus for improved mass separation. Its performance is studied in simulations to guide experimental work on a future ISOLDE MR-ToF mass separator. An overview of the proposed setup is shown in figure 15. The radioactive ion beam produced at ISOLDE is injected into MIRACLS' linear room-temperature buffer-gas filled Paul trap, which is floated to 50 kV. After the ions are extracted as bunches from the Paul trap with an extraction field strength of around 14 V/mm, they are accelerated to a kinetic energy of 2 keV. They pass two einzel lenses (L1 and L2) before they are reaccelerated to 50 keV at the entrance of the MR-ToF device. By switching the in-trap lift from around 20 kV to ground potential the ions are stored in the MR-ToF device at around 30-keV beam energy until the necessary mass resolving power is reached.

The removal of the time-of-flight mass separated contaminants is either possible by dedicated deflector electrodes installed between the central drift tube and the MR-ToF mirrors during the ions storage time in the MR-ToF device [65], by mass-selective ion ejection via a pulsed

in-trap lift [66] or by a Bradbury-Nielsen-Gate [67] installed downstream of the MR-ToF device, possibly after a dedicated deceleration region for a reduction of the beam energy from 50 keV down to a few kiloelectronvolts. A retractable ion detector downstream of the Bradbury-Nielsen-Gate (BNG) allows time-of-flight measurements of the extracted ions as well as beam diagnostics. When retracting the ion detector the purified ion beam can be transported to the dedicated experimental setups.

The transfer beam line between Paul trap and reacceleration region is floated to 48 kV, whereas the beam line housing the 30-keV MR-ToF device is grounded.

The distance between Paul trap and MR-ToF device should be as short as possible such that the time-focus point can be matched onto a detector/BNG plane installed directly downstream of the MR-ToF device for large extraction field strengths from the Paul trap. This enables a fast mass separation as beneficial for radionuclides with very short half-lives. Since there needs to be space for two einzel lenses and a reacceleration region which also serves as a differential pumping barrier, a Paul-trap operation with initial time spreads below 16 ns will not allow to match the time-focus point at the detector plane. As discussed in previous sections, a fast mass separation will for most applications not boost the ion flux. Hence, initial time spreads of around 16 ns are sufficient.

The 30-keV MR-ToF device itself is based on MIRACLS' instrument as designed for high-resolution collinear laser spectroscopy [45]. The potential combination of the MR-ToF mirror electrodes as optimized for collinear laser spectroscopy also leads to a reasonably large mass resolving power, once the length of the central drift tube is properly chosen. The standard optimization procedure to obtain suitable injection and MR-ToF mirror potentials (see section 4.2), did not reveal a configuration with significant improved performance in mass separation. The highest mass resolving power  $R_{\text{inf}}$  is achieved for a length of the central drift tube corresponding to 425 mm, a potential of  $-1.6$  kV applied to lens 1 and  $-18.1$  kV applied to lens 2 with respect to the 48-kV potential of the transfer beam line. The in-trap lift potential is found to be optimal at 18.79 kV. For this in-trap lift potential the setup is operated in isochronous mode, hence the revolution period is fairly independent of the energy of the individual ions. All other operational settings and geometries are identical to the ones stated in reference [45].

### 7.2. Mass resolving power

The simulated total transport and storage efficiency from extraction from the Paul trap, ion transfer and ion storage in the MR-ToF device is found to be 91%. The simulated mass resolving power for the new 30-keV MR-ToF system for  $^{24}\text{Mg}^+$  ions is shown in figure 16 as a function of storage time in comparison to the simulated mass resolving power for MIRACLS' 1.5-keV MR-ToF setup, for 300-K buffer-gas cooling as well as for hypothetical 5-K buffer-gas cooling. In the proposed setup, the simulations

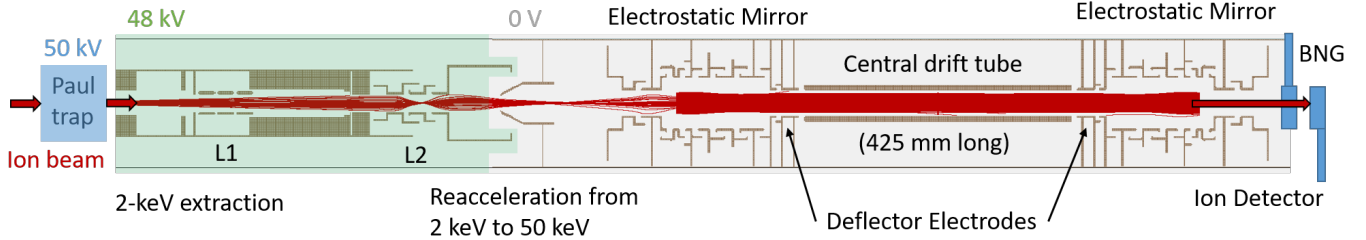


Figure 15: Proposed 30-keV MR-ToF mass separator system: Cut view of its electrode structure together with the ions' trajectories in red for 100 ions performing 100 revolutions (the electrode structures are to scale, the housing vacuum chambers are simplified). Additionally, the Paul trap for preparation of the ion bunches upstream of the MR-ToF setup and the potential location of a (retractable) BNG and detector system downstream of the MR-ToF device are schematically shown (not to scale). The full system takes up a floor space of around 1 m x 3 m.

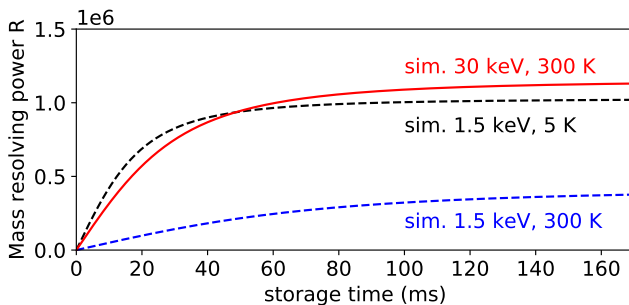


Figure 16: Simulated mass resolving power versus storage time of MIRACLS' new 30-keV mass separator (full line) in comparison to the simulations performed in MIRACLS' low-energy MR-ToF setup (dashed lines) for  $^{24}\text{Mg}^+$  ions. In the MIRACLS low-energy setup the revolution period is 6.62  $\mu\text{s}$  for 1.5-keV beam energy and in the new 30-keV setup it is 4.00  $\mu\text{s}$ .

predict a mass resolving power of  $1\text{e}5$  after a storage time of 3 ms, corresponding to 750 revolutions in the MR-ToF device. The maximal achievable mass resolving power  $R_{\text{inf}}$  is  $1.15\text{e}6$ . Note that in practice the experimentally achievable mass resolving power is expected to be lower due to the non-ideal vacuum pressure and voltage fluctuations. As discussed in section 4.3 for MIRACLS' 1.5-keV system, the reduction from simulated to experimental  $R_{\text{inf}}$  has been a factor 3. It is assumed that the impact of the residual gas pressure on  $R_{\text{inf}}$  will be less severe for the 30-keV MR-ToF device since the vacuum quality in the new 30-keV device will be improved compared to the one in MIRACLS' low-energy apparatus, e.g. by proper differential pumping to prevent He gas from the Paul trap to reach the MR-ToF device.

### 7.3. Ion Flux

Figure 17 shows the simulated maximal ion flux in the proposed 30-keV MR-ToF system for different masses, abundance ratios and in-trap lift potentials. The ratio  $m/\Delta m$  is 25,000 for all cases investigated to achieve a mass separation within less than 500 revolutions. The necessary storage time for  $R = 50,000$ , in which a full mass separation of non-interacting ions is possible, is 1.52 ms for

$A = 24$ , 3 ms for  $A = 132$  and 4.7 ms for  $A = 250$ . For almost all simulations there is hardly any dependence of the maximal ion flux on the abundance ratio (see figure 17(a) for  $A = 24$  and 18790 V applied to the in-trap lift). Only the simulations with abundance ratios of 9 or 49 show a factor 2-4 loss of ion-flux capabilities. For those the less abundant mass (e.g. 24.00096 u) starts for a higher number of stored ions to be hidden in the tail of the more abundant mass (e.g. 24 u). The tail in the ToF spectrum towards higher ToF values is attributed to reheating effects in the Paul trap due to buffer gas collisions during ion beam extraction [50].<sup>11</sup>

When increasing the mass to  $A = 250$ , the maximal ion flux drops by a factor 2-4 for all three abundance ratios studied (see figures 17(b-d) for an in-trap lift potential of 18790 V). Thus, the ion flux is only very slightly dependent on mass or studied abundance ratio. The maximal ion flux however shows some dependence on the in-trap lift potentials (see figures 17(e,f) for  $A=24$  and two different abundance ratios). Slight selfbunching (18740 V applied to the in-trap lift) can be beneficial in specific cases compared to isochronous operation (18790 V) or especially the dispersive region (18850 V).

The achievable ion flux of around  $7\text{e}6$  ions/s for  $A = 24$  and  $m/\Delta m = 25,000$  is around a factor 70 larger compared to the MIRACLS' low-energy device. A factor of around 20 can be explained by the increase in ion-beam energy from 1.5 to 30 keV, see section 6.3. The remaining factor  $\approx 3.5$  is attributed to changes in the MR-ToF design.

Based on the studies in section 6.3, a similar improvement can be expected for higher  $m/\Delta m$  and other masses. Figure 18 shows the simulated maximal ion flux of MIRACLS' new 30-keV MR-ToF device for  $A = 132$  and an abun-

<sup>11</sup>Simulations in the MIRACLS low-energy apparatus show that there is no difference in maximal ion flux irrespective if an abundance ratio of 9 or 0.11 of the 24 u and 24.0096 u ions is chosen. The simulations are performed for  $A = 24$  and  $m/\Delta m = 2500$ , a buffer-gas temperature of either 300 or 5 K and an extraction field strength of 3.3 V/mm. For the Paul trap in MIRACLS' low-energy setup the tail towards higher ToF values is much less pronounced than for the new MIRACLS Paul trap [50], which is still under commissioning and optimization.

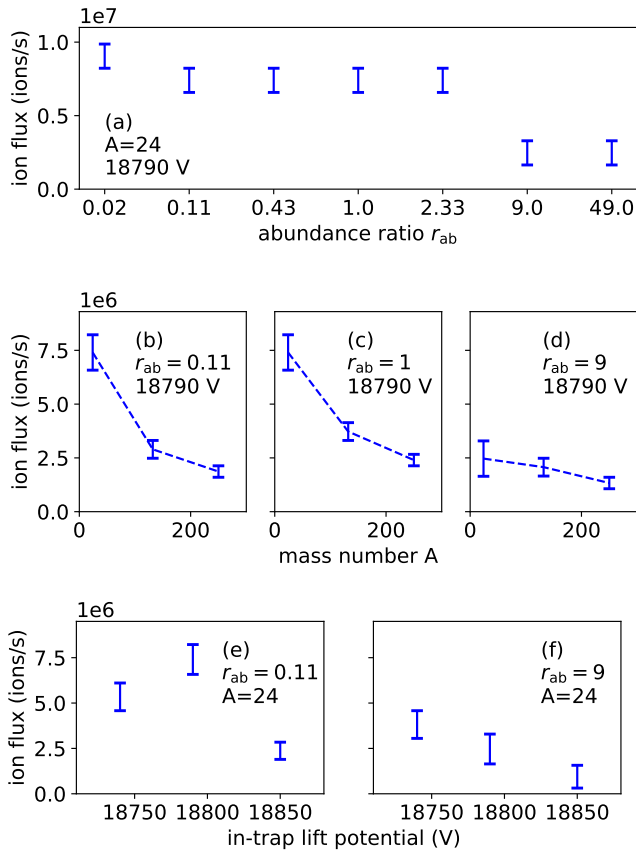


Figure 17: Maximal ion flux for  $m/\Delta m = 25,000$  in the new 30-keV MR-ToF mass separator for different masses, abundance ratios and in-trap lift potentials. (a) Maximal ion flux as a function of the abundance ratio for  $A = 24$  and 18790 V applied to the in-trap lift (isochronous mode). (b-d) Maximal ion flux as a function of the mass number  $A$  of the ions for three different abundance ratios and isochronous operation. (e,f) Maximal ion flux as a function of the in-trap lift potential. For 18740-V applied to the in-trap lift the device is operated in selfbunching mode, for 18790 V in isochronous mode and for 18850 V in dispersive mode. In total always 500 ions are simulated with different charge repulsion factors up to 30, to simulate up to 15,000 simultaneously stored ions.

dance ratio of 1 as a function of  $m/\Delta m$  in comparison to low-energy MR-ToF devices discussed above. In all cases studied the maximal ion flux of MIRACLS' new 30-keV MR-ToF device is significantly larger than the one in existing state-of-the-art MR-ToF devices.

A further increase of maximal ion flux could be envisioned by stacking several ion bunches simultaneously in the MR-ToF apparatus similar to reports of stacking different ion species [68] or by a further optimization of the operational parameters (e.g. by studying the influence of the in-trap lift potential in more depth). When there are two or more different species of contaminants with quite different mass ratios  $m/\Delta m$ , 2-step MR-ToF cleaning could allow a larger ion flux. Such a 2-step MR-ToF cleaning could become possible by mass selective retrapping in a dedicated Paul trap [14, 62, 63] or by beam cleaning with the deflector electrodes during the first few revolutions of

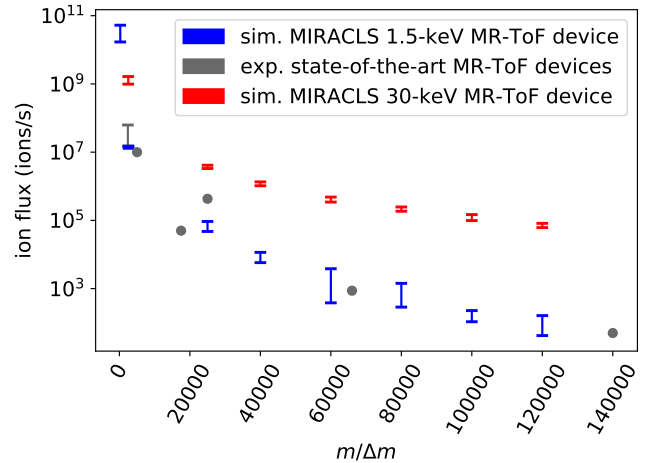


Figure 18: Simulated maximal ion flux versus  $m/\Delta m$  for MIRACLS' 1.5-keV MR-ToF device, experimental maximal ion flux for different low-energy MR-ToF devices and simulated maximal ion flux for MIRACLS' new 30-keV MR-ToF mass separator operating at 30-keV beam energy. The black and gray data are the same as shown in figure 13. The simulations for MIRACLS' 30-keV MR-ToF device are performed for  $A = 132$ . For the 30-keV simulations the charge repulsion factor is always smaller than 30, except for  $m/\Delta m = 2500$  where it is 500 in order to simulate 250,000 interacting ions. As of computational limitations, the number of sample ions used for  $R > 80,000$  is decreased from 500 to 300 ions.

one measurement cycle [65].

## 8. Conclusion and Outlook

Mass resolving power and space-charge simulations for MR-ToF devices have been carried out, and show a good agreement with time-of-flight and collisional-induced fluorescence measurements performed with the MIRACLS low-energy MR-ToF device operating at 1.5-keV beam energy. Building on the successful benchmarking of the simulation approach against the experimental data, simulations with different beam energies and Paul-trap settings are carried out. These suggest that the maximal ion flux can be increased by a factor of 13 to 25 when increasing the kinetic energy of the stored ions in the MR-ToF device from 1.5 keV to 30 keV. Different ion preparation schemes to reduce the temporal ion bunch width resulted in little influence on the maximal ion flux per unit of time. In these scenarios, the gain in MR-ToF processing time is counter-balanced by stronger space-charge effects. Hence, no notable net gain in ion flux is observed. Only when dealing with very short-lived ions, the Paul-trap preparation becomes important. For this case a small initial time spread is preferred in order to reach a given mass resolving power within a storage time shorter than the half life of the ion of interest.

Small initial time spreads can either be achieved by Doppler/sympathetic cooling [34] or cryogenic buffer-gas cooling. An alternative method is increasing the extraction field strength during the ion extraction from the Paul-

trap cooler-buncher. However, this approach will lead to a larger energy spread worsening the mass resolving power in the limit of infinite revolutions. Following our simulation studies, for a 30-keV MR-ToF device the energy-spread tolerance is significantly larger than for a 1.5-keV MR-ToF device allowing to reach a mass resolving power exceeding 1e5 with a very large extraction field strength. Hence, when a 30-keV MR-ToF device is coupled to a dedicated Paul trap allowing these very small initial time spreads, a given mass resolving power can be obtained within shorter time than in a 1.5-keV MR-ToF device, also for a room-temperature Paul trap and without compromising the maximal attainable mass resolving power.

Because of this shorter processing time and, even more importantly, its larger ion flux a 30-keV MR-ToF device is a very beneficial tool for mass separation at RIB facilities. For this reason, the discussed simulation code is finally used to reconfigure and optimize MIRACLS' 30-keV MR-ToF design for a high mass resolving power and a large ion-flux. Once constructed and commissioned, this 30-keV setup will serve as a prototype towards a general-purpose mass separator for the ISOLDE community. At this initial stage it is planned to deliver purified beams to PUMA and possibly traveling experiments. Based on the simulation work, this instrument has the prospect of improving the maximal ion flux by a factor of around 70 compared to the MIRACLS 1.5-keV MR-ToF setup or other existing state-of-the-art MR-ToF systems. Ultimately, such an MR-ToF system shoud be embedded into a wider effort for RIB purification, including also next generation magnetic separators. We envision that at each purification stage, i.e. target, ion source, magnetic separator and finally MR-ToF device the maximal amount of contaminants is suppressed such that a highly purified ion sample is delivered at high ion rates to RIB experiments. Isobaricly pure beams with an high ion intensity will be beneficial for virtually all fields of rare isotope science, ranging from fundamental symmetry studies, nuclear structure, astrophysics, material science, production of medical isotopes to rare isotope studies with antimatter.

## Appendix

If not indicated differently, all the simulations are performed with SIMION, version 8.1. Similar to the discussion in reference [45], the simulation is split into different geometrical segments. For the MR-ToF simulations a grid resolution of 0.1 mm/grid unit and a convergence objective of 1e-7 V is chosen, for the Paul trap and ion transport simulations the grid resolution is 0.2 or 0.5 mm/grid unit and the convergence objective is 1e-5 V. For selected simulations it is verified, that a smaller grid resolution or a smaller time step size do not lead to any notable changes on the relevant parameters, such as maximal ion flux or mass resolving power. Note that this point was in particular checked for the simulations with 30-keV beam energy. When going from 0.05 to 0.1 mm/grid unit the

simulated mass resolving power remains the same, when going further to 0.2 mm/grid unit it is slightly reduced. The simulated maximal ion flux, however, remains similar for all tested grid resolutions between 0.05 mm/grid unit and 0.5 mm/grid unit. Since computational errors shift the energy of both ion species almost equally, the mass separation and hence maximal ion flux is hardly affected by computational errors as long as  $m/\Delta m \ll R_{\text{inf}}$ .

Moreover, a simulation with 1000 interacting ions is leading to the same results as a simulation with 100 interacting ions and a charge repulsion factor of 10 for the selfbunching, dispersive and isochronous mode. Additionally, it is verified that e.g. 100 ions with a charge repulsion factor of 250 lead to the same results as 1000 ions with a charge repulsion factor of 25, as tested for the isochronous and selfbunching mode. Based on the comparison with experimental collision-induced fluorescence data, we conclude that the simulations with up to at least a charge repulsion factor of 250 lead to reliable results.

## Acknowledgments

The research leading to these results has received funding from the European Research Council (ERC) under the European Union's Horizon 2020 research and innovation programme under grant agreement No. 679038. The work of F.M.M. has been sponsored by the Wolfgang Gentner Programme of the German Federal Ministry of Education and Research (grant no. 05E18CHA). We are grateful for support of the MIRACLS project from CERN, the ISOLDE Collaboration, and the Max-Planck-Institut für Kernphysik (MPI K) in Heidelberg. This work is supported by the CERN Budget for Knowledge Transfer to Medical Applications and by the Natural Sciences and Engineering Council of Canada (NSERC). TRIUMF receives federal funding via a contribution agreement with the National Research Council of Canada. We thank Mark Bisell, Wouter Gins, Kim Dieter Kreim and Stefan Sailer for sharing their optical ray-tracing codes. Additionally, F.M.M. thanks Moritz Pascal Reiter for fruitful discussions on topics related to this manuscript.

## References

- [1] T. Giles, R. Catherall, V. Fedosseev, U. Georg, E. Kugler, J. Lettry, and M. Lindroos, "The high resolution spectrometer at ISOLDE," *Nuclear Instruments and Methods in Physics Research Section B: Beam Interactions with Materials and Atoms*, vol. 204, pp. 497–501, 2003. 14th International Conference on Electromagnetic Isotope Separators and Techniques Related to their Applications.
- [2] C. N. Davids and D. Peterson, "A compact high-resolution isobar separator for the CARIBU project," *Nuclear Instruments and Methods in Physics Research Section B: Beam Interactions with Materials and Atoms*, vol. 266, no. 19, pp. 4449–4453, 2008. Proceedings of the XVth International Conference on Electromagnetic Isotope Separators and Techniques Related to their Applications.

[3] S. Grévy, "High intensity ion guides and purification techniques for low energy radioactive ion beams," *Nuclear Instruments and Methods in Physics Research Section B: Beam Interactions with Materials and Atoms*, vol. 376, pp. 200–206, 2016. Proceedings of the XVIIth International Conference on Electromagnetic Isotope Separators and Related Topics (EMIS2015), Grand Rapids, MI, U.S.A., 11-15 May 2015.

[4] T. Kurtukian-Nieto, R. Baartman, B. Blank, T. Chiron, C. Davids, F. Delalee, M. Duval, S. El Abbeir, A. Fournier, D. Lunney, F. Méot, L. Serani, M.-H. Stodel, F. Varenne, and H. Weick, "SPIRAL2/DESIR high resolution mass separator," *Nuclear Instruments and Methods in Physics Research Section B: Beam Interactions with Materials and Atoms*, vol. 317, pp. 284–289, 2013. XVIIth International Conference on Electromagnetic Isotope Separators and Techniques Related to their Applications, December 2–7, 2012 at Matsue, Japan.

[5] J. Michaud, P. Alfaut, A. Balana, B. Blank, L. Daudin, T. K. Nieto, B. Lachacinski, L. Serani, and F. Varenne, "Status on the DESIR High Resolution Separator Commissioning," 2022.

[6] M. Marchetto, F. Ames, R. Baartman, C. Barquest, S. Kiy, T. Planche, S. Saminathan, J. Maloney, S. Brown, M. Corwin, D. Sehayek, and J. Laroche, "Status of the CANREB high-resolution separator at TRIUMF," *Nuclear Instruments and Methods in Physics Research Section B: Beam Interactions with Materials and Atoms*, vol. 463, pp. 227–231, 2020.

[7] A. Piechaczek, V. Shchepunov, H. K. Carter, J. C. Batchelder, E. F. Zganjar, S. N. Liddick, H. Wollnik, Y. Hu, and B. O. Griffith, "Development of a high resolution isobar separator for study of exotic decays," *Nuclear Instruments and Methods in Physics Research Section B: Beam Interactions with Materials and Atoms*, vol. 266, no. 19, pp. 4510–4514, 2008.

[8] W. R. Plaß, T. Dickel, U. Czok, H. Geissel, M. Petrick, K. Reinheimer, C. Scheidenberger, and M. I. Yavor, "Isobar separation by time-of-flight mass spectrometry for low-energy radioactive ion beam facilities," *Nuclear Instruments and Methods in Physics Research Section B: Beam Interactions with Materials and Atoms*, vol. 266, no. 19-20, pp. 4560 – 4564, 2008.

[9] P. Schury, K. Okada, S. Shchepunov, T. Sonoda, A. Takamine, M. Wada, H. Wollnik, and Y. Yamazaki, "Multi-reflection time-of-flight mass spectrograph for short-lived radioactive ions," *The European Physical Journal A*, vol. 42, no. 3, p. 343, 2009.

[10] F. Wienholtz, D. Beck, K. Blaum, C. Borgmann, M. Breitenfeldt, R. B. Cakirli, S. George, F. Herfurth, J. D. Holt, M. Kowalska, S. Kreim, D. Lunney, V. Manea, J. Menéndez, D. Neidherr, M. Rosenbusch, L. Schweikhard, A. Schwenk, J. Simonis, J. Stanja, R. N. Wolf, and K. Zuber, "Masses of exotic calcium isotopes pin down nuclear forces," *Nature*, vol. 498, no. 7454, pp. 346–349, 2013.

[11] R. N. Wolf, D. Beck, K. Blaum, C. Böhm, C. Borgmann, M. Breitenfeldt, F. Herfurth, A. Herlert, M. Kowalska, S. Kreim, D. Lunney, S. Naimi, D. Neidherr, M. Rosenbusch, L. Schweikhard, J. Stanja, F. Wienholtz, and K. Zuber, "Online separation of short-lived nuclei by a multi-reflection time-of-flight device," *Nuclear Instruments and Methods in Physics Research Section A*, vol. 686, pp. 82–90, 2012.

[12] R. Wolf, F. Wienholtz, D. Atanasov, D. Beck, K. Blaum, C. Borgmann, F. Herfurth, M. Kowalska, S. Kreim, Y. A. Litvinov, D. Lunney, V. Manea, D. Neidherr, M. Rosenbusch, L. Schweikhard, J. Stanja, and K. Zuber, "ISOLTRAP's multi-reflection time-of-flight mass separator/spectrometer," *International Journal of Mass Spectrometry*, vol. 349-350, pp. 123 – 133, 2013. 100 years of Mass Spectrometry.

[13] T. Dickel, W. Plaß, A. Becker, U. Czok, H. Geissel, E. Haettner, C. Jesch, W. Kinsel, M. Petrick, C. Scheidenberger, A. Simon, and M. Yavor, "A high-performance multiple-reflection time-of-flight mass spectrometer and isobar separator for the research with exotic nuclei," *Nuclear Instruments and Methods in Physics Research Section A: Accelerators, Spectrometers, Detectors and Associated Equipment*, vol. 777, pp. 172 – 188, 2015.

[14] M. Reiter, S. A. S. Andrés, J. Bergmann, T. Dickel, J. Dilling, A. Jacobs, A. Kwiatkowski, W. Plaß, C. Scheidenberger, D. Short, C. Will, C. Babcock, E. Dunling, A. Finlay, C. Horning, C. Jesch, R. Klawitter, B. Kootte, D. Lascar, E. Leistenschneider, T. Murböck, S. Paul, and M. Yavor, "Commissioning and performance of TITAN's Multiple-Reflection Time-of-Flight Mass-Spectrometer and isobar separator," *Nuclear Instruments and Methods in Physics Research Section A: Accelerators, Spectrometers, Detectors and Associated Equipment*, vol. 1018, p. 165823, 2021.

[15] P. Chauveau, P. Delahaye, G. De France, S. El Abir, J. Lory, Y. Merrer, M. Rosenbusch, L. Schweikhard, and R. Wolf, "PILGRIM, a Multi-Reflection Time-of-Flight Mass Spectrometer for Spiral2-S3 at GANIL," *Nuclear Instruments and Methods in Physics Research Section B: Beam Interactions with Materials and Atoms*, vol. 376, pp. 211 – 215, 2016. Proceedings of the XVIIth International Conference on Electromagnetic Isotope Separators and Related Topics (EMIS2015), Grand Rapids, MI, U.S.A., 11-15 May 2015.

[16] B. Liu, M. Brodeur, D. Burdette, J. Kelly, T. Kim, J. Long, and P. O'Malley, "The performance of the commissioned Notre Dame multi-reflection time-of-flight mass spectrometer," *Nuclear Instruments and Methods in Physics Research Section A: Accelerators, Spectrometers, Detectors and Associated Equipment*, vol. 985, p. 164679, 2021.

[17] M. Rosenbusch, M. Wada, S. Chen, A. Takamine, S. Iimura, D. Hou, W. Xian, S. Yan, P. Schury, Y. Hirayama, Y. Ito, H. Ishiyama, S. Kimura, T. Kojima, J. Lee, J. Liu, S. Michimasa, H. Miyatake, J. Moon, M. Mukai, S. Nishimura, S. Naimi, T. Niwase, T. Sonoda, Y. Watanabe, and H. Wollnik, "The new MRTOF mass spectrograph following the ZeroDegree spectrometer at RIKEN's RIBF facility," *Nuclear Instruments and Methods in Physics Research Section A: Accelerators, Spectrometers, Detectors and Associated Equipment*, p. 167824, 2022.

[18] H. B. Pedersen, D. Strasser, S. Ring, O. Heber, M. L. Rappaport, Y. Rudich, I. Sagi, and D. Zajfman, "Ion motion synchronization in an ion-trap resonator," *Phys. Rev. Lett.*, vol. 87, p. 055001, Jul 2001.

[19] D. Zajfman, O. Heber, M. L. Rappaport, H. B. Pedersen, D. Strasser, and S. Goldberg, "Self-bunching effect in an ion trap resonator," *J. Opt. Soc. Am. B*, vol. 20, pp. 1028–1032, May 2003.

[20] H. B. Pedersen, D. Strasser, B. Amarant, O. Heber, M. L. Rappaport, and D. Zajfman, "Diffusion and synchronization in an ion-trap resonator," *Phys. Rev. A*, vol. 65, p. 042704, Mar 2002.

[21] D. Strasser, T. Geyer, H. B. Pedersen, O. Heber, S. Goldberg, B. Amarant, A. Diner, Y. Rudich, I. Sagi, M. Rappaport, D. J. Tannor, and D. Zajfman, "Negative Mass Instability for Interacting Particles in a 1D Box: Theory and Application," *Phys. Rev. Lett.*, vol. 89, p. 283204, 2002.

[22] P. Bolotskikh, D. Grinfeld, A. Makarov, and M. Monastyrskiy, "Coulomb dynamics of ion bunches in multi-reflection electrostatic traps," *Nuclear Instruments and Methods in Physics Research Section A: Accelerators, Spectrometers, Detectors and Associated Equipment*, vol. 645, no. 1, pp. 146–152, 2011. The Eighth International Conference on Charged Particle Optics.

[23] M. W. Froese, M. Lange, S. Menk, M. Grieser, O. Heber, F. Laux, R. Repnow, T. Sieber, Y. Toker, R. von Hahn, A. Wolf, and K. Blaum, "The decay of ion bunches in the self-bunching mode," *New Journal of Physics*, vol. 14, p. 073010, jul 2012.

[24] S. Lechner, P. Fischer, H. Heylen, V. Lagaki, F. Maier, P. Plattner, M. Rosenbusch, S. Sels, F. Wienholtz, R. N. Wolf, W. Nörterhäuser, L. Schweikhard, and S. Malbrunot-Ettenauer, "Fluorescence detection as a new diagnostics tool for electrostatic ion beam traps," *Hyperfine Interactions*, vol. 240, no. 1, p. 95, 2019.

[25] D. Gupta, R. Singh, R. Ringle, C. R. Nicoloff, I. Rahinov, O. Heber, and D. Zajfman, "Particle-in-cell techniques for the study of space charge effects in an electrostatic ion beam trap," *Phys. Rev. E*, vol. 104, p. 065202, Dec 2021.

[26] M. Rosenbusch, S. Kemnitz, R. Schneider, L. Schweikhard, R. Tschiersch, and R. N. Wolf, "Towards systematic investiga-

tions of space-charge phenomena in multi-reflection ion traps,” *AIP Conference Proceedings*, vol. 1521, no. 1, pp. 53–62, 2013.

[27] M. Rosenbusch, P. Chauveau, P. Delahaye, G. Marx, L. Schweikhard, F. Wienholtz, and R. N. Wolf, “Delayed bunching for multi-reflection time-of-flight mass separation,” *AIP Conference Proceedings*, vol. 1668, no. 1, p. 050001, 2015.

[28] T. Aumann, W. Bartmann, O. Boine-Frankenheim, A. Bouvard, A. Broche, F. Butin, D. Calvet, J. Carbonell, P. Chiggiato, H. De Gersem, R. De Oliveira, T. Dobers, F. Ehm, J. F. Somoza, J. Fischer, M. Fraser, E. Friedrich, A. Frotscher, M. Gomez-Ramos, J.-L. Grenard, A. Hobl, G. Hupin, A. Husson, P. Indelicato, K. Johnston, C. Klink, Y. Kubota, R. Lazauskas, S. Malbrunot-Ettenauer, N. Marsic, W. F. O Müller, S. Naimi, N. Nakatsuka, R. Necca, D. Neidherr, G. Neyens, A. Obertelli, Y. Ono, S. Pasinelli, N. Paul, E. C. Pollacco, D. Rossi, H. Scheit, M. Schlaich, A. Schmidt, L. Schweikhard, R. Seki, S. Sels, E. Siesling, T. Uesaka, M. Vilén, M. Wada, F. Wienholtz, S. Wycech, and S. Zacarias, “PUMA, antiProton unstable matter annihilation,” *The European Physical Journal A*, vol. 58, p. 88, May 2022.

[29] C. Müller, K. Zhernosekov, U. Köster, K. Johnston, H. Dorfer, A. Hohn, N. T. van der Walt, A. Türler, and R. Schibli, “A unique matched quadruplet of terbium radioisotopes for PET and SPECT and for  $\alpha$ - and  $\beta$ - radionuclide therapy: an in vivo proof-of-concept study with a new receptor-targeted folate derivative,” *J Nucl Med*, vol. 53, pp. 1951–1959, Nov. 2012.

[30] C. Müller, C. Vermeulen, K. Johnston, U. Köster, R. Schmid, A. Türler, and N. P. van der Meulen, “Preclinical in vivo application of  $^{152}\text{Tb}$ -DOTANOC: a radiolanthanide for PET imaging,” *EJNMMI Research*, vol. 6, p. 35, Apr 2016.

[31] F. M. Maier, P. Fischer, H. Heylen, V. Lagaki, S. Lechner, P. Plattner, S. Sels, F. Wienholtz, W. Nörtershäuser, L. Schweikhard, and S. Malbrunot-Ettenauer, “Simulations of a proof-of-principle experiment for collinear laser spectroscopy within a multi-reflection time-of-flight device,” *Hyperfine Interactions*, vol. 240, no. 1, p. 54, 2019.

[32] K. Kreim, M. Bissell, J. Papuga, K. Blaum, M. D. Rydt, R. G. Ruiz, S. Goriely, H. Heylen, M. Kowalska, R. Neugart, G. Neyens, W. Nörtershäuser, M. Rajabali, R. S. Alarcón, H. Stroke, and D. Yordanov, “Nuclear charge radii of potassium isotopes beyond  $N=28$ ,” *Physics Letters B*, vol. 731, pp. 97 – 102, 2014.

[33] K. Kreim, “Collinear laser spectroscopy of potassium.” PhD thesis, University Heidelberg, 2013.

[34] S. Sels, F. M. Maier, M. Au, P. Fischer, C. Kanitz, V. Lagaki, S. Lechner, E. Leistenschneider, D. Leimbach, E. M. Lykiardopoulou, A. A. Kwiatkowski, T. Manovitz, Y. N. Vila Gracia, G. Neyens, P. Plattner, S. Rothe, L. Schweikhard, M. Vilen, R. N. Wolf, and S. Malbrunot-Ettenauer, “Doppler and sympathetic cooling for the investigation of short-lived radioactive ions,” *Phys. Rev. Research*, vol. 4, p. 033229, Sep 2022.

[35] S. Sels, P. Fischer, H. Heylen, V. Lagaki, S. Lechner, F. Maier, P. Plattner, M. Rosenbusch, F. Wienholtz, R. Wolf, W. Nörtershäuser, L. Schweikhard, and S. Malbrunot-Ettenauer, “First steps in the development of the multi ion reflection apparatus for collinear laser spectroscopy,” *Nuclear Instruments and Methods in Physics Research Section B: Beam Interactions with Materials and Atoms*, vol. 463, pp. 310 – 314, 2020.

[36] V. Lagaki, H. Heylen, I. Belosevic, P. Fischer, C. Kanitz, S. Lechner, F. Maier, W. Nörtershäuser, P. Plattner, M. Rosenbusch, S. Sels, L. Schweikhard, M. Vilen, F. Wienholtz, R. Wolf, and S. Malbrunot-Ettenauer, “An accuracy benchmark of the MIRACLS apparatus: Conventional, single-passage collinear laser spectroscopy inside a MR-ToF device,” *Nuclear Instruments and Methods in Physics Research Section A: Accelerators, Spectrometers, Detectors and Associated Equipment*, vol. 1014, p. 165663, 2021.

[37] T. Beyer, K. Blaum, M. Block, C. E. Düllmann, K. Eberhardt, M. Eibach, N. Frömmgen, C. Geppert, C. Gorges, J. Grund, M. Hamm, S. Kaufmann, A. Krieger, S. Nagy, W. Nörtershäuser, D. Renisch, C. Smorra, and E. Will, “An RFQ cooler and buncher for the TRIGA-SPEC experiment,” *Applied Physics B*, vol. 114, pp. 129–136, Jan 2014.

[38] R. N. Wolf, G. Marx, M. Rosenbusch, and L. Schweikhard, “Static-mirror ion capture and time focusing for electrostatic ion-beam traps and multi-reflection time-of-flight mass analyzers by use of an in-trap potential lift,” *International Journal of Mass Spectrometry*, vol. 313, pp. 8–14, 2012.

[39] T. Dickel, M. I. Yavor, J. Lang, W. R. Plaß, W. Lippert, H. Geissel, and C. Scheidenberger, “Dynamical time focus shift in multiple-reflection time-of-flight mass spectrometers,” *International Journal of Mass Spectrometry*, vol. 412, pp. 1–7, 2017.

[40] V. Lagaki, P. Fischer, H. Heylen, F. Hummer, S. Lechner, S. Sels, F. Maier, P. Plattner, M. Rosenbusch, F. Wienholtz, R. Wolf, W. Nörtershäuser, L. Schweikhard, and S. Malbrunot-Ettenauer, “Stray-light suppression for the MIRACLS proof-of-principle experiment,” *Acta Physica Polonica B*, vol. 51, pp. 571–576, (2020).

[41] T. Murböck, S. Schmidt, Z. Andelkovic, G. Birk, W. Nörtershäuser, and M. Vogel, “A compact source for bunches of singly charged atomic ions,” *Review of Scientific Instruments*, vol. 87, no. 4, p. 043302, 2016.

[42] F. Wienholtz, K. Blaum, J. Karthein, D. Lunney, S. Malbrunot-Ettenauer, V. Manea, M. Mougeot, L. Schweikhard, T. Steinsberger, and R. Wolf, “Improved stability of multi-reflection time-of-flight mass spectrometers through passive and active voltage stabilization,” *Nuclear Instruments and Methods in Physics Research Section B: Beam Interactions with Materials and Atoms*, vol. 463, pp. 348–356, 2020.

[43] P. Fischer and L. Schweikhard, “Multiple active voltage stabilizations for multi-reflection time-of-flight mass spectrometry,” *Review of Scientific Instruments*, vol. 92, no. 6, p. 063203, 2021.

[44] D. Manura, “SIMION HS1 collision model REV4,” 2007.

[45] F. Maier, M. Vilen, I. Belosevic, F. Buchinger, C. Kanitz, S. Lechner, E. Leistenschneider, W. Nörtershäuser, P. Plattner, L. Schweikhard, S. Sels, F. Wienholtz, and S. Malbrunot-Ettenauer, “Simulation studies of a 30-kev mr-tof device for highly sensitive collinear laser spectroscopy,” *Nuclear Instruments and Methods in Physics Research Section A: Accelerators, Spectrometers, Detectors and Associated Equipment*, vol. 1048, p. 167927, 2023.

[46] Y. Tian, Y. Wang, J. Wang, X. Zhou, and W. Huang, “Designing a multi-reflection time-of-flight mass analyzer for LPT,” *International Journal of Mass Spectrometry*, vol. 408, pp. 28–32, 2016.

[47] D. Manura, “SIMION Simplex optimizer,” 2007.

[48] S. Schwarz, G. Bollen, R. Ringle, J. Savory, and P. Schury, “The LEBIT ion cooler and buncher,” *Nuclear Instruments and Methods in Physics Research Section A: Accelerators, Spectrometers, Detectors and Associated Equipment*, vol. 816, pp. 131–141, 2016.

[49] G. E. P. Box and M. E. Muller, “A Note on the Generation of Random Normal Deviates,” *The Annals of Mathematical Statistics*, vol. 29, no. 2, pp. 610 – 611, 1958.

[50] C. Kanitz, “Construction and characterization of a Paul trap for laser spectroscopy of exotic radionuclides in an MR-ToF device.” M.Sc. thesis, Friedrich-Alexander-University Erlangen-Nürnberg, 2019.

[51] A. Verenchikov, M. I. Yavor, and T. V. Pomozov, “Electrostatic ion mirrors,” 2016. US Patent 9,396,922 B2.

[52] M. Yavor, N. Gall, M. Muradymov, T. Pomozov, I. Kurnin, A. Monakov, A. Arsenev, Y. T. Oganessian, A. Karpov, A. Rodin, L. Krupa, T. Dickel, W. Plaß, and C. Scheidenberger, “Development of a mass spectrometer for high-precision mass measurements of superheavy elements at JINR,” *Journal of Instrumentation*, vol. 17, p. P11033, nov 2022.

[53] W. R. Plaß, T. Dickel, S. A. S. Andres, J. Ebert, F. Greiner, C. Hornung, C. Jesch, J. Lang, W. Lippert, T. Majoros, D. Short, H. Geissel, E. Haettner, M. P. Reiter, A.-K. Rink, C. Scheidenberger, and M. I. Yavor, “High-performance multiple-reflection time-of-flight mass spectrometers for re-

search with exotic nuclei and for analytical mass spectrometry," *Physica Scripta*, vol. T166, p. 014069, nov 2015.

[54] S. Sailer, "Improvements of the Optical Detection Setup for Collinear Laser Spectroscopy of Short-Lived Radioactive Nuclides and Spectroscopic Studies on the Hyperfine Parameters of  $^{208}\text{Bi}.$ ." M.Sc. thesis, TU Munich, 2016.

[55] W. Gins, "Development of a dedicated laser-polarization beamline for ISOLDE-CERN." PhD thesis, KU Leuven, 2019.

[56] F. Hummer, "Investigation of space charge effects in MIRACLS' proof-of-principle MR-ToF device." B.Sc. thesis, Johannes Kepler University Linz, 2019.

[57] D. Manura, "SIMION Charge Repulsion," 2007.

[58] A. Nieminen, P. Campbell, J. Billowes, D. Forest, J. Griffith, J. Huikari, A. Jokinen, I. Moore, R. Moore, G. Tungate, and J. Äystö, "Cooling and bunching of ion beams for collinear laser spectroscopy," *Nuclear Instruments and Methods in Physics Research Section B: Beam Interactions with Materials and Atoms*, vol. 204, pp. 563–569, 2003. 14th International Conference on Electromagnetic Isotope Separators and Techniques Related to their Applications.

[59] S. Van Gorp, M. Beck, M. Breitenfeldt, V. De Leebeeck, P. Friedag, A. Herlert, T. Iitaka, J. Mader, V. Kozlov, S. Roccia, G. Soti, M. Tandecki, E. Traykov, F. Wauters, C. Weinheimer, D. Zákoucký, and N. Severijns, "Simbuca, using a graphics card to simulate Coulomb interactions in a Penning trap," *Nuclear Instruments and Methods in Physics Research Section A: Accelerators, Spectrometers, Detectors and Associated Equipment*, vol. 638, no. 1, pp. 192–200, 2011.

[60] R. Hipple and S. Lund, "Modeling of Space-Charge Effects in the ORISS MRTOF Device for Applications to FRIB," *Proc. NAPAC'19*, pp. 786–788, 10 2019. <https://doi.org/10.18429/JACoW-NAPAC2019-WEPLS10>.

[61] Personal Communications with Frank Wienholtz, ISOLTRAP collaboration, 2018.

[62] C. Izzo, J. Bergmann, K. A. Dietrich, E. Dunling, D. Fusco, A. Jacobs, B. Koote, G. Kripkó-Koncz, Y. Lan, E. Leistenschneider, E. M. Lykiardopoulou, I. Mukul, S. F. Paul, M. P. Reiter, J. L. Tracy, C. Andreou, T. Brunner, T. Dickel, J. Dilling, I. Dillmann, G. Gwinner, D. Lascar, K. G. Leach, W. R. Plaß, C. Scheidenberger, M. E. Wieser, and A. A. Kwiatkowski, "Mass measurements of neutron-rich indium isotopes for  $r$ -process studies," *Phys. Rev. C*, vol. 103, p. 025811, Feb 2021.

[63] S. F. Paul, J. Bergmann, J. D. Cardona, K. A. Dietrich, E. Dunling, Z. Hockenberry, C. Hornung, C. Izzo, A. Jacobs, A. Javaji, B. Koote, Y. Lan, E. Leistenschneider, E. M. Lykiardopoulou, I. Mukul, T. Murböck, W. S. Porter, R. Silwal, M. B. Smith, J. Ringuette, T. Brunner, T. Dickel, I. Dillmann, G. Gwinner, M. MacCormick, M. P. Reiter, H. Schatz, N. A. Smirnova, J. Dilling, and A. A. Kwiatkowski, "Mass measurements of  $^{60-63}\text{Ga}$  reduce x-ray burst model uncertainties and extend the evaluated  $T = 1$  isobaric multiplet mass equation," *Phys. Rev. C*, vol. 104, p. 065803, Dec 2021.

[64] Open-source, "WARP: open-source particle-in-cell Python package," 2022.

[65] P. Fischer, S. Knauer, G. Marx, and L. Schweikhard, "In-depth study of in-trap high-resolution mass separation by transversal ion ejection from a multi-reflection time-of-flight device," *Review of Scientific Instruments*, vol. 89, no. 1, p. 015114, 2018.

[66] F. Wienholtz, S. Kreim, M. Rosenbusch, L. Schweikhard, and R. Wolf, "Mass-selective ion ejection from multi-reflection time-of-flight devices via a pulsed in-trap lift," *International Journal of Mass Spectrometry*, vol. 421, pp. 285–293, 2017.

[67] N. E. Bradbury and R. A. Nielsen, "Absolute values of the electron mobility in hydrogen," *Phys. Rev.*, vol. 49, pp. 388–393, Mar 1936.

[68] P. Fischer, G. Marx, and L. Schweikhard, "Multiple ion capture and separation in an electrostatic storage device," *International Journal of Mass Spectrometry*, vol. 435, pp. 305–314, 2019.

# **Eigenständigkeitserklärung**

Hiermit erkläre ich, dass diese Arbeit bisher von mir weder an der Mathematisch-Naturwissenschaftlichen Fakultät der Universität Greifswald noch einer anderen wissenschaftlichen Einrichtung zum Zwecke der Promotion eingereicht wurde.

Ferner erkläre ich, dass ich diese Arbeit selbstständig verfasst und keine anderen als die darin angegebenen Hilfsmittel und Hilfen benutzt und keine Textabschnitte eines Dritten ohne Kennzeichnung übernommen habe.

Franziska Maier

## **9 Curriculum vitae**

# Franziska Maria Maier

147 Alle des Quercus  
F-01630 Saint-Genis-Pouilly  
📞 +491788680542  
✉️ franziska.maria.maier@cern.ch  
date of birth: 1994, July 28  
nationality: Austria + Germany  
[ORCID](#), [ResearchGate](#), [LinkedIn](#)

## Education

2020–now **CERN Doctoral student**  
PhD candidate at the University of Greifswald, Germany.  
Research work performed full time at ISOLDE/CERN.  
Supervisors: Stephan Malbrunot-Ettenauer, Lutz Schweikhard.

2017–2019 **Technical Physics - Master of Science with Honours**  
Johannes Kepler University, Linz, Austria.  
Master thesis about “*Laser Spectroscopy of Short-Lived Radionuclides in an Ion Trap: MIRACLS’ proof-of-principle experiment and the simulation of the future 30-keV MR-ToF device*”. Research work performed full time at ISOLDE/CERN.  
Supervisors: Thomas Klar, Stephan Malbrunot-Ettenauer, Lutz Schweikhard.

2013–2016 **Technical Physics - Bachelor of Science with Honours**  
Johannes Kepler University, Linz, Austria.  
Bachelor thesis about “*Difference Fluorescence Line-Narrowing Spectroscopy on Pigment-Protein Complexes*”, Institute for Theoretical Physics, Linz, Austria.  
Supervisors: Julian Adolphs, Thomas Renger.

## Awards

09/2022 Best Poster Award at the TCP conference in Glashütten. There were in total 62 posters.

09/2022 LISA ITN Achievement Award for the outstanding research in laser spectroscopy presented at the LISA School 'Structure of Complex Atoms'.

09/2020 Wilhelm Macke Master Thesis Prize at the Johannes Kepler University.

2013–2017 Study Achievement Award for excellent grades.

## Scholarships

10/2022 Grant to cover the full conference fees awarded by the European Nuclear Physics Conference Organization.

2020–2023 Wolfgang Gentner Scholarship for my PhD at CERN.

2017–2019 Member of Pro Scientia.

2016 & 2018 IPS Stipendium des Landes Oberösterreich for the “Utrecht Summer School in Theoretical Physics” lead by Prof. Rembert Duine in 2016 and the research stay at CERN in 2018.

2018 Wilhelm Macke Mobilitätsstipendium for the research stay at CERN.

2016 Scholarship awarded by the Internationale Akademie Traunkirchen to take part in the workshop “Von Einstein zu Teleportation und Quantencomputer” lead by Prof. Anton Zeilinger.

## Outreach Experience

- Feb. 2023: Ambassador for science via the program “Femmes et filles de science et technologie” for the German School in Geneva.
- 2022–now: Tour guide of the ISOLDE facility for students, teachers and the general public.
- 2021–now: Responsible for the MIRACLS homepage.
- 2022: Participation in one video for CERN’s Science Gateway Exhibition for the general public.
- 2022: First author of the article “Doppler and sympathetic cooling for the investigation of short-lived ions” in the ISOLDE Newsletter for 2022.

## Talks and Poster Presentations

2x Invited Seminar	High Flux Mass Separation and Highly Sensitive Laser Spectroscopy in MR-ToF Devices, Seminar at LP2i, Bordeaux & Seminar at FRIB, East-Lansing, 2023.
Talk	Optimisation of the MIRACLS components for MR-ToF mass separation, PUMA collaboration meeting, CERN, 2023.
Seminar	Simulation and Experimental Study for a Highly Selective and High-Flux MR-ToF Mass Separator, ISOLDE Seminar, CERN, 2023.
Talk	Towards a Highly Selective and High Flux Mass Separator for Medical Applications, Medical Applications Project Forum, CERN, 2022.
Poster	Towards a Highly Selective and High Flux MR-ToF Mass Separator, ISOLDE workshop, CERN, 2022.
3x Talk, 3x Poster	Highly-Sensitive Photodetachment Spectroscopy in an MR-ToF Device. DESIREE Symposium, Stockholm & LISA Summer School, Normandy & TCP conference, Glashütten & EuNPC, Santiago de Compostela & Physikerinnentagung, Karlsruhe, 2022 & DPG Spring Meeting, Hanover, 2023.
Seminar, 2x Invited Seminar	The MIRACLS Technique: In-Trap Laser Spectroscopy for Nuclear Structure Studies. Nuclear Physics Seminar, KTH Stockholm & Seminar für Kern- und Radiochemie, University of Mainz, 2022 & Seminar at University of Edinburgh, 2023.
Talk	The Multi Ion Reflection Apparatus for Highly Sensitive Laser Spectroscopy. Gentner Day, CERN, 2022.
3x Talk, 3x Poster	Doppler- and Sympathetic Cooling for the Investigation of Short-Lived Radionuclides. ISOLDE seminar, CERN & ISOLDE Workshop and Users Meeting, CERN & Joliot International School, France, 2021 & ECCTI, CERN & TCP conference, Glashuetten, 2022 & DPG Spring Meeting, Hanover, 2023.
Talk	MIRACLS: From Proof of Principle Towards First Online Operation. ISOLDE Workshop and Users Meeting, CERN, 2020.
Invited Talk	Dem Atomkern auf der Spur - Mit der JKU ans CERN. Wilhelm Macke Master Thesis Prize Talk, Johannes Kepler University, Austria, 2020.
Poster	High Resolution Tomography of Mesoscopic Pore Structures. Status-Seminar of the CRC 1333, Germany, 2019.
Poster	Simulations of Ion Trajectories inside the Multi Ion Reflection Apparatus for Collinear Laser Spectroscopy (MIRACLS). ISOLDE Workshop and Users Meeting, CERN, 2018.
2x Talk	Laser Spectroscopy of Short-Lived Radionuclides in an Ion Trap: MIRACLS’ Proof-of-Principle Experiment. ISOLDE Seminar & Summer Student Session, CERN, 2017.

## Publications

F.M. Maier & E. Leistenschneider, et al. **Highly-Sensitive Photodetachment Spectroscopy in an MR-ToF Device.** *In preparation.*

Leading efforts for developing and commissioning of the new technique. E. Leistenschneider and I performed all the measurements and the analysis and we will write the manuscript together.

F.M. Maier, et al. **Study of the Drift Tube Length on the Performance of MR-ToF Devices.** *In preparation.*

Supported by my supervisors, I figured out that the drift tube length has a significant impact on the performance of MR-ToF devices for mass separation and laser spectroscopic applications. I developed the simulation code and performed all the simulations. In order to benchmark the simulation code, I carried out the measurements and the analysis supported by contributions from some of the co-authors. I currently write the manuscript.

F.M. Maier, F. Buchinger, L. Croquette, P. Fischer, H. Heylen, F. Hummer, C. Kanitz, A.A. Kwiatkowski, V. Lagaki, S. Lechner, E. Leistenschneider, G. Neyens, P. Plattner, A. Roitman, M. Rosenbusch, L. Schweikhard, S. Sels, M. Vilen, F. Wienholtz, S. Malbrunot-Ettenauer. **Increased Beam Energy as a Pathway Towards a Highly Selective and High-Flux MR-ToF Mass Separator.** *Submitted to Nucl. Instrum. Meth. A.*

I took the lead in performing the mass resolving power measurements, corresponding optimizations and some of the collisional excitation measurements. I developed most of the simulation code, performed the simulations and the analysis. Supported by my supervisor, I wrote the manuscript.

F.M. Maier, M. Vilen, I. Belosevic, F. Buchinger, C. Kanitz, S. Lechner, E. Leistenschneider, W. Nörtershäuser, P. Plattner, L. Schweikhard, S. Sels, F. Wienholtz, S. Malbrunot-Ettenauer. **Simulation Studies of a 30-keV MR-ToF Device for Highly Sensitive Collinear Laser Spectroscopy.** *Nucl. Instrum. Meth. A* Vol 1048, 2023.

I was largely involved in the conceptual design of the apparatus. I wrote the simulation code and performed the simulations. Supported by my supervisor, I wrote the manuscript.

S. Sels, F.M. Maier, M. Au, P. Fischer, C. Kanitz, V. Lagaki, S. Lechner, E. Leistenschneider, D. Leimbach, E.M. Lykiardopoulou, A.A. Kwiatkowski, T. Manovitz, G. Neyens, S. Rothe, L. Schweikhard, M. Vilen, R.N. Wolf, S. Malbrunot-Ettenauer. **Doppler- and Sympathetic Ion Cooling for the Investigation of Short-Lived Radio-nuclides.** *Phys. Rev. Res.* 4, 033229, 2022.

I coordinated many of the necessary modifications of the setup for laser cooling and lead many measurement campaigns, for which I also analysed the data. I developed simulation and calculation tools and performed the simulations. I also was involved in the finalization of the manuscript.

V. Lagaki, H. Heylen, I. Belosevic, P. Fischer, C. Kanitz, S. Lechner, F.M. Maier, W. Nörtershäuser, P. Plattner, M. Rosenbusch, S. Sels, L. Schweikhard, M. Vilen, F. Wienholtz, R.N. Wolf, S. Malbrunot-Ettenauer. **An Accuracy Benchmark of the MIRACLS Apparatus: Conventional, Single-Passage Collinear Laser Spectroscopy inside a MR-ToF Device.** *Nucl. Instrum. Meth. A* Vol 1014, 2021.

I coordinated many of the necessary modifications of the ion-optical apparatus for laser spectroscopic applications. I performed the initial ion optical tuning as well as first test measurements including the first isotope shift measurements and their analysis supported by contributions from other team members. I also did the field calculations in the Paul trap.

V. Lagaki, P. Fischer, H. Heylen, F. Hummer, S. Lechner, F.M. Maier, P. Plattner, M. Rosenbusch, S. Sels, F. Wienholtz, R. Wolf, W. Nörtershäuser, L. Schweikhard, S. Malbrunot-Ettenauer. **Stray-Light Suppression for the MIRACLS Proof-of-Principle Experiment.** *Acta Physica Polonica B* Vol 51 571-576, 2020.

I designed and installed the aperture tubes, set up the spatial filter and performed the very first stray-light reduction measurements allowing to reduce the laser-induced background by an order of magnitude.

S. Sels, P. Fischer, H. Heylen, V. Lagaki, S. Lechner, F.M. Maier, P. Plattner, M. Rosenbusch, F. Wienholtz, R. Wolf, W. Nörtershäuser, L. Schweikhard, S. Malbrunot-Ettenauer. **First Steps in the Development of the Multi Ion Reflection Apparatus for Collinear Laser Spectroscopy.** *Nucl. Instrum. Meth. B.* Vol 467 310-314, 2020.

I coordinated many of the necessary modifications of the ion-optical apparatus for laser spectroscopic applications. I performed the ion optical tuning and together with the other team members the measurements and analysis. I also was involved in setting up the laser system after the frequency doubler.

S. Lechner, P. Fischer, H. Heylen, V. Lagaki, F.M. Maier, P. Plattner, M. Rosenbusch, S. Sels, F. Wienholtz, R. Wolf, W. Nörtershäuser, L. Schweikhard, S. Malbrunot-Ettenauer. **Fluorescence Detection as a New Diagnostics Tool for Electrostatic Ion Beam Traps.** *Hyperfine Interactions* 240:95, 2019.

I wrote the simulation code, performed first test simulations and explained the simulation code to one PhD student who performed all the simulations discussed in this manuscript.

F.M. Maier, P. Fischer, H. Heylen, V. Lagaki, S. Lechner, P. Plattner, S. Sels, F. Wienholtz, W. Nörtershäuser, L. Schweikhard, S. Malbrunot-Ettenauer. **Simulations of a Proof-of-Principle Experiment for Collinear Laser Spectroscopy within a Multi-Reflection Time-of-Flight Device.** *Hyperfine Interactions* 240:54, 2019.

I wrote the simulation code and performed the simulations. Based on the simulation results, I coordinated necessary modifications of the ion-optical apparatus for laser spectroscopic applications. I performed the ion beam tuning, the measurements, analysis and the comparison to the simulations. I wrote the paper together with my supervisor.

J. Adolp, F.M. Maier, T. Renger. **Wavelength-Dependent Exciton-Vibrational Coupling in the Water-Soluble Chlorophyll Binding Protein Revealed by Multi-Level Theory of Difference Fluorescence Line Narrowing.** *The Journal of Physical Chemistry B*, 122, 8891-8899, 2018.

Supported by my supervisors, I developed a new method for the calculation of difference fluorescence line-narrowing spectra, calculated the spectra and compared them with experimental data.

# 10 Acknowledgments

I would like to thank all the people who contributed in one way or the other to this PhD thesis. These include my supervisors and colleagues, my family, friends and flatmates. It was not easy to start my PhD work at the begin of the Covid pandemic, so thanks to all of you who made the period of lockdown and teleworking not just bearable but often also a very nice time. As usual there are a few people who extraordinarily stood out. I hence want to say a big thank you to

- Erich Leistenschneider: I am very glad that I had the chance to work with you on our photodetachment project. Thank you very much for your guidance and mentoring as well as for your calmness in stressful situations. Thanks for all the many discussions as well as your regular feedback allowing myself to grow both personally and professionally. Your comments also helped me a lot to improve the quality of my talks and manuscripts. Thank you very much!
- Liss Rodriguez, Simon Lechner, Peter Plattner, Agi Koszorus, Katerina Chrysalidis: Thank you very much for jumping in whenever I needed help on our laser system and especially a big thank you to Liss for explaining many aspects of our laser-related equipment to me.
- Simon Sels: Thank you for giving an excellent introduction into the laser cooling project to me, which allowed me to fastly take over and complete the experimental laser cooling program after you had left CERN.
- Carina Kanitz: Thank you very much for joining myself on many long evenings in the lab during the finalization phase of the laser cooling project and in your starting phase as a MSc thesis student. Also thanks a lot for the interesting discussions we had and for performing the simulation studies of MIRACLS' new Paul trap, which served as important input parameter for many of my CLS and space-charge simulations in MIRACLS' 30-keV MR-ToF setup.
- Sebastian Rothe, David Leimbach and Yago Gracia: Thank you for installing a surface ion source at the MIRACLS' low-energy setup and commissioning it together with myself and Carina Kanitz. This ion source was very useful for demonstrating sympathetic cooling of Potassium ions and a prerequisite for the photodetachment project.
- Hanne Heylen and Fabian Hummer: Thank you for performing some of the collisional excitation measurements which were very useful for benchmarking the space-charge simulation code. An additional thank you to Fabian, who performed as BSc student a preliminary analysis of some of the collisional excitation measurements and a first comparison to preliminary space-charge simulations.
- Stephan Malbrunot-Ettenauer: Thank you very much for your constant support, for all the meetings and discussions, your optimism and for your detailed proof-reading and editing of my manuscripts! Even though the very limited in-person contact due to Covid restrictions and due to your move to Canada after those were lifted was far from ideal, we nevertheless could obtain nice measurement results. Thank you!
- Lutz Schweikhard: Thank you very much for your detailed proof-reading of my manuscripts and the corresponding discussions.